

# NAVAL POSTGRADUATE SCHOOL

## Monterey, California

AD-A218 667



The Viability of Acoustic Tomography in  
Monitoring the Circulation of  
Monterey Bay

by

James H. Miller, Laura L. Ehret,  
Robert C. Dees and Theresa M. Rowan

October 1989 to December 1989

Approved for public release; distribution unlimited.

Prepared for:

Monterey Bay Aquarium Research Institute  
Pacific Grove, CA 93950

DTIC  
ELECTE  
MAR 5 1990  
S B D

20 03 02 070

NAVAL POSTGRADUATE SCHOOL  
Monterey, CA

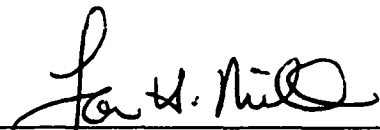
Rear Admiral R.W. West, Jr.  
Superintendent

H. Shull  
Provost



This report was prepared for the Monterey Bay Aquarium Research Institute (MBARI) and funded by MBARI, the Office of Naval Research, and the Naval Postgraduate School Research Council.

Reproduction of this report is authorized.

This report was prepared by:

  
James H. Miller  
Assistant Professor  
Department of Electrical and  
Computer Engineering

Reviewed by:

  
John P. Powers  
Chairman, Department of Electrical  
and Computer Engineering  
Gordon E. Schacher  
Dean of Faculty and Graduate Education

Unclassified

Security Classification of this page

## REPORT DOCUMENTATION PAGE

1a Report Security Classification <b>Unclassified</b>		1b Restrictive Markings				
2a Security Classification Authority		3 Distribution Availability of Report <b>Approved for public release; distribution is unlimited.</b>				
2b Declassification/Downgrading Schedule		5 Monitoring Organization Report Number(s)				
4 Performing Organization Report Number(s)		7a Name of Monitoring Organization <b>Naval Postgraduate School</b>				
6a Name of Performing Organization <b>Naval Postgraduate School</b>	6b Office Symbol (If Applicable) <b>62</b>	7b Address (city, state, and ZIP code) <b>Monterey, CA 93943-5000</b>				
6c Address (city, state, and ZIP code) <b>Monterey, CA 93943-5000</b>	8a Name of Funding/Sponsoring Organization	9 Procurement Instrument Identification Number				
8b Office Symbol (If Applicable)	8c Address (city, state, and ZIP code)	10 Source of Funding Numbers				
<table border="1"> <tr> <td>Program Element Number</td> <td>Project No</td> <td>Task No</td> <td>Work Unit Accession No</td> </tr> </table>			Program Element Number	Project No	Task No	Work Unit Accession No
Program Element Number	Project No	Task No	Work Unit Accession No			

11 Title (Include Security Classification) **The Viability of Acoustic Tomography in Monitoring the Circulation of Monterey Bay**

12 Personal Author(s) **James H. Miller, Laura L. Ehret, Robert C. Dees, and Theresa M. Rowan**

13a Type of Report <b>Technical Report</b>	13b Time Covered <b>From Oct 88 To Dec 89</b>	14 Date of Report (year, month, day) <b>December 29, 1989</b>	15 Page Count <b>200</b>
---	--	--	-----------------------------

16 Supplementary Notation **The views expressed in this thesis are those of the authors and do not reflect the official policy or position of the Department of Defense or the U.S. Government.**

17 Codes  
Field Subgroup  
18 Subject Terms (continue on reverse if necessary and identify by block number)  
**Acoustic Tomography, Underwater Acoustics. (EG)**

19 Absira. (c. use if necessary and identify by block number)

This report presents the results of a fifteen month study on the viability of acoustic tomography in monitoring the circulation of Monterey Bay, California. The basis for ocean acoustic tomography is the measurement of travel times of coded acoustic signals between the transceivers. The sound speed field and current structure can be inferred from the fluctuations in the travel times. However, the extreme bathymetry of the Monterey Submarine Canyon complicates the acoustic transmissions in the Bay. The study consisted of an experiment and a computer modeling effort. The experiment consisted of transmitting tomography signals in the Bay for four days. The signals were received with a sonobuoy-based telemetry system. The experimental effort showed multipath arrivals that were stable and resolvable. The modeling effort involved the use of 2-D and 3-D ray tracing computer programs. The programs had difficulty in modeling the effects of Monterey Bay's extreme bathymetry making the multipath identification challenging. Progress is expected with the augmentation of the ray tracing programs with Gaussian beam and time front postprocessors.

20 Distribution/Availability of Abstract <input checked="" type="checkbox"/> unclassified/unlimited <input type="checkbox"/> same as report <input type="checkbox"/> DTIC users		21 Abstract Security Classification <b>Unclassified</b>
22a Name of Responsible Individual <b>James H. Miller</b>		22b Telephone (Include Area code) <b>(408) 646-2384</b>
		22c Office Symbol <b>62Mr</b>

DD FORM 1473, 84 MAR

83 APR edition may be used until exhausted

security classification of this page

All other editions are obsolete

Unclassified

### **Abstract**

This report presents the results of a fifteen month study on the viability of acoustic tomography in monitoring the circulation of Monterey Bay, California. The basis for ocean acoustic tomography is the measurement of travel times of coded acoustic signals between the transceivers. The sound speed field and current structure can be inferred from the fluctuations in the travel times. However, the extreme bathymetry of the Monterey Submarine Canyon complicates the acoustic transmissions in the Bay. The study consisted of an experiment and a computer modeling effort. The experiment consisted of transmitting tomography signals in the Bay for four days. The signals were received with a sonobuoy-based telemetry system. The experimental effort showed multipath arrivals that were stable and resolvable. The modeling effort involved the use of 2-D and 3-D ray tracing computer programs. The programs had difficulty in modeling the effects of Monterey Bay's extreme bathymetry making the multipath identification challenging. Progress is expected with the augmentation of the ray tracing programs with Gaussian beam and time front postprocessors.

Accession For	
NTIS GRA&I	<input checked="" type="checkbox"/>
DTIC TAB	<input type="checkbox"/>
Unannounced	<input type="checkbox"/>
Justification	
By	
Distribution/	
Availability Codes	
Dist	Avail and/or Special
A-1	

# Contents



<b>1</b>	<b>Introduction</b>	<b>11</b>
1.1	The Original Concept . . . . .	12
1.2	Results of the study . . . . .	13
1.3	Report Overview . . . . .	16
<b>2</b>	<b>Background</b>	<b>17</b>
2.1	Ocean Acoustic Tomography . . . . .	17
2.1.1	The Forward Problems . . . . .	18
2.1.2	The Inverse Problem . . . . .	21
2.1.3	Discussion . . . . .	22
2.2	Monterey Bay . . . . .	23
2.2.1	Bathymetry . . . . .	23
2.2.2	Geology and Sediments . . . . .	26
2.2.3	Currents . . . . .	30
2.2.4	Temperature and Salinity Variations . . . . .	33
2.2.5	Tides . . . . .	35
2.2.6	Surface Waves . . . . .	35
2.2.7	Internal Waves and Canyon Currents . . . . .	37
<b>3</b>	<b>Experimental Effort</b>	<b>43</b>
3.1	Experiment Objectives . . . . .	43
3.1.1	Location and Description . . . . .	44
3.1.2	Receiver Placement . . . . .	46
3.2	Equipment . . . . .	47
3.2.1	Transmitter . . . . .	47
3.2.2	Receivers . . . . .	49
3.2.3	Acoustic Data Recording . . . . .	49
3.2.4	NDBC Wave Measurement and ARGOS buoys . . . . .	51
3.2.5	Sound Speed Profile Measurement . . . . .	54

3.2.6	Acoustic Doppler Current Profiler . . . . .	55
3.3	Summary of the Experimental Procedure . . . . .	55
3.4	Signal Processing . . . . .	56
3.4.1	Signal design . . . . .	56
3.4.2	Signal demodulation and correlation system . . . . .	60
3.4.3	Travel time estimation . . . . .	64
3.4.4	Summary of signal processing . . . . .	66
3.5	Experimental Results . . . . .	67
3.5.1	General Summary of Data . . . . .	67
3.5.2	Station J Data . . . . .	69
3.5.3	Analysis of Arrival Time Fluctuations at Surface Wave Frequencies . . . . .	74
3.5.4	Analysis of Arrival Time Fluctuations at Internal Wave Frequencies . . . . .	81
3.5.5	Summary of experimental results . . . . .	81
4	Modeling Effort . . . . .	86
4.1	The Multiple Profile Ray-Tracing Program . . . . .	86
4.1.1	Description . . . . .	86
4.1.2	Program Flow . . . . .	87
4.1.3	MPP Input/Output . . . . .	93
4.2	3-D Ray Tracing with HARPO . . . . .	109
4.2.1	Hamiltonian Ray Tracing . . . . .	110
4.2.2	Application . . . . .	111
5	Conclusions . . . . .	116
A	MPP Data . . . . .	118
A.1	Bathymetry Data for Receiver Locations . . . . .	118
A.2	MPP Ray Traces and Stick Plots . . . . .	125
B	Chronologic Summary of Events in the 1988 Monterey Bay Experiment . . . . .	142
B.1	12 December 1988 . . . . .	142
B.2	13 December 1988 . . . . .	142
B.3	14 December 1988 . . . . .	144
B.4	15 December 1988 . . . . .	144
B.5	16 December 1988 . . . . .	145
B.6	Data Disposition . . . . .	146

<b>C</b>	<b>Maximal-length Sequences and the Fast Hadamard Transform</b>	<b>147</b>
C.1	Introduction . . . . .	147
C.2	Generating the M-sequence . . . . .	148
C.3	The Hadamard Matrix . . . . .	150
C.4	Input and Output Vector Order Permutation . . . . .	152
C.5	The Fast Hadamard Transform . . . . .	154
C.6	Using the Reverse Code . . . . .	156
C.7	Correlation Procedure . . . . .	156
C.8	Example . . . . .	158
C.9	Summary . . . . .	158
<b>D</b>	<b>Additional Data for Station J</b>	<b>160</b>
D.1	Hadamard Transformed Acoustic Signal . . . . .	160
D.2	Arrival Time and Surface Wave Spectra . . . . .	187
	<b>Initial Distribution List</b>	<b>199</b>

# List of Figures

1.1	Possible Monterey Bay tomography transceiver locations. . .	14
1.2	An example of the multipaths between tomography source and receiver in Monterey Bay. . . . .	15
2.1	(top) Several transmitters (T) and receivers (R) give many ray paths as viewed from above. (bottom) Each slice may contain numerous eigenrays connecting the transmitters and receivers. This diagram is from a 1983 experiment near Bermuda.	19
2.2	Monterey Bay, California. . . . .	24
2.3	Distribution of sediment types in Monterey Bay. . . . .	28
2.4	Offshore surficial geologic map of Monterey Bay. . . . .	29
2.5	Monterey Bay seasonal current patterns. . . . .	32
2.6	Mean temperature and salinity variation at the mouth of Monterey Bay (station 3) and CalCOFI station during 1950-1962. . . . .	34
2.7	Monterey Bay tidal pattern. . . . .	36
2.8	North Monterey Bay buoy, December 1987, wave energy data.	38
2.9	North Monterey Bay buoy, December 1987, wave energy spectra graph. . . . .	39
2.10	Temperature distribution at (a) high and (b) low internal tide, Monterey Canyon axis, 13-14 September 1979. . . . .	41
3.1	Monterey Bay showing the positions of the tomography source and receivers (positions marked with ●). The source is at station A while all others are receivers. The shore station is marked with Δ. . . . .	45
3.2	The 224 Hz resonant tomography source and mooring configuration. . . . .	48



3.3	Modified AN/SSQ-57 sonobuoy as used in the Monterey Bay Acoustic Tomography Experiment. The hydrophone rests on the bottom to eliminate motion. . . . .	50
3.4	Sonobuoy data recording system located in the van. This system receives the sonobuoy radio transmission, demodulates it for the acoustic signal, and records that signal on videotape using pulse code modulation. . . . .	52
3.5	Comparison of resolved and unresolved pulses. . . . .	57
3.6	Quadrature demodulation and digitization performed in the Monterey Bay Acoustic Tomography Experiment . . . . .	61
3.7	Diagram of tomography signal data flow for 'real time' digitization and code correlation. . . . .	63
3.8	Two dimensional ray path predicted using MPP. This eigenray connects the source at Station A to the receiver at Station J. . . . .	70
3.9	Sound speed profile from near Station J. Note that any ray path will be refracted downward. The trace has two lines, one as the CTD goes down and the other as it is brought back to the surface. . . . .	72
3.10	Sound speed profile from near mid-Bay. This profile is typical of the profiles found in deep water at the time of the experiment and very close to the profile used in MPP for eigenray prediction. . . . .	73
3.11	Received acoustic signal after Hadamard transforming for maximal-length sequence from Station J, 14DEC88 1855 to 1957 PST. Each line is 31 seconds of data coherently averaged to one 1.9375 second period. The earliest period is in the foreground and the latest is at the back. . . . .	75
3.12	Arrival time estimate for Station J from 1855 to 1924 PST on 14Dec88. The fast fluctuations in arrival time are due to surface waves changing the path length. Lower frequency oscillations from other causes are also seen. . . . .	76
3.13	Arrival time estimate for Station J from 1925 to 1955 PST on 14Dec88. The fast fluctuations in arrival time are due to surface waves changing the path length. Lower frequency oscillations from other causes are also seen. . . . .	77
3.14	Arrival time power spectrum for Station J. Spectrum from 2.2 hours of arrival times series, 1855 to 2107 14 Dec88 PST. . . . .	79

3.15	Surface wave power spectrum in Monterey Bay at 2000 PST on 14 Dec88 as taken from the NDBC wave measuring buoy southwest of Santa Cruz. . . . .	80
3.16	Arrival time data for Station J lowpass filtered to 0.00258 Hz (Period = 6.4 minutes). . . . .	82
3.17	Arrival time data for Station J lowpass filtered to 0.00258 Hz (Period = 6.4 minutes). . . . .	83
3.18	Arrival time data for Station J lowpass filtered to 0.00258 Hz (Period = 6.4 minutes). High amplitude after 0400 is due to low SNR during storm. . . . .	84
3.19	Arrival time data for Station J lowpass filtered to 0.00258 Hz (Period = 6.4 minutes). . . . .	85
4.1	MPP block diagram with input and output files. . . . .	88
4.2	Receiver hydrophone locations for ray tracing. . . . .	94
4.3	Typical December sound speed profile for Monterey Bay. . . . .	98
4.4	A model of the bathymetry of Monterey Bay region. . . . .	113
4.5	Planar view of rays calculated from Station J towards the tomography transmitter. . . . .	114
4.6	Top view of rays calculated from Station J towards the tomography transmitter. . . . .	115
A.1	Ray trace for receiver location 1. . . . .	126
A.2	Stick plot for receiver location 1. . . . .	127
A.3	Ray trace for receiver location 2. . . . .	128
A.4	Stick plot for receiver location 2. . . . .	129
A.5	Ray trace for receiver location 4. . . . .	130
A.6	Stick plot for receiver location 4. . . . .	131
A.7	Ray trace for receiver location 5. . . . .	132
A.8	Stick plot for receiver location 5. . . . .	133
A.9	Ray trace for receiver location 7. . . . .	134
A.10	Stick plot for receiver location 7. . . . .	135
A.11	Ray trace for receiver location 8. . . . .	136
A.12	Stick plot for receiver location 8. . . . .	137
A.13	Ray trace for receiver location 13. . . . .	138
A.14	Stick plot for receiver location 13. . . . .	139
A.15	Ray trace for receiver location 17. . . . .	140
A.16	Stick plot for receiver location 17. . . . .	141
C.1	Shift register realization . . . . .	149

C.2	Indices formed from matrix octal equivalents. . . . .	153
C.3	Basic Fast Hadamard Transform element for cascading additions and the full diagram for an eight point FHT. . . . .	157
D.1	Tomographic signal, coherently averaged 16 times then magnitude squared. Station J, 1317 to 1419 14DEC88. High ambient noise at the start is from the R/V Point Sur after deploying buoy. . . . .	161
D.2	Tomographic signal, coherently averaged 16 times then magnitude squared. Station J, 1419 to 1521 14DEC88. . . . .	162
D.3	Tomographic signal, coherently averaged 16 times then magnitude squared. Station J, 1521 to 1623 14DEC88. . . . .	163
D.4	Tomographic signal, coherently averaged 16 times then magnitude squared. Station J, 1623 to 1725 14DEC88. . . . .	164
D.5	Tomographic signal, coherently averaged 16 times then magnitude squared. Station J, 1725 to 1827 14DEC88. . . . .	165
D.6	Tomographic signal, coherently averaged 16 times then magnitude squared. Station J, 1827 to 1929 14DEC88. Signal cutoff is due to tape change. . . . .	166
D.7	Tomographic signal, coherently averaged 16 times then magnitude squared. Station J, 1957 to 2059 14DEC88. The previous hour is included as Figure 12 on page 58. Note that the arrival structure is shifted for data from a new tape. . . . .	167
D.8	Tomographic signal, coherently averaged 16 times then magnitude squared. Station J, 2059 to 2201 14DEC88. . . . .	168
D.9	Tomographic signal, coherently averaged 16 times then magnitude squared. Station J, 2201 to 2303 14DEC88. . . . .	169
D.10	Tomographic signal, coherently averaged 16 times then magnitude squared. Station J, 2303 14DEC88 to 0005 15DEC88. . . . .	170
D.11	Tomographic signal, coherently averaged 16 times then magnitude squared. Station J, 0005 to 0107 15DEC88. Note that computer generated time scale is extended past 0000 for convenience in processing. The reason for signal cutoff is that the end of the tape was reached. . . . .	171
D.12	Tomographic signal, coherently averaged 16 times then magnitude squared. Station J, 0052 to 0154 15DEC88. Note that the arrival structure is shifted because of the start of a new tape. . . . .	172

D.13 Tomographic signal, coherently averaged 16 times then magnitude squared. Station J, 0154 to 0256 15DEC88. . . . .	173
D.14 Tomographic signal, coherently averaged 16 times then magnitude squared. Station J, 0256 to 0358 15DEC88. . . . .	174
D.15 Tomographic signal, coherently averaged 16 times then magnitude squared. Station J, 0358 to 0500 15DEC88. High scattering and ambient noise were present at this time because of high winds (the worst windstorm of the year to hit the central California coast). . . . .	175
D.16 Tomographic signal, coherently averaged 16 times then magnitude squared. Station J, 0500 to 0602 15DEC88. High ambient noise and high scattering continue from windstorm. .	176
D.17 Tomographic signal, coherently averaged 16 times then magnitude squared. Station J, 0602 to 0704 15DEC88. The reason for signal cutoff is that the end of the tape was reached. .	177
D.18 Tomographic signal, coherently averaged 16 times then magnitude squared. Station J, 0647 to 0749 15DEC88. The reason for the increased amplitude is unknown. Note that the arrival structure is shifted at the start of the new tape. . .	178
D.19 Tomographic signal, coherently averaged 16 times then magnitude squared. Station J, 0749 to 0851 15DEC88. . . . .	179
D.20 Tomographic signal, coherently averaged 16 times then magnitude squared. Station J, 0851 to 0953 15DEC88. . . . .	180
D.21 Tomographic signal, coherently averaged 16 times then magnitude squared. Station J, 0953 to 1055 15DEC88. . . . .	181
D.22 Tomographic signal, coherently averaged 16 times then magnitude squared. Station J, 1055 to 1157 15DEC88. . . . .	182
D.23 Tomographic signal, coherently averaged 16 times then magnitude squared. Station J, 1157 to 1259 15DEC88. The reason for the signal cutoff is that the end of the tape was reached.	183
D.24 Tomographic signal, coherently averaged 16 times then magnitude squared. Station J, 1226 to 1328 15DEC88. Note that the arrival structure is shifted at the start of the new tape. .	184
D.25 Tomographic signal, coherently averaged 16 times then magnitude squared. Station J, 1328 to 1430 15DEC88. . . . .	185
D.26 Tomographic signal, coherently averaged 16 times then magnitude squared. Station J, 1430 to 1532 15DEC88. Signal cutoff is due to buoy failure. . . . .	186

D.27	Arrival time power spectrum for Station J. Spectrum from 2.2 hours of Arrival Time Series, 2001 to 2213 14DEC88 PST.	188
D.28	Surface wave power spectrum in Monterey Bay. Data is from the NDBC buoy southwest of Santa Cruz, 2100 14DEC88 PST.	189
D.29	Arrival time power spectrum for Station J. Spectrum from 2.2 hours of Arrival Time Series, 2107 to 2319 14DEC88 PST.	190
D.30	Surface wave power spectrum in Monterey Bay. Data is from the NDBC buoy southwest of Santa Cruz, 2200 14DEC88 PST.	191
D.31	Arrival time power spectrum for Station J. Spectrum from 2.2 hours of Arrival Time Series, 2213 14DEC88 to 0005 15DEC88 PST. . . . .	192
D.32	Surface wave power spectrum in Monterey Bay. Data is from the NDBC buoy southwest of Santa Cruz, 2300 14DEC88 PST.	193
D.33	Arrival time power spectrum for Station J. This spectrum was generated using the segmented FFT method on the data from an entire 6 hour tape (the maximum length time series without tape-to-tape synchronization). . . . .	194

# List of Tables

2.1	Up and down-canyon reversal cycle data for Monterey Canyon.	40
2.2	Up and down-canyon reversal cycle data for Carmel Canyon.	42
4.1	Position, range and depth of simulation receivers. . . . .	95
4.2	December sound speed profile values for Monterey Bay region.	99
4.3	Eigenray information for site 16 based on change of source placement. . . . .	101
4.4	Eigenray information for sites 1,2,4,5,7,8 and 13. . . . .	102
4.5	Eigenray information for site 17. . . . .	107
A.1	Bathymetry data for receiver locations 1, 2, and 3. . . . .	119
A.2	Bathymetry data for receiver locations 4, 5, and 6. . . . .	120
A.3	Bathymetry data for receiver locations 7, 8, and 9. . . . .	121
A.4	Bathymetry data for receiver locations 10, 11, and 12. . . . .	122
A.5	Bathymetry data for receiver locations 13, 14, and 15. . . . .	123
A.6	Bathymetry data for receiver locations 16 and 17. . . . .	124
C.1	Shift register contents when generating M-sequence. . . . .	149
C.2	Re-ordering of input and output vectors. . . . .	155

# Chapter 1

## Introduction

This report presents the results of a fifteen month study on the viability of acoustic tomography in monitoring the circulation of Monterey Bay, California. It is envisioned that the Bay could be surrounded by shore-linked acoustic transceivers that would transmit and receive coded acoustic signals. Ocean acoustic tomography uses the fluctuations of measured travel times from a number acoustic multipaths through an ocean body. These travel time fluctuations can be "inverted" to provide an estimate of the intervening sound speed structure (and hence density) and current structure.

Acoustic tomography has been used with success in deep ocean environments where bottom bathymetry has been not a factor. However, applying it to an ocean body like Monterey Bay with its Submarine Canyon introduces a number of questions. These questions deal with the character of acoustic transmissions in the Bay. Namely, for acoustic tomography to be viable, four questions must be answered affirmatively:

1. Are the acoustic arrivals strong enough to accurately estimate their arrival time?
2. Are the acoustic arrivals resolvable from one another?
3. Are the acoustic arrivals stable over time?
4. Are the arrivals identifiable (i.e. comparable) with computer-modeled arrivals?

This study attempts to answer the above questions through two efforts: experiment and computer modeling. The experiment involved the transmission of acoustic signals from a source off of Point Sur to a number of

receivers on the northern shelf of Monterey Bay. The computer modeling effort used two acoustic ray tracing programs to simulate the multipath arrival structure of the received acoustic signals.

## 1.1 The Original Concept

The presence in Monterey Bay of MBARI and five other institutions with strong oceanography programs provides a unique opportunity for a long-term interdisciplinary study of the biology and physics of a coastal environment. This tomography system is intended to be a core measurement system which, with ancillary measurements colocated at the hard-wired tomographic transceivers, would provide a real-time view of the circulation and density structure within the Bay. Data from the relatively sparse spot measurements and integrated tomographic data will be assimilated into dynamical models to provide an interpolated and displayable view of the physical properties (e.g., velocity and thermal structure at selected depths) spanning the measurement domain. These physical models further provide the basis for incorporating biological variables to study (and display) a wide range of physical and biological processes.

The state-of-the-art in ocean acoustic tomography and in associated signal processing and data storage technology has advanced to the point where we can think about the long-term (five year) imaging of the complete oceanographic structure of Monterey Bay.

Recently, much progress has been made in *data assimilation*, the process of integrating data into a dynamical model of the circulation of both large and small scale oceanographic systems. With the measurements available from acoustic tomography and other traditional oceanographic instruments, dynamic models of Monterey Bay could be verified. Acoustic tomography could provide the boundary conditions for the open end of the Bay and verification of the models as time progressed.

The Monterey Bay is a unique location in which to conduct ocean acoustic tomography. The semi-circular geometry of the Bay enables acoustic transceivers to be placed around the Bay near enough to shore to be linked by an underwater cable. The more coverage in angle around the Bay, the better resolved are the oceanographic features. The transceivers would not be data-storage limited as data could be sent up the cable to shore. They would not be power limited as power could come from shore down the cable.

The Monterey Bay tomography system would include a number of tomo-



graphic transceivers placed at the bottom surrounding the bay near shore. The shore substations would be linked to the main data collection station via either land lines or RF telemetry links. An example tomographic system is shown in Figure 1.1. It consists of eight transceivers placed on the periphery of the bay between the depths of 25 to 100 meters. An additional transceiver has been placed near the mouth of the Bay. An array consisting of  $J$  transceivers has  $J \cdot (J - 1)$  horizontal paths across the volume of interest. This includes a two-way path between each transceiver. In addition, depending on the acoustic conditions, there are a number  $K$  vertical multipaths for each horizontal path as illustrated in Figure 1.2. An estimate of the average number of usable multipaths for Monterey Bay is three. Therefore, the total number,  $N$ , of individual acoustic paths through the Bay is  $N = J \cdot (J - 1) \cdot K$  or 168 paths through Monterey Bay for the array pictured in Figure 1.1.

Ongoing oceanographic studies on Monterey Bay could be integrated into the tomography system. A primary forcing mechanism for circulation of the Bay is the oceanic currents at the mouth of the Bay. Planned hydrographic, constituent and current measurements by MBARI, NPS, and other institutions will be extremely useful for this purpose. In addition to the *in situ* measurements, satellite AVHRR (Advanced Very High Resolution Radiometer) thermal maps could be integrated routinely with the tomography. The system could be a focal point for research on the Bay to foster cooperation and improve the communication between the various oceanographic institutions around the Bay.

## 1.2 Results of the study

As mentioned above, the viability of acoustic tomography in monitoring the circulation of an ocean body like Monterey Bay depends on four characteristics of the acoustic arrivals:

1. signal-to-noise ratio,
2. resolvability,
3. stability, and
4. identifiability.

This study has looked at each of the above necessary characteristics with a two-pronged study: an experiment and modeling with a ray-tracing com-

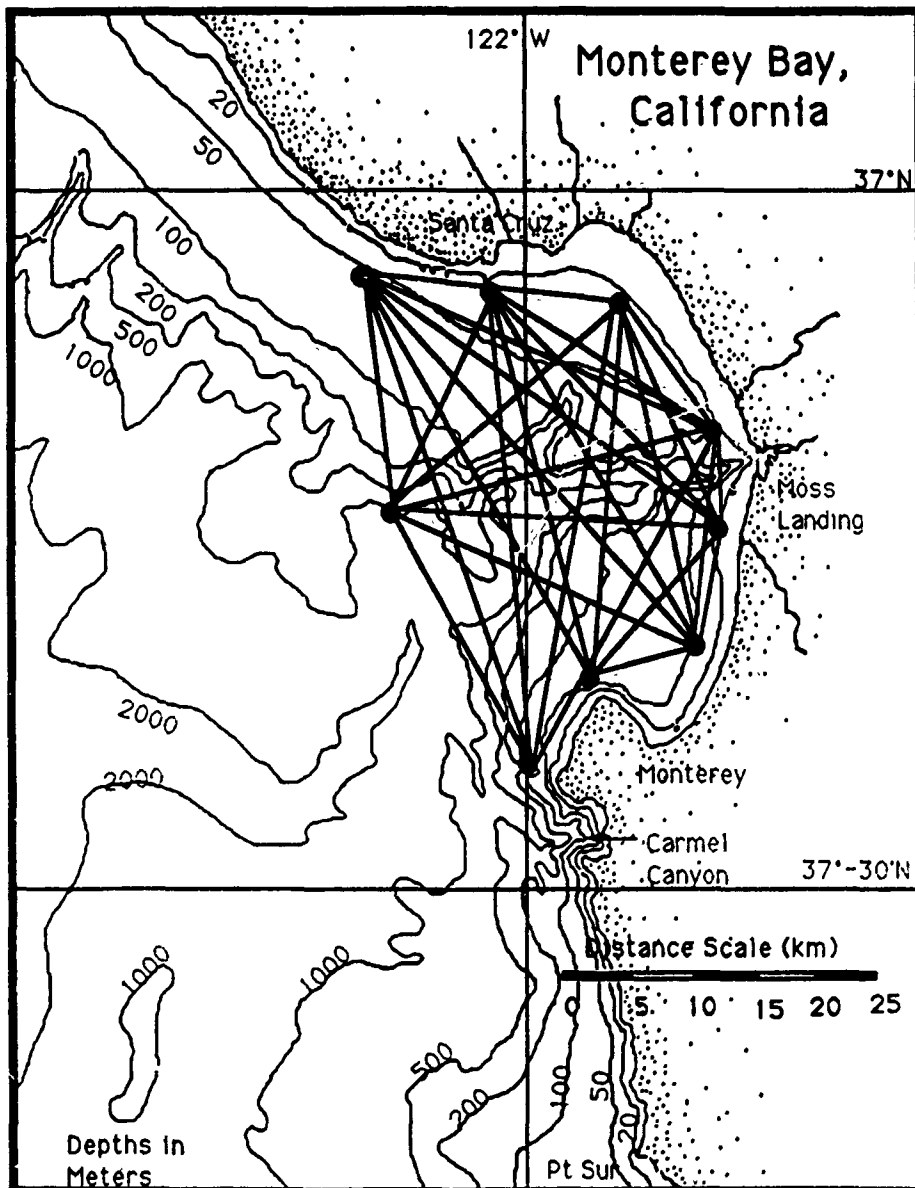


Figure 1.1: Possible Monterey Bay tomography transceiver locations.



puter program. A experiment was held in Monterey Bay in December, 1988 in which a single tomography source off Point Sur transmitted to a number of receivers in the northern part of the Bay. The modeling effort involved the use of two acoustic ray-tracing programs that attempted to model the multipath arrival structure.

The results of this study support the feasibility of acoustic tomography in Monterey Bay. The Monterey Bay Acoustic Tomography Experiment of December 1988 showed strong acoustic arrivals that were mostly resolved and stable over the cross-canyon paths for the 3 day experiment. However, one important piece of the puzzle is still missing: the identification of multipath arrivals measured in the experiment. The MPP (Multiple Profile Program) 2-D ray tracing program was able to identify a few eigenrays (rays connecting source and receiver). The HARPO (HAmiltonian Ray Program for the Ocean) 3-D ray tracing program has not been able to find any eigenrays. The inability of these programs to model the acoustic propagation in Monterey Bay stems from the extreme bathymetry of the Bay. These eigenrays exist because the experiment measured them. The lack is not in the existence of stable, resolvable arrivals but in our ability to model them correctly. In the next few months, as part of another feasibility study for the Norwegian-Barents Sea Tomography Experiment, HARPO capabilities will be increased with the addition of Gaussian beam and time front post-processing routines. These routines eliminate the need for modeling eigenrays and should be able to identify the arrivals measured in the Monterey Bay Experiment.

### 1.3 Report Overview

This report into five chapters including this introduction. Chapter 2 provides a background on Monterey Bay including oceanography, bathymetry, and geology. Chapter 3 describes the experiment carried out in Monterey Bay in December, 1988. Chapter 4 describes the work to date on modeling acoustic propagation in Monterey Bay. Chapter 5 lists our conclusions about the feasibility of an acoustic tomography system in Monterey Bay.

## Chapter 2

# Background

### 2.1 Ocean Acoustic Tomography

"Ocean acoustic tomography is a technique for observing the dynamic behavior of ocean processes by measuring the changes in travel time of acoustic signals transmitted over a number of ocean paths." [1] The word tomography is derived from two Greek roots meaning "to slice" and "to look at." Ocean acoustic tomography uses sound energy to look at a "slice" of the ocean by measuring the travel time of signals propagating through the water. Sound speed in the ocean is a function of salinity, pressure, and temperature. As acoustic energy travels along its path, its rate of travel varies with these quantities as well as with the speed and direction of any currents. Mathematical inverse methods are applied to these travel time fluctuations to estimate the variation of these dynamic ocean variables.

Ocean acoustic tomography was originally proposed by Munk and Wunsch in 1977. In 1979, they presented methods for inverting the data to estimate the sound speed field.[3] This procedure is similar to the procedure used in medical x-ray tomography where the measuring signal travels in a straight line from transmitter to receiver. Ocean acoustic tomography may have energy traveling along several curving paths with different travel times and from one transmitter to several receivers simultaneously, as shown in Figure 2.1. Thus, with several sound sources and receivers, the amount of data collected grows multiplicatively rather than additively (as in point sampling). The sound speed fluctuations along the entire path affect the travel time of a signal. Because of this integrating characteristic of the travel time, small inhomogeneities will have a negligible effect. Sound also has the advantage of sampling along its path very quickly - approximately

1500 meters per second. If transmissions are made in both directions along a path, the difference in travel time is related to currents along the path.[1] Ocean acoustic tomography is a valuable tool for monitoring the ocean interior. Its overall system performance can be improved, however, if it is supplemented by in situ measurements by ships and buoys.

### 2.1.1 The Forward Problems

Treating the ocean medium as a large, time-varying distortionless filter, the impulse response of the source-receiver channel is just the sum of the impulse responses of the individual paths [5]

$$h(t) = \sum_{i=1}^P a_i \delta(t - \tau_i) \quad (2.1)$$

where  $P$  is the number of paths,  $a_i$  is the amplitude, and  $\tau_i$  is the total travel time along the path. If the transmitted signal is an impulse then the received signal will be the impulse response. The separate paths can be predicted from ray theory. The limits placed on the sound speed structure for ray theory to be valid can be described as:[6]

- The amplitude of the wave must not change appreciably in distances comparable to a wavelength.
- The speed of sound must not change appreciably in distances comparable to a wavelength.
- The channel depth and source-receiver distance must be large in comparison to a wavelength.

If these conditions cannot be met, other methods must be used, and "full wave" or modal solutions can be attempted[6,4].

### Density Tomography

The travel time for a ray path can be found by integrating the sound slowness (inverse speed) over the specific ray path denoted by  $P_i$  (the  $i$ th ray path)[6]

$$\tau_i = \int_{P_i} \frac{ds}{c(x, y, z, t)} \quad (2.2)$$

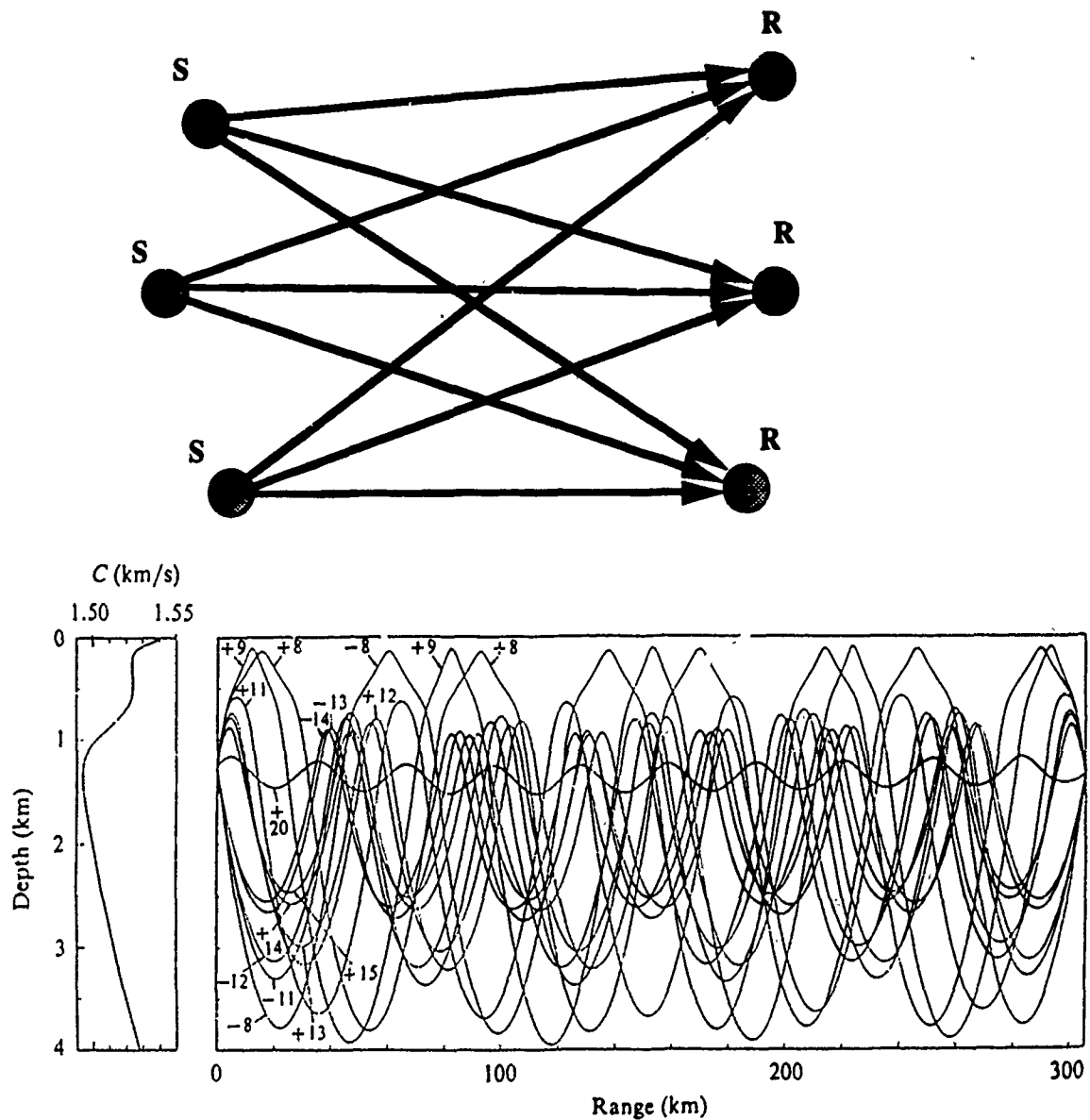


Figure 2.1: (top) Several transmitters (T) and receivers (R) give many ray paths as viewed from above. (bottom) Each slice may contain numerous eigenrays connecting the transmitters and receivers. This diagram is from a 1983 experiment near Bermuda[2].

The fluctuations in sound speed can be thought of as perturbations from some arbitrary base speed  $c_o(z)$ ,

$$c(x, y, z, t) = c_o(z) + \delta c(x, y, z, t) \quad (2.3)$$

so that the travel time becomes a constant travel time with a perturbation

$$\tau_{i,o} + \delta\tau_i = \int_{P_i} \frac{ds}{c_o + \delta c(x, y, z, t)} \quad (2.4)$$

For  $\delta c \ll c_o$ , an approximation from the binomial expansion can be used

$$\begin{aligned} \tau_{i,o} + \delta\tau_i &= \int_{P_i} \frac{1}{c_o(z)} \frac{ds}{\left(1 + \frac{\delta c(x, y, z, t)}{c_o(z)}\right)} \\ &\simeq \int_{P_i} \frac{1}{c_o(z)} \left(1 - \frac{\delta c(x, y, z, t)}{c_o(z)}\right) ds \\ &\simeq \int_{P_i} \left(\frac{1}{c_o(z)} - \frac{\delta c(x, y, z, t)}{c_o^2(z)}\right) ds \end{aligned} \quad (2.5)$$

The perturbation is [6]

$$\delta\tau_i = - \int_{P_i} \frac{\delta c(x, y, z, t)}{c_o^2(z)} \quad (2.6)$$

### Current Tomography

In the above development, the arrival time of an acoustic pulse was assumed to be only a function of sound speed, a scalar quantity. However, if a current field exists in the ocean between transceivers, the travel time of a pulse in one direction is different from the other direction. If we define  $\Delta\tau_i$  to be the difference in the to and fro travel times of the  $i$ th ray, then

$$\Delta\tau_i = \int_{S_i} \frac{ds}{c + \vec{u} \cdot \hat{s}} - \int_{S_i} \frac{ds}{c - \vec{u} \cdot \hat{s}} \quad (2.7)$$

where  $\vec{u}$  is the space varying current field and  $\hat{s}$  is the unit tangent vector to the ray. Implicit in Equation 2.7 is that the ray path is same for both directions, a very good approximation.



### 2.1.2 The Inverse Problem

The inverse problem is to determine  $\delta c(x, y, z, t)$  ( $\bar{u}$ ) from  $\delta \tau_i$ . The travel time perturbation  $\delta \tau_i$  ( $\Delta \tau_i$ ) depends on the magnitude of sound speed (current) fluctuations and the path of the ray, which determines the water that is sampled by that ray. Note that this perturbation relation has now been linearized. Inverse mathematical methods are often used in connection with geophysical problems where some characteristic is measured by its effect in perturbing some transmitted signal, rather than direct observation of that characteristic. There is a large body of information relating to linear and nonlinear inverse techniques - many of which can be applied to acoustic tomography inversions. [12]

Briefly, one inverse approach is to discretize Equation 2.6 (we shall concentrate on density tomography here), so that

$$t = Gc \quad (2.8)$$

where we have assumed that the unknown sound speed perturbation field has been discretized into a vector  $c$  of dimension  $(N_c \times 1)$  and we have formed a vector of dimension  $(N_t \times 1)$ ,  $t$ , of the known travel time perturbations of each ray at each receiver. In all realistic ocean acoustic tomography problems,  $N_c > N_t$ , i.e. we have an underdetermined inverse problem with more unknowns than independent pieces of data.  $G$  is the known kernel matrix of dimension  $N_t \times N_c$  that has the information about each of the paths and background sound speed profile. Since  $G$  is not square, we cannot simply say that  $c = G^{-1}t$ .

One way to solve Equation 2.8 is to form a quadratic functional that is sensitive to model (sound speed) estimation error and model smoothness given by

$$L(c) = (Gc - t)^T W (Gc - t) + \lambda c^T S c \quad (2.9)$$

where  $W$  is a weighting matrix which allows us to use different types of measurements with different levels of confidence and  $S$  is a matrix which smooths the estimate over space. The Lagrange multiplier  $\lambda$  determines how important the error is versus the smoothness of the estimated model.

We now derive the  $c$  which minimizes  $L$ . First, we expand Eq. (2.9) (following Liebelt[7])

$$L(c) = (c^T G^T - t^T) W (Gc - t) + \lambda c^T S c \quad (2.10)$$

$$L(c) = c^T G^T W G c - c^T G^T W t - t^T W G c + t^T W t + \lambda c^T S c \quad (2.11)$$

Because the third term in the preceding equation is a scalar, we can transpose this term to obtain

$$L(c) = c^T G^T W G c - 2c^T G^T W t + t^T W t + \lambda c^T S c. \quad (2.12)$$

We next differentiate Eq. (2.12) with respect to the components of  $c$  yielding

$$\frac{dL}{dc} = 2G^T W G c - 2G^T W t + 2\lambda S c. \quad (2.13)$$

Setting the expression above to zero and solving for  $c$  we get

$$c = (G^T W G + \lambda S)^{-1} G^T W t. \quad (2.14)$$

The solution given in Eq. 2.14 is analogous to the *weighted damped least squares*[8,9,10,11,12]. The choice of smoothing matrix  $S$  and its weight  $\lambda$  is a tradeoff between the resolution and error in the sound speed field estimate.

### 2.1.3 Discussion

The solution of the the ocean acoustic tomography problem is tied directly to the "forward" problem. The path of each eigenray between the source and receiver must be identified before the integral relating time perturbation to sound speed perturbation can be inverted. This eigenray is normally considered to be fixed spatially (usually a good approximation) with the sound speed perturbations acting on this path. Fluctuation in the sound speed field is the data upon which ocean acoustic tomography depends, but if the fluctuation is too great, the ray path may become unstable and no longer reach the receiver. Rays do not arrive as a single point but cover an area measured by the Fresnel zone size. The size of the Fresnel zone depends on the sound speed structure and acoustic frequency but for channel transmission remains fairly constant after 20 kilometers.[4] This size and knowledge of sound speed fluctuations along the path can be used to estimate path stability. In summary, ocean acoustic tomography requires a sufficient understanding of the ocean along the source-receiver path that eigenrays along which the signal will travel can be predicted. The received signal must have an "arrival" structure which is stable and does not fade or disappear. The arrival must be identifiable as to its path for the tomographic inversion to proceed. The transmitted signal must be constructed to facilitate an accurate estimate of the travel time perturbations and should be resolvable from other arrivals at very close intervals. Finally, these time perturbations will be used to estimate the fluctuations in the ocean sound speed field using inverse methods.

## 2.2 Monterey Bay

Monterey Bay is a semi-enclosed elliptical embayment along the Central Coast of California between latitudes  $36^{\circ}36.05'N$  and  $36^{\circ}58.70'N$  as described in Figure 2.2. Moss Landing is located at the easternmost point of the bay at longitude  $121^{\circ}47.30'W$ . Since the bay is open to the Pacific Ocean along its western side, we assume an artificial line between Point Piños to the south ( $121^{\circ}56.20'W$ ) and Point Santa Cruz along the north shore ( $122^{\circ}01.60'W$ ). Based on these positions, the bay is 42 km long and 17.6 km wide from Moss Landing due west to the open bay boundary. The surface area of the bay is approximately  $534 \text{ km}^2$ , of which 81% is above the continental shelf while the rest overlies the submarine canyons.[13]

Fresh water enters the bay via the San Lorenzo River, Soquel Creek, Aptos Creek, Pajaro River and Salinas River. These streams have a combined mean annual discharge of  $1.85 \times 10^6 \text{ m}^3/\text{day}$  with the Salinas River having the greatest contribution at 55% [14]. Precipitation and river runoff are normally greatest during the winter rainy season. During the dry months of May through October, a sand bar blocks the Salinas River, forcing its water to flow north and discharge through Elkhorn Slough[13].

### 2.2.1 Bathymetry

#### Continental Shelf and Slope

The continental shelf is fairly narrow south of Monterey Bay, ranging in width from less than 1.6 km at Cypress Point on the Monterey Peninsula to about 14 km at Point Sur. North of the Bay the shelf is wider, ranging from about 9.3 km to 37 km width south of San Francisco. The shelf in Monterey Bay is cut by submarine canyons and the shelf bottom slopes toward the edge of the canyons. The northern bay shelf is approximately  $238 \text{ km}^2$  in area and is at a maximum depth of 90 m at the canyon rim, as compared to the shelf in the south bay that is  $195 \text{ km}^2$  and deepens to 180 m[13;15]. The maximum slope near Seaside is 2%, while offshore of the the Salinas River it is 1-1.5%[16].

Between the continental shelf and the deep ocean floor lies the continental slope with it steeper gradient. According to Shepard[17], the slope in the greater Monterey Bay area is not consistent. Just south of Monterey Bay the outer part of the slope is set toward the northeast for 30 km or more. Further south, the slope spreads over a wide area. North of the bay, the continental slope is narrower, has an average grade of 10%, and is marked

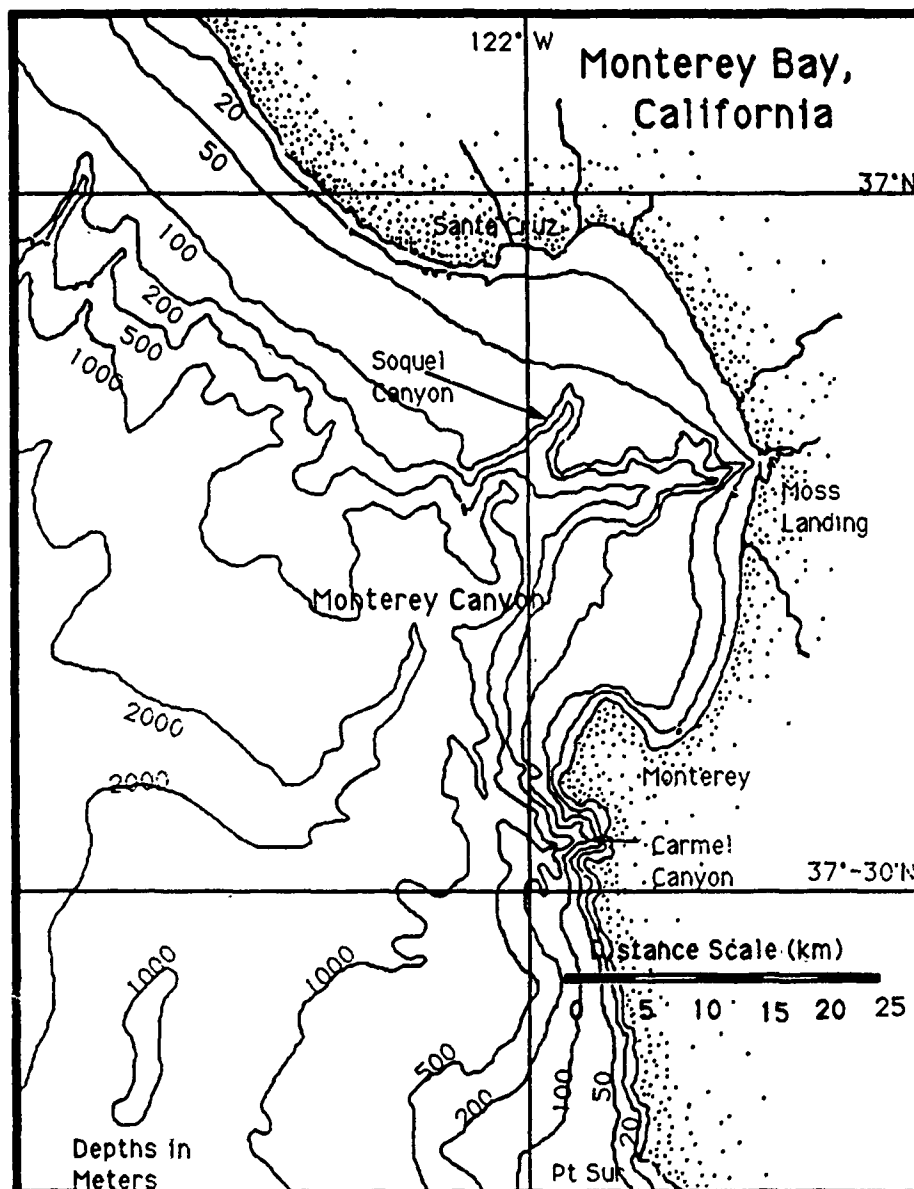


Figure 2.2: Monterey Bay, California.

by a number of submarine canyons.

### **Submarine Canyons**

The most prominent feature of Monterey Bay is the Monterey Submarine Canyon (MSC), depicted in Figure 2.2, which bisects the fairly symmetrical bay at Moss Landing. With a volume of  $450 \text{ km}^3$ , MSC has the distinction of being the largest submarine canyon on the California continental slope [18]. Shepard, Emery, and Dills [17,19] have described the MSC system in considerable detail, so the canyon system specification given in this report is based on their work.

Monterey Canyon has an axis length of about 94.5 km and ranges in depth from 18 m to 2925 m where the true canyon ends and the Monterey Fan-valley begins. The two largest tributaries entering MSC are the Soquel Submarine Canyon from the north and the Carmel Submarine Canyon from the south. After the Carmel Canyon juncture, only small tributaries enter the MSC.

The Soquel Canyon joins the MSC at the 915-m depth after dropping at a rate of 74% along its 12 km length, giving the appearance of a hanging valley. The axis of MSC winds and meanders beyond the Soquel Canyon juncture, especially off of the Monterey Peninsula where the floor is granite. At the beginning of this granite ridge, at the 1525 m mark, the axis gradient increases to over 10% or 100 m/km. The MSC is V-shaped from its head to past the granite rock, until at an axial depth of 1920 m the canyon floor becomes more irregular and broader. This is the point where a northern trough-like valley enters the MSC.

The trough-shaped valley section of the canyon runs southwest for about 35 km. The walls increase in height along the canyon with the northwest wall reaching up to 370 m. The southeast wall is the continental slope and has a number of valleys entering it with heads as deep as 1520 m.

The Carmel Submarine Canyon connects with the MSC at a depth of 2010 m. Carmel Canyon is about 30 km long with an axial slope of 73 m/km. At its 9 m head in Carmel Bay, which may be considered a drowned river valley, are several tributaries cut into the granite walls along the shore with no intervening shelf. The head has some portions with gradients as large as 30%, but the base is smooth, probably due to recent erosion. After large storms, there are considerable changes in the nature and thickness of the fill in the head of the canyon.

The V-shaped submarine canyon of Carmel first runs west, then winds

northwest and parallels the coast. It appears to run along a fault in soft rock that lies between two hard rock masses. The inner portion of the canyon has an axial slope of 10% with a drop of 550 m and a floor width of about 75 m. It ends as a hanging valley at the Monterey Canyon with no fan-valley

At approximately  $122^{\circ}40'W$ , the high northwest wall of the MSC drops down to a low ridge where the southeast wall leaves the continental slope and a levee forms on top of the wall. The channel then takes a large 24 km meander before returning to its general course only 3 km downstream from the point where the meander began. A little farther down the channel, the trough-like portion of the MSC opens up into a modified fan-valley with convex-upward levees bordering an eroded valley. This fan-valley is approximately 320 km long and 280 km wide with an axial gradient of 4.8m/km, its apex at a depth of 3050 m and base at 4600 m[20]. The fan valley eventually opens up into the deep ocean basin of the Pacific.

## 2.2.2 Geology and Sediments

The coastline depression of Monterey Bay was probably carved out by wave attack on the relatively soft sedimentary rocks in the center of the Salinas River Valley trough[21]. The promontories at Soquel Point and Point Piños are rocks that were better able to resist the erosional action.

The rivers that empty into Monterey Bay deposit igneous, sedimentary and metamorphic rocks of the central and southern Coast Ranges. The igneous rocks are Mesozoic granite, while the metamorphic rocks are of the Sur Series. Monterey, Pancho Rico, Paso Robles and Aromas Formations contribute to the Tertiary sedimentary rocks.[21]

The sediment within Monterey Bay is composed of gravel, various sizes of sand, silt and clay. The following excerpt from a report by Engineering-Science, Inc., for the Monterey Peninsula Water Pollution Control Agency [16] provides a succinct description of the Monterey Bay sediment.

The bottom sediments vary in size and composition according to depth contour, as shown in Figure 2.3. The nearshore bottom and beach consist of coarse and medium sand. The bottom gradates to fine sand down to a depth of 36 m. The sides and bottom of the submarine canyon nearshore are characterized by silt and clay which gradate into gravel and coarse sediments in the deeper parts. The lower portion of the south bay is semiprotected from wave action by the protruding headlands at Point

Piños. This topographical feature, which refracts and diminishes wave energy, produces a pronounced sorting of coarse and medium sand particles in the south bay below the Salinas River.

Monterey Canyon with its Soquel and Carmel tributaries is the predominant feature of the tomography experimental region. MSC's axial path appears to meander and wind in relationship to hard and soft rock zones. The tributaries enter the main canyon as hanging valleys with trellis drainage pattern[17]. There are many large-scale slumps along the walls of the Monterey Submarine Canyon, indicating a history of undercutting and erosion[16].

At the head of MSC, directly off Elkhorn Slough, there is only unconsolidated sediment. The inner canyon cuts into unconsolidated sediment for about 8 miles, and along the walls and floor of the canyon for this stretch is silt and clay. Based on information from Shepard and Dill, the first rock to appear is Upper Pliocene mudrock at an axial depth of 640 m. The north wall of MSC beyond this point is Pliocene sedimentary rock which also comprises the west wall of Soquel Canyon. A box core sample taken in Soquel Canyon yielded surface mud above rounded pebbles with shells and fragment of siltstone.[19]

The first granite to appear in Monterey Canyon is an extension of the Monterey Peninsula formation, and is found only along the south wall where MSC axis makes a large bend to the south. The opposite wall is still sedimentary rock. Beyond the Carmel Canyon junction, the MSC north wall sedimentary rocks include limestone, sandstone, mudstone and Lower Miocene foraminifera and coccoliths (organic calcareous ooze). The south wall is just mud. [19]

Based on the Offshore Surficial Geologic Map (Figure 2.4), the Monterey Canyon beyond Monterey Bay is sandy mud until it becomes mud (silt and clay) after the granite outcroppings. For most of the receiver locations, the rays from the acoustic source will initially bounce off of mud, and then a sandymud bottom, before reaching the canyon(s).[22]

Carmel Submarine Canyon appears to be a seaward extension of the land canyon, with no continental shelf between the canyon heads and the beach. The main head begins directly off the mouth of San Jose creek. As expected, the head fills rapidly with sediment from the creek and is then cleaned out. This fill appears to undergo continuous change in nature and thickness, but changes are especially noticeable after a large storm. [19,23]

The Carmel Canyon is narrow, V-shaped and cut in granite. The steep

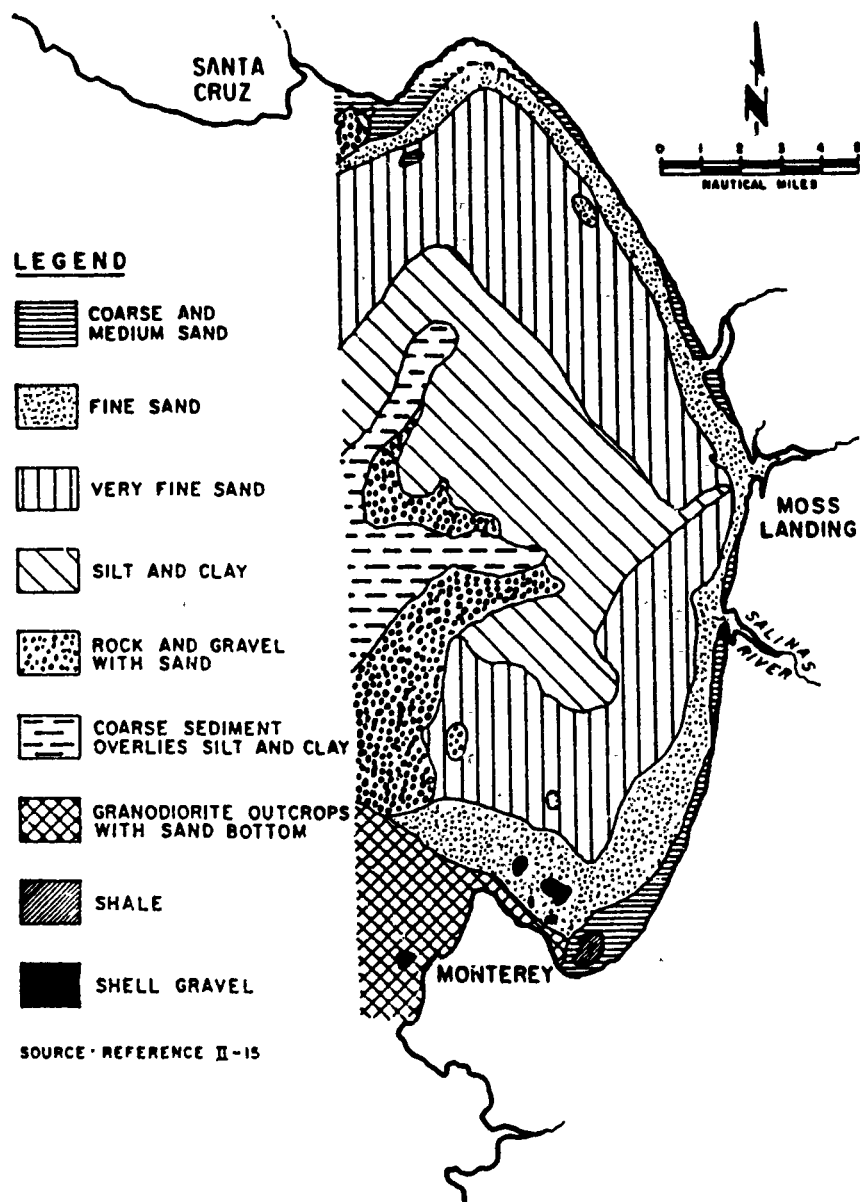


Figure 2.3: Distribution of sediment types in Monterey Bay.[16]



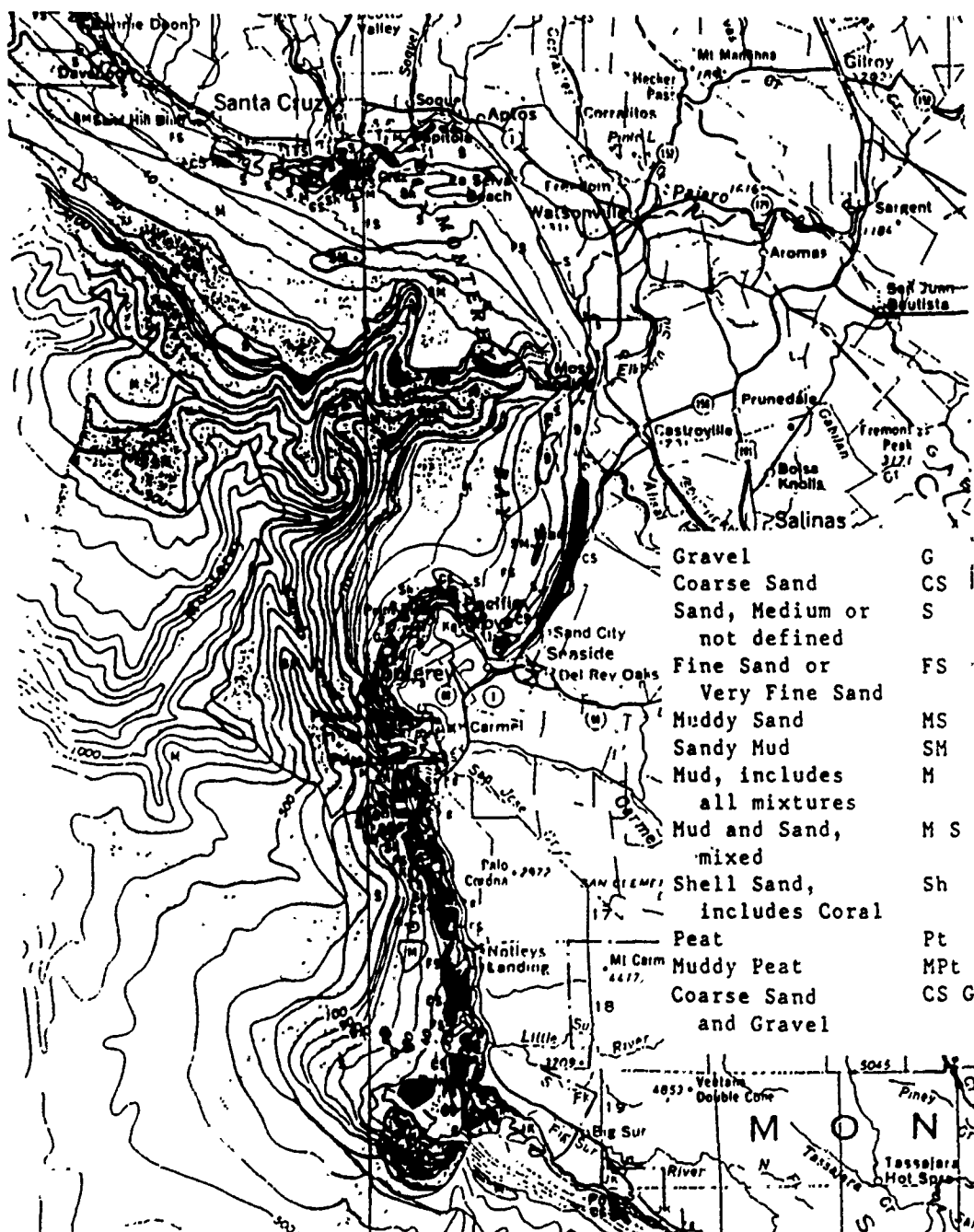


Figure 2.4: Offshore surficial geologic map of Monterey Bay.[22]

rock walls are mostly granite with a smooth base. The floor is sandy or rocky. Near the juncture to the Monterey Canyon, Carmel Canyon's east wall is composed of weathered granite, while the west wall has Mid-Miocene sedimentary rock. [19,23]

### 2.2.3 Currents

#### California Current System

Flowing along western North America in a south to southeasterly direction is the eastern boundary current called the California Current. This current brings Subarctic water to California, which is low in both temperature and salinity but high in nutrients. The California Current is wide, shallow and slow, extending maybe 700-1000 km off the coast, down to a depth less than 500 m, and flows at a speed that is less than 25 cm/sec.[13,16]

A subsurface current, the California Countercurrent, moves warm and highly saline Equatorial Pacific water north along the coast from Baja California to Cape Mendocino (41°N latitude). The core of this current is at about the 200 m depth, extending 50-100 km offshore, with a velocity of less than 22 cm/sec north of 30° N latitude. In the fall or early winter, the California Countercurrent surfaces and becomes the Davidson Current. This surfacing of the current, which occurs somewhere between British Columbia and Point Conception, now provides for another surface current to move along the coast inward of the California Current. The Davidson Current, flowing between 16 and 47 cm/sec, is found as far as 80 km offshore. [13,16]

Associated with the California Current system are three oceanic seasons, designated the Davidson period, the upwelling period and the oceanic period. These periods appear to be directly affected by wind speed and direction.

The Davidson period generally occurs between November and February, when a semi-permanent Pacific high pressure cell weakens, moves southward, and is replaced by an intermittent low pressure cell. The winds are very light in the fall, and from the west or southwest in the winter. The Davidson Current surfaces and is pushed toward the coast, due to the wind direction and Coriolis force. This water converges along the western North America coast and then sinks, resulting in nutrient-poor water along the coast. [13]

From about February to July, the winds are strong and blow out of the north or northwest. The surface water along the shore is carried away from the coast by the Coriolis force, based on the wind direction. Upwelling occurs as subsurface water rises to replace the vacated surface water. The water

level is generally a little higher away from the shore, where the surface water has been pushed, rather than close to shore, where the subsurface water has risen. The upwelled water is cooler but high in salinity and nutrients. Upwelling occurs at a rate of 0.7-2.7 m/day and is found as far as 50 km offshore. [13,16]

At the end of the upwelling period, the regular current pattern collapses into irregular eddies in connection with the wind abatement. Smethie [13] indicated that during this oceanic period "... the sea surface slopes downward, isotherms slope upward toward the coast, and the geostrophic current flows southward." With the irregular eddies, the currents are usually weak and variable.

### Monterey Bay Current Flow

The surface water in Monterey Bay appears to originate from three water types [14]:

1. recently upwelled water;
2. freshwater from the rivers and streams; and
3. warmer, low-nutrient water which has been warmed at the surface.

The bay currents appear to be regulated by the oceanic seasons. Figure 2.5 illustrates the seasonal surface current flow within Monterey Bay.

Engineering-Science, Inc., in their report to the Monterey Peninsula Water Pollution Control Agency [16], indicated that during the upwelling period, the bay flow is dominated by the southward flowing offshore current. They cited Broenkow and Smethie's [14] conclusion that the offshore waters enter mostly from the southwest up the Monterey Canyon, separate, and then flow over the northern and southern continental shelves in the bay. Clockwise and counterclockwise gyres over the shelves result, with speeds anywhere from 2.5 to 26 cm/sec, but the predominant flow is north and northeast. Even through in the oceanic period the currents become irregular and the wind is light, the bay current continues the pattern established in the upwelling period, except that irregular eddies form over the north shelf. The nearshore ocean currents shift from southerly to northerly, and pass through Monterey Bay as a large, open eddy. However, the bay currents circulate irregularly and slowly.

Broenkow and Smethie [14] studied and reported on the Monterey Bay surface circulation and water replenishment during a 27 month period in

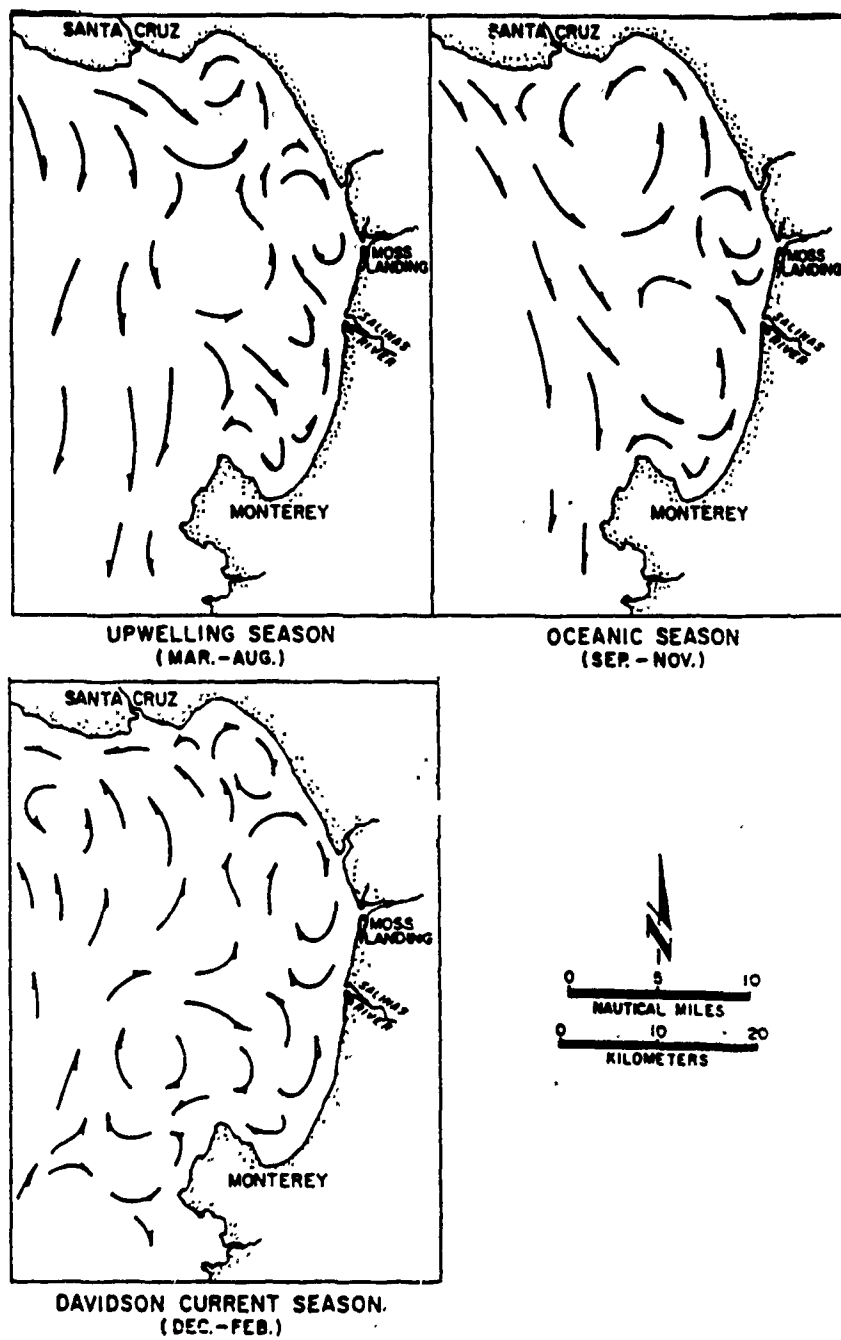


Figure 2.5: Monterey Bay seasonal current patterns.[16]

the mid 1970's. As stated earlier, offshore water predominantly enters up the canyon into the bay, but sometimes flows directly from the west. The replacement time for the north and south bay waters is between 2 and 14 days, during which time their characteristics can be modified by air temperature at the surface, photosynthesis, sewage outflow and freshwater river discharge. The water parcels had longer paths near the shoreline, and therefore, had longer replenishment times than the water over the canyon. During the period of October 1972 through March 1973, the largest volume of bay freshwater replenishment occurred in February with an estimate of  $86 \times 10^6 \text{ m}^3$ . October had the smallest volume at  $2 \times 10^6 \text{ m}^3$ . During most of the year the freshwater lens is above the 10m depth mark, except for January and February when about 1/8 of the freshwater falls to a depth between 10 and 30 m.

#### 2.2.4 Temperature and Salinity Variations

The temperature and salinity within Monterey Bay appear to coincide with seasonal oceanic periods associated with the California Current system, amount of river runoff and with variations in the wind. Figure 2.6 shows the mean variation of temperature and salinity at the mouth of Monterey Bay, and at a point 40 km south of the bay, during the years 1950-1962. On any given day the temperature throughout the bay is not uniform, varying from 1 to 3°C for a particular layer, while the salinity is laterally consistent [14,16]. The surface waters in the north and south bight areas are generally warmer in the spring and summer than the mid-bay waters. Also, the maximum temperatures often occur after days of southerly winds. The lowest salinity readings generally occur with the highest temperatures for the year, or during the period of maximum freshwater runoff. The late upwelling period yields the highest salinity levels.

Each seasonal oceanic period greatly affects the temperature and salinity of the Monterey Bay water. In the late fall and early winter, the sinking of nearshore waters during the Davidson period results in a fairly deep layer where the temperature is uniform, with little variance in surface water temperature over the entire bay. The 8°C isotherm deepens and all the isotherms slope deeper towards the coast. Seasonal rainfall, together with large river runoff, combine to dilute the surface water to measurable depths, which brings the salinity in this diluted layer down to around 33.4 ‰ and variable. Late in the winter the southerly winds die out, and strong northeasterly winds arise. This is the onset of the upwelling period. [16]

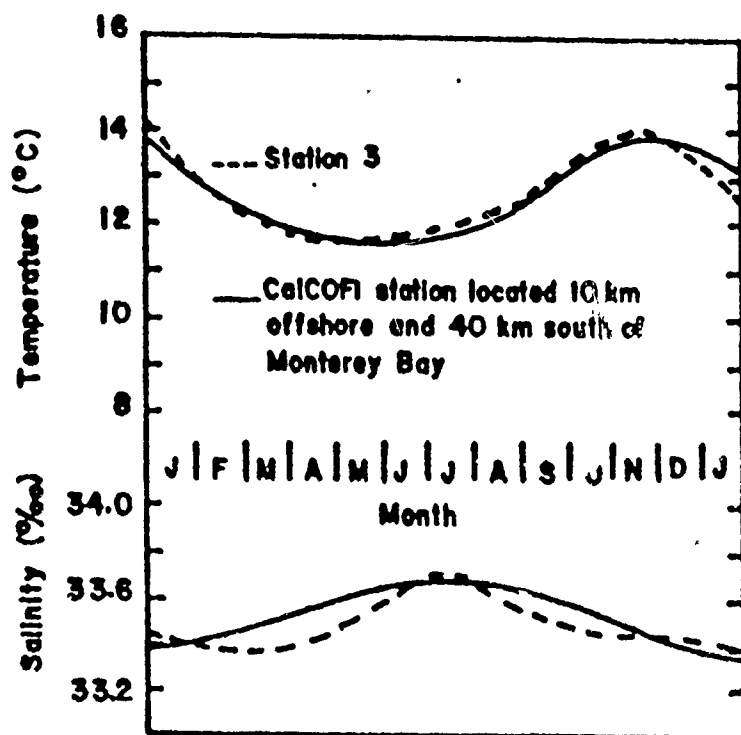


Figure 2.6: Mean temperature and salinity variation at the mouth of Monterey Bay (station 3) and CalCOFI station during 1950-1962.[13]

During early upwelling the cool subsurface water replaces the vacated surface water, bringing the surface temperature down to its lowest yearly value of around 10 – 11°C. The south and north bights are warmer than the middle of the bay, which lead to a variation of surface temperature by greater than 3°C. The isotherms rise, so the 8°C isotherm is usually above the 100 m mark during this period. Even with intermittent upwelling in the summer, the water temperature remains cool; however, the maximum salinity level occurs near the end of upwelling in the July timeframe. During the entire upwelling period, the salinity is high because the rising subsurface water has a high salinity value. [16]

The oceanic period generally takes place from July to November. The surface temperatures ascend to their warmest yearly values to 13 – 16°C, but the temperature varies horizontally throughout the bay by 2 – 3°C. The 8°C isotherm drops, and all of the isotherms slope upward toward the coast. There is usually a sharp thermocline within the first 50 m. Since the upwelling has ceased during this period, the salinity level first declines and then levels off, due to the ingress of offshore water that is lower in salinity.[16].

### 2.2.5 Tides

The tidal pattern along the west coast of the United States is classified as a mixed semidiurnal tide. As shown by the tidal curve of Figure 2.7, two high tides and two low tides occur each day; however, the high tides are of different heights with respect to each other. The same is true for the two daily low tides. In Monterey Bay, the tidal range between the lower low tide and the higher high tide is on the order to 2 m [23], with the tides arriving in the order of lower low tide, lower high tide, higher low tide and higher high tide in a 24-hour day cycle.

### 2.2.6 Surface Waves

The waves that arrive in Monterey Bay hit all points of the shoreline, due to refraction and defraction of the waves as they wrap around the bay. The bay experiences two general types of waves. Winter waves occur usually from November to March and have a short period of 8-10 seconds. These swells come out of the northwest and are the product of local storms or may originate from as far away as the Gulf of Alaska. Winter waves severely erode beaches because the short wave action keeps the beach face saturated with water and the swash cannot permeate the sand. Instead, this type of

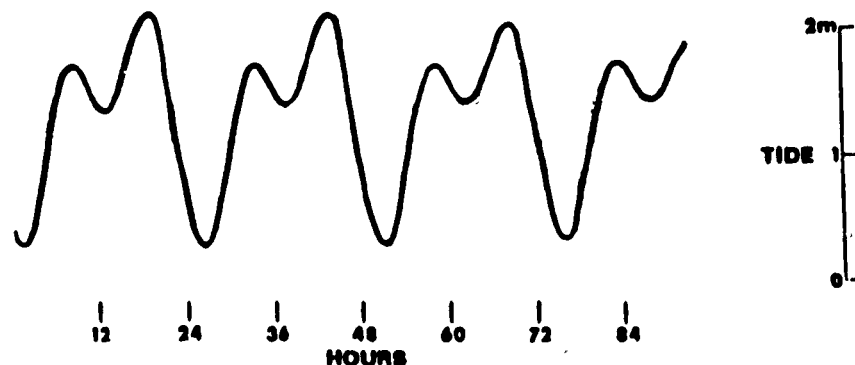


Figure 2.7: Monterey Bay tidal pattern.[23]

wave returns as a backwash, carrying much of the beach sand with it and depositing the sand on a sand bar at a typical depth of 9 m.

Summer waves have a longer period of 14-16 seconds, arrive at Monterey Bay from the southwest, originate in the Antarctic region, and have flattened out due to the long travel time. These waves move the sand bar deposit back to the shore, so the beach widens. The longer wave action allows the beach face to dry out a little between waves, so the swash permeates the sand and there is no backwash to carry the beach away.

Monthly and annual reports on the surface wave and current conditions along the California coast are distributed through the Coastal Data Information Program (CDIP), a cooperative program by the U.S. Army Corps of Engineers and the California Department of Boating and Waterways [24,25]. The data for these reports are gathered by four types of ocean measuring equipment:

1. four gage slope array for nearshore direction and energy measurement;
2. surface following buoy for deepwater wave energy measurement;
3. single point gage for nearshore wave energy measurement; and
4. single point gage for deep ocean wave energy measurement.



A station of particular interest in connection with the tomography experiment is Station 8, North Monterey Bay buoy, at latitude  $36^{\circ}56.9'N$ , longitude  $122^{\circ}25.1'W$  and depth of 320 m. Figure 2.8 and Figure 2.9 are two pages taken out of the December 1987 report [24]. The data page for a period of time from 9 December to 19 December 1987, exactly one year prior to the December 1988 tomography experiment, provides numerical information on significant wave height, total amount of wave energy and the percent of energy per band period. Note the high wave energy level on 16 December 1987, with the greatest energy occurring in the period between 8-14 seconds. The wave energy spectra of Figure 2.9 visually illustrates this surge. In all likelihood, a storm passed through the area on this date, kicking up the waves.

Based on a chart from the CDIP Annual Report [25], the October through December 1987 period had the highest average wave height. There was a 58% seasonal probability that the significant wave height would exceed 2 m, 32% for 3 m and 13% for significant wave heights greater than 4 m.

### 2.2.7 Internal Waves and Canyon Currents

As defined by Clay and Medwin [26], internal waves "... are volume gravity waves having their maximum vertical displacement amplitude at a plane where the density is changing most rapidly with depth or between two water masses of different densities." A number of studies [14,23,27,28], have presented evidence that the Monterey Submarine Canyon commonly has internal waves of a semidiurnal nature. The results of a conductivity-temperature-depth (CTD) time series for five stations in the Monterey Canyon have indicated that these internal tides had heights of 50 m to 120 m [27].

Along the bottom of the Monterey Canyon the currents are strong and fluctuating, with speeds up to 50 cm/s [14]. These flows are generally in an upcanyon direction, but in truth they appear to have almost no connection with the canyon axis. Cross valley flows are a predominant feature along MSC [23], but there has not been a determination as to the cause of this phenomenon. Tides and wind direction appear to have no relationship to the cross currents [23].

Current-meter data (Table 2.1) from MSC provide information on the internal tide up- and downcanyon reversal cycles. Estimated upcanyon advance rates for an internal wave in the Monterey Canyon is 25 cm/sec between 7.5 km and 8.5 km away from the canyon head (depth of 400-375 m),

NORTH MONTEREY BAY BUOY  
DEC 1987

PST DAY/TIME	SIG. (CM.)	HT (CM.)	TOT. EN (CM. SQ)	PERCENT ENERGY IN BAND (TOTAL ENERGY INCLUDES RANGE 2048-4 SECS) BAND PERIOD LIMITS (SECS)								
				22+	22-18	18-16	16-14	14-12	12-10	10-8	8-6	6-4
9 1501	324.4	6577.5	0.3	0.5	9.1	23.8	25.3	11.4	18.4	7.7	4.1	
9 2100	357.4	7983.0	0.2	0.3	1.5	25.1	38.3	14.9	10.7	6.3	3.1	
10 0300	338.7	7170.8	0.1	0.1	1.9	11.6	30.2	23.0	20.1	7.9	3.5	
10 0906	309.3	5979.7	0.4	0.4	1.4	19.0	30.9	22.2	13.8	8.4	4.0	
10 1523	363.2	8246.5	9.2	5.4	3.0	14.9	27.7	20.6	9.9	7.4	2.4	
10 2101	490.2	15016.1	2.1	16.3	13.2	20.1	15.5	13.2	6.8	7.3	6.0	
11 0300	461.5	13308.6	0.8	7.0	19.2	11.9	12.8	11.3	17.1	13.9	6.5	
11 0900	461.7	13322.3	0.4	4.3	14.3	14.5	16.7	21.3	16.8	8.2	4.1	
11 1503	470.4	13829.8	1.1	2.3	8.3	11.9	20.6	24.8	15.7	9.8	6.0	
11 2102	455.9	12990.1	0.3	1.7	8.3	16.4	20.0	20.4	18.9	9.9	4.5	
12 0302	449.5	12626.9	0.2	0.3	2.1	10.5	36.9	22.5	15.1	7.9	5.0	
12 0902	414.0	10714.6	0.3	0.3	1.7	3.8	19.0	34.2	18.1	16.0	7.1	
12 2058	471.4	13891.1	0.2	0.2	0.4	7.2	22.2	20.2	22.6	19.8	7.6	
13 0302	391.7	9590.0	0.1	0.1	0.2	6.0	21.0	23.4	21.1	19.1	9.5	
13 0902	370.2	8567.1	0.2	0.2	0.3	3.3	10.5	28.4	21.5	24.2	11.8	
13 2102	207.5	2690.8	0.2	0.3	0.3	1.0	11.1	26.1	16.4	17.0	28.1	
14 0302	187.4	2194.2	0.1	0.1	0.3	1.2	12.7	18.2	36.5	16.2	15.2	
14 0901	133.5	1113.2	0.1	1.0	1.2	4.5	22.3	13.8	23.5	19.9	14.2	
14 2059	140.8	1239.3	0.2	1.6	23.3	11.4	12.8	28.6	12.8	6.0	3.7	
15 0251	136.4	1162.4	0.2	0.6	18.4	26.4	13.9	7.1	6.5	4.0	23.3	
15 0857	220.1	3027.9	0.3	0.2	3.0	9.5	7.4	3.9	1.5	37.6	37.1	
16 0255	732.4	33523.8	0.3	0.3	0.4	2.5	23.3	41.5	17.4	9.7	4.9	
16 0855	597.2	22293.1	0.2	0.2	0.9	5.4	26.7	28.0	18.9	13.3	7.0	
16 1501	520.0	16897.0	2.1	1.1	0.7	1.9	5.9	38.8	27.3	13.8	8.8	
16 2057	347.8	7559.9	0.1	0.1	0.5	1.6	11.4	31.2	30.6	15.9	9.0	
17 0257	309.3	5981.0	0.1	0.1	0.3	2.0	8.0	34.4	40.0	10.1	5.5	
17 0857	294.3	5414.7	0.1	0.1	0.3	1.8	13.6	32.9	35.3	12.1	4.1	
17 1459	285.4	5091.9	0.6	0.5	0.5	1.6	20.1	36.4	20.8	13.6	6.4	
17 2059	265.3	4400.3	0.2	0.2	0.2	1.4	15.8	34.0	23.1	16.8	8.9	
18 0259	252.5	3984.2	0.1	0.2	0.3	1.1	6.7	38.3	28.9	16.4	8.5	
18 1459	207.0	2677.9	0.2	0.7	0.3	0.7	2.6	26.7	30.8	26.5	11.9	
18 2059	228.8	3270.8	0.7	2.9	0.7	0.9	1.9	15.1	44.7	21.6	11.8	
19 0259	269.4	4537.2	0.2	10.5	4.5	0.4	1.7	8.9	34.3	26.2	13.9	

Figure 2.8: North Monterey Bay buoy, December 1987, wave energy data.[24]

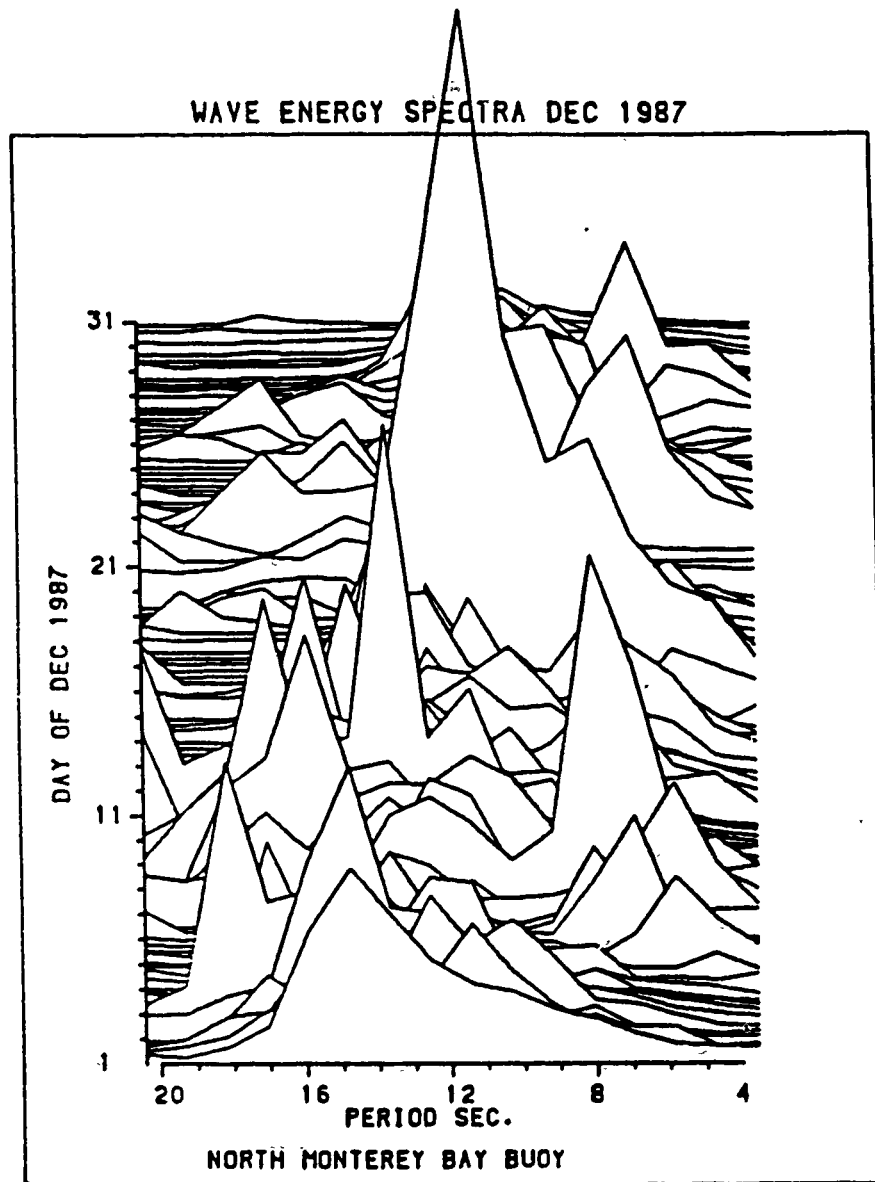


Figure 2.9: North Monterey Bay buoy, December 1987, wave energy spectra graph.[24]

METER POSITION		AVERAGE CYCLE LENGTH (hrs)	DIRECTION OF NET FLOW	AVERAGE SPEED (cm/sec)		
DEPTH (m)	HEIGHT ABOVE FLOOR (m)			UP	DOWN	CROSS
155	3	7.2	down	9.2	10.3	4.0
155	30	4.4	up	8.5	6.7	3.7
357	3	8.8	down	13.8	11.4	5.2
384	3	8.0	up	12.1	13.1	5.6
1061	3	6.5	up	19.7	16.6	15.3
1061	30	6.5	up	20.3	26.0	9.8
1445	3	8.7	up	13.2	11.1	5.8
1445	30	10.0	up	13.6	10.0	4.2

Table 2.1: Up and down-canyon reversal cycle data for Monterey Canyon.[23]

and 38 cm/sec from 7.5 km to 2 km up the canyon (375-150 m depth) [28].

Based on small amplitude wave theory, a long wave will increase in height as it moves into shallow water, but its period will remain constant. As an internal wave advances up the canyon towards the head, where it is narrow and shallow, the wave energy may become focused and the wave height increase, taking on the appearance of an internal tidal bore. This bore "... is characterized by a rapid increase in temperature at a fixed position, in which the advancing water forms an abrupt front." An internal bore at the MSC head has been indicated by thermistor data showing a  $3.8^{\circ}\text{C/hr}$  temperature change. [27]

Broenkow and Smethie [14] conducted a 24 hr time series study at two stations near the head of the Monterey Submarine Canyon. They observed internal tidal oscillations with the same period as the surface tides, but approximately 180 out of phase. The wave height was 80 m at a depth of 130 m, while at 250 m deep the height of the wave was about 120 m.

The oscillating internal tide produces a volume convergence at flood tide. During volume convergence, the denser canyon water rises above the rim and

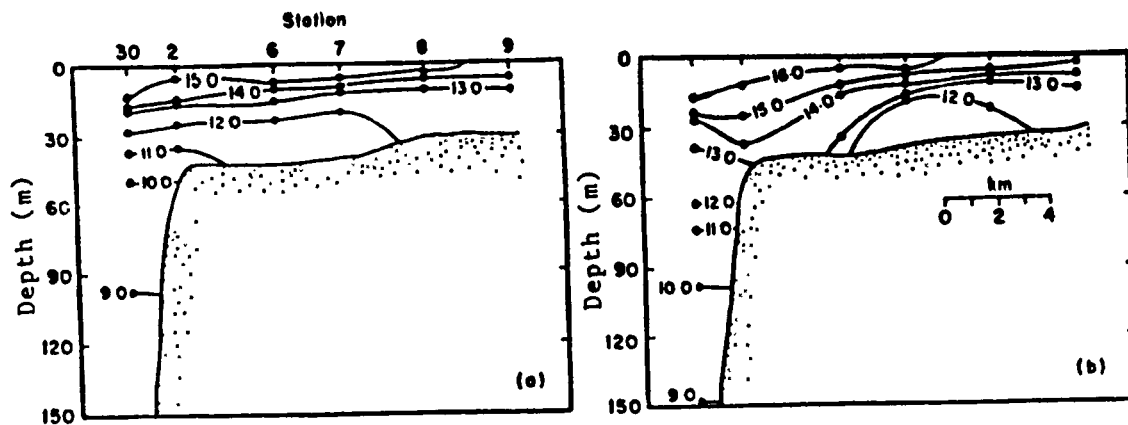


Figure 2.10: Temperature distribution ( $^{\circ}\text{C}$ ) at (a) high and (b) low internal tide, Monterey Canyon axis, 13-14 September 1979.[27]

settles on the shelf. When the internal tide reverses and goes downcanyon, the dense canyon water on the shelf starts flowing back into the canyon; however, as a result of mixing, surface heating and inertia, the edge of this dense water remains behind on the shelf. Figure 2.10 illustrates volume convergence and divergence for 13 and 14 September 1979. A 20 m thick lens of  $12^{\circ}\text{C}$  water flowed out of the canyon as the internal tide rose, and remained on the north shelf when the rest of the dense water fell back into MSC at tidal reversal. This lens was estimated to affect an area of  $26 \text{ km}^2$ . Data indicate that the volume convergence is about  $240 \times 10^6 \text{ m}^3 / 8 \text{ hr}$ , which would put the speed of water crossing the rim of MSC at about  $13 \text{ cm/s}$ .[27]

Internal waves along Carmel Submarine Canyon appear to follow the axis, unlike the situation in Monterey Canyon. The currents at 3 and 30 m above the floor showed very similar characteristics. Current-meter data (Table 2.2) is given for Carmel Canyon's up- and downcanyon reversal cycles for internal tides. Interestingly, almost all of the northern cross canyon flows occurred at ebb tide.[23]

METER POSITION		AVER- AGE CYCLE LENGTH (hrs)	DIREC- TION OF NET FLOW	AVERAGE SPEED (cm/sec)		
DEPTH (m)	HEIGHT ABOVE FLOOR (m)			UP	DOWN	CROSS
156	3	3.6	down	5.0	7.6	4.0
205	3	4.1	down	12.4	14.5	4.3
348	3	5.1	down	15.8	19.5	7.9
1070	3	10.2	down	9.6	15.0	4.4
1445	3	11.7	down	11.3	10.3	5.2

Table 2.2: Up and down-canyon reversal cycle data for Carmel Canyon.[23]

## Chapter 3

# Experimental Effort

### 3.1 Experiment Objectives

The December, 1988 Monterey Bay Acoustic Tomography Experiment had four goals:

- Investigate the relation between the frequency-direction spectrum of surface waves and the spectra of travel time changes in tomography signals experimentally.
- Investigate the effect of internal waves on tomography signals in a coastal environment.
- Investigate the effect of complex three dimensional bathymetry on long range acoustic propagation.
- Test the first real-time shore-based tomography data acquisition system.

The most significant difference between this experiment and other ocean tomography experiments was in the transmitted signal. For this experiment the signal repeated every 1.9375 seconds, allowing sampling above the Nyquist frequency of dynamic ocean processes with frequencies below 0.258 Hz, which includes the longer period surface gravity waves. Surface gravity waves are classified by their period length: fully developed seas - 5 to 12 seconds, swell - 6 to 22 seconds, and surf beat - 1 to 3 minutes[29]. All of these could have observable effects, depending on their orientation to the signal path. The signal was also transmitted continuously. In most other

experiments the signal is transmitted periodically to reduce the power consumption and amount of data to be recorded. The continuous transmission permits long period disturbances to be investigated without the aliasing effects of higher frequency internal waves and surface waves. Aliasing of high frequency energy to low frequencies could be a problem if only a few, time-separated transmissions are used. Internal waves and tidal fluctuations will be of much longer period than the longest swell - periods of 6 minutes (internal waves in shallow water) to 24 hours are possible.

### 3.1.1 Location and Description

The tomography experiment extended from a transmitter placed on an unnamed seamount 36 kilometers west of Point Sur to receivers placed along the north side of Monterey on the continental shelf between Moss Landing and Santa Cruz. This area and the placement of the transmitter and receivers is detailed in Figure 3.1. Monterey Bay is a semi-enclosed bay containing a submarine canyon cut into the continental shelf. This canyon (the largest on the California coast) dominates the bathymetry by cutting the bay into two roughly equal halves. The continental shelf surrounding the canyon is fairly smooth with a slope of 1 - 2 percent from shore to a depth of 90 to 100 meters on the north canyon rim and approximately 180 meters on the south rim. The canyon itself drops sharply from the shelf. The axis of the canyon is steep with a grade of around 7 percent for most of its length and ends in a fan valley at a depth of 2925 meters. Several smaller canyons join the Monterey submarine canyon, most notably the Soquel and Carmel canyons. See Chapter 2 for more detailed information on Monterey Bay.

The initial ray tracing done in preparation for the experiment used a two-dimensional ray-tracing program called Multiple Profile Ray-Tracing Program (MPP). See Section 4.1 for a description of the two-dimensional ray tracing results. This program used various sound speed profiles and took into consideration the bathymetry along planar paths between source and receiver. The shortcoming of this program is that it neglects horizontal deflection of acoustic energy. Eigenrays which leave a vertical plane between source and receiver can be reflected or refracted back to the receiver in such a complicated environment dominated by rough bathymetry. It is possible that there are stable raypaths which arrive at the receiver by bouncing off the submarine canyon walls via three-dimensional paths which are not close enough to two-dimensional solutions to be identified. See Section 4.2 for a



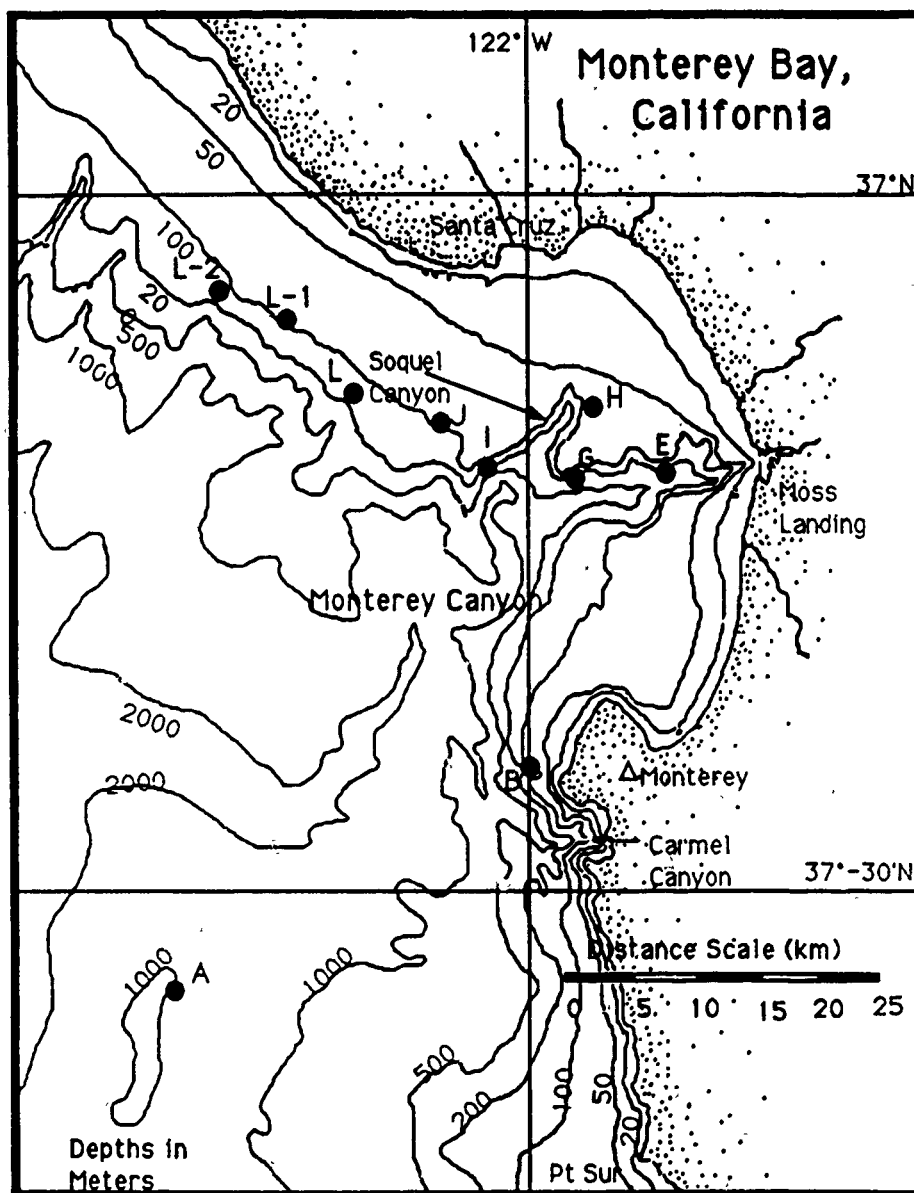


Figure 3.1: Monterey Bay showing the positions of the tomography source and receivers (positions marked with ●). The source is at station A while all others are receivers. The shore station is marked with Δ.

description of the the three-dimensional ray tracing results to date.

### 3.1.2 Receiver Placement

The tomography signal receivers for the experiment utilize fixed hydrophones located on the ocean bottom so that receiver motion would not cause arrival time fluctuations. The placement of the receiver was dictated by several requirements. First and most important, the paths of the eigenrays must pass through the water that is of interest in order to sample the sound speed. Second, there should be several eigenrays identifiable passing from the source to the receiver to give vertical resolution. Third, there should be enough separation in the arrival times of the rays traveling along different paths for the received signal to be resolved into distinct arrival times. The area of interest in this experiment is the Monterey Bay submarine canyon and the edge of the continental shelf along the north rim of the canyon. In order to sample the fluctuations due to surface waves, the path should have surface interactions. The greatest effect on the tomography signal should occur when the ray path is almost perpendicular to the direction of travel of the surface waves[30]. As can be seen in Figure 3.1, lines connecting the receivers to the transmitter would spread over an arc of about 45 degrees from north to northeast relative to the signal transmitter. If the eigenray paths are planar, then these ray paths would be perpendicular to the expected swell direction, that is from the west or northwest. Eigenrays and their travel times were predicted using the program MPP as described in Chapter 4. All of the raypaths had many surface interactions as a consequence of the shallow location of the receivers. It should also be noted that moving the location of the receiver a few meters would give much the same path in deep water but could significantly change the number of surface interactions in shallow water.

Internal waves will also have the greatest effect if propagating perpendicular to the path of the ray. The direction of propagation of internal waves in Monterey Bay is unknown but is expected to vary with orientation with the submarine canyon rim. Internal tidal bores occur in submarine canyons and have been observed in Monterey Bay [28]. Internal tides force cold, dense water over the rim of the canyon[27]. This may be one of the forcing functions generating the internal waves. All the receivers were positioned in about 100 meters of water. This was predicted to give several eigenrays without too many bottom interactions ( $<10$  in most cases) which could seriously attenuate the signal. This depth still supports the approximations

used in ray theory propagation and sea surface waves are only beginning to feel the effects of the continental shelf on their motion[30]. The receiver locations will be designated by letters as are shown in Figure 3.1. Stations J, L, L-1, and L-2 are located so that eigenrays will have relatively little travel in the submarine canyon. Their paths cross the canyon and continue up a fairly gradual slope. Stations G, H, and I require the eigenrays to pass through the most complex asymmetry along the length of the canyon, which could lead to complicated arrival time fluctuations. Station E has a path requiring propagation through 100 to 200 meter water for almost 20 kilometers. This leads to many surface and bottom interactions which could make the signal too weak to be received. Position B is the closest station and paths to B cross the Carmel Canyon but not the Monterey Canyon.

## 3.2 Equipment

### 3.2.1 Transmitter

The tomography transmitter is a 224 Hz resonant system controlled by a microprocessor and powered by batteries. It was modeled after neutrally buoyant SQFAR floats and is ruggedly designed for deep water use. As shown in Figure 3.2, it consists of four quarter-wavelength aluminum pipes, each about two meters long, and each driven at the closed end by a piezoelectric driver. The system has a high Q, limiting the useable signal bandwidth to 16 Hz when demodulated to baseband. The central tube contains the batteries, microprocessor, digital to analog converter, amplifier, and clock. The clock is a low-power quartz clock carefully calibrated with respect to temperature for very accurate time keeping. The source is held tightly between a large anchor and glass flotation balls. A tension of about 2,000 pounds with only a 1 meter distance from the anchor is expected to keep transmitter motion to a minimum. Other experiments with long mooring distance have measured the position of the transmitter as it moves in the current [2]. For recovery, two acoustically triggered releases are attached to a chain led through the eye on the anchor. Only one release need operate for recovery. The transmitter used in this experiment is one of those used in a 1981 experiment off Bermuda and in several other experiments. It transmitted a phase-modulated signal continuously for four days at an approximate source level of 172 dB re 1 microPascal at 1 meter. This same source has been used for intermittent transmission of signals at up to 185 dB re 1 microPascal at 1 meter. [1,2]

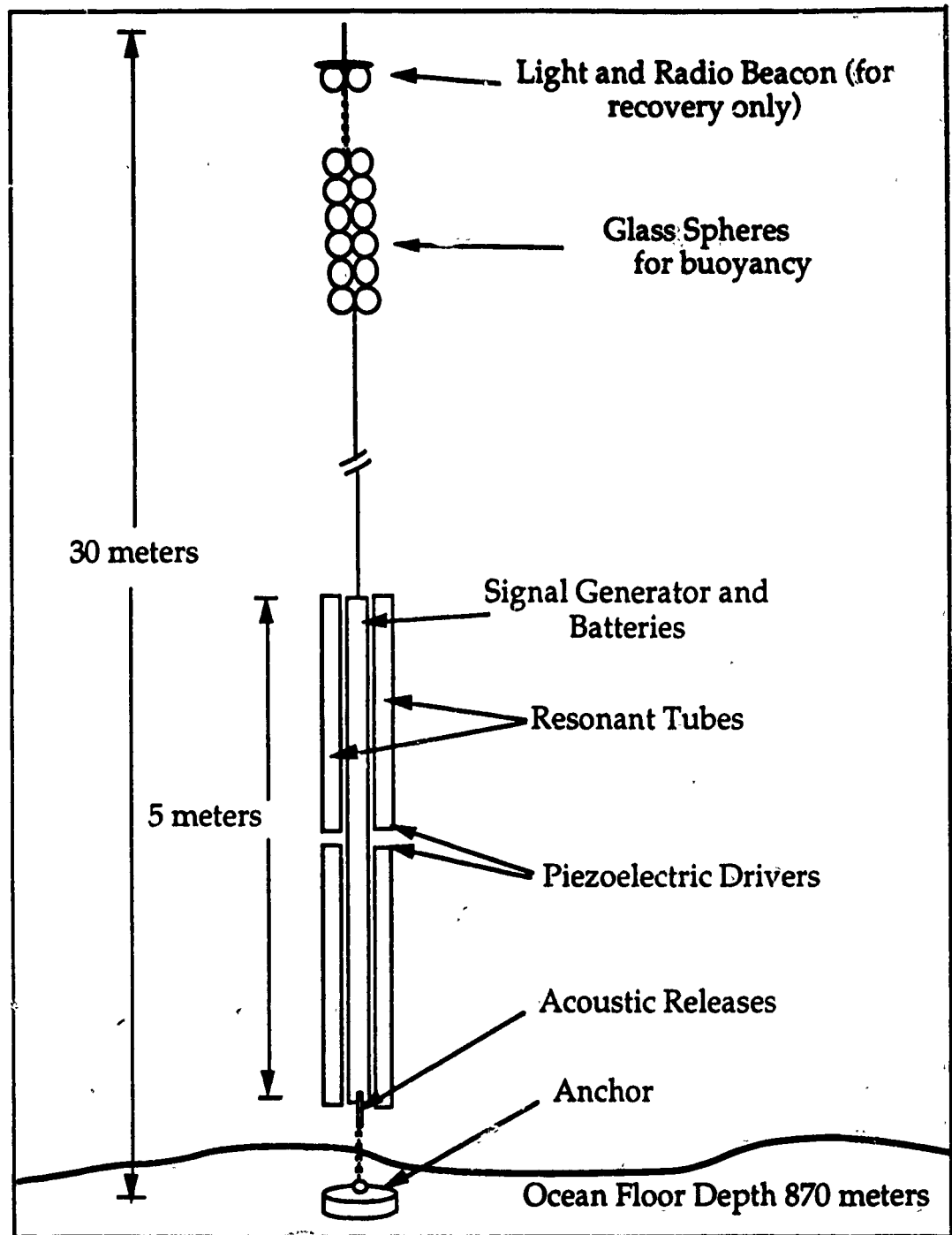


Figure 3.2: The 224 Hz resonant tomography source and mooring configuration.

### 3.2.2 Receivers

The acoustic receivers used in the experiment were modified AN/SSQ- 57 sonobuoys configured as shown in Figure 3.3. The unmodified sonobuoys have a single omnidirectional hydrophone connected by wire to a VHF radio transmitter, all powered by a salt-water battery and having a lifetime of about 8 hours. The buoys as modified used the same hydrophone, radio transmitter and antenna but had a longer life battery and an anchor so that they could be used for a longer period. During modification, the antenna and the buoy electronics package were attached to a building foam insulation and plywood float which also supported a waterproof battery compartment. Panasonic LCL12V38P wheelchair batteries were used to power the buoy. The battery could power the buoy for up to one week. The buoys were moored using 15 pound mushroom anchors and about 250 meters of polypropylene line. The hydrophone wire was attached to the anchor line so that the hydrophone would rest on the bottom near the anchor. The sonobuoy electronics packages were modified by Sparton Electronics (manufacturer of the unmodified buoys) and installed in the floats and anchor systems by Woods Hole Oceanographic Institution personnel.

A total of 11 modified AN/SSQ-57 buoys were prepared, of which there were several failures. In addition to these, two experimental Moored Inshore Undersea Warfare (MIUW) buoys, AN/SSQ-58, were deployed. One MIUW buoy was deployed with a modified AN/SSQ-57 buoy at station B and the other was deployed alone at station L-1. The data recorded from the MIUW buoys is probably not useable for tomography inversions as the hydrophone is suspended in the water below the floating buoy. Shifts in the travel time of signals received due to buoy motion probably cannot be sorted out from arrivals due to ocean path fluctuations.

The modified AN/SSQ-57 buoys have an acoustic bandwidth from 10 Hz to 20 kHz. The AN/SSQ-58 MIUW buoys have a useable acoustic bandwidth from 50 Hz to 10 kHz. Both types use an FM radio transmitter with a transmitted power out of about .5 to 1 watt on any of 31 selectable VHF channels.[31,32]

### 3.2.3 Acoustic Data Recording

The sonobuoys transmit to a receiver in a van located on Huckleberry Hill during the experiment. Huckleberry Hill on the grounds of the Defense Language Institute (DLI) at the Presidio of Monterey is one of the highest unobstructed points on Monterey Peninsula. The antenna on the van is

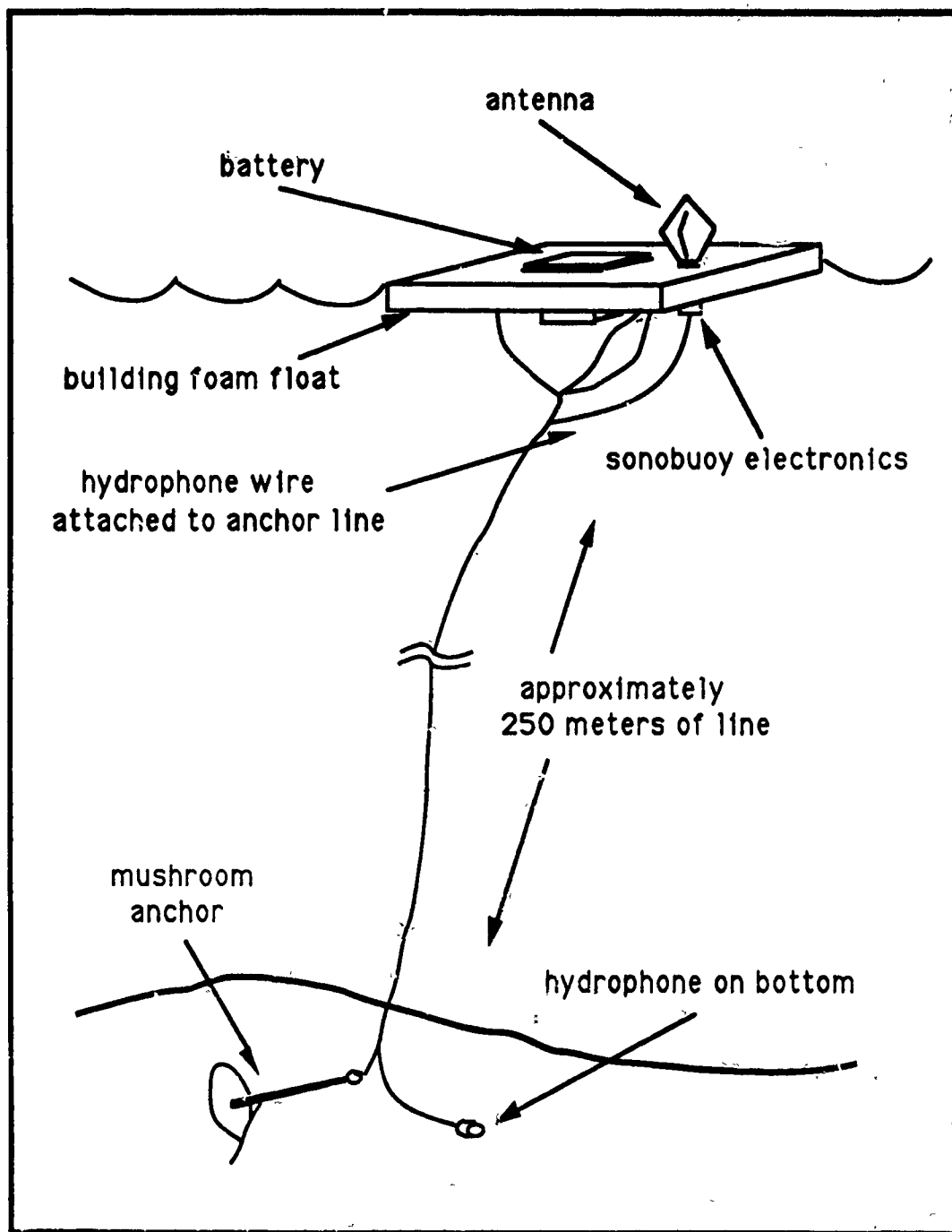


Figure 3.3: Modified AN/SSQ-57 sonobuoy as used in the Monterey Bay Acoustic Tomography Experiment. The hydrophone rests on the bottom to eliminate motion.

about 260 meters above sea level and can receive VHF and UHF radio signals from Monterey Bay and beyond to a radius of about 60 kilometers, just over 30 nautical miles. Close along the coast to the south of Point Lobos there are areas where radio shadows exist but at Point Sur good reception begins about 10 kilometers off the coast. Good radio communications were maintained throughout the area of the experiment.

The sonobuoy receiving system, shown in Figure 3.4, consists of a directional antenna which feeds the received signal through a filter and preamplifier to an AN/ARR-72 sonobuoy receiver. The AN/ARR-72 is a multi-channel sonobuoy receiver used by the U.S. Navy in aircraft. The outputs from the receiver are routed to a patch panel where they can be connected to test equipment (for analyzing the signal as it is received) or to the data recording system.

The recording system uses Yamaha Hi-Fi Stereo videocassette recorders (YV-1000) which have been modified to record two audio channels, two digital pulse-code-modulated (PCM) audio channels, and a time code signal on standard commercial videotapes. In this experiment Maxell XL Hi-Fi 120 videotapes on extended play would record 6 hours of data. One audio channel on each tape recorded a 7168 Hz synchronization square wave signal from a signal generator stabilized by a 1 MHz rubidium frequency standard. This signal is used for accurate demodulation and sampling of the recorded data. When replayed, the time-code signal displays the hour, minute, and second that the data was recorded. Data was normally recorded on the two PCM channels of each recorder but in a few cases the last audio channel was also used. All channels appear to reproduce the signal adequately, 30 Hz to 20 kHz for the PCM channels, with a slight lowering in frequency. The 7168 Hz recorded signal is shifted to  $7160.85 \pm 0.05$  Hz.

### 3.2.4 NDBC Wave Measurement and ARGOS buoys

The National Data Buoy Center (NDBC) has operated several types of directional wave measurement buoys since 1977. The moored buoys collect surface wave spectrum and direction and are usually equipped with other meteorological sensors such as thermometers and anemometers to help give a complete picture of the weather affecting the sea surface. The buoys measure the surface elevation and wave slope in order to calculate the wave spectrum and direction. The method has undergone extensive testing and has been shown to be accurate in most cases[33]. The spectrum coefficients are calculated using a segmented fast fourier transform on 100 seconds of

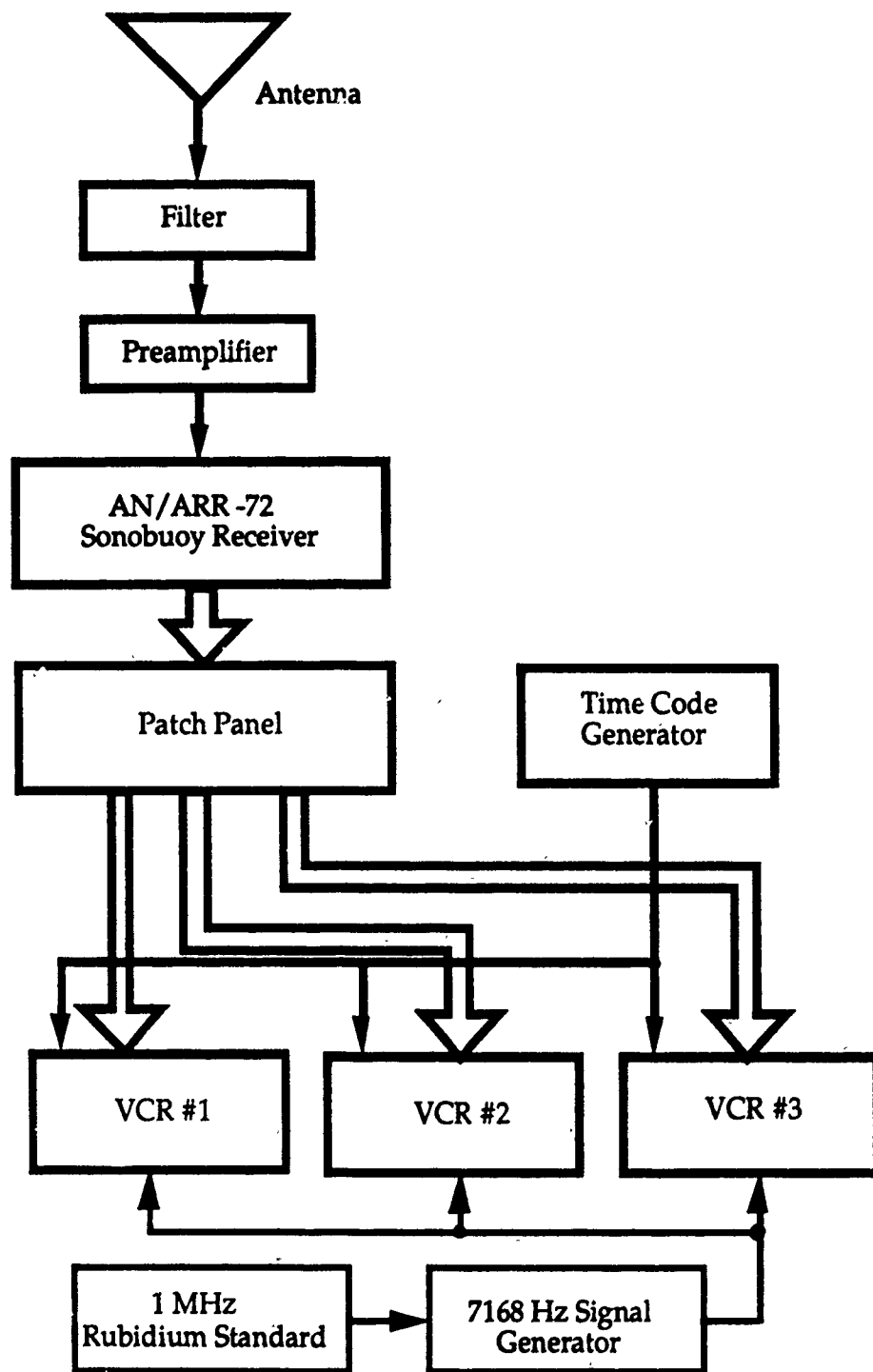


Figure 3.4: Sonobuoy data-recording system located in the van. This system receives the sonobuoy radio transmission, demodulates it for the acoustic signal, and records that signal on videotape using pulse code modulation.



data. An average is made of 19 sequential data segments with an overlap of 49 seconds, giving the data 28 equivalent degrees of freedom. After correcting for various scaling factors resulting from the parabolic windowing used before the transform, the data is ready for transmission. Once an hour the data is transmitted by the buoy to the Geostationary Operational Environmental Satellite (GOES). From the satellite the data is downlinked and relayed to NDBC and other users. The data contains information on wave height and direction as well as the power spectrum from 0.03 to 0.30 Hz with 0.01 Hz resolution. The three meter diameter discus buoy in Monterey Bay (station 46042) also measures wind speed and direction. The buoy is located in deep water (about 2000 meters) southwest of Santa Cruz (36°45'N - 122°23.5'W). Four free-drifting ARGOS buoys were obtained for additional data collection. Two of the buoys were designed to measure wave spectra in much the same way as the NDBC discus buoy. These are designated TMD by the manufacturer. The other two (designated TZD) suspend a 600 meter thermistor string below them to make temperature measurements. The buoys were designed and built by Polar Research Laboratory, Incorporated and utilize the ARGOS system for telemetry. ARGOS is a joint program of the CNES (the French space agency), NASA, and NOAA. The ARGOS transmitters are a very simple, small package (< 1 kg) powered by batteries (approximately 200 milliwatts) and used for many data transmission and tracking systems. The transmitter sends a message of up to 256 bits once every minute at 401.650 MHz automatically, whether there is a satellite overhead or not. Multiplexing occurs at the receiver through random timing of transmissions as well as through doppler frequency shifting due to satellite motion - up to 24 kHz for older TIROS low earth orbit satellites and 80 kHz for newer ones. The location of the transmitter is calculated from doppler shift measurements made by the satellite. Normal accuracy for location is about 300 meters. Typical data delivery time is three hours from uplink. NDBC receives and processes the ARGOS wave buoy data.[34]

The ARGOS buoy measurements were expected to supplement the more accurate data from the NDBC moored buoy and from other measurements. The uneven time spacing and random drift pattern of the buoys would decrease the expected usefulness of the data. But as it turned out, the data from the buoys was corrected onboard with erroneous dynamical parameters which involved zeroing wave spectral data less than zero. This erroneous correction was not recoverable and all data from the ARGOS buoys was lost.

### 3.2.5 Sound Speed Profile Measurement

The vertical structure of the sound speed in the ocean determines to a large extent the path sound energy will travel through the ocean. Records of many measurements of the sound speed profile are averaged and kept in databases in order to predict sound propagation through the oceans and this type of data was used in the initial ray tracing for this experiment. Fluctuations around this average profile are caused by numerous different forces, and to both verify the climatological data and to look for fluctuations the sound speed profiles at various locations were measured. The speed of sound in sea water can be found from an empirically derived function of pressure, salinity, and temperature. The dominant effect in shallow water is the variation of temperature. The salinity of sea water can be calculated from the conductivity of the water and the depth (or density) can be found from the pressure. A set of CTD measurements (conductivity, temperature, density) can be combined to generate a sound speed profile.

In this experiment a digital, recording, battery-powered CTD measuring device manufactured by Neil Brown Instruments was used. This system is powered by a rechargeable battery but is limited by its data storage capacity to about four hours of continuous data collection. After four hours of recording, the CTD data is transferred via cable to a personal computer for storage on floppy disks. In addition to CTD measurements the device measures the transmissivity of light in the water with a low power transmissometer. In use, the CTD device is weighted to help it sink quickly while being lowered by cable from the research vessel. The device could be lowered at about 45 meters per minute and is usually raised at the same rate. A battery powered acoustic transmitter is attached to the frame of the CTD device as a safety precaution. The transmitter "pings" every few seconds and the received sound registers on a recording fathometer trace. As it nears the bottom, the bottom reflected signal grows stronger and also appears on the trace. The distance between the two signal receptions gives the distance remaining to the bottom and so a collision with the bottom can be avoided.

Several problems are inherent with this device. Because of the limited vertical speed of the device, consecutive measurements in deep water may be separated by intervals of 30 to 45 minutes. Drift of the deploying vessel can easily be greater than one knot (1.8 kilometer/hour) and consecutive measurements might be a kilometer apart. "Yo-yo" measurements, maintaining position as much as possible, may give adequate information about internal wave amplitude but frequency and direction will be difficult to determine.

### 3.2.6 Acoustic Doppler Current Profiler

The acoustic doppler current profiler (ADCP) transmits four narrow, 120 kHz beams of sound in pulses from the bottom of the research vessel. The profiler looks at various time delays of sound scattered back to the transducers to range gate the signal. By measuring the doppler shift of returned pulses in four directions and comparing it to the ship's course and speed from the ship's navigation system, an estimate of the north-south and east-west water velocity as a function of depth is obtained. Because of the boundary conditions of internal wave motion, these create a characteristic movement of the water around the pycnocline related to the horizontal motion caused by vertical displacement in the internal wave. This may appear in the ADCP data.

## 3.3 Summary of the Experimental Procedure

The Research Vessel Point Sur, operated by Moss Landing Marine Laboratories for the National Science Foundation, was used for deployment and recovery of all equipment as well as a platform for the CTD and ADCP data measurements. The van located on the hill at DLI began recording when the first sonobuoys were placed in the water. The plan for the experiment was fairly straightforward, but evolved during the experiment as weather, equipment, and luck in locating deployed equipment began to affect schedules. The actual chronology of events is given in Appendix A. The R/V Point Sur was to begin by proceeding south to the seamount and deploying the tomography signal transmitter. During the transit to the north rim of the canyon the four drifting ARGOS buoys would be deployed. Upon reaching the continental shelf at the edge of the submarine canyon, the modified sonobuoys would be deployed, working from west to east. CTD measurements were to be made at each station and, after completion of buoy deployment, the vessel would proceed to different parts of the experiment area to make CTD "yo-yo" measurements. A "yo-yo" measurement is repeated raising and lowering of the CTD to resample the same water column, hopefully to gain information about internal waves at that position. At the end of the experiment, 96 hours after the beginning, the equipment would be recovered, probably in reverse order to the way it was deployed.

## **3.4 Signal Processing**

### **3.4.1 Signal design**

#### **System Requirements**

The basic task of signal processing in tomography is to receive the tomographic signal, decompose the received signal into individual eigenray arrivals, and estimate the arrival time of these arrivals. The processing should assist in improving the signal-to-noise ratio of the received signal if this can be done without an adverse effect on the received data. Eventually, the signal-to-noise ratio will limit the accuracy of the estimation of the arrival time. This chapter will discuss the various questions involved in signal design and processing and the solutions chosen in this experiment.

#### **Signal Resolution**

The time separation required of signals traveling along different eigenrays can be predicted by ray tracing programs such as MPP. The results described in Chapter 4 give predictions of arrival time separations between consecutive ray arrivals ranging from 2 to 500 milliseconds, with most separated by more than 80 milliseconds. In order to separate the closest arrivals, the signal would have to be less than 2 milliseconds in duration. The tomographic source that was used in the Monterey Bay experiment has a bandwidth of only 16 Hz, limiting the shortest pulse that can be efficiently transmitted to about 62.5 milliseconds ( $1/16$  Hz). Pulses arriving with less than 62.5 milliseconds separation may appear as one pulse of greater amplitude, and not be resolvable into separate pulses. Figure 3.5 shows an example of such an arrival. In this experiment, the transmitter bandwidth of 16 Hz limited the signal to a minimum period of 62.5 milliseconds, even though that could not resolve all eigenrays into distinct arrivals.

#### **Pulse Compression**

A finite length pulse signal is the closest practical equivalent of an impulse (a signal of infinitesimal length and infinite magnitude) that can be transmitted. The amplitude and length of the pulse are limited by the peak power and bandwidth, respectively, of the transmitter. An effective method of boosting the peak amplitude is pulse compression. Pulse compression has been used extensively in RADAR applications but to a lesser extent in underwater sound transmission[5]. Simply stated, a long coded signal is

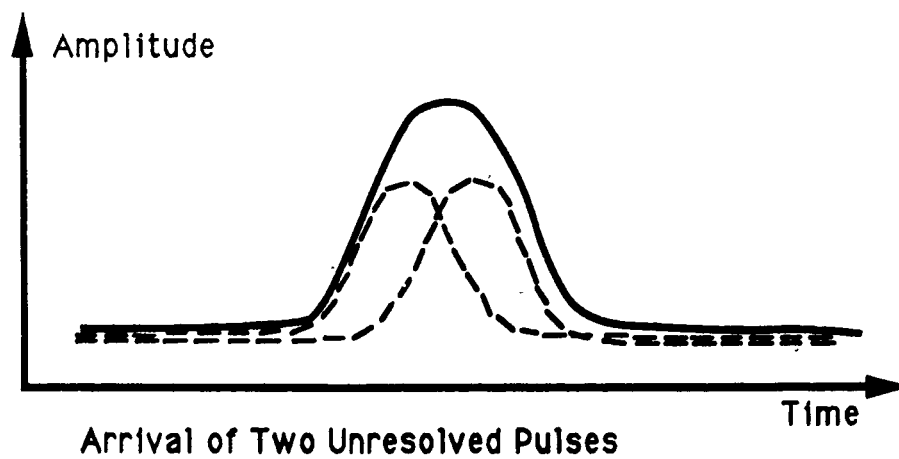
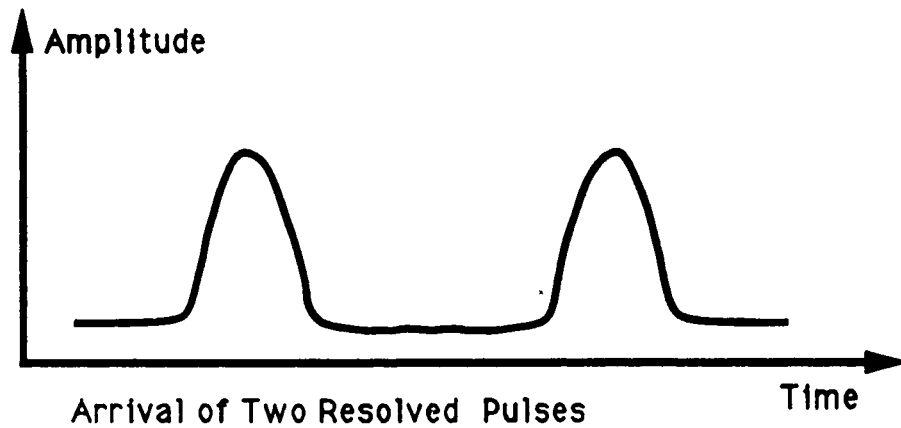


Figure 3.5: Comparison of resolved and unresolved pulses. If two pulses arrive without enough time separation they will interfere with one another. This figure shows the case where they constructively interfere.

transmitted and the received signal is passed through a matched filter which compresses the long transmission into a short, high energy pulse. One relatively easy technique for doing this is to use maximal-length sequences. This method uses a phase-modulated carrier signal to transmit a specific maximal-length code. The autocorrelation of the code with the received signal produces a single pulse at the point where the code and received signal match with an increase in amplitude equal to the number of digits in the code. The width of the pulse is equal to the width of one individual digit of the code. The length of the code is only limited by the system limitations for which it will be applied so the amplitude gain can be quite large when compared to the power the transmitter can send in a single pulse. Appendix B discusses the generation and autocorrelation of the maximal-length sequences.

### Signal Period

The maximal-length sequence consists of a number of digits determined by the order of the sequence. The code is transmitted continuously, phase modulating a carrier frequency, for the period of the sequence. If the code is transmitted at the maximum rate allowed by the bandwidth of the transmitter, the length will be determined as a compromise between two characteristics:

- The shorter the code length, the greater the repetition frequency and the higher the sampling frequency for ocean data. This determines the highest frequency which may be observed.
- The longer the code, the greater the increase in signal-to-noise ratio of the signal and the more accurately the arrival time of the signal can be estimated.

The driving consideration in this experiment is the period of the surface waves to be investigated - fully developed seas of greater than 5 seconds period. To sample the fluctuations due to the surface waves at the Nyquist frequency, the period of the signal must be less than 2.5 seconds. A maximal-length sequence 31 digits long transmitted at a digit frequency of 16 Hz has a period of 1.9375 seconds. This length was chosen for the Monterey Bay experiment. As discussed in Appendix B, the code is generated from a primitive polynomial. The polynomial for this case is

$$g(D) = D^5 + D^2 + 1, \quad (3.1)$$

resulting in the (reverse) code

$$M^T = [0000100101100111110001101110101]. \quad (3.2)$$

This code is mapped from 0,1 to 1,-1 and used to phase modulate a 224 Hz carrier signal. The transmitted signal is given by

$$s(t) = \cos(2\pi f_c t + M_i \theta), \quad (3.3)$$

where  $f_c = 224$  Hz and  $M_i$  is the  $i$ th digit in the (mapped) maximal-length sequence. The power spectrum of this signal has an envelope characterized by the familiar  $\sin x/x$  squared function

$$P(f) = \left( \frac{\sin \pi d f}{\pi d f} \right)^2, \quad (3.4)$$

where  $d$  is the digit period. The envelope is filled by impulse functions separated by the code repetition frequency. Some advantage can be taken of this. If  $\theta$  is chosen so that

$$\theta = \tan^{-1}(\sqrt{N}) \quad (3.5)$$

for  $N$  equal to the number of digits in the code, the carrier signal will fall exactly on the envelope and result in the maximum signal-to-noise performance after demodulation and pulse compression.[5]

### Arrival Time Estimation

The resulting pulse after pulse compression of the maximal-length sequence is a flat topped pulse of one code digit duration. The estimation of the arrival time of the pulse must produce two results:

1. Find a characteristic of the received pulse which can be reliably located on each arrival and the arrival time estimated.
2. Estimate the uncertainty in the arrival time estimate.

Because the signal is transmitted with a finite bandwidth and suffers some dispersion during its travel, the received signal is rounded at the edges of the pulse, sometimes so much that it resembles the peak of a Gaussian distribution curve. One method of finding a consistent point on each pulse arrival is to correlate the signal again with a square pulse of the same duration as the signal. For the perfect received flat topped pulse, this is the correlation of

two squares, the result is a triangle with the peak at the center of the signal. In effect, this gives the received signal a sharper peak. Since this processing is done using discrete points of much greater separation than the expected uncertainty in the best estimation, the position of the peak is found by interpolation. Various methods such as parabolic fit, Gaussian fit, and cubic spline are available to fit curves to the discrete points with a separation of points somewhat less than the expected uncertainty. The time of arrival of the interpolated (or original) point with the highest magnitude is the arrival time estimate. If the code is transmitted continuously then the arrival time is compared to an arbitrary starting point recurring at the code repetition frequency. The accuracy of the time estimate depends on the bandwidth of the signal and the received signal-to-noise ratio. The calculation of this type of non-linear estimate with white Gaussian noise is discussed by Van Trees[36]. Spindel gives the result as

$$\sigma_t = \frac{1}{2\pi B \sqrt{\text{SNR}}} \quad (3.6)$$

with  $\sigma_t$  the arrival time uncertainty,  $B$  the bandwidth of the signal, and SNR the signal-to-noise ratio.[5] For 10 dB signal-to-noise ratio and a 16 Hz bandwidth, this equation gives an uncertainty  $\sigma_t$  of 3.1 milliseconds.

### 3.4.2 Signal demodulation and correlation system

#### Analog Processing

The received acoustic signals from the sonobuoys are recorded on videotape for storage. This analog or pulse-code-modulated recording is played back for quadrature demodulation and digitization as shown in Figure 3.6. The tomography signal is contained in a band 16 Hz above and below the carrier frequency of 224 Hz. In order to ensure the proper frequencies and timing of the tape recordings, the 7168 Hz synchronization signal is used both to demodulate the signal and to generate an interrupt signal for the analog to digital converter. An unsynchronized demodulation system must demodulate the signal without knowing its phase. The received signal can be represented as

$$s(t) = A \cos(2\pi f_c t + M_i \theta + \phi) \quad (3.7)$$

which is the same as the transmitted signal but with an unknown phase shift  $\phi$  caused by the delay due to the travel time. Because this phase is unknown, the signal must be multiplied by both the cosine and sine at



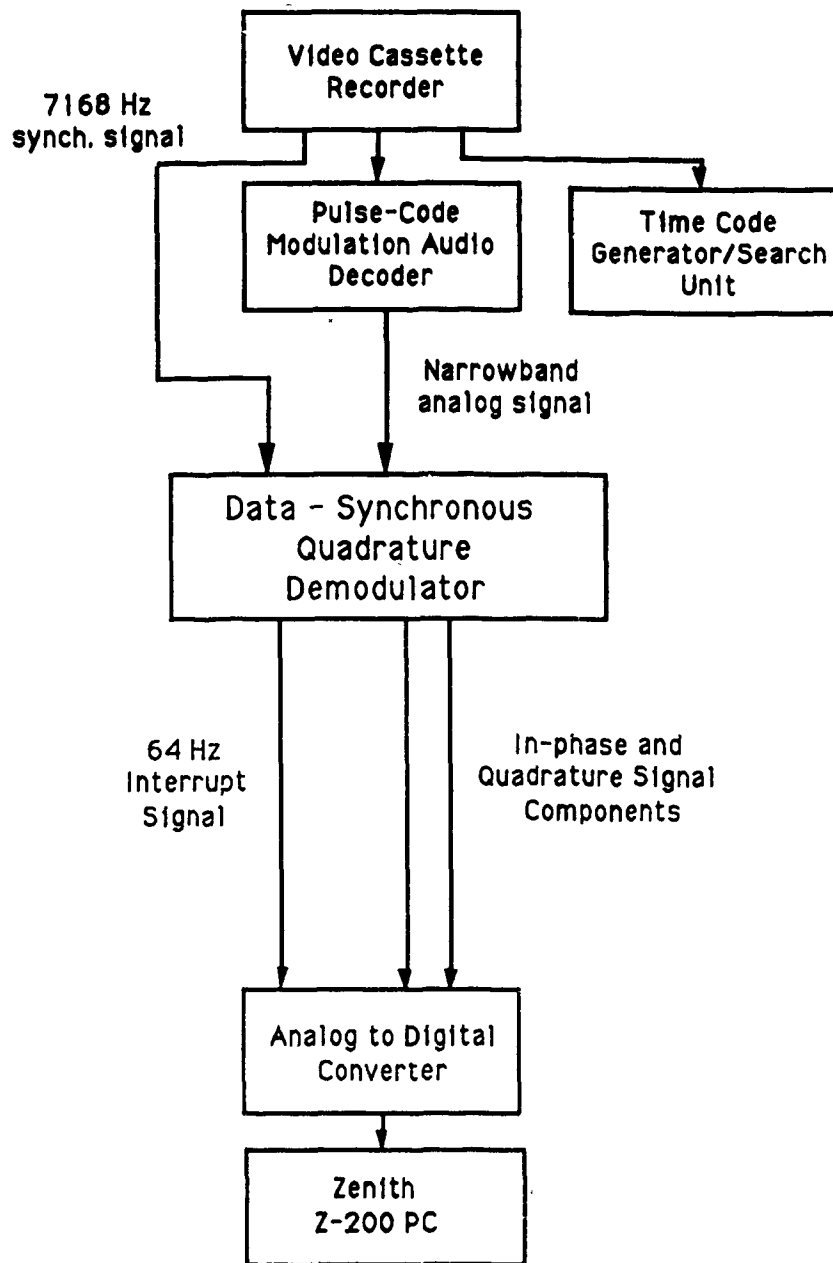


Figure 3.6: Quadrature demodulation and digitization performed in the Monterey Bay Acoustic Tomography Experiment

the carrier frequency to recover all of the magnitude of the signal in the baseband. Multiplication gives

$$\begin{aligned} I(t) &= A \cos(2\pi f_c t + M_i \theta + \phi) \cos(2\pi f_c t) \\ &= \frac{A}{2} [\cos(M_i \theta + \phi) + \cos(4\pi f_c t + M_i \theta + \phi)] \end{aligned} \quad (3.8)$$

and

$$\begin{aligned} Q(t) &= A \cos(2\pi f_c t + M_i \theta + \phi) \cos(2\pi f_c t + \frac{\pi}{2}) \\ &= \frac{A}{2} \left[ \cos(M_i \theta + \phi - \frac{\pi}{2}) + \cos(4\pi f_c t + M_i \theta + \phi + \frac{\pi}{2}) \right] \end{aligned} \quad (3.9)$$

These signals are passed through a low-pass filter to remove their high frequency components and produce the in-phase and quadrature signals

$$I_{LP}(t) = \frac{A}{2} \cos(M_i \theta + \phi) \quad (3.10)$$

and

$$Q_{LP}(t) = \frac{A}{2} \sin(M_i \theta + \phi) \quad (3.11)$$

These signals are now baseband and limited by both the input bandpass and output lowpass filters to 16 Hz bandwidth. Since all the information is contained at frequencies below 16 Hz, the digital sampling rate for the signal must be greater than the Nyquist frequency of 32 Hz to avoid aliasing. The sample rate chosen for the experiment was 64 Hz. This gives a period between samples of 15.625 milliseconds, or four samples for each digit in the maximal-length sequence.

### Digital System

The conversion from analog to digital data was accomplished with a Zenith Z-200 PC (6 MHz, 80286 based machine) equipped with a MetraByte DASH 16F data acquisition and control interface board. The mode in which the DASH 16F was used was to scan 4 channels on receipt of an external interrupt signal and store the 12-bit voltage code in memory via Direct Memory Access (DMA). During DMA the computer Central Processing Unit (CPU) is left free to execute other parts of the program. In this manner the code correlation could be performed in parallel with the analog to digital conversion, resulting in a large processing time savings. A diagram of the operation

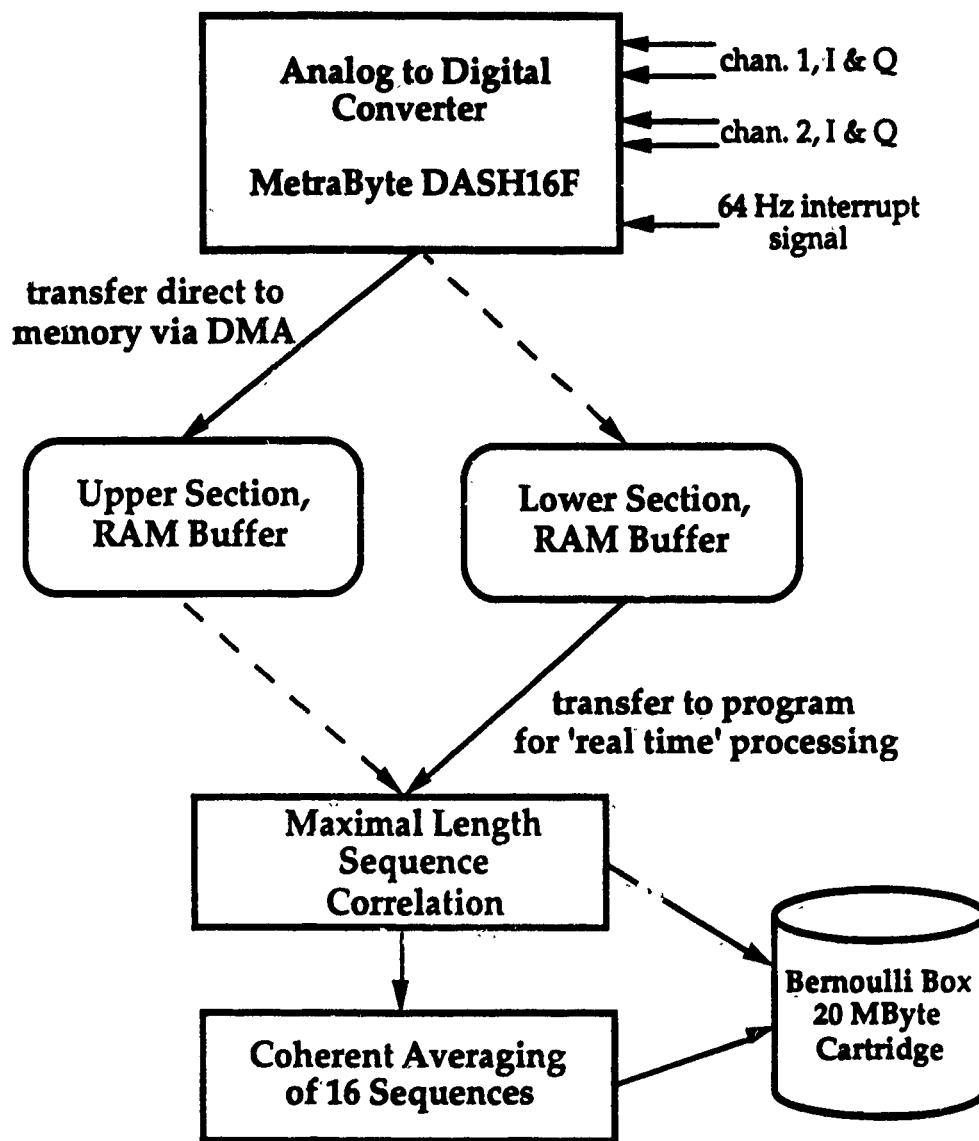


Figure 3.7: Diagram of tomography signal data flow for 'real time' digitization and code correlation.

is shown in Figure 3.7. The Fast Hadamard Transform described in the Appendix was used to perform the matched-filtering for the code correlation with sufficient efficiency to be run concurrently with the digitization. Equivalent programs performing the correlation using Discrete Fourier Transforms took approximately 300 times as long to perform and could not be used for "real-time" processing of the recorded data. The in-phase and quadrature components of the signal are combined after the code correlation and are stored as magnitude and phase. This results in about 44 kilobytes of data per channel per minute. This data was stored on 20 megabyte cartridges with a dual drive Bernoulli Box manufactured by IOMEGA. One six hour videotape containing two recorded channels of information was converted to about 17 megabytes of data on each of two cartridges. In addition a coherent average of 16 time periods is conducted and stored. The source code for FORTRAN programs to conduct the signal digitization and correlation are contained in Appendix C. The program AMORE was used for the data conversion with concurrent code correlation and is the program described in this section. The programs AINPUT and AHAD perform the same operations but in two steps, storing the digitized samples before correlating for the maximal-length sequence. Both AMORE and AINPUT make use of library routines provided with the DASH 16F board for controlling the board, including the interrupt handler for the external interrupt.

### 3.4.3 Travel time estimation

#### Eigenray Arrival Selection

An important part of understanding the data was an effective display of the data. Programs AGRAF4 and AGRAF5, listed in Appendix C, were used to generate files of magnitude and/or phase for plotting routines in MATLAB and SURFER. MATLAB is a product of The Mathworks, Inc. of Sherborn, MA and SURFER is a product of Golden Software, Inc. of Golden, CO. Both routines generate a plot usually described as a "waterfall" plot. This plot places one 1.9375 second period of the signal behind another for up to about 70 lines so that any feature common to all the sequences will stand out clearly. For the data coherently averaged for sixteen periods, if every other sequence is skipped, 62 minutes of data can be displayed on a single plot. From these plots an estimate of the resolution and stability can be made by eye. The arrival must not disappear (an indication of an unstable path) and it should not merge or split with another arrival (an indication that the ray arrivals are not resolved).

### **Interpolation between Signal Points**

The points of the received signal are separated by the sample period of 15.625 milliseconds. The points can be interpolated to a smaller separation by using curve fitting. A cubic spline curve fitting routine adapted from Press, et al., generates points separated by 0.976 milliseconds[37]. Until this point all the calculations have been conducted using integer mathematics. This gives insufficient separation for selecting the highest magnitude point after interpolation. The interpolation is therefore done with floating point decimal mathematics in FORTRAN.

### **Signal-to-Noise Ratio Calculation**

Although the point interpolation allows the selection of the time of arrival of the point of highest highest magnitude to less than a millisecond, the actual uncertainty is a function of the signal-to-noise ratio. A pessimistic estimate of the signal-to-noise ratio is made by finding the mean amplitude of all the points in a 1.9375 second data string, not trying to sort out signal from noise. The peak magnitude is then divided by this value to obtain a signal-to- noise ratio.

### **Methods of Selecting Peak Magnitude**

Two different algorithms were used to estimate the arrival time and signal-to-noise ratio. Both programs could perform coherent averaging of consecutive signal periods for up to sixteen periods. This will increase the signal-to-noise ratio but reduces the sampling rate below what is necessary for surface wave data. The method could be of use for investigating internal wave frequency fluctuations. Both programs could also perform a correlation with a square pulse. This correlation results in low-pass filtering of the data and smooths out fast fluctuations(< 65 milliseconds) as well as increasing the peak amplitude of features longer than 65 milliseconds. The noise improvement was very slight and the amplitude gain for arrivals did not greatly increase the signal-to-noise ratio or estimation accuracy. The first program, AGONY, is an interactive program which requires the user to input a window size for the program to search for a peak, a starting position, and a minimum threshold for the signal-to-noise ratio. If the maximum amplitude of the peak found does not exceed the SNR threshold, the program stops, displays the signal period in question and asks the operator to pick the peak. The window shifts to take the last peak found as its starting point.

The second program, ACRID, was both less flexible and more efficient. The window for the peak-picking was rigid and the maximum amplitude found inside the window would be the chosen arrival peak. If the signal-to-noise threshold was not attained, the previous arrival time would be repeated with the lower signal-to-noise ratio. The SNR would serve as a flag for a repeated arrival but would still allow for relatively little noise contamination. Having a uniform separation of the samples is important for Fast Fourier Transform analysis and segmented sample power spectrum estimation. Typical window sizes were about 80 milliseconds to either side of a starting position.

#### 3.4.4 Summary of signal processing

The signal processing system estimates the arrival time perturbations from the analog recordings through the following procedure:

1. The signal passes through a band-pass filter to remove any out-of-band noise.
2. The signal is quadrature-demodulated to baseband and low-pass filtered to remove the high frequency components.
3. The signal in-phase and quadrature components are sampled at 64 Hz and digitized.
4. The Fast Hadamard Transform is used to matched-filter for the maximal-length sequence code and the result is stored.
5. Given a certain window around an eigenray arrival, the arrival time of the ray is estimated with respect to an arbitrary code starting position, and the signal-to-noise ratio is calculated.
6. The geophysical time (clock time) of the data point, time of arrival, peak magnitude, and signal-to-noise ratio are stored. This stored data contains the fluctuations due to path length and sound speed perturbations and will be the input data for the tomographic inversion to estimate the ocean conditions.

## 3.5 Experimental Results

### 3.5.1 General Summary of Data

#### Acoustic Data

Approximately 300 hours of acoustic data was recorded on videotapes. This data varied because of the location of the receivers and inconsistencies in the operation of the equipment. Ambient noise at all stations was often stronger than the 224 Hz signal but, after the maximal-length sequence correlation, all sonobuoys which functioned showed some ray arrival signature. The amplitude of the received signal varied with time but does not appear to correlate with tidal fluctuations. Interfering acoustic sources were dolphins, whales, and fishing boats. Of these, only the fishing boats adversely affected the signal reception. Radio frequency interference occurred to a greater degree than expected, with most channels having some minor interference and a few having the sonobuoy signal completely blocked for several minutes. Some of the identified sources of interference were a pocket-pager transmitting station, walkie-talkies used by personnel at the Defense Language Institute, marine-band radios, vehicle dispatch radios, and the McDonald's Restaurant radio-intercom for their drive-up window. Most of the interference only degraded the signal for short periods and only on a few channels. The following is a short description by station of the received data from the time the transmitter was activated:

- Station B - 1710 12DEC to 0250 13DEC This is the shortest path and has several resolved arrivals. The buoy appears to have broken free or been dragged away in the early morning of the second day. The signal-to-noise ratio until then was good.
- Station B-1 (MIUW) - 1700 12DEC to 0130 16DEC Several resolved arrivals are present. The arrival structure appears stable but moves quickly, apparently due to buoy motion. The fluctuation in arrival time due to buoy motion probably cannot be sorted out of the motion due to path and sound speed fluctuations.
- Station E - 1430 13DEC to 2400 15DEC Only very unstable arrivals with a low signal-to-noise ratio are present. This path travels through shallow water for longer than any other path and bottom losses may have reduced the signal below a useable level.

- Station G - 1300 14DEC to 2400 15DEC This stations early data was lost because of a malfunctioning receiver. The data shows one fairly stable arrival and several unstable arrivals. This ray path travels through most of the Monterey Canyon.
- Station H - 1330 13DEC to 2230 15DEC Several unstable arrivals are present, usually with a low signal-to-noise ratio. Two dimensional ray tracing may be inadequate to predict the paths of eigenrays which reach this buoy at the head of Soquel Canyon.
- Station I - 1300 13DEC to 2200 15DEC Usually several arrivals with good signal-to-noise ratio are present. The arrivals have large magnitude fluctuations and the paths seem to be unstable over a period of hours. Again, the complex bathymetry may lead to unstable three-dimensional raypaths.
- Station J - 1300 14DEC to 1400 15DEC This ray path has simpler bathymetry than paths to G, H, and I. After the path crosses the canyon the path has a steady grade into shallow water. Several resolved rays with good signal-to-noise ratio are present. This data record is short because the first sonobuoy at this position never functioned and the second failed after 25 hours.
- Station L - 1000 13DEC to 2000 14DEC Many arrivals with good signal- to-noise ratio are present but some of the strongest are sometimes unresolved. This path also had simple bathymetry with a steady slope into shallow water after crossing the canyon. Poor reproduction from a faulty PCM encoder may have contributed to loss of signal at some points. Back up audio tapes will be examined to see if the recording is better.
- Station L-1 (MIJW) - 1400 14DEC to 1900 15DEC This buoy required the replacement of a circuit board before it could be deployed. The ray arrivals varied from two resolved arrivals to many unresolved arrivals. The shifts due to buoy motion are not as apparent as for station B-1.
- Station L-2 - This buoy failed and was immediately recovered. Data for Station J will be presented as an example data set.



### **Surface Wave Data**

The NDBC moored surface wave buoy operated as designed and hourly reports of the surface wave power spectral density, wave direction, barometric pressure, and temperature for the entire experiment have been received. This data will be compared to the data derived from tomography in the same frequency band. Unfortunately, all the data from the ARGOS drifting buoys is unusable. The algorithm used in calculating the power spectral density from the accelerometer inputs uses the lowest frequency information (0.01 and 0.02 Hz) to calculate a noise correction factor. Somewhere in the process an error was made and since neither the raw data nor the correction factor is transmitted or recorded, the correct results cannot be calculated. The data from the moored NDBC buoy should be sufficient.

### **Sound Speed Profile and Current Measurements**

The data taken during conductivity, temperature, and density (CTD) measurements and by the acoustic Doppler current profiler is being analyzed at Woods Hole Oceanographic Institution. The sound speed profile results for two positions near the path to Station J will be presented. The ADCP data is not ready at the time of writing.

#### **3.5.2 Station J Data**

##### **Station J Eigenray Prediction**

The bathymetry along a two dimensional slice between the transmitter and the receiver and the eigenray predicted MPP are shown in Figure 3.5.2 as described in Chapter 4. Although the eigenray was predicted from a historical sound speed data base, the measured profile in deep water very nearly matched and the original prediction is probably accurate enough until a three dimensional prediction can be made. The single eigenray predicted has few interactions with the surface or bottom before reaching the shelf water. Once in the shallow water of the shelf the ray has many reflections. The number of bounces predicted was seven but a small change in the angle of the ray could easily double or halve the number of surface interactions in the last 8 kilometers before the receiver.

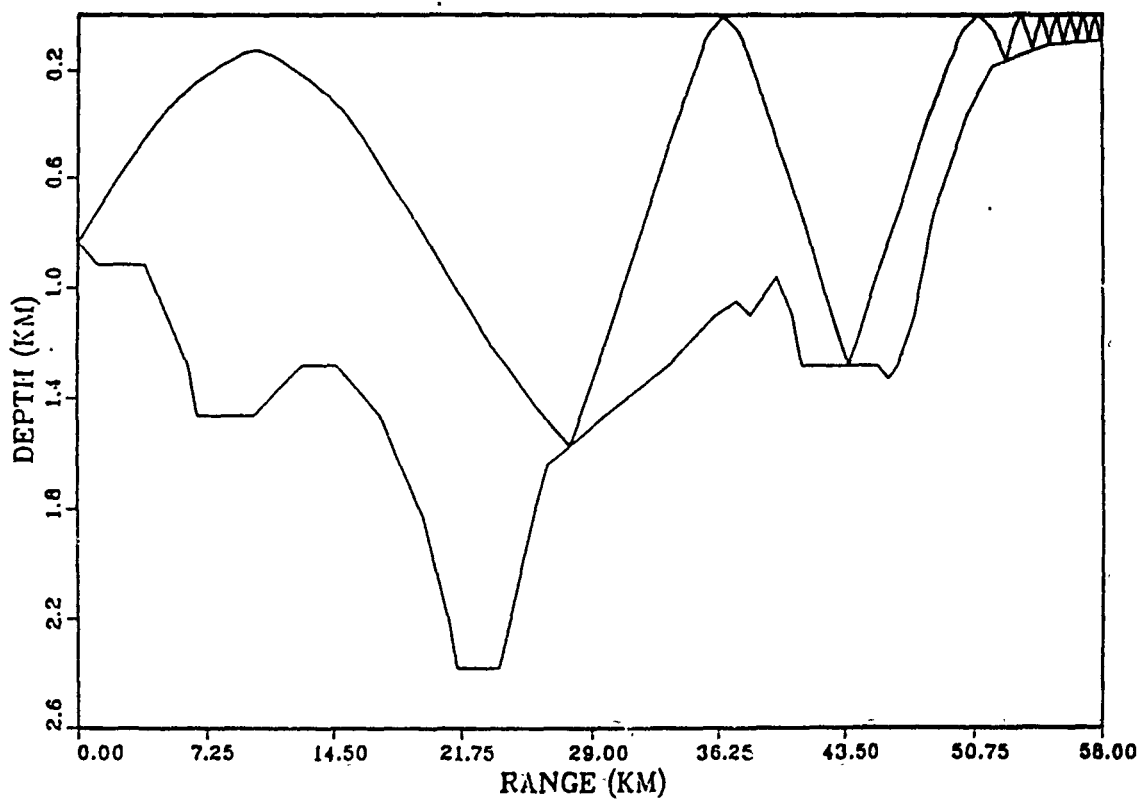


Figure 3.8: Two dimensional ray path predicted using MPP. This eigenray connects the source at Station A to the receiver at Station J.

### Measured Sound Speed Profiles

Sound speed profiles from two positions near the ray path connecting the transmitter and Station J are shown in Figures 3.5.2 and 3.5.2. Figure 3.5.2 shows the profile for shallow water at  $36^{\circ}51.095'N - 122^{\circ}04.798'W$ , near Station J. The profile in Figure 3.5.2 is from deep water at  $36^{\circ}32.906'N - 122^{\circ}16.210'W$ , near the transmitter. Both profiles show two traces, one for measurements while the CTD instrument is descending and the other while its ascending through the water column. The difference between the curves where the sound speed gradient is steepest is evidence of internal waves. The difference in depth of a certain sound speed gives a minimum vertical displacement for the internal wave but gives no information about the period or actual amplitude of the oscillation. The two points at 30 meters on Figure 3.5.2 are about 4 minutes apart, based on a 30 meter per minute rate for the CTD. Similarly, in Figure 3.5.2, the 100 meter points were crossed about an hour apart, based on a 45 meter per minute rate. Analysis of the CTD "yo-yo" measurements may give information on the deep water, lower frequency internal waves however no "fast" measurements were made in shallow water. Using the CTD measurements, the Brunt-Väisälä frequency at the density gradient can be calculated as

$$n = \sqrt{-\frac{g}{\rho} \frac{d\rho}{dz}} \quad (3.12)$$

for depth  $z$ , density  $\rho$ , and gravitational acceleration  $g$ . The Brunt-Väisälä frequency is the highest where the gradient is greatest. In the case of the shallow water with the sound speed profile shown in Figure 3.5.2, the minimum period (maximum frequency) the gradient will sustain is about 8.3 minutes. The density gradient can support much longer period oscillations also.[4]

### Received Acoustic Signal

The data recorded for Station J only covers 25 hours during the experiment because of failures in the first and second modified sonobuoys placed there. The received signal shows three or four ray arrivals throughout the functioning span. All of the arrivals fluctuate in strength over time. Shown in Figure 3.11 is an example of the received signal. This plot is the result of coherent averaging of 16 sequences and then only plotting every other averaged sequence. The data shown covers 62 minutes for each plot and is used for

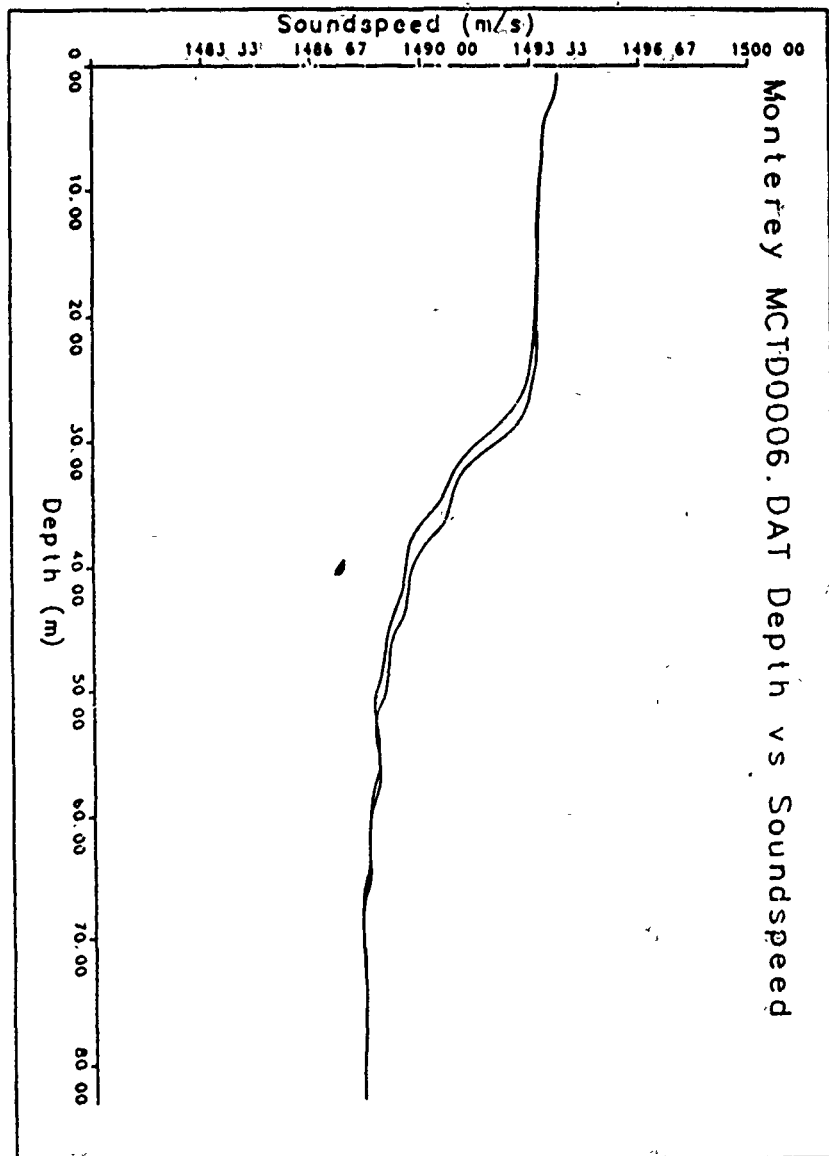


Figure 3.9: Sound speed profile from near Station J. Note that any ray path will be refracted downward. The trace has two lines, one as the CTD goes down and the other as it is brought back to the surface.

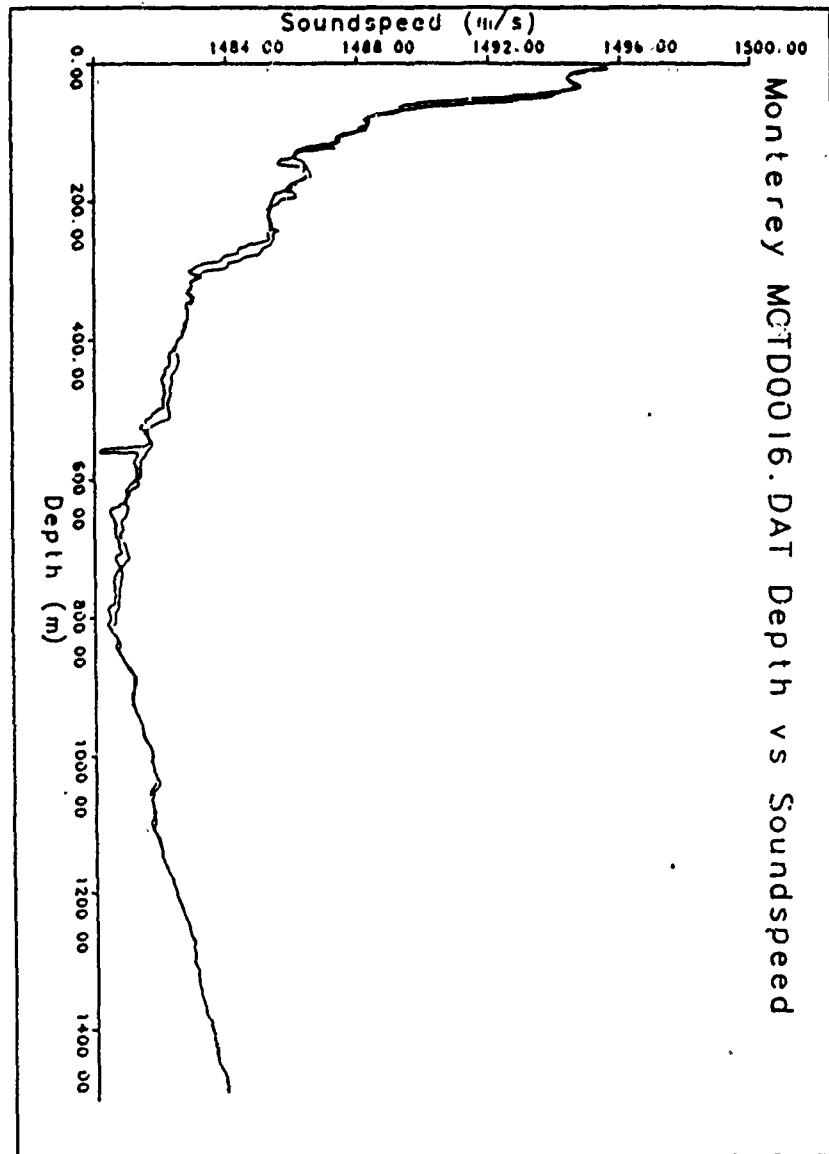


Figure 3.10: Sound speed profile from near mid-Bay. This profile is typical of the profiles found in deep water at the time of the experiment and very close to the profile used in MPP for eigenray prediction.

determining which arrival to track for the travel time fluctuation data. The orientation of the plot assists in visually integrating the data to spot characteristics recurring at the code repetition frequency. The remaining plots for Station J are in Appendix D. Note that the data from different videotapes has a new arbitrary starting point for timing the arrival estimations. This random displacement is unimportant when measuring ocean perturbations with periods somewhat shorter than six hours. If investigation of tidal frequency phenomenon was a goal of this experiment then some method of synchronizing the different data sets would be required. The individual eigenray arrivals can be located (for stable paths) on different tapes by observing the location of a ray relative to the others. The analysis of one ray arrival will be shown to demonstrate the data for travel time fluctuations. In Figure 3.11, the selected arrival has its peak at about 0.85 seconds after the arbitrary start point as shown on the sequence repetition time scale. While the signal-to-noise ratio of this arrival varies, there is always enough so that it can be measured during the 25 hour interval.

### **Travel Time Fluctuations**

The arrival time is estimated by finding the peak of the ray arrival signal. The absolute travel time is something around 50 seconds and is not measured. Each cycle of the maximal-length code is the same as the others and cannot be identified. Moreover, since the fluctuation of the absolute travel time is the same as the fluctuation in the arrival time as measured from an arbitrary starting point, only the latter will be measured. The arrival time estimation vs. time for the selected arrival shown in Figure 12 is shown in Figures 13 and 14. The uncertainty calculated from the signal-to-noise ratio is between 2.5 and 4.5 milliseconds for most of the estimates. The perturbations have a peak-to-peak amplitude of about 50 milliseconds. Also visible are some lower-frequency oscillations.

#### **3.5.3 Analysis of Arrival Time Fluctuations at Surface Wave Frequencies**

The power spectral density of the arrival time fluctuations caused by the surface waves should reflect the power spectral density measured by the NDBC surface wave measurement buoy. The power spectral density of the arrival time perturbation was estimated using a segmented Fast Fourier Transform. The individual segments were chosen to be 64 samples long to match the frequency resolution of the NDBC data. Approximately 2.2 hours of data

# Signal Magnitude Squared Station J 14DEC88

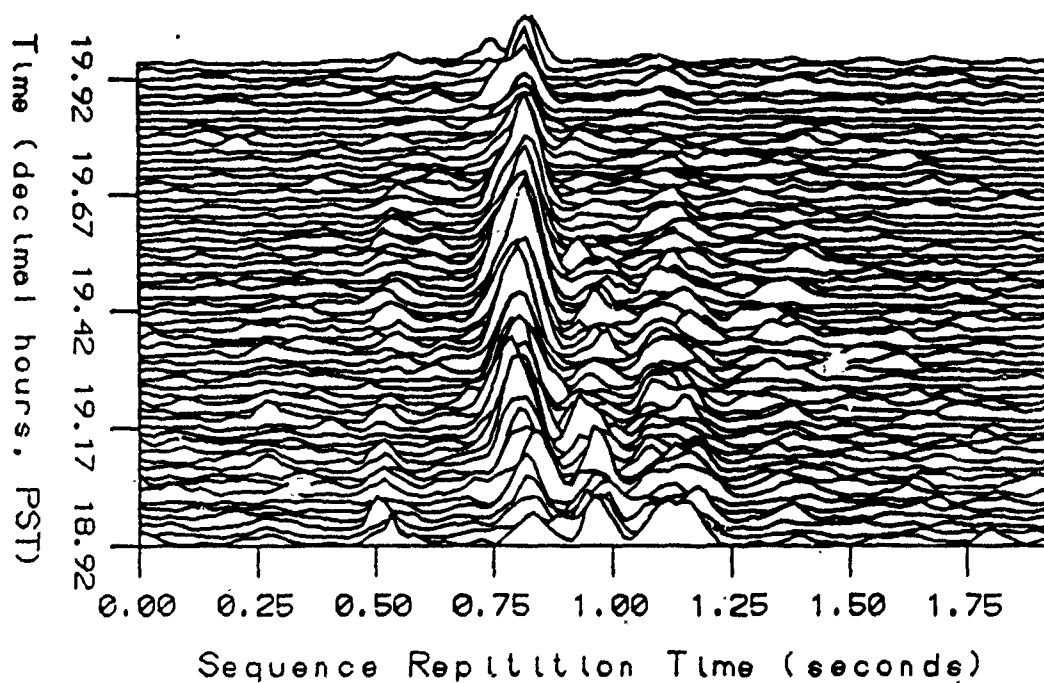


Figure 3.11: Received acoustic signal after Hadamard transforming for maximal-length sequence from Station J, 14DEC88 1855 to 1957 PST. Each line is 31 seconds of data coherently averaged to one 1.9375-second period. The earliest period is in the foreground and the latest is at the back.

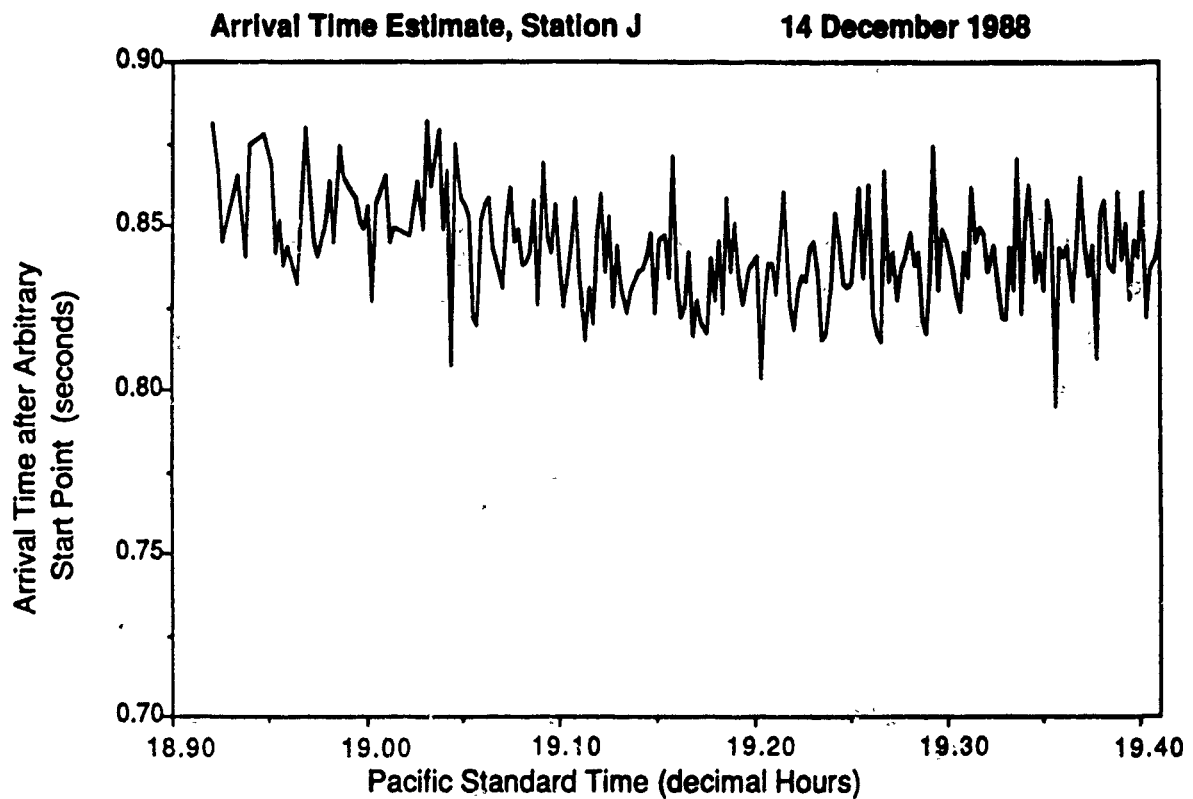


Figure 3.12: Arrival time estimate for Station J from 1855 to 1924 PST on 14Dec88. The fast fluctuations in arrival time are due to surface waves changing the path length. Lower frequency oscillations from other causes are also seen.



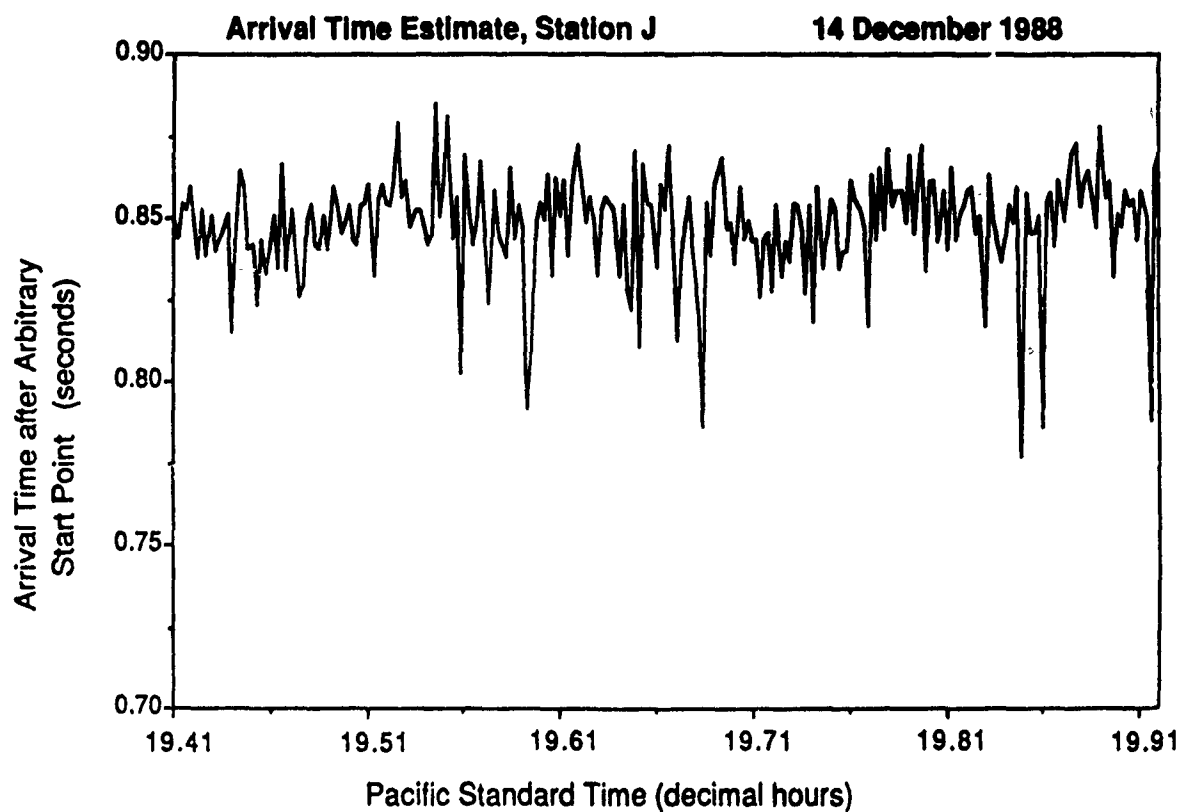


Figure 3.13: Arrival time estimate for Station J from 1925 to 1955 PST on 14Dec88. The fast fluctuations in arrival time are due to surface waves changing the path length. Lower frequency oscillations from other causes are also seen.

points provides 64 segments for 128 degrees of freedom. An example of the arrival time power spectrum is shown in Figure 3.14. The resolution bandwidth is 0.00806 Hz. This value is used to normalize the magnitude so that other spectra of the same data will have a directly comparable magnitude although a different resolution bandwidth is used. Note that the segmented transform method sums (instead of averaging) the result of the FFT's so that the total power will contribute to the magnitude. [38] The power spectrum from surface waves provided by the National Data Buoy Center has already been described. An example of the wave data is shown in Figure 3.15. The spectral resolution is 0.01 Hz. Additional sea surface and arrival time spectra are included in Appendix D. A comparison of the arrival time and surface wave power spectra immediately shows agreement in the general shape and frequency distribution with the largest concentration of power in the long period swell frequency region of 0.07 to 0.09 Hz. The arrival time spectrum also shows a smaller but still significant peak at about 0.03 Hz. This is a longer period than is normally observed for sea swell in the Pacific. This frequency of fluctuation is higher than can be attributed to internal waves and must be due to a path length change, but either a modulation on the swell or an extremely long period wave could cause it. A possible explanation is "beating" between two systems of long period swell propagating in slightly different directions. A source of this surf beat could be swell that has been reflected or refracted off the shallow water or shoreline along the north side of the Bay. The arrival time spectrum shows a nearly white noise floor. This is due in part to the random uncertainty in the estimation of the arrival estimation. All fluctuations of higher frequency than 0.258 Hz will spread out the arrival pulse width and lower the signal-to-noise ratio, contributing to the uncertainty. The spectrum for the surface wave buoy data does not show this kind of noise. The algorithm for calculating the wave data calculates a noise correction factor from the two lowest frequency data points, 0.01 and 0.02 Hz, and applies this to the rest of the data. Since the accelerometer calculations are most sensitive to noise and least sensitive to motion at the lower frequencies this is convenient. Unfortunately, the energy seen by the tomography signal may indicate that "zeroing" the low frequencies may not always be correct.

**Arrival Time Power Spectrum  
Station J 14DEC88 2001 PST**

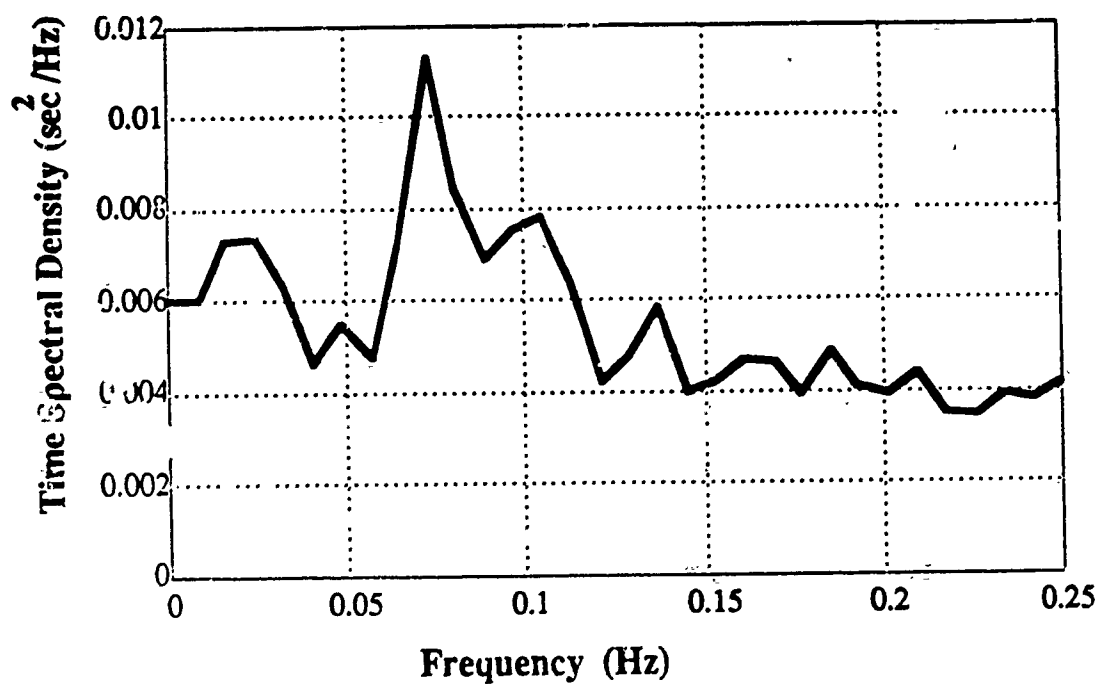
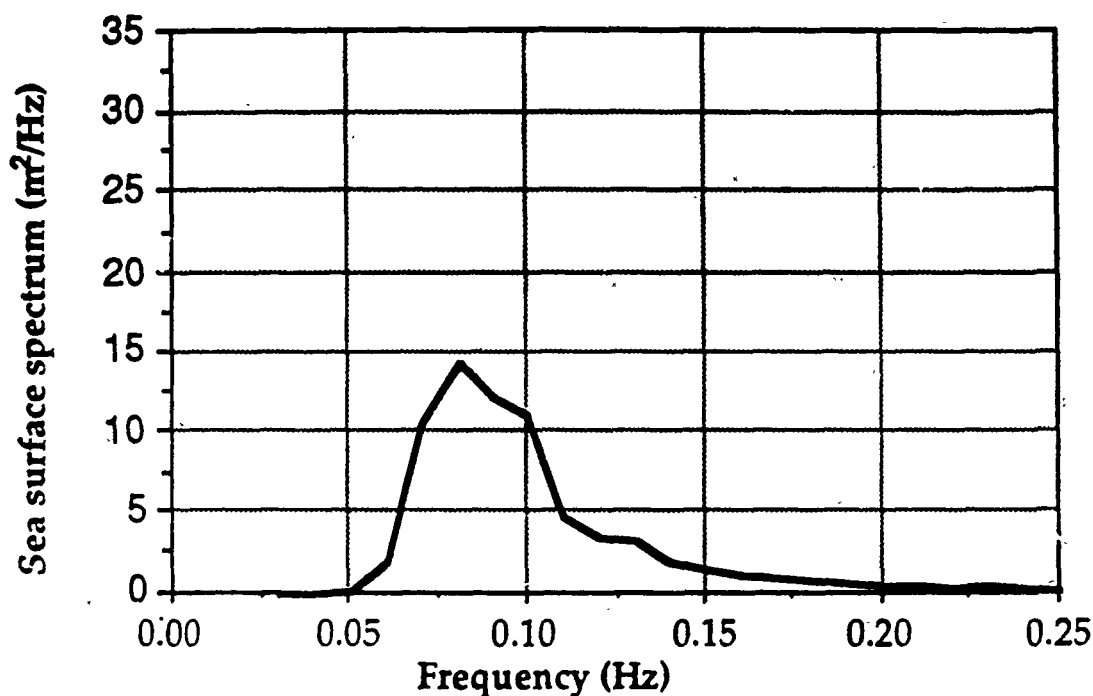


Figure 3.14: Arrival time power spectrum for Station J. Spectrum from 1855 to 2107 hours of arrival times series, 14 Dec88 PST.

**Sea Surface Spectrum**  
**NDBC Buoy 14Dec88 2000 PST**



**Significant Wave Height 4.10 m**  
**Average Period 9.67 sec**  
**Dominant Period 12.50 sec**  
**Dominant Direction 308°N**

Figure 3.15: Surface wave power spectrum in Monterey Bay at 2000 PST on 14 Dec88 as taken from the NDBC wave measuring buoy southwest of Santa Cruz.

### 3.5.4 Analysis of Arrival Time Fluctuations at Internal Wave Frequencies

The magnitude of time fluctuations at internal wave frequencies is expected to be of somewhat lower magnitude than fluctuations due to surface waves. Figure 3.5.2 shows a sound speed difference of only 5 meters per second across the thermocline, a change of only 0.33%. The surface wave causes a 300 times greater time perturbation for the same amplitude as an internal wave. To begin analysis of the data, the time perturbation data series was detrended by subtracting the mean and then low-pass filtered with an 8th order Chebyshev digital filter to a cutoff frequency of .01 of the original maximum digital frequency. Oscillations of period greater than 6.4 minutes pass through the filter including any perturbations due to internal waves. The result for Station J is shown in Figures 3.16, 3.17, 3.18, and 3.19. This data appears to show the presence of several different frequencies but segmented FFT methods were unsuccessful in measuring their distribution. It is probable that the record length before the oscillations become uncorrelated is not long enough to form a statistically significant group and still have the frequency resolution necessary to analyze the waveform. Other methods such as the Prony method, maximum entropy method, or a frequency-time spectral density may identify these frequencies[37,38].

### 3.5.5 Summary of experimental results

For the stations analyzed to date, many of the acoustic arrivals are observed to be resolved and stable. The arrivals shown in Figure 3.11 illustrate a typical arrival pattern for about an hour. The strong central arrival is present in the Station J data for the 17 hours that the sonobuoy was operating. The lowpass-filtered arrival time of that central peak is shown in Figures 3.16, 3.17 and 3.18. A key result is that tidal effects do not destroy the stability of the multipath arrival that has traversed the Monterey Submarine Canyon. This result bodes well for the stability of arrivals in a permanent tomography system in the Bay.

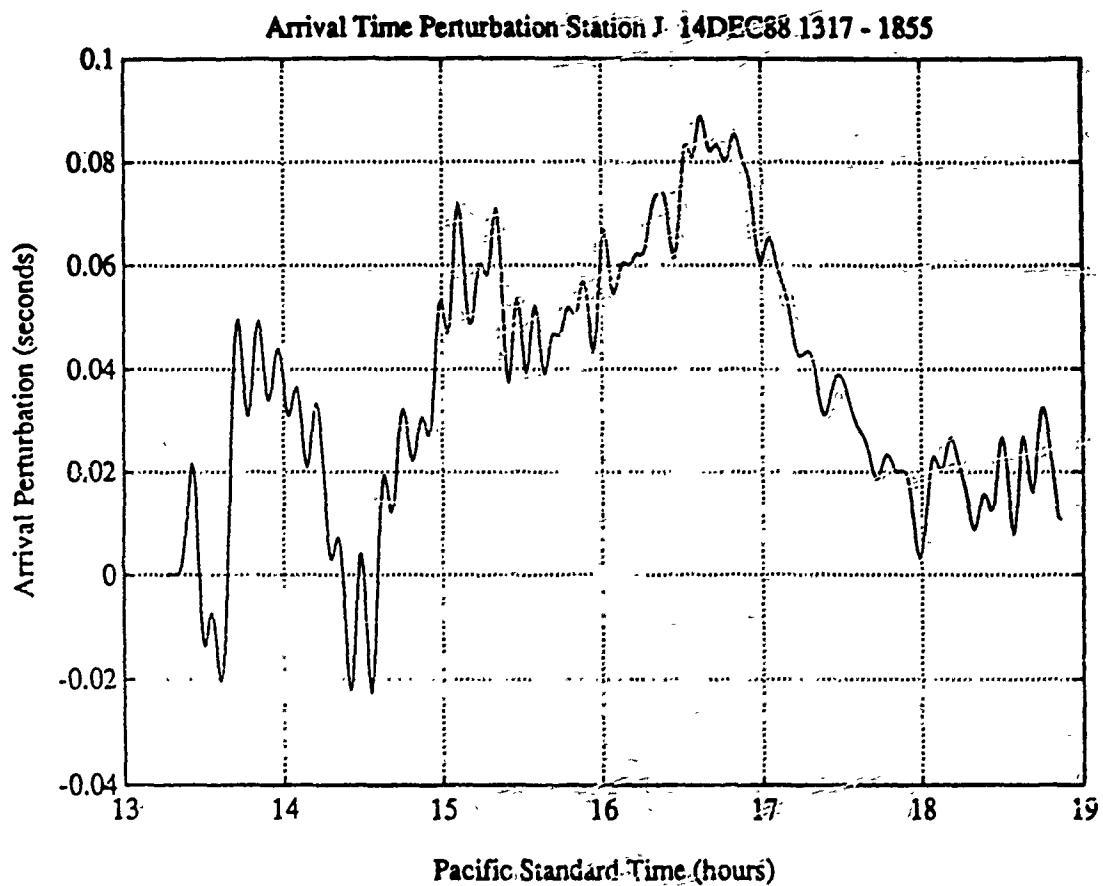


Figure 3.16: Arrival time data for Station J lowpass filtered to 0.00258 Hz (Period = 6.4 minutes).

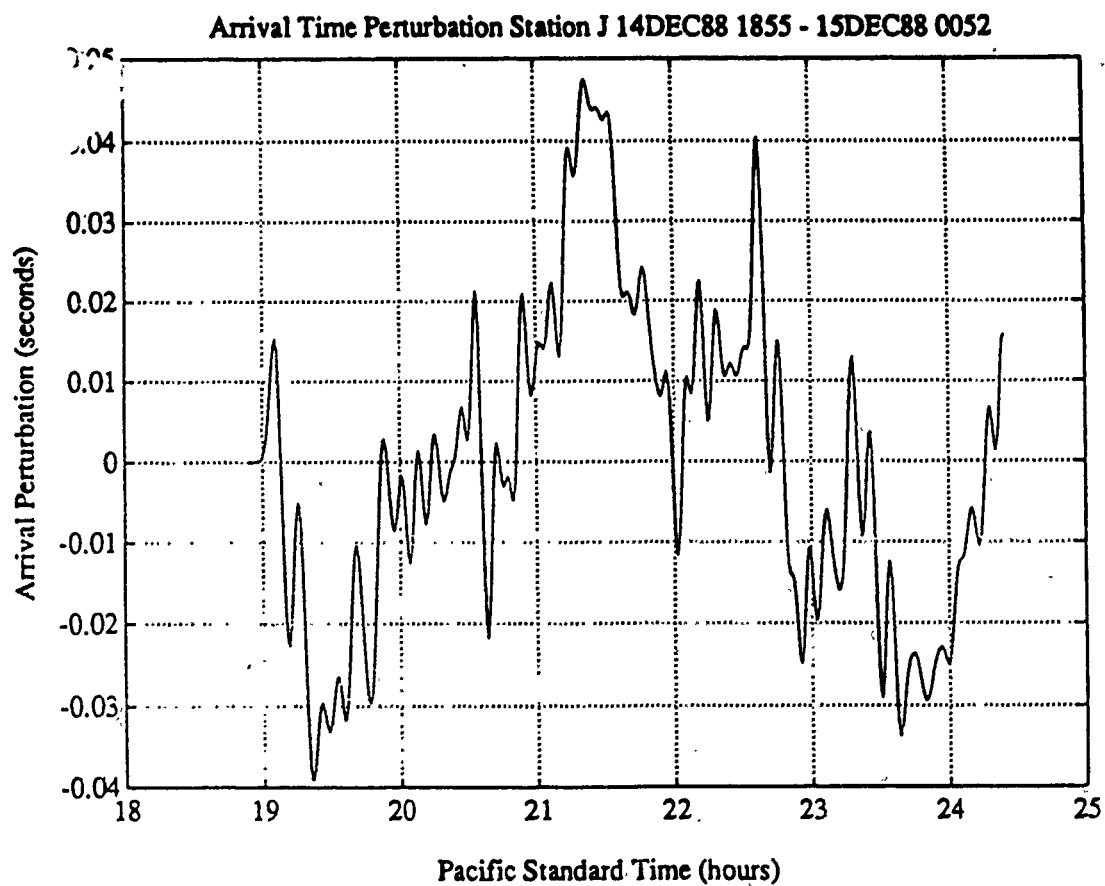


Figure 3.17: Arrival time data for Station J lowpass filtered to 0.00258 Hz (Period = 6.4 minutes).

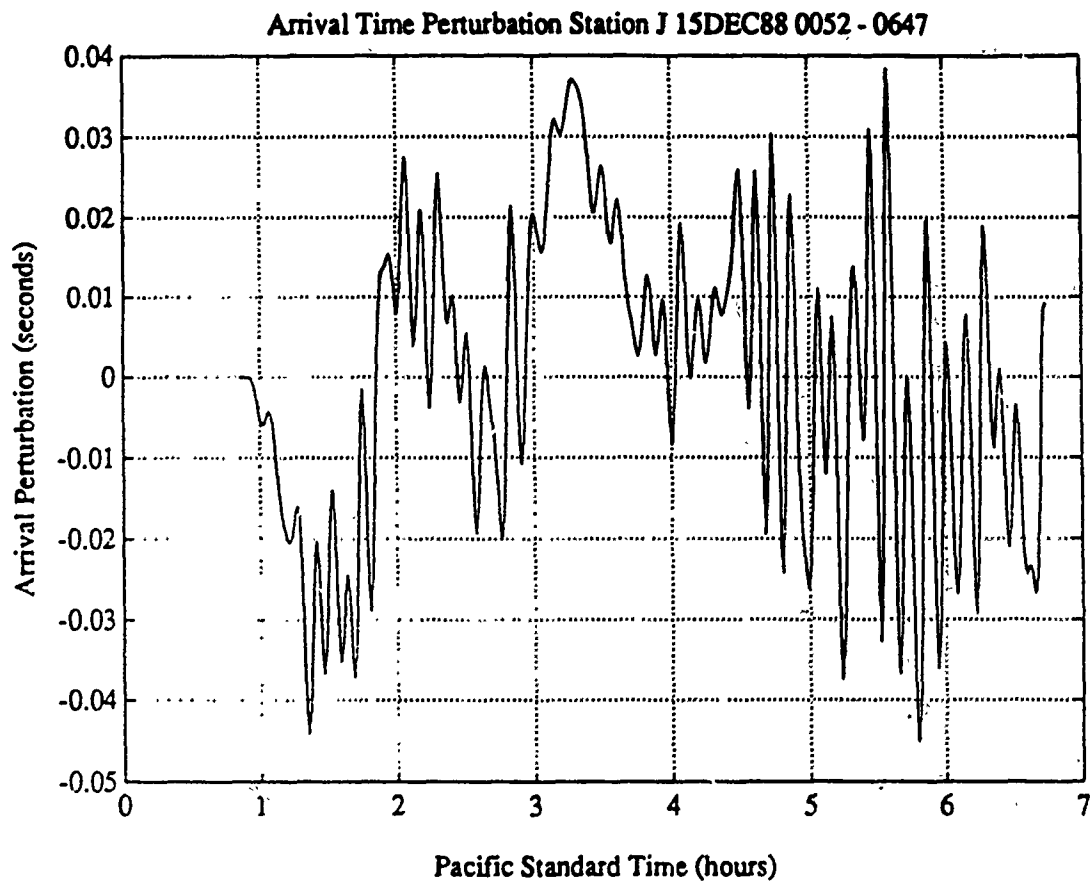


Figure 3.18: Arrival time data for Station J lowpass filtered to 0.00258 Hz (Period = 6.4 minutes). High amplitude after 0400 is due to low SNR during storm.



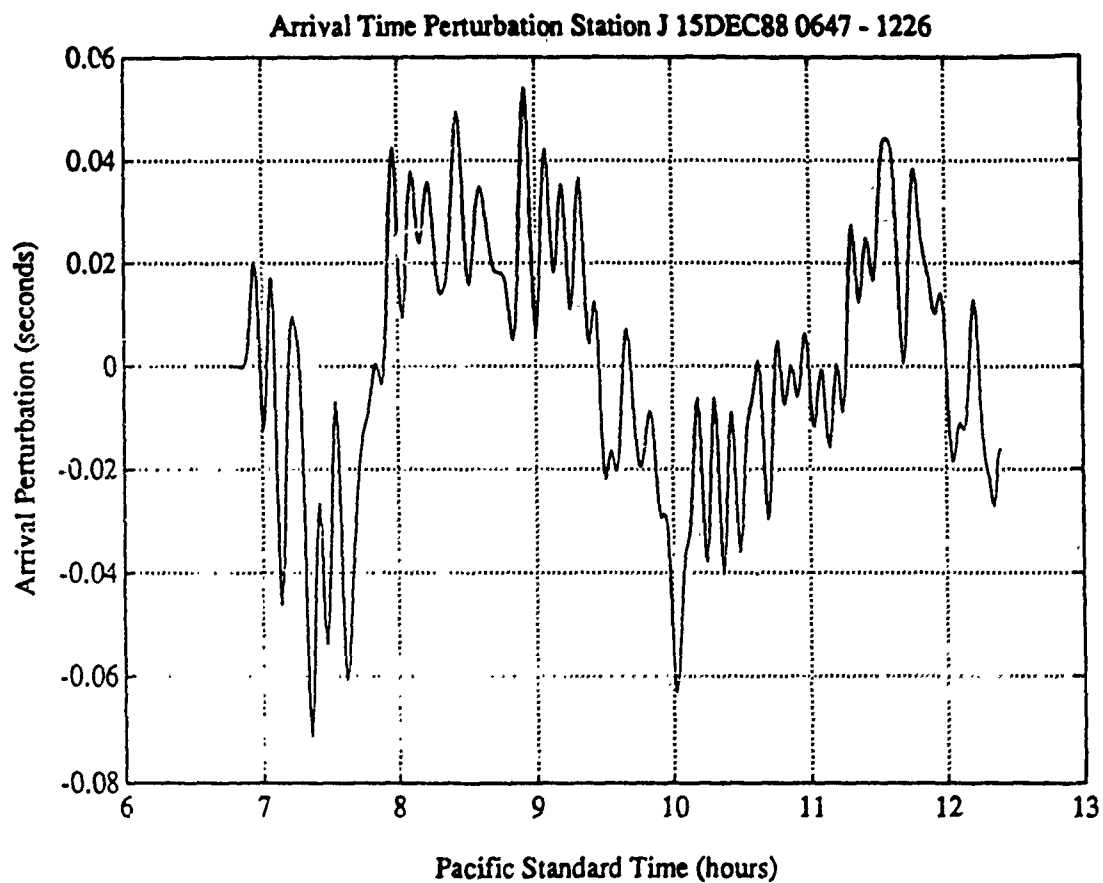


Figure 3.19: Arrival time data for Station J lowpass filtered to 0.00258 Hz (Period = 6.4 minutes).

## Chapter 4

# Modeling Effort

### 4.1 The Multiple Profile Ray-Tracing Program

#### 4.1.1 Description

The analysis tool that was the basis for the selection of receiver locations in Monterey Bay for the December 1988 tomography experiment is called the Multiple Profile Ray-Tracing Program (MPP). Originally written as five separate programs by Ocean Data, Inc., for the Office of Naval Research [35], the MPP program has evolved to its present form through extensive modification by John Spiesberger of the Woods Hole Oceanographic Institution. This program computes transmission loss and arrival structure for the eigenrays that it determines will arrive at a fixed receiver, from a source at a fixed depth. The ocean is modeled with a range-dependent sound speed profile (SSP), variable bottom depth and bottom reflectivity. Transmission loss is calculated under a variety of options, including

1. asymptotic treatment of caustics with rms or fully coherent addition of the two paths in the interference region of the airy functions;
2. surface-image interference at the source; and
3. source and/or receiver vertical directivity patterns.

Output generated, based on a successful finding of eigenrays, are

1. all input data;
2. ray trajectories at arrivals;

3. sequential signature groups;
4. precise angle, time and intensity at a limited number of range points using quadratic interpolation;
5. transmission loss versus range;
6. plot of eigenray path from source to receiver; and
7. stick plot of transmission loss versus arrival time for the eigenrays.

#### 4.1.2 Program Flow

Figure 4.1 is a block diagram of the program flow, with input files shown on the left side of each routine and output files on the right side of the routine block. The command file runart is called upon to execute the routines writefiles2art, mpp1, mpp2cout(1st pass), zofth, post63 and mpp2cout(2nd pass), after an input data file has been created by the user. The routine nrayfil2 is used to generate the ray tracing and stick plot graphs from binary data in file TAPE16.DAT and TAPE 20.DAT.

Writefiles2art is a small routine that separates and reformats the user-generated input data into six different files. These six files are accessed by the other programs that runart executes. Zofth is another short routine that plots initial angle versus the depth at which its ray path arrives at the receiver location (rang). Most of these rays do not arrive at the receiver, i.e., they are beyond the vertical miss allowance. For the simulation, a ray has to come within a vertical distance of 15m from the receiver, either above or below. Since the receiver was placed 1m below the receiver. Post63 is the eigenray post-processor routine. It determines the eigenrays' arrival angle at the receiver, creates file TAPE16.DAT which is used by nrayfil2 to generate the ray trace graph, and produces a printout enumerating the eigenrays in three sorted lists, based on increasing travel time, decreasing initial angle and increasing transmission loss. The function and logical flow of the four main programs, used to determine and plot the eigenrays at a given receiver location, will be described in more detail.

#### Mpp1

Mpp1 is the second routine called by the command file runart. Its purpose is to determine the sectors within the region between two range-stipulated input SSPs. These sector determinations are required for calculating ray

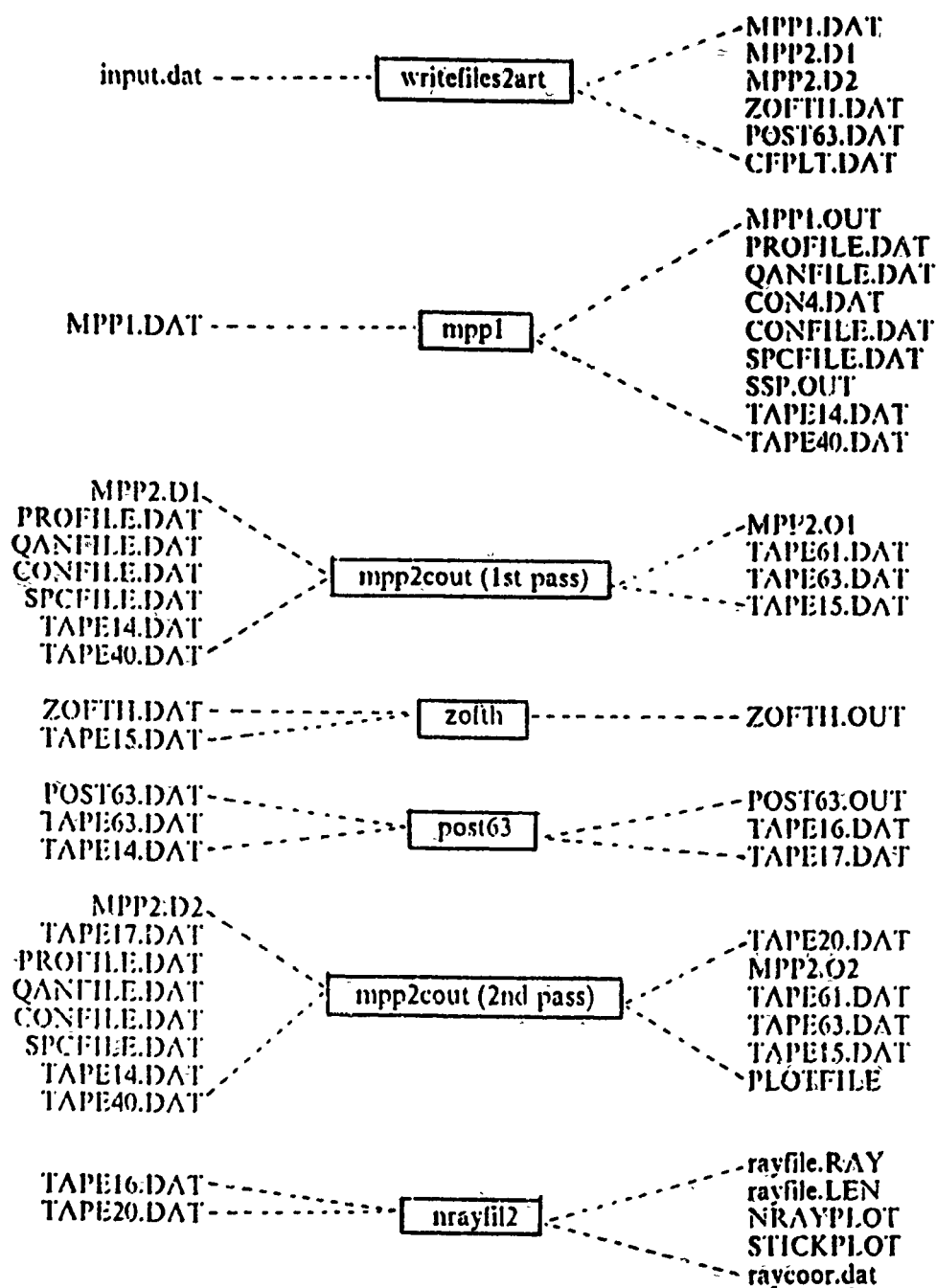


Figure 4.1: MPP block diagram with input and output files.

paths in mpp2cout. Mpp1 also uses the input bottom data to assemble the bottom profile and tabulate the bottom loss as a function of grazing angle in each of the range domains. If a loss function is specified as "Modified Rayleigh", the program tabulates it on a variable mesh to yield accurate values by linear interpolation.

Sectors can be either triangular or rectangular. Rectangular sectors ease the computational crunching of the ray path determination logic, and speeds up the computer time. Sector determination begins with a comparison of the sound speed at the very bottom of the first SSP (sspl) versus the very bottom of the second SSP (ssp2). If sspl equals ssp2 at the bottom, then a horizontal line is attached between the two points, and the next higher profile values for sspl and ssp2 are compared. If the two values are not identical, then a triangular sector will be specified. Once one sector has been determined to be a triangle, the entire upper region will be triangularized, even though all shallow points of the two SSPs may match. The only way to have all rectangular sectors is to have completely identical SSPs.

#### Mpp2cout(1st pass)

Mpp2cout(1st pass) is the first half of the eigenray processing programs. The main program is very small, but it calls seven subroutines that in turn call other subroutines. The first subroutine, ctl1, inputs data and takes care of initialization. The program then loops through the rest of the subroutines, until it equals the number of passes that the user's input file stipulated as a maximum number of passes. The first subroutine in the loop, reset, locates the sound speed triangular section that encompasses the receiver.

The next subroutine, ctl2, is the longest and accomplishes the most. After initialization, it determines the initial velocity sector for the ray and the direction that the ray will go. As the ray travels toward the receiver, ctl2 computes the ray intersections with sector boundaries (top, bottom and sides), stores parameters and checks for bottom reflections. Next, it calculates the spreading factors and performs a check for caustics. If there is a caustic, it locates the caustic for both curved and straight rays. Continuing, this subroutine updates the intensity derivatives for bottom reflection, surface reflection, sector crossings and region crossings, and the transmission loss is then updated. After arrival information is stored, then the ray is checked to see if it should be cut. The following are reasons to cut a ray:

1. ray has reached maximum range (ray range > target range);

2. ray angle too steep (ray has reflected at an angle > 85;
3. max bottom reflections exceeded (as stipulated by the user);
4. max turning events exceeded (the total number of bottom reflections, bottom horizontals, surface reflections and surface horizontals have exceeded the maximum number of turning points as stipulated by the user).

The rays that were not cut are now sorted in increasing angle order by the subroutine sort61. The second biggest subroutine, iterat, then determines the relationship of the uncut rays with the receiver at the target range. It also extrapolates new rays and checks the angle loss tolerance for these new extrapolated rays. All of the uncut rays have one of the following ray/target relationships:

1. good bracketted source depth (IDENT=2), where a pair of rays vertically surround the receiver;
2. good diffraction field (IDENT=3), where a pair of rays do not bracket the source but they appear to be within the receiver's focus or convergence region;
3. badly bracketted source depth (IDENT=4), where a pair of rays fail the criteria for the above relationships;
4. bad diffraction field (IDENT=5), where the ray pair appear to be within the receiver's focus but they are outside of the time tolerance;
5. good bracketted source, two eigenrays (IDENT=6);
6. badly bracketted source, two eigenrays (IDENT=7); and
7. bad signature pair of rays (IDENT=8), which is the most common ray/target relationship, resulting from the ray pair being too close to each other.

Mpp2cout concludes by calling subroutines clean, which removes the deletable angles from file TAPE61, and dump63, which prints out the ray status for all uncut rays. The program then increments the pass number counter and starts all over again.

### **Mpp2cout(2nd pass)**

The second pass of mpp2cout is the eigenray plotting run and is logically very similar to the first pass of mpp2cout. It is executed after post63. This run begins with the "good bracketted source" and "good diffraction field" rays that were first identified in mpp2cout (1st pass) and post-process in post63. A trace for each of these rays is produced. The following information is provided in the trace at every surface reflection, bottom reflection, refraction and caustic along each ray's path:

1. range (km),
2. depth (m),
3. angle (deg),
4. time (sec),
5. loss (dB),
6. number of caustics,
7. arrival number,
8. number of surface horizontals (refractions),
9. number of surface reflections,
10. number of bottom horizontals (refractions),
11. number of bottom reflections, and
12. total number of turning points.

Another main difference between the two passes is that this second pass generates the file TAPE20.DAT, used by nrayfil2 to graph the ray plots and stick plots. For each coordinate on the ray trace, not just the turning points, TAPE20.DAT stores the range (km), depth (km), angle (radians) and sound speed (km/sec). In the beginning of this pass, angle values are read in from file TAPE17.DAT. Otherwise, mpp2cout (2nd pass) goes through the same logical flow as mpp2cout (1st pass), and is the final eigenray processing program executed by the command file runart.

## Nrayfil2

The routine nrayfil2 is called by the user after the command file runart has executed all of the eigenray-determining programs and eigenrays have been identified. Since nrayfil2 is used to generate the ray tracing and stick plot graphs, there is no reason to execute this routine if there are not any eigenrays. This routine should be run immediately after the programs executed by runart determine one or more successful eigenray(s), or else rename TAPE16.DAT and TAPE20.DAT files so that they can be accessed later by nrayfil2.

There are six options that can be accessed in this program : 1. make, 2. inspect, 3. rayplot, 4. stick, 5. add, and 6. delete. "Make" has to be the first option specified since it generates two files of ray data that is used by the other options. It requires as input the files TAPE16.DAT and TAPE20.DAT that were generated for the last executed MPP run. The output file name, has to be all capitalized and end in. RAY. If, for example, the user specifies the ray file name as RCVR2.RAY, this "make" option creates a file with that name and another file with the name RCVR2.LEN. Both are needed for the other options.

"Inspect" allows the user to inspect the rays and to store all of the ray coordinates in the file RAYCOOR.CAT. These ray coordinates are used to graph the ray trace, and include the values of range, depth, angle and sound speed for every specified point on the ray trace graph. "Add" allows a new ray to be added to an existing ray file, while "delete" removes an unwanted ray from the ray file.

The last two options plot graphs. "Rayplot" will plot the ray trace of one or more rays, based on the inputted ray file name. For the first ray file stipulated, a list of all the initial ray angles are displayed on the screen, after the user has specified the graph dimensions and titles. The user indicates the ray angle that is to be plotted, and has the option of plotting more rays on the same graph or stopping. Another ray file can be accessed, and those angles can be added to the graph with the first ray file angles. The graph data is placed in the NRAYPLOT file, which is then plotted. The ray traces in Appendix A.2 were produced with this option. "Stickplot" graphs the transmission loss for all the rays that are contained in the user-specified ray file. The only input options are graph dimensions, graph title and ray file name.



### **4.1.3 MPP Input/Output**

The focus of this effort was to recommend the locations for six receiver hydrophones that were used in the December, 1988 tomography experiment, and to provide eigenray and travel time information related to each site. The recommendations were based on the results from two-dimensional, range and bathymetry dependent, ray tracing computer simulations for various locations in and around the bay, as well as a preliminary assessment of the oceanographic and geo-acoustic environment of the region. This section will identify the receiver locations that were addressed, the input parameters used in the MPP computer program, and the results from the simulations.

#### **Simulated Receiver Locations**

Seventeen locations for possible receiver hydrophone placement were tested using the MPP program. These points are on the continental shelf surrounding the Monterey Canyon, from southwest of Santa Cruz to Pacific Grove, excluding the Monterey Seaside nearshore area where a direct ray from the Point Sur seamount (source location) could not reach. All of these sites are shallower than 100m, and the hydrophone in the simulation were placed 1 m above the sea floor.

All of these locations were selected for specific reasons. Figure 4.2 delineates the position of these receiver location in the area of Monterey Bay, while Table 4.1 provides the specific position. Any eigenrays arriving at receiver numbers 6 and 7 will have traveled through Carmel Canyon the trough of Monterey Canyon. Sites 4, 8 and 15 are in the general area of the Monterey Canyon head, where internal waves are at their highest amplitudes. Receiver 5 is located on the edge of the south wall of Monterey Canyon, and was selected for comparison between rays going through the narrow part of MSC and those that do not. Any eigenrays that receiver 14 would pick up have traveled right down the Monterey Canyon in the granite wall formation. Locations 3, 9, 10, 12 and 13 surround the Soquel Canyon. Finally, receiver positions 1, 2, 16 and 17 are out of Monterey Bay and would have eigenrays that traveled through the trough of Monterey Canyon, where the floor is wider.

#### **Input**

For each receiver location of interest, an input file was created that provided the MPP routines with the following information:

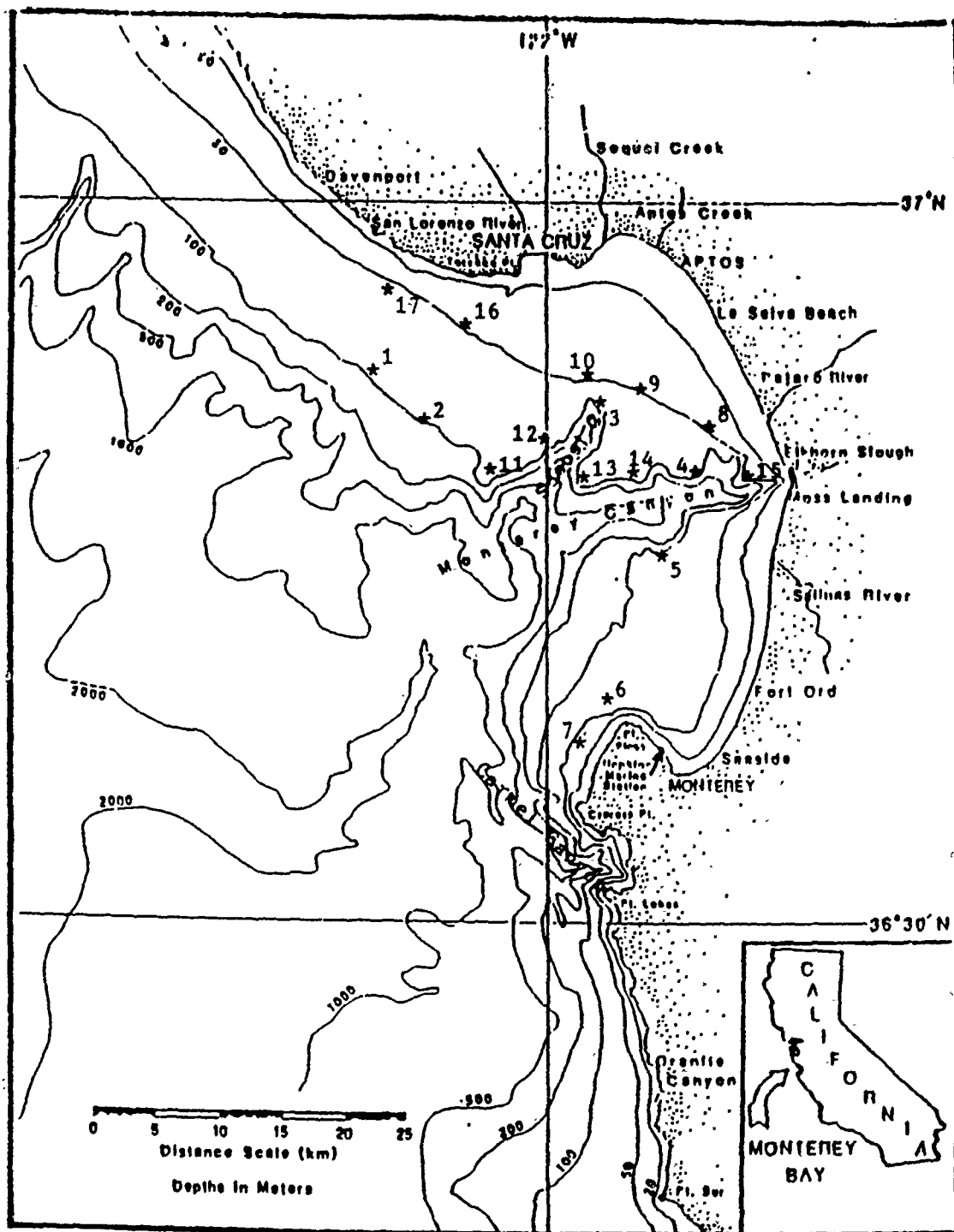


Figure 4.2: Receiver hydrophone locations for ray tracing.

RCV NO	LOCATION	LONGITUDE	LATITUDE	RANGE (km)	DEPTH (m)
1	SW of Santa Cruz	122°09.60'W	36°53.10'N	59.35	97.76
2	SSW of Santa Cruz	122°05.00'W	36°51.20'N	57.99	90.44
3	Head of Soquel Canyon	121°57.35'W	36°51.75'N	63.87	90.44
4	W of Moss Landing, Monterey Canyon north wall	121°52.20'W	36°48.65'N	63.49	90.44
5	W of Salinas River mouth, Monterey Canyon south wall	121°54.10'W	36°45.00'N	56.51	90.44
6	NW of Point Piños	121°58.35'W	36°39.25'N	44.43	90.44
7	WSW of Point Piños	121°59.25'W	36°37.60'N	42.02	50.21
8	W of Pajaro River mouth	121°51.00'W	36°50.00'N	67.49	54.00
9	ENE of Soquel Canyon head	121°54.90'W	36°57.00'N	67.15	48.38
10	N of Soquel Canyon head	121°57.40'W	36°52.75'N	68.39	44.72
11	North wall, west of Soquel Canyon juncture	122°01.55'W	36°48.80'N	56.04	90.44
	North wall, Soquel Canyon	121°59.65'W	36°50.25'N	59.72	90.44
13	East side, Soquel Canyon juncture	121°57.90'W	36°48.65'N	58.53	90.44
14	North wall of Monterey Canyon, prior to Soquel Canyon juncture	121°55.00'W	36°48.25'N	60.36	90.44
15	Near head of Monterey Canyon	121°50.20'W	36°47.90'N	64.36	90.44
16	SW of Santa Cruz, nearshore	122°03.50'W	36°54.50'N	66.20	45.00
17	W of Santa Cruz, nearshore	122°08.17'W	36°56.50'N	67.47	48.93

Table 4.1: Position, range and depth of simulation receivers.

1. range and depth of source;
2. range and depth of receiver;
3. minimum and maximum angle range for the eigenray search;
4. number of initial rays;
5. number of turning points and bottom reflections;
6. sound speed profile (SSP) data;
7. bathymetry data from source location to beyond the receiver location;  
and
8. bottom reflectivity values, i.e., loss for a given angle.

MPP sets limits on some of the input variables. For instance, the maximum number of initial rays is 80, the maximum number of points in the SSP is 100, the maximum number of bottom loss domains is five and the maximum number of bathymetry points is 62. The source and receiver were placed 1m above the floor; otherwise, negative initial rays would have been deleted immediately. All of the individual input files contained exactly the same information on the source position, SSP, initial rays, turning points and bottom reflection data. The source and receiver were always placed 1m above the sea floor.

A 15 December 1987 sound speed profile (Figure 4.3), generated by a computer system called ICAPS [39], was used for both SSP curves in each individual file. The ICAPS-generated sound speed profiles for an approximate source position (36°21'N, 122°18'W) and a general receiver position in the bay (36°50'N, 121°51'W) were identical down to a depth of 360 m. which was the cutoff for the receiver area SSP. The MPP computer routines triangularize all sectors between two inputted sound speed profiles if the SSPs do not begin at the same maximum depth, which complicates the ray tracing calculations and requires much longer processing time. Since it was advantageous to have rectangular sectors for the SSP region, the deeper ICAPS SSP (source location) was specified for both the source location and for spot about 2 km beyond the receiver location. This did put the profile through the sea and shelf floor in all areas. The exact values used for the sound speed profile in the MPP computer simulation are specified in Table 4.2. each receiver location's input file contained the following parameters with associated values:

1. source depth = 831.1 m and source range = 0.0 km;
2. minimum and maximum angles allowed in eigenray search = -15.0 to -10.0, -10.0 to -5.0, -5.0 to 0.0 to 5.0, 5.0 to 10.0 and 10.0 to 15.0 degrees (six separate computer runs);
3. minimum and maximum angles allowed in eigenray search = 31;
4. maximum number of passes allowed for ray search = 100;
5. total number of turning points or reflections allowed = 350;
6. maximum number of bottom reflections = 100;
7. number of loss domains = 1; and
8. bottom loss at angles of 0 and 90 degrees = 0.0 dB.

This data facilitated a "best case" simulation in which there was no bottom loss when rays bounced off the sea floor and canyon walls (total reflectivity), while allowing for a large number of surface and bottom reflections.

The range value for each receiver was determined by a computer program that used the longitude and latitude of both source and receiver positions to determine the range and bearing from source to receiver. This program included a correction for search curvature. Table 4.1 gives the range and depth for all 17 locations.

Bathymetry values along a straight line from source to receiver were manually extracted from a NOAA ocean bottom contours chart [40]. The selected depths were generally contour rings of some multiple of 100 fathoms. Every once in a while a significant reading (based on the author's subjectivity) that wasn't a contour ring was included in the bathymetry data to provide a more relevant and accurate bottom profile. The maximum number of bathymetric points that could be entered per input file was 62, but none of the files contained more than 50 points. The distance of each bathymetric point from the source location was calculated by using linear interpolation between source and receiver positions. All points beyond the receiver were considered to be at the same depth as the receiver location for this simulation. The program appeared to prefer this little idiosyncrasy, but the eigenray results were not affected. The bathymetric data for all 17 receiver hydrophone sites are provided in Appendix A.1.

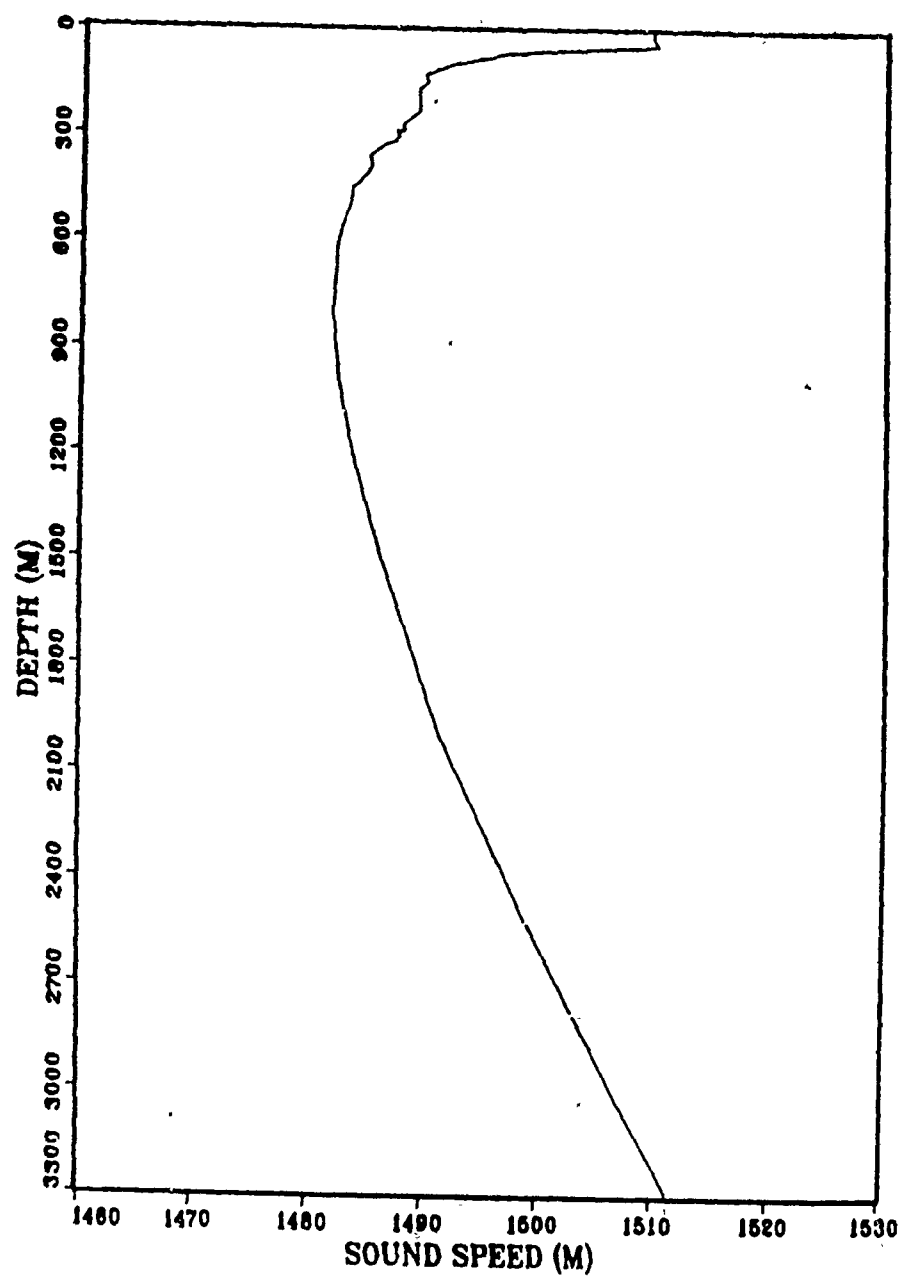


Figure 4.3: Typical December sound speed profile for Monterey Bay.

DEPTH (m)	SOUND SPEED (m/s)		DEPTH (m)	SOUND SPEED (m/s)
0.	1509.46		321.	1487.08
16.	1509.40		327.	1486.41
43.	1509.85		357.	1485.00
58.	1500.48		390.	1485.18
65.	1497.58		438.	1484.04
68.	1496.60		451.	1483.47
82.	1494.82		475.	1483.49
95.	1492.64		600.	1482.32
116.	1490.60		800.	1481.89
128.	1489.78		1000.	1482.54
150.	1489.91		1200.	1483.73
169.	1489.18		1500.	1486.26
230.	1489.26		2000.	1491.41
273.	1487.77		2500.	1498.67
287.	1488.01		3000.	1506.65
291.	1487.32		3290.	1511.51
303.	1487.53			

Table 4.2: December sound speed profile values for Monterey Bay region.

## Output

More than 100 computer runs were performed to determine possible eigenrays with associated travel time and transmission loss for the December tomography experiment. In a majority of these runs, no eigenrays were identified. This Monterey Bay experimental region is a particularly tough area to conduct a tomography experiment due to the wide fluctuations in the sea floor. The MPP program would drop a ray if it ever exceeded a  $\pm 85$  deg angle anywhere along its path. Most of the time when a ray hit one of the steep canyon walls, the ray would bounce off at greater than 85. A few of the rays exceeded the maximum number of turning points or reflections that was stipulated in the input file, and thus were dropped along the way of the ray search.

The MPP program identified rays that either bracketed the receiver or were within the diffraction field. The bracketing rays were shown to arrive at the receiver, and will be considered eigenrays. The diffraction field rays passed through the receiver's focus or convergence zone, but did not necessarily arrive at the receiver. For this simulation, the maximum vertical distance that a ray could miss the receiver was stipulated at  $\pm 15$  m. Of the 58 rays that the program identified, 17 diffraction field rays were outside of the vertical miss tolerance. These 17 rays are not considered eigenrays and have been eliminated from post-program analysis. Twenty-six of the remaining 41 rays arrived at location 17.

Nine locations had no rays arriving at the receiver. These were sites 3, 6, 9, 10, 11, 12, 14, 15 and 16. Five of these positions are in the area of Soquel Canyon, one was near the head of Monterey Canyon, another (receiver 14) was at a position selected for its difficult ray path due to the winding canyon, the seventh was off of Point Piños in a shallow area, and the last was in the shallow nearshore area of Santa Cruz. The results for the other eight receiver spots will be outlined and a table of all eigenrays with initial angle, arrival angle, travel time and transmission loss will follow the output discussion.

An interesting result occurred for receiver location 16 when the source was positioned down the slope in front of the seamount at the 913.0 m depth (which changed the range to 64.0 km), instead of on the top of the seamount where the source was placed for all of the other simulations. Four eigenrays in the 0 to -5 range now arrived at receiver 16 when before all rays were lost. On top of the seamount these initial rays bounced off of the seamount immediately and were driven upward, eventually to be lost by exceeding



TRAVEL TIME (sec)	INITIAL ANGLE (degrees)	ARRIVAL ANGLE (degrees)	TRANSMISSION LOSS (dB)
47.0753	-2.8463	-32.0741	93.6
47.4651	-2.9378	-54.3062	94.1
47.4652	-4.6413	-54.3904	94.2
47.4872	-2.9774	55.7486	94.1

Table 4.3: Eigenray information for site 16 based on change of source placement.

the 85 deg angle. However, on the side of the seamount they continued at downward trace until they refracted up (did not hit the bottom). Table 4.3 provides data on these four eigenrays. For the simulation, the source was placed on the top of the mount because the author felt that in the actual experiment, it would be easier to moor the source on the top rather than at some particular point on the slope of the seamount. This is just one indication that the eigenray arrivals are very sensitive to both source and receiver placement.

Because a 16 Hz bandwidth pseudo-random phase-encoded signal of 1.9375 s duration is planned to be used in the December experiment, a separation of ray arrivals by 1/16 Hz (62.5 ms) is necessary for resolving those arrivals [5]. Also, the entire bundle of eigenrays must arrive at the receiver with a total separation time of under 1.9375 s. The description of the output is based on this requirement.

**Receiver Location 1.** Receiver 1 was southwest of Santa Cruz on the continental slope not far from the canyon edge. Eigenrays would have to travel along a path that brings them over the deepest but widest part of Monterey Canyon in this experimental area. Two eigenrays at initial an-

RCVR	TRAVEL TIME (sec)	RAY SEPA- RATION (sec)	INITIAL ANGLE (degrees)	ARRIVAL ANGLE (degrees)	TRANS- MISSION LOSS (dB)
1	40.0920	40.0920	2.0837	20.1333	98.1
	40.1353	0.0433	-3.9048	23.5287	95.9
2	39.3994	39.3994	-14.8056	-17.1602	95.9
4	45.7964	45.7964	-9.5632	-51.3754	95.6
	45.9304	0.1340	-5.9567	-28.2386	84.8
	45.9312	0.0008	-5.9841	40.3657	83.5
5	43.4764	43.4764	6.4800	56.6509	97.7
7	28.6596	28.6596	3.6113	41.5440	92.1
	28.7173	0.0577	1.7916	6.2005	79.0
	29.2176	0.5003	1.7497	55.4856	89.6
	29.2177	0.0001	1.5429	55.1058	90.5
8	49.7370	49.7370	6.4825	-34.7151	106.0
	49.8610	0.1240	6.4969	-39.4762	105.7
	49.8610	0.0000	6.4969	-39.5973	105.7
13	39.6526	39.6526	-13.6680	-33.1896	83.7

Table 4.4: Eigenray information for sites 1,2,4,5,7,8 and 13.

gles of 2.0837 and -3.9048 deg were identified (Table 4.4). These two rays have a fairly clean ray path. After leaving the seamount with one possible bounce, the rays travel along the sound channel axis track until they hit the north wall of the Monterey Canyon through at around 31 and 39 km downrange. They then bounce up and have a turning point refraction before again bouncing off of the now gentler slope at around the 52.0 km mark. Either three or four bottom reflections occur before each ray arrives at the receiver. These ray experience very few bottom bounces that could absorb some of the sound or change the direction of the rays.

The separation time between the 2.0837 and -3.9048 deg ray is not good at 43ms. This spacing is below the experiment's separation minimum for identifying the individual rays. The transmission loss values for both rays

are in the upper 90 dB. The ray trace and the transmission loss profile graphs for these rays can be found in Appendix A.2.

**Receiver Location 2.** East-southeast of receiver 1 is the site for receiver 2. The simulated hydrophone is placed on a gentle slope a little north of the main Monterey Canyon wall. Rays arriving at this receiver would travel across a wide and deep portion of the canyon, similar to the receiver 1 rays. The north wall rises until at about 39 km downrange of the source, there is a drop of the sea floor for about 6 km before rising steeply again up to the continental shelf.

One eigenray was identified by the simulation with a 96 dB transmission loss. The -14.8056 deg ray initially bounces off of the seamount and refracts before striking the north wall close to 28 km away from the seamount. It then reflects off the surface and bounces in the dropped floor of the north wall before surface reflecting and bouncing its way on the shelf, prior to arriving at the receiver. It bounces off of the continental shelf six times. Information on this ray is found in Table 4.4, and the graphs for the ray trace and transmission loss are located in Appendix A.2.

**Receiver Location 4.** Receiver 4 is due west of Moss Landing, situated on the Monterey Canyon north wall edge. Rays arriving at this location will pass over Carmel Canyon and the continental shelf before crossing Monterey Canyon. This position is above the narrower and shallower portion of Monterey Canyon, so it may be a good location for an internal waves study.

Three eigenrays were identified, having transmission losses between 83.5 dB and 95.6 dB, and with good arrival separation between the first two rays (Table 4.4). A graphical depiction of the ray paths can be found in Appendix A.2, along with the transmission loss graph. The arrival time separation between the last two rays (-5.9567 and -5.9841) of 0.8 ms is too short for the conditions of the experiment. The ray with the initial angle of -9.5632 arrives first and is followed in 134ms by ray -5.9567.

The three eigenrays have the same general ray path. Ray - 9.5632 has one refractive turning point, while the other two rays display one cycle of refraction (two turning points). All of the rays have a multitude of surface and bottom bounces as they proceed along the shelf, and they bounce twice in Monterey Canyon with one refraction between the bounces. Ray -9.5632 has three surface reflections at the end of its path, and the other two rays have two surface bounces. All of the rays have paths that could be used in both the internal wave and surface wave studies.

**Receiver Location 5.** Situated on the south edge of the Monterey Canyon, due west of the Salinas River mouth, is the location for receiver 5. It was selected to give the tomography experiment a means by which to possibly recognize the effects that traveling through the Monterey Canyon head would have on an eigenray, such as internal waves or internal bores. The unfortunate aspect of this location is that the rays have to travel over 16 km of shallow shelf, which manifests itself in possibly a hundred or more surface and bottom reflections. The ray trace graph in Appendix B illustrates this oscillation. Transmission loss plot follows the ray trace. Table 4.4 contains tabularized data on the two eigenrays.

Ray 6.4800 refracts once on either side of reflecting off the bottom, then hits high on the side of the Carmel Canyon east wall, before oscillating its way along the continental shelf. The shelf is sandy, so there will be some absorption and not the total reflectivity that was simulated. Simulated transmission loss for the ray is 97.7 dB, but parameters for bottom loss were not included in the computer input because of the great variation in the sediment and geology along any one path. It should be expected that the real world case would have a larger dB loss.

**Receiver Location 7.** The shallow nearshore region just off of Asilomar Beach in Pacific Grove is the location for receiver 7. This is the closest position to the source-moored experiment in this simulation. The rays pass perpendicularly over the Carmel Canyon axis and the wider Monterey Canyon trough, but a straight path from source to receiver stays clear of the narrower portion of the winding canyon. Since the receiver site is situated on the shelf at approximately 3 km from the edge of the Carmel Canyon, most of the rays oscillate between the surface and shelf bottom before completing the trek to the receiver.

Four eigenrays were identified by the simulation process. Specific values for these rays are given in Table 4.4. Ray trace and transmission loss graphs are found in Appendix A.2. Rays 1.5429 and 1.7497 appear to travel together because their paths are almost identical and there is only a 0.1 ms timespan between them. These two rays refract prior to bouncing off the trough wall just before the 31 km range. They then reflect off the surface and hit the Carmel Canyon wall twice before oscillating on the continental shelf.

The first eigenray to arrive at 28.6596 s is the 3.6113 deg initial angle ray. It first refracts before reflecting off the sea floor, hitting the wall above the Carmel Canyon, and oscillating along the shelf. It was a slightly weaker signal at 92 dB loss than the 2-ray pair. Arriving 57.7 ms later but a full

1/2 second before the ray pair is initial ray 1.7916. This ray refracts once before bouncing off of the trough wall, reflecting off the surface, reflecting off Carmel Canyon west wall, and then refracting and bottom reflecting along the shelf. Of all the eigenrays identified in this simulation, ray 1.7916 was the strongest with only a 79 dB loss.

**Receiver Location 8.** Receiver 8 is positioned due west of the mouth of the Pajaro River. Rays traveling from the source location to this receiver would follow nearly the same horizontal path as do the eigenrays to receiver 4, except that site 8 is situated a little further behind location 4 on the continental shelf. Eigenrays have to pass over Carmel Canyon, not far from the Monterey Canyon junction, and over the continental shelf before crossing Monterey Canyon just a little downslope from its head.

The MPP program determined that three eigenrays would be picked up by receiver 8; however, two of these rays are almost identical. These two rays (initial angle of 6.4969 deg) will be treated as though they were just one ray for the rest of the discussion. A comparison of the eigenrays may be found in Table 4.4 while graphs of the ray trace and transmission loss are located in Appendix A.2. Ray 6.4825 makes two refracted-bottom reflected (RBR) cycles, with bounces at 22.0 nm and 40.5nm, prior to oscillating on the continental shelf between the surface and shelf floor. This oscillating portion of the ray path covers 15.5 nm in about 14.2 s. At Monterey Canyon it bounces off the wall twice, with one refraction within the canyon, before making 13 surface/bottom reflection cycles just prior to arriving at the hydrophone. The other ray (6.4969) follows an almost identical path to ray 6.4825, with its first two bounces at the same location, one refraction within Monterey Canyon, and the same number of surface and bottom reflections at the end of its path.

Even though the paths of these two eigenrays are very similar, there is a good arrival time separation of 124.0 ms between them. Transmission losses range between 105.7 dB for the slower ray and 106.0 dB for the faster ray. These rays bounce in an area of Monterey Canyon that should exhibit internal wave effects, plus they have a considerable number of surface reflections.

**Receiver Location 13.** The juncture of the Soquel Canyon east wall and the Monterey Canyon north wall is the location of receiver 13. The straight-line path from source to receiver is over the section of the Monterey Canyon that has many winding and meandering turns, and includes the

Carmel Canyon joins Monterey Canyon. It is not a good prospect for finding any eigenrays, but fortunately one lone ray, which happened to stay in the deep sound channel for a long distance after its initial seamount bounce, was identified by the MPP simulation.

The first time that this ray bounces off any canyon walls is at the 54.79 km mark, not far from the edge of the continental shelf. After hitting the wall, the ray surface refracts and shelf bounces seven times before it is picked up by receiver 13. It should be a fairly strong signal at only an 84 dB transmission loss which is received in 39.6526s at an angle of -33.2. The eigenray data is given in Table 4.4 while the ray trace and dB loss graphs are in Appendix A.2.

**Receiver Location 17.** This last receiver position is located slightly south of due west of Santa Cruz in the open nearshore shelf area. It was one of the first sites to be simulated, but the resulting large number of identified eigenrays oscillating along the continental shelf made a change in receiver depth a necessity. The rest of the locations were selected based on their proximity to the canyon edge. The rays which arrive at location 17 travel about the same course as they would if going to receiver 1, except that they have longer trek along the shelf.

The ray tracing simulation and eigenray identification at this receiver location can be best described as a complete mess. Twenty-six eigenrays were identified by the MPP program and almost all of them have a tremendous number of surface reflections and continental shelf bounces before arriving at the receiver. Needless to say, this would be an extremely complicated experimental site and probably not a good one for a first time tomography experiment in these waters.

The ray trace graph in Appendix A.2 for location 17 only contains a few representative rays, since graphing all of the rays would annihilate any possible distinguishing individual lines. All of the stick plots (dB losses) are on the transmission loss graph following the ray trace graph. Travel time, transmission loss and arrival angle for each ray are listed in Table 4.5.

The entire package of rays can be categorized in just a few groups. Eight rays follow an almost identical path of two refractions before bouncing off of the steep slope above the Monterey Canyon, from a downward approach at a depth of 780 m and a range of around 44.6 km from the source. They continue bouncing up the slope and onto the shelf with one or two refractions and the rest surface reflections. These rays start at angles of -1.6163, -2.0828, -3.0111, -3.0509, -3.1028, -3.1411, -3.1431 and -3.2418. Rays of -3.6277 and

TRAVEL TIME (sec)	RAY SEPA- RATION (sec)	INITIAL ANGLE (degrees)	ARRIVAL ANGLE (degrees)	TRANS- MISSION LOSS (dB)
45.4324	45.4324	-1.1110	5.4710	110.6
45.4508	0.0184	0.3232	-4.6675	100.9
45.5656	0.1148	-3.0111	-19.9961	104.4
45.5825	0.0169	-4.5475	-19.6807	97.7
45.6019	0.0194	-3.9658	-20.3254	91.1
45.6364	0.0345	-3.2418	-23.1483	93.2
45.6641	0.0277	-8.6415	-23.5988	90.5
45.6641	0.0000	-8.7093	-23.5525	89.5
45.6645	0.0004	4.0027	24.7201	91.1
45.6647	0.0002	-8.7180	24.7281	90.3
45.6656	0.0009	-3.1411	-24.1419	99.6
45.6656	0.0000	-1.6163	-24.1725	99.4
45.6656	0.0000	-3.1431	-24.5613	99.8
45.6938	0.0282	-3.1028	-25.6257	100.8
45.6960	0.0022	-5.3708	-25.7395	100.6
45.7237	0.0277	-3.0509	27.8458	98.4
45.7567	0.0330	-2.0828	-28.2343	93.8
46.0462	0.2895	2.1406	39.3321	96.5
46.0939	0.0477	-3.6277	-39.6695	97.0
46.3275	0.2336	-12.5001	-44.7474	93.8
46.9973	0.6698	-6.4559	-60.2335	99.5
47.0004	0.0031	1.7248	-60.4129	99.8
47.0019	0.0015	-6.4516	61.2411	99.6
47.4270	0.4251	-6.3988	69.1542	100.2
47.4272	0.0002	1.6711	69.1952	100.4
47.6187	0.1915	-6.3534	72.1043	101.5

Table 4.5: Eigenray information for site 17.

-5.3708 deg are very similar to the first eight with the exceptions that they bounce off the slope at just a slightly longer range and a few meters more shallow, and the -5.3708 ray hits at an upward angle. An 11th ray at -4.5475 refracts three times before hitting the slope at about the same spot of the first group of eight, following the path of the above 10 rays up the slope with the exception that this ray has three more refractions.

Another set of seven rays (1.6711, 1.7248, 2.1406, -6.3534, -6.3988, -6.4516 and -6.4559) are very similar to the first group of eight, with two refractions before bouncing up the slope. The three main differences are that this second set reflect off the wall at a spot with a slightly shorter range and lower depth (41.3 km and 950 m), the rays are heading upward just before their first wall bounce, and that they have many more oscillations on the shelf than does the first group. With the abundance of reflections, it is understandable why this group as a whole has the slowest arrival times to the receiver.

Ray -3.9658 has two refractions before striking the sloping wall at a depth of 860m and a range of 42.9 km. It then bounces up the slope with three refractions and 14 surface reflections. The last three individual and one group of four rays are different from the preceding 19 rays.

The rays -8.6415, -8.7093, -8.7180 and 4.0027 are grouped together due to their parallel paths and they arrive as a group in a span of 0.6 ms. These rays make one refractive turn before colliding with a lower north canyon wall point at a depth of 1410 m and a range of 32.85 km from the source on the seamount. They next hit the upper slope at the 53.8 km mark and 300 m depth after one refraction. One more refractive turn remains for this group prior to 17 surface and bottom oscillations along the shelf.

The last three rays are individuals. The fastest eigenray originates at an angle of -1.1110 deg, reaches receiver 17 in 45.4324 s, but has the largest transmission loss at 110.6 dB. This ray has two refractive turns before striking the slope at 45.67 km downrange and 734 m deep. It refracts and then bounces off the shelf area (178 m deep) at a distance of 56.64 km from the source. It makes three more refracted-bottom reflected (RBR) cycles and one surface reflection before arriving at its destination. Ray 0.3232 arrives 18.4 ms later and has a somewhat similar path. It has three refractions prior to colliding with the wall 44.48 km away at a depth of 788 m. The second bounce occurs at the 59.4 km mark on the shelf in 124m of water. Seven RBR cycles and one surface reflection complete this ray's path. It takes another 114.8 ms of time before the third fastest ray (-3.0111) arrives on the scene.



The very last ray to be described should be easily identified in an experimental situation. Arriving at the 46.3275 s time mark, ray -12.5001 follows the next faster ray by 233.6 ms and is followed by another ray 669.8 ms later. This is the best separation for the entire 26-ray package. Another interesting fact is that this ray strikes the Monterey Canyon on its south wall and refracts once in the canyon before one more refraction and a bounce at 50.48km range and 460m depth. It then oscillates along the shallow shelf with one more refraction but a multitude of surface and bottom reflections.

Looking at the results in Table 4.5, one can begin to understand why this location would be a bit of a problem in a tomography experiment. The dB loss ranges from 89.5 dB for ray - 8.7093 to 110.6 dB for the first arriving ray (-1.1110). There is not enough arrival time separation for most of these rays, based on 16 Hz bandwidth, except for the following:

1. 114.8 ms between ray 0.3232, arriving at 45.4508 s, and ray - 3.0111;
2. 289.5 ms between ray-2.0828, arriving at 45.7567 s, and ray 2.1406;
3. 233.6 ms between ray-3.6277, arriving at 46.0939 s, and ray- 12.5001;
4. 669.8 ms between ray -12.5001, arriving at 46.3275 s, and ray - 6.4559;
5. 425.3 ms between ray -6.4516, arriving at 47.0019 s, and ray 1.6711;  
and
6. 191.7 ms between ray -6.3988, arriving at 47.4270 s, and ray - 6.3534.

Six adequate arrival time separations with 26 arriving rays does not put this receiver location on the top of the list for best spots. The condition that eliminates this location as a recommended receiver site is that the arrival separation between the first and last eigenray is 2.1863s. The acoustic signal from the source is of 1.9375s duration, which is the maximum separation time that will be experimentally allowed for all of the rays arriving at one location.

## 4.2 3-D Ray Tracing with HARPO

NOAA'S Hamiltonian Acoustic Ray-tracing Program for the Ocean (HARPO) is well documented[41]. It has recently been enhanced by Newhall, Lynch, Chiu, and Daugherty[42]. The program entails a core integration model and interchangeable models defining distribution of sound speed, current, sea

surface, bottom bathymetry, and dispersion relation or Hamiltonian. The application of HARPO to the Monterey Bay and its canyon centered on two efforts: IBM conversion of the VAX-originating code from WHOI; and simulating the complex bathymetry.

#### 4.2.1 Hamiltonian Ray Tracing

Hamiltonian ray tracing requires the sound speed of the ocean to be modeled as a continuous three-dimensional function. Each raypath is computed by numerically integrating Hamilton's equations with a different set of initial conditions. In modeling wave propagation with Hamilton's equations, the point of view is taken that in a high-frequency limit, waves behave like particles and travel along rays, according to equations that exactly parallel those governing changes of position and momentum in mechanical systems. These ray paths satisfy Fermat's principle, that is, the paths are those for which the action is stationary for variations in the path. For the wave equation, one forms a Hamiltonian that gives the dispersion relation for the wave in question when it is set to zero. Integrating Hamilton's equations then gives a path which satisfies Fermat's principle.

In Cartesian coordinates, Hamilton's equations take the simple form

$$\begin{aligned}\frac{dx_i}{d\tau} &= \frac{\partial H}{\partial k_i} \\ \frac{dk_i}{d\tau} &= -\frac{\partial H}{\partial x_i} \quad i = 1, 2, 3\end{aligned}\tag{4.1}$$

where  $\tau$  is time,  $H$  is the Hamiltonian,  $k_i$  are the wave number components, and  $x_i$  are the coordinates of a point on the raypath.

To solve Eq. 4.1 for one of the raypaths, one chooses initial values for the six quantities  $x_i$  and  $k_i$  and performs a numerical integration of the system in Eq. 4.1 of six total differential equations. The integration of Hamilton's equations is performed using the implicit Adams-Moulton method with a Runge-Kutta start up. For our case of acoustic waves in the ocean, the Hamiltonian (which is constant along a ray path) is defined as the dispersion relation

$$H(x_i, k_j) = [\omega - \vec{k} \cdot \vec{V}(x_i)]^2 - C^2(x_i)k^2 = 0\tag{4.2}$$

where  $\vec{V}(x_i)$  is the ocean current,  $C(x_i)$  is the sound speed field, and  $\omega$  is the angular wave frequency.

For earth-centered spherical polar coordinates, Hamilton's equations (see Lighthill) in four dimensions are:

$$\frac{dr}{d\tau} = \frac{\partial H}{\partial k_r} \quad (4.3)$$

$$\frac{d\theta}{d\tau} = \frac{1}{r} \frac{\partial H}{\partial k_\theta} \quad (4.4)$$

$$\frac{d\phi}{d\tau} = \frac{1}{r \sin \theta} \frac{\partial H}{\partial k_\phi} \quad (4.5)$$

$$\frac{dt}{d\tau} = -\frac{\partial H}{\partial \omega} \quad (4.6)$$

$$\frac{dk_r}{d\tau} = -\frac{\partial H}{\partial r} + k_\theta \frac{d\theta}{d\tau} + k_\phi \sin \theta \frac{\partial \phi}{\partial \tau} \quad (4.7)$$

$$\frac{dk_\theta}{d\tau} = \frac{1}{r} \left( -\frac{\partial H}{\partial \theta} - k_\theta \frac{dr}{d\tau} + k_\phi r \cos \theta \frac{\partial \phi}{\partial \tau} \right) \quad (4.8)$$

$$\frac{dk_\phi}{d\tau} = \frac{1}{r \sin \theta} \left( -\frac{\partial H}{\partial \phi} - k_\phi \sin \theta \frac{dr}{d\tau} - k_\theta r \cos \theta \frac{\partial \theta}{\partial \tau} \right) \quad (4.9)$$

$$\frac{d\omega}{d\tau} = \frac{\partial H}{\partial t} \quad (4.10)$$

where  $r, \theta, \phi$  are the Earth-centered spherical polar coordinates of a point on the raypath;  $k_r, k_\theta, k_\phi$  are the local components of the propagation vector (a vector whose magnitude

$$h = \sqrt{k_r^2 + k_\theta^2 + k_\phi^2} = 2\pi/\lambda, \quad (4.11)$$

is the wavenumber, and that points in the wave normal direction) in the  $r, \theta$ , and  $\phi$  directions;  $t$  is the propagation time of the wave packet.

#### 4.2.2 Application

HARPO was used to calculate raypaths in the extreme bathymetry of the Monterey Bay Canyon. This bathymetry was a focal point of effort in this application. Sea surface was modeled as a sphere of constant radius; the current field was set to zero; absorption was calculated as a function of frequency using a Skretting-Leroy empiricism; a single sound speed profile based on data from the December '88 Monterey Bay Tomography Experiment (MBTE) was used everywhere. The bottom was defined on a 1 km by 1 km grid over 122°20' to 121°50'W and 36°23' to 37° N producing a 42 by 65 bathymetric array. The depth values were a result of the union of the 200 m resolution bathymetry set of Thornton and Purych for north

of Pt. Joe and a .5' resolution bathymetric set read from a NOAA depth chart for south of Pt. Joe. The later was projected on an x,y grid with the same origin ( $36^{\circ}36'N$ ,  $122^{\circ}20'W$ ) and reference location as the Thornton-Burych data. The two data were then combined using a spine interpolation routine provided by DISSPLA software. HARPO used this bathymetric grid to calculate a bi-cubic spline with knots at each grid point. From the discontinuous behavior of adjacent raypaths, the bottom surface derivatives, as calculated using the splines, were suspected of having an intra-grid variability analogous to Gibbs phenomena. The bathymetry was modified using a 1-6-1 filter to remedy this problem. Figure 4.4 shows the resulting bathymetry.

Raypaths were calculated originating from the location of the transmitter in for Monterey Bay Tomography Experiment on an underwater knoll at a depth of 1020.6 m just north of the Pt. Sur area and 35 km off the coast. Initial azimuth angle was set on a near direct path to receiver J on the shelf due south of Santa Cruz and 94.2 m in depth. The calculated raypaths were channeled by the shelf and reflected back into the canyon. As a remedy the raypaths were then calculated as originating from receiver J on the shelf and directed toward the transmitter location. Figures 4.5 and 4.6 show a planar and top view of typical ray paths within Monterey Canyon between Station J and the transmitter.

A program is available from WHOI that operates in conjunction with HARPO and calculates eigenrays. This program interpolates launch angles from previously calculated ray path intersections with receiver depth and eigenrange (the distance between receiver and transmitter.) The eigenray program, as it stands, is IBM I/O incompatible and is biased toward direct-path eigenrays. The Monterey Bay application of HARPO was loaded on the WHOI VAX 8800 and run with their eigenray program over an elevation range of  $27^{\circ}$ . No eigenrays were found. At NPS, an effort to use HARPO alone with a human interpolator proved to be too slow for the fully three-dimensional Monterey Bay problem. An effort is under way to develop and/or modify an Gaussian beam/timefront postprocessor for this application. Future work is likely to be performed on a SUN workstation which may eliminate the I/O problem.

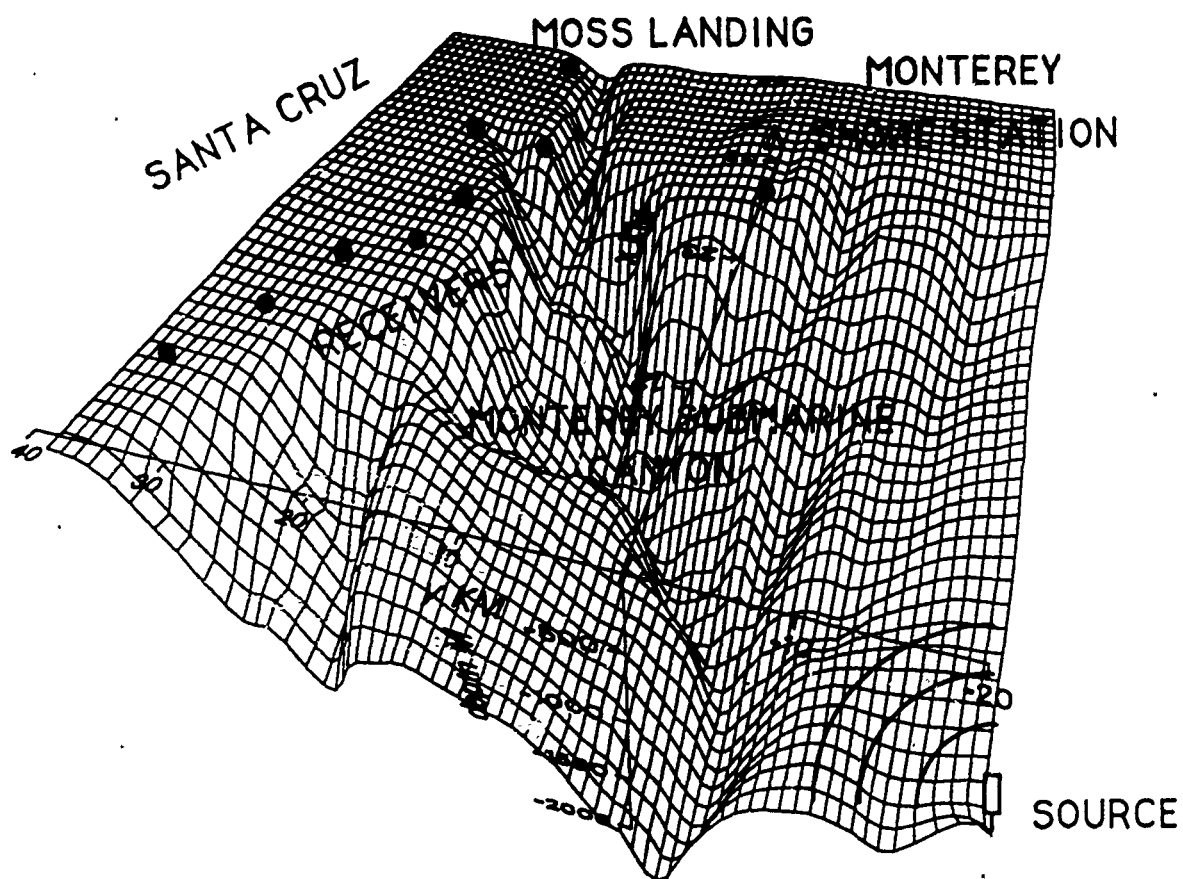


Figure 4.4: A model of the bathymetry of Monterey Bay region.

**1 MONTEREY BAY CANYON**

**MODEL = MBJ , FREQ = 400.000 HZ, AZ = 201.054 DEG**

**EL = 7.20 DEG TO 10.20 DEG, STEP = 1.00 DEG**

**XMTR HT = -0.09 KM , LAT = 0.47 DEG, LONG = 0.18 DEG**

**ACOUSTIC WAVE \*\*\* WITH CURRENT \*\*\* WITH LOSSES**

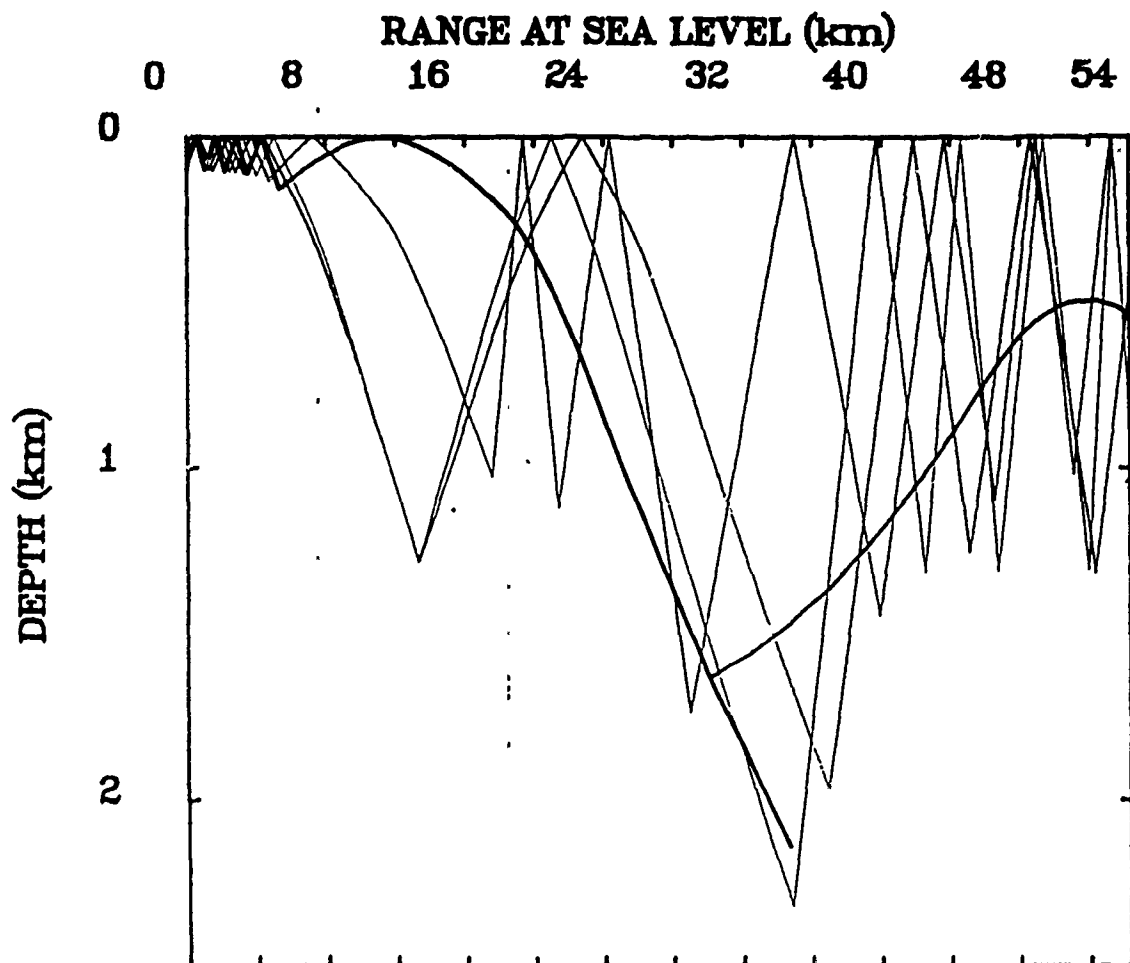


Figure 4.5: Planar view of rays calculated from Station J towards the tomography transmitter.

2 REPEAT SAMPLE CASE W/HORIZONTAL PLOT, W/NO PRINT  
 MODEL = MBJ ,FREQ = 400.000 HZ, AZ =201.054 DEG  
 EL = 7.20 DEG TO 10.20 DEG, STEP = 1.00 DEG  
 XMTR HT = -0.09 KM ,LAT = 0.47 DEG, LONG = 0.18 DEG  
 ACOUSTIC WAVE \*\*\* WITH CURRENT \*\*\* WITH LOSSES

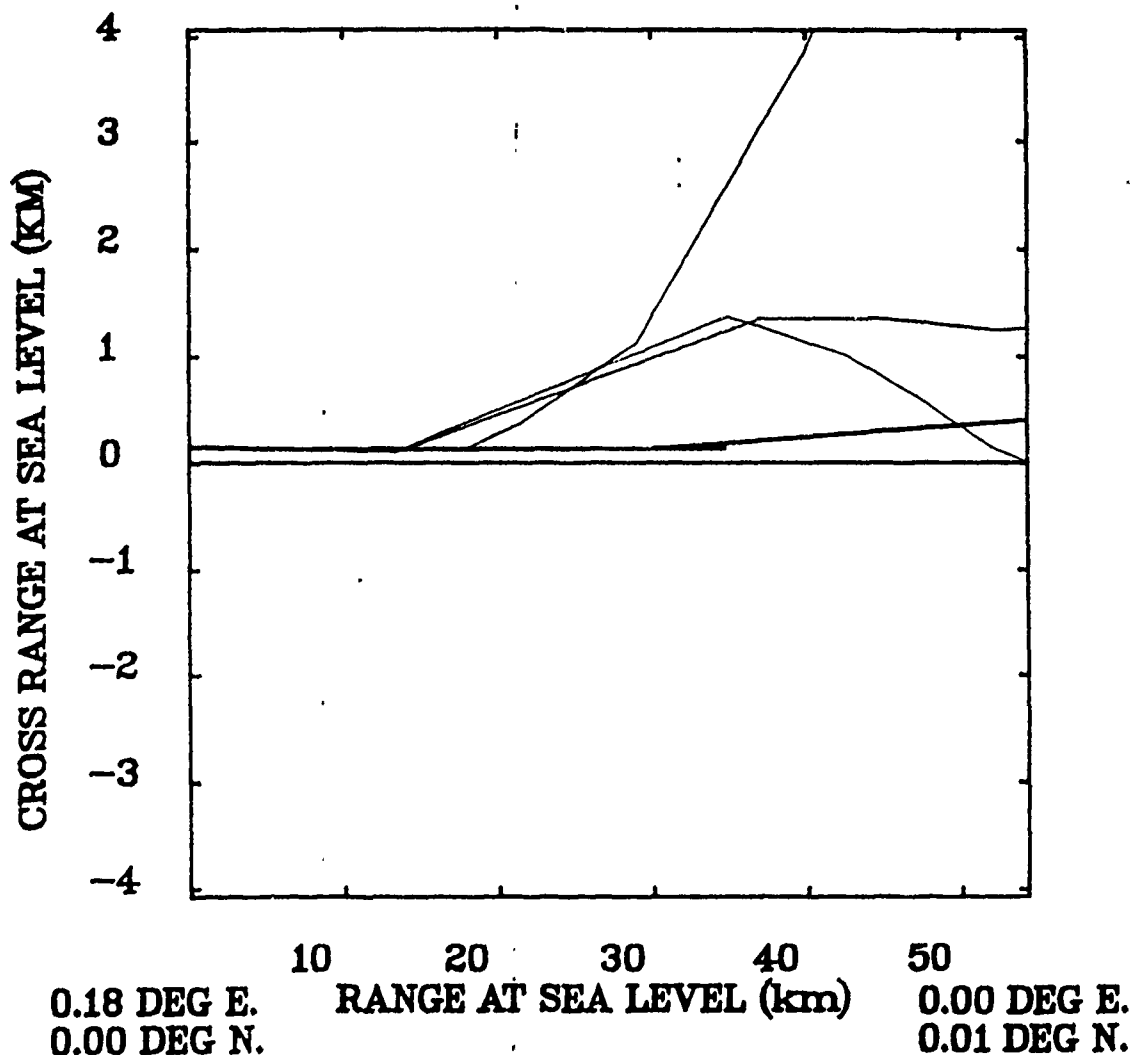


Figure 4.6: Top view of rays calculated from Station J towards the tomography transmitter.

## Chapter 5

# Conclusions

All results to date have shown that acoustic tomography is a viable technique for monitoring the circulation of Monterey Bay:

1. Acoustic arrivals were received in the 1988 Monterey Bay Tomography Experiment that were strong enough to observe the fluctuations due to surface waves, internal waves, and tides. Lengthening the code in the future tomography system would provide enough signal-to-noise ratio for ocean current tomography. Limitations to the code length due to surface wave-induced Doppler are under study.
2. The acoustic arrivals were mostly resolved for the 16 Hz bandwidth signal. It is foreseen that a future tomography system in the Bay would use a much larger bandwidth signal, e.g. 100 Hz. Even with the shorter distances involved with the proposed tomography array in the Bay, this larger bandwidth signal would eliminate the small number of resolution difficulties observed.
3. Stable acoustic arrivals were observed for the entire 4 day experiment through several tidal cycles for cross-canyon paths. This experimental result was the most important for demonstrating the viability of tomography in the Bay.
4. The identification of the multipath arrivals measured in the experiment was attempted with the MPP 2-D and HARPO 3-D ray tracing programs. MPP found some eigenrays (rays connecting source and receiver) while HARPO did not find any eigenrays because of the difficulty in modeling the effect of the extreme bathymetry of the Bay



on acoustic propagation. The lack is not in the existence of stable, resolvable arrivals but in our ability to model them correctly. These eigenrays exist because the experiment measured them. In the next few months, as part of another feasibility study for the Norwegian-Barents Sea Tomography Experiment, HARPO capabilities will be increased with the addition of Gaussian beam and time front post-processing routines. These routines will eliminate the need for modeling eigenrays and should be able to identify the arrivals measured in the Monterey Bay Experiment.

## **Appendix A**

# **MPP Data**

### **A.1 Bathymetry Data for Receiver Locations**

RECEIVER LOCATION 1		RECEIVER LOCATION 2		RECEIVER LOCATION 3	
Range (km)	Depth (m)	Range (km)	Depth (m)	Range (km)	Depth (m)
0.0	832.10	0.0	832.10	0.0	832.10
3.26	826.62	1.09	914.40	0.76	914.40
4.07	914.40	3.75	914.40	4.07	1097.28
7.06	1463.04	6.16	1280.16	5.75	1280.16
17.37	1463.04	6.74	1463.04	6.64	1463.04
18.57	1645.92	9.96	1463.04	7.32	1463.04
21.53	2560.32	12.71	1280.16	12.14	1280.16
21.89	2560.32	14.67	1280.16	15.54	1280.16
23.07	2377.44	17.17	1463.04	18.80	1463.04
24.61	2194.56	19.56	1828.80	20.39	1828.80
25.65	2011.68	21.01	2194.56	22.36	1828.80
27.25	1828.80	21.51	2377.44	23.80	2011.68
27.69	1645.92	23.85	2377.44	27.65	2011.68
30.07	1463.04	25.75	1828.80	29.46	2194.56
35.29	1280.16	26.51	1645.92	30.54	2011.68
37.51	1097.28	29.74	1463.04	32.71	1828.80
40.31	914.40	33.32	1280.16	35.02	2011.68
44.11	731.52	36.07	1097.28	39.31	1828.80
46.68	548.64	37.30	1047.90	39.96	1645.92
51.84	365.76	38.03	1097.28	41.53	1463.04
55.55	182.88	39.60	958.29	42.47	1645.92
59.35	98.76	40.47	1097.28	43.10	1828.80
70.50	98.76	41.01	1280.16	43.43	1828.80
		45.41	1280.16	44.10	1463.04
		45.99	1325.88	45.65	1097.28
		46.45	1280.16	46.95	731.52
		47.42	1097.28	48.52	731.52
		48.53	731.52	49.52	1097.28
		50.34	365.76	50.29	1097.28
		51.72	182.88	50.96	914.40
		54.87	106.07	51.78	806.50
		57.99	91.44	53.00	914.40
		70.50	91.44	53.40	1005.84
				54.35	914.40
				55.30	731.52
				57.06	548.64
				61.26	365.76
				62.89	182.88
				63.87	91.44
				70.50	91.44

Table A.1: Bathymetry data for receiver locations 1, 2, and 3.

RECEIVER LOCATION 4		RECEIVER LOCATION 5		RECEIVER LOCATION 6	
Range (km)	Depth (m)	Range (km)	Depth (m)	Range (km)	Depth (m)
0.0	832.10	0.0	832.10	0.0	832.10
0.54	914.40	0.60	914.40	0.60	914.40
3.30	1097.28	2.89	1097.28	2.35	1097.28
5.19	1280.16	4.76	1280.16	4.33	1280.16
6.38	1351.48	6.60	1351.48	6.76	1351.48
10.33	1280.16	10.01	1280.16	9.52	1280.16
14.25	1252.73	15.83	1280.16	11.85	1126.54
16.05	1280.16	16.73	1463.04	16.34	1280.16
17.04	1463.04	19.16	1463.04	17.14	1463.04
23.54	1463.04	20.57	1280.16	17.68	1556.31
24.67	1645.92	23.06	1280.16	18.40	1463.04
25.61	1828.80	25.98	1828.80	19.54	1280.16
26.24	1828.80	26.74	1828.80	24.41	1280.16
27.78	1463.04	29.28	1280.16	25.80	1645.92
28.73	1280.16	29.91	1097.28	26.65	1645.92
32.33	1280.16	31.83	1097.28	28.50	1463.04
33.73	1097.28	32.48	914.40	29.66	1280.16
35.22	1097.28	34.28	914.40	30.17	1280.16
35.71	1280.16	34.75	1097.28	31.39	914.40
36.79	1280.16	36.67	1097.28	33.77	914.40
38.24	731.52	38.65	365.76	34.31	1097.28
39.68	548.64	39.62	182.88	34.58	1097.28
40.26	365.76	44.79	107.90	35.45	731.52
43.56	182.88	54.78	91.44	37.23	548.64
46.89	118.87	70.50	91.44	38.06	182.88
52.70	104.24			41.40	91.44
56.33	182.88			70.50	91.44
57.46	365.76				
58.33	548.64				
58.80	548.64				
61.63	365.76				
62.63	182.88				
63.49	91.44				
70.50	91.44				

Table A.2: Bathymetry data for receiver locations 4, 5, and 6.

RECEIVER LOCATION 7		RECEIVER LOCATION 8		RECEIVER LOCATION 9	
Range (km)	Depth (m)	Range (km)	Depth (m)	Range (km)	Depth (m)
0.0	824.79	0.0	825.	0.0	824.79
1.21	1097.28	0.37	915.	1.61	1097.28
14.24	1097.28	1.73	1097.	2.26	1280.16
18.97	1280.16	6.35	1251.	17.30	1280.16
21.55	1097.28	7.75	1280.	20.04	1645.92
24.72	1097.28	8.18	1280.	21.22	1645.92
26.38	1280.16	13.56	1127.	22.62	1463.04
27.67	1645.92	17.65	1280.	24.28	1463.04
29.34	1463.04	18.46	1463.	26.00	1828.80
31.11	914.40	18.90	1556.	27.29	1828.80
32.72	731.52	20.26	1463.	28.63	1463.04
33.26	731.52	21.27	1280.	30.08	1463.04
34.01	914.40	24.68	1280.	30.73	1645.92
34.39	914.40	25.55	1463.	32.39	1645.92
35.79	548.64	26.44	1646.	36.21	1463.04
37.13	365.76	27.32	1829.	37.07	1280.16
37.99	182.88	27.91	1829.	37.82	1280.16
39.12	91.44	28.57	1646.	39.22	1645.92
39.98	73.15	29.05	1562.	40.45	1645.92
40.84	73.15	29.39	1463.	41.79	1097.28
41.91	54.86	30.35	1280.	43.62	1097.28
42.02	51.21	31.31	1097.	45.18	1645.92
45.0	51.21	32.19	1097.	45.80	1645.92
		33.82	1097.	47.11	1097.28
		35.00	915.	48.17	1097.28
		35.82	940.	49.15	1280.16
		36.18	1097.	50.07	1280.16
		36.60	1280.	52.29	731.52
		37.91	1280.	55.01	731.52
		38.57	1097.	57.96	182.88
		38.95	915.	59.41	91.44
		39.28	732.	64.57	73.15
		41.06	366.	66.72	54.86
		42.17	229.	67.15	49.38
		44.56	183.	70.15	49.38
		48.07	119.		
		53.61	104.		
		56.41	99.		
		56.98	183.		
		57.90	366.		
		59.08	549.		
		59.67	549.		
		62.40	366.		
		63.06	183.		
		63.63	91.		
		64.48	75.		
		67.33	73.		
		67.49	55.		

Table A.3: Bathymetry data for receiver locations 7, 8, and 9.

RECEIVER LOCATION 10		RECEIVER LOCATION 11		RECEIVER LOCATION 12	
Range (km)	Depth (m)	Range (km)	Depth (m)	Range (km)	Depth (m)
0.0	824.79	0.0	832.10	0.0	832.10
1.84	1097.28	0.81	914.40	0.81	914.40
2.43	1280.16	2.81	914.40	2.81	914.40
18.20	1280.16	5.95	1280.16	5.85	1280.16
21.01	1463.04	6.60	1463.04	6.60	1463.04
22.43	1828.80	7.17	1463.04	7.17	1463.04
24.05	1645.92	12.31	1280.16	12.31	1280.16
24.88	1645.92	15.01	1280.16	15.26	1280.16
26.25	2011.68	17.96	1463.04	18.22	1463.04
26.61	2011.68	20.83	2011.68	20.89	2011.68
27.47	1828.80	22.50	2011.68	23.22	2011.68
29.84	1828.80	23.31	2194.56	24.36	2194.56
30.67	2011.68	23.94	2194.56	35.18	2194.56
32.43	2011.68	24.48	2377.44	36.05	2011.68
33.59	1828.80	26.07	2377.44	39.84	2011.68
41.64	1828.80	31.37	2194.56	41.00	1828.80
42.84	1645.92	33.08	2194.56	41.86	1775.76
44.73	1645.92	33.75	2011.68	42.35	1828.80
45.34	1828.80	34.75	1828.80	42.97	1828.80
45.72	1828.80	39.22	1828.80	44.11	1463.04
46.47	1463.04	39.76	2011.68	46.14	1097.28
48.15	1097.28	40.57	2011.68	46.44	914.40
49.42	731.52	41.16	1828.80	47.22	731.52
51.11	731.52	42.84	1828.80	49.31	731.52
52.23	1097.28	44.63	1463.04	50.77	1097.28
52.95	1097.28	45.26	1463.04	51.74	1097.28
53.83	914.40	46.30	1097.28	52.86	914.40
56.26	914.40	47.92	731.52	53.91	731.52
57.64	548.64	49.22	731.52	54.85	548.64
60.56	548.64	50.36	548.64	56.02	365.76
61.50	365.76	53.37	548.64	57.19	182.88
62.16	182.88	54.81	365.76	59.72	91.44
66.63	91.44	55.28	182.88	70.50	91.44
67.18	73.15	56.04	91.44		
67.84	54.86	70.50	91.44		
68.39	45.72				
71.39	45.72				

Table A.4: Bathymetry data for receiver locations 10, 11, and 12.

RECEIVER LOCATION 13		RECEIVER LOCATION 14		RECEIVER LOCATION 15	
Range (km)	Depth (m)	Range (km)	Depth (m)	Range (km)	Depth (m)
0.0	832.10	0.0	832.10	0.0	832.10
0.87	914.40	0.59	914.40	0.54	914.40
3.90	1097.28	3.25	1097.28	2.29	1097.28
5.69	1280.16	5.30	1280.16	4.43	1280.16
6.68	1463.04	6.36	1351.48	6.48	1351.48
7.32	1463.04	10.60	1280.16	9.90	1280.16
11.60	1280.16	13.93	1252.73	11.82	1126.54
16.15	1280.16	16.05	1280.16	15.79	1280.16
19.10	1463.04	17.67	1463.04	16.87	1463.04
19.87	1645.92	18.80	1645.92	18.90	1463.04
20.32	1828.80	19.83	1645.92	19.87	1280.16
20.77	1828.80	21.15	1463.04	23.49	1280.16
21.89	1645.92	21.91	1431.95	25.27	1645.92
23.03	1645.92	23.04	1463.04	27.75	1645.92
23.71	1828.80	24.99	1828.80	28.98	1463.04
24.39	2011.68	26.14	1828.80	29.80	1280.16
24.66	2011.68	27.26	1463.04	30.18	1097.28
25.36	1828.80	28.23	1404.52	31.75	914.40
26.66	1645.92	29.48	1463.04	32.88	731.52
27.31	1645.92	32.05	1463.04	33.20	691.29
28.51	1828.80	34.26	1280.16	33.65	731.52
29.13	2011.68	34.94	1097.28	34.61	1097.28
30.08	2011.68	35.88	1097.28	34.96	1097.28
30.35	1828.80	36.29	1463.04	36.77	914.40
32.25	1645.92	37.00	1463.04	38.51	365.76
38.80	1645.92	37.64	1280.16	39.20	182.88
39.13	1728.22	39.30	1097.28	42.06	102.41
39.62	1645.92	40.13	731.52	53.51	91.44
39.89	1463.04	42.05	548.64	61.87	91.44
40.92	1280.16	42.73	429.77	62.99	182.88
42.14	1280.16	43.45	548.64	63.82	182.88
43.63	1828.80	44.71	731.52	64.36	91.44
43.84	1907.44	47.73	731.52	70.50	91.44
44.03	1828.80	48.52	548.64		
44.87	1280.16	49.87	365.76		
46.34	914.40	52.03	182.88		
46.79	914.40	53.98	182.88		
48.23	1097.28	55.53	365.76		
49.05	1280.16	56.66	548.64		
49.32	1280.16	58.47	548.64		
51.43	731.52	59.55	182.88		
53.19	731.52	60.36	91.44		
53.47	914.40	70.50	91.44		
54.47	548.64				
56.63	182.88				
58.53	91.44				
70.50	91.44				

Table A.5: Bathymetry data for receiver locations 13, 14, and 15.

RECEIVER LOCATION 16		RECEIVER LOCATION 17	
Range (km)	Depth (m)	Range (km)	Depth (m)
0.0	825.	0.0	824.79
8.4	1463.	6.60	1097.28
9.0	1463.	8.00	1280.16
14.1	1280.	8.59	1463.04
16.6	1280.	11.65	1463.04
24.2	2378.	14.63	1280.16
25.8	2378.	16.37	1280.16
41.2	958.	19.05	1463.04
42.4	1280.	20.13	1645.92
47.8	1280.	20.93	1828.80
53.5	139.	21.58	2011.68
66.2	46.	22.22	2194.56
70.0	46.	22.87	2377.44
		24.90	2377.44
		25.76	2194.56
		27.80	2011.68
		28.82	1828.80
		29.68	1645.92
		31.40	1463.04
		36.39	1280.16
		39.24	1097.28
		41.71	914.40
		45.73	731.52
		48.68	548.64
		52.39	365.76
		56.41	182.88
		61.14	91.44
		64.14	73.15
		66.99	54.86
		67.47	49.93
		70.47	49.93

Table A.6: Bathymetry data for receiver locations 16 and 17.



## A.2 MPP Ray Traces and Stick Plots

## RECEIVER LOCATION 1: RAY TRACE

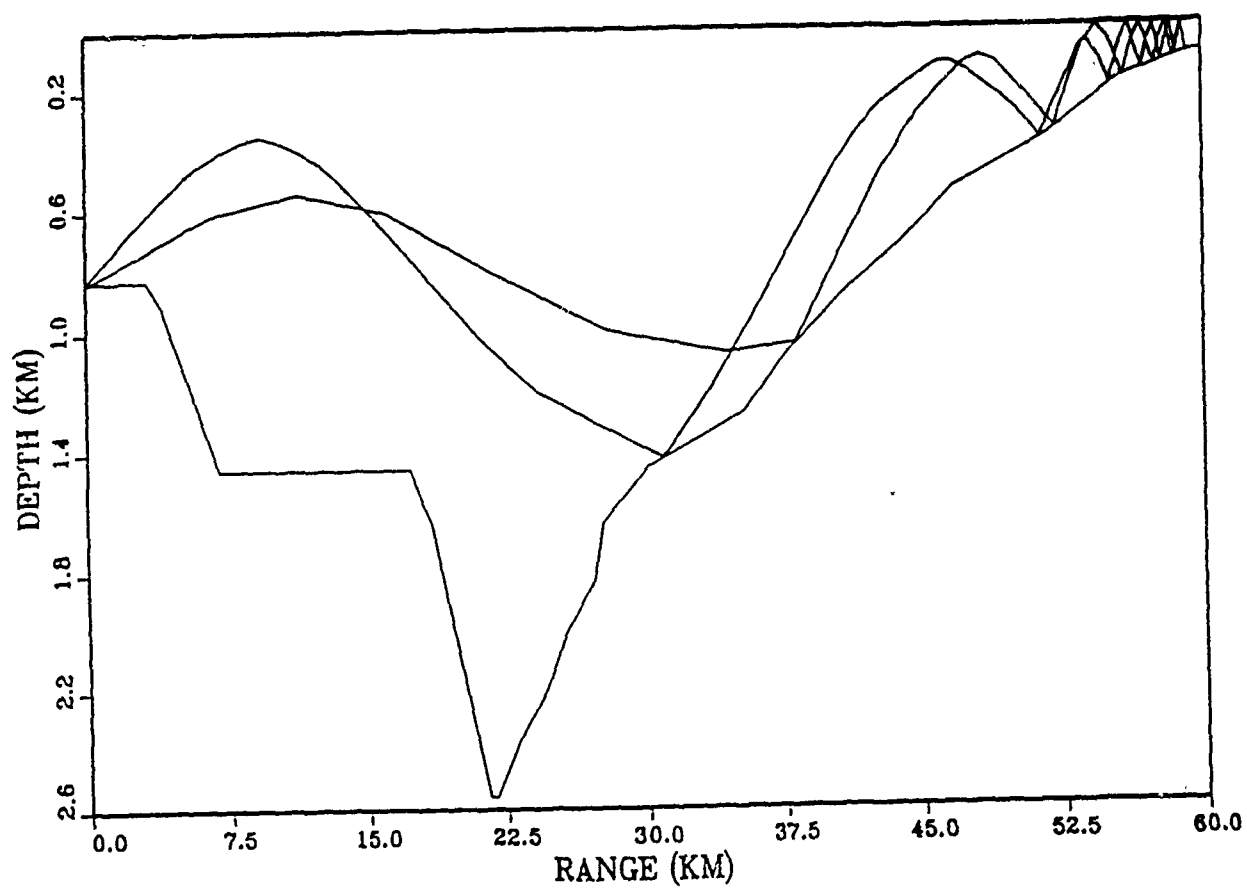


Figure A.1: Ray trace for receiver location 1.

## RECEIVER LOCATION 1: STICK PLOT

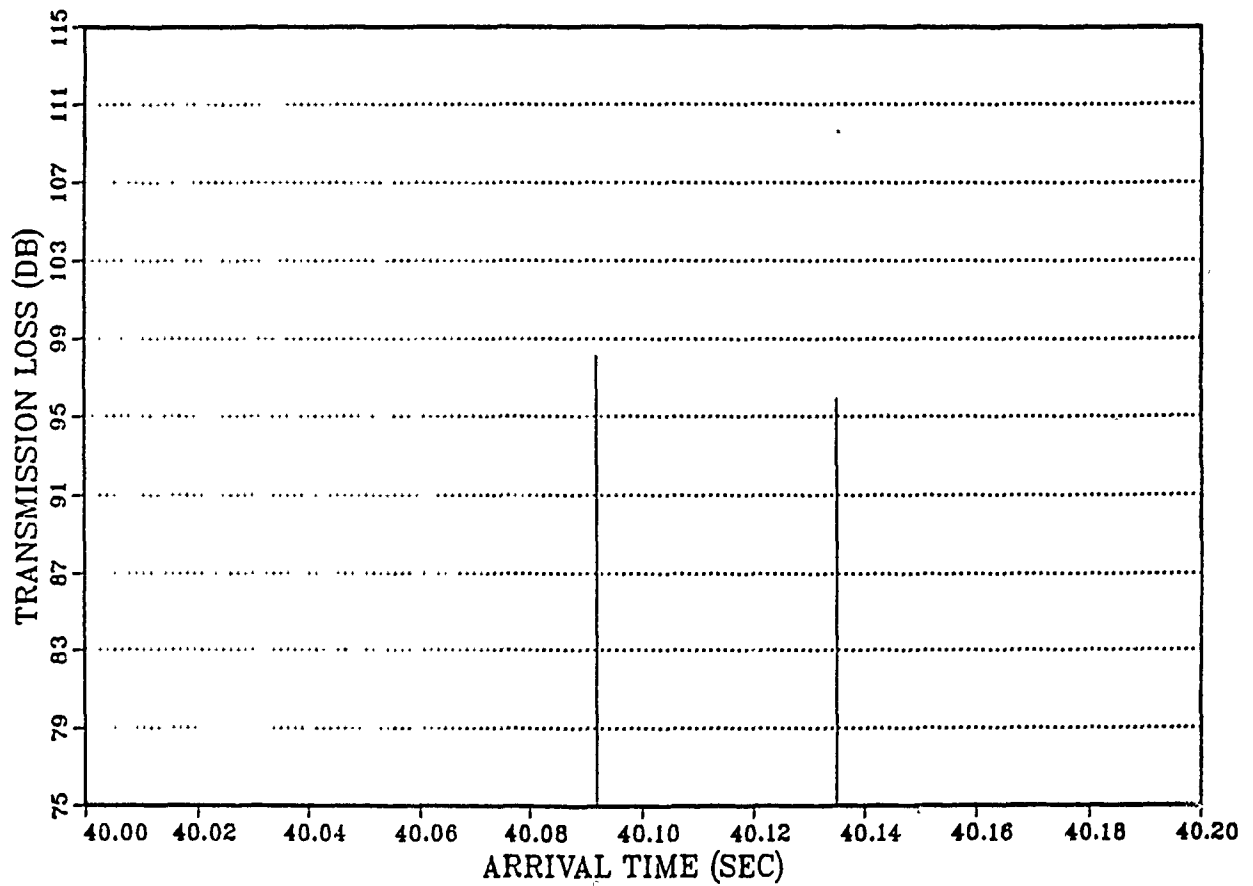


Figure A.2: Stick plot for receiver location 1.

## RECEIVER LOCATION 2: RAY TRACE

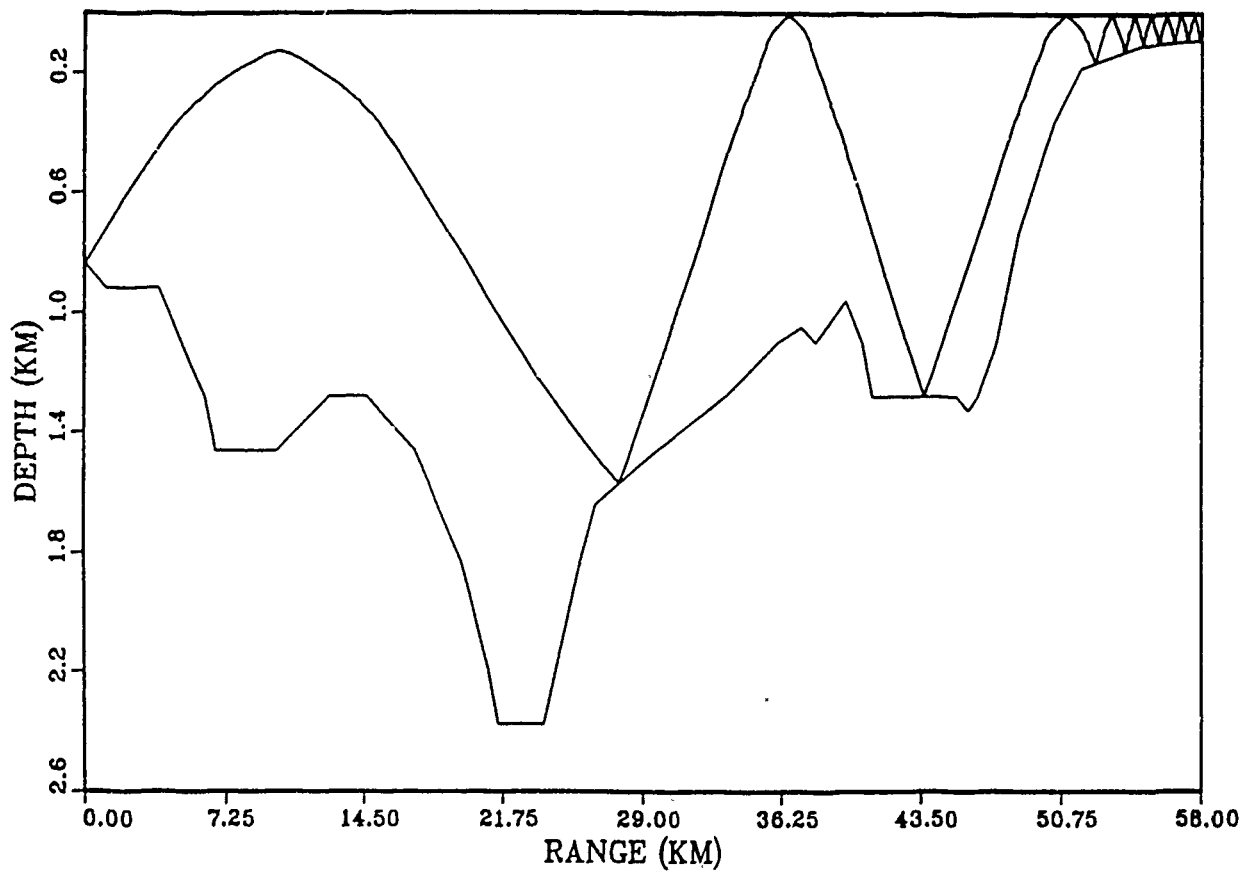


Figure A.3: Ray trace for receiver location 2.

## RECEIVER LOCATION 2: STICK PLOT

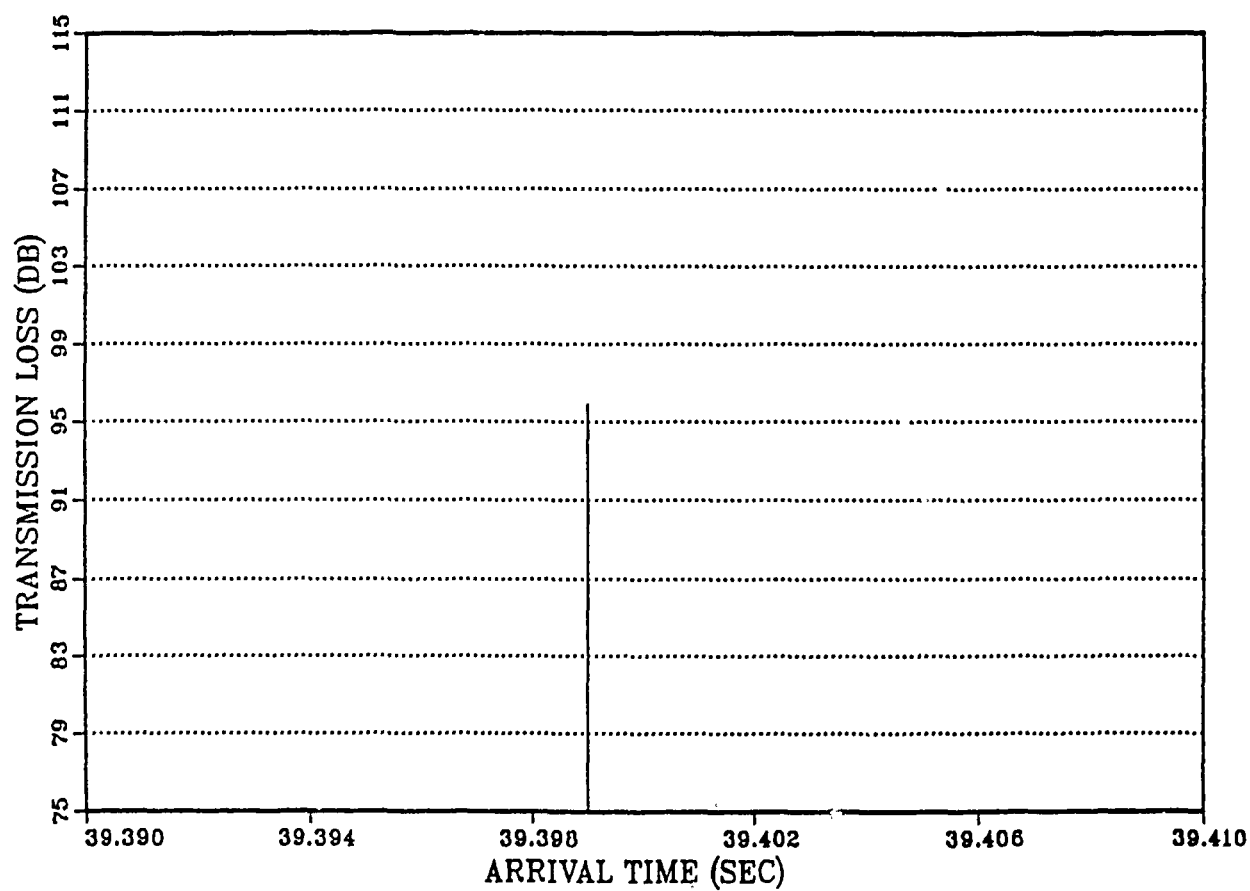


Figure A.4: Stick plot for receiver location 2.

## RECEIVER LOCATION 4: RAY TRACE

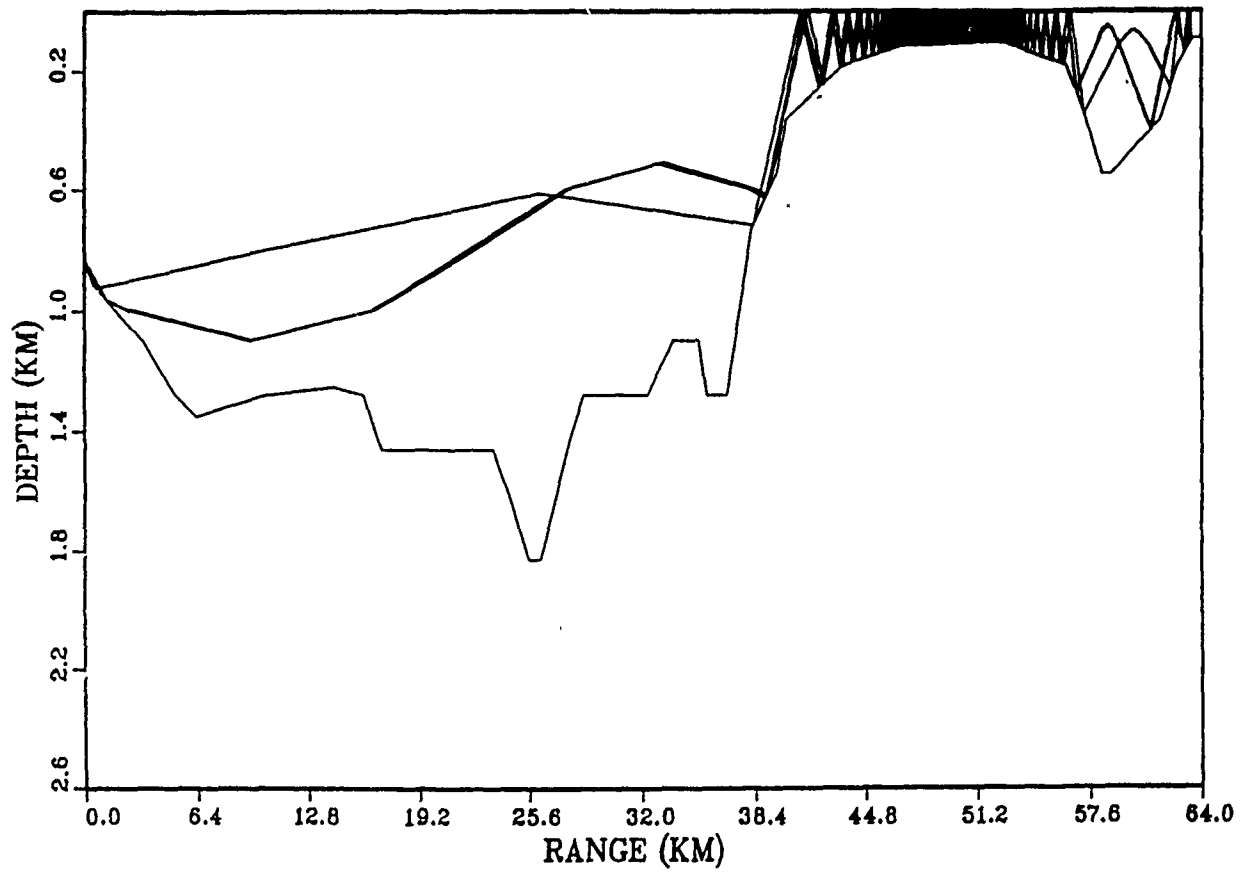


Figure A.5: Ray trace for receiver location 4.

## RECEIVER LOCATION 4: STICK PLOT

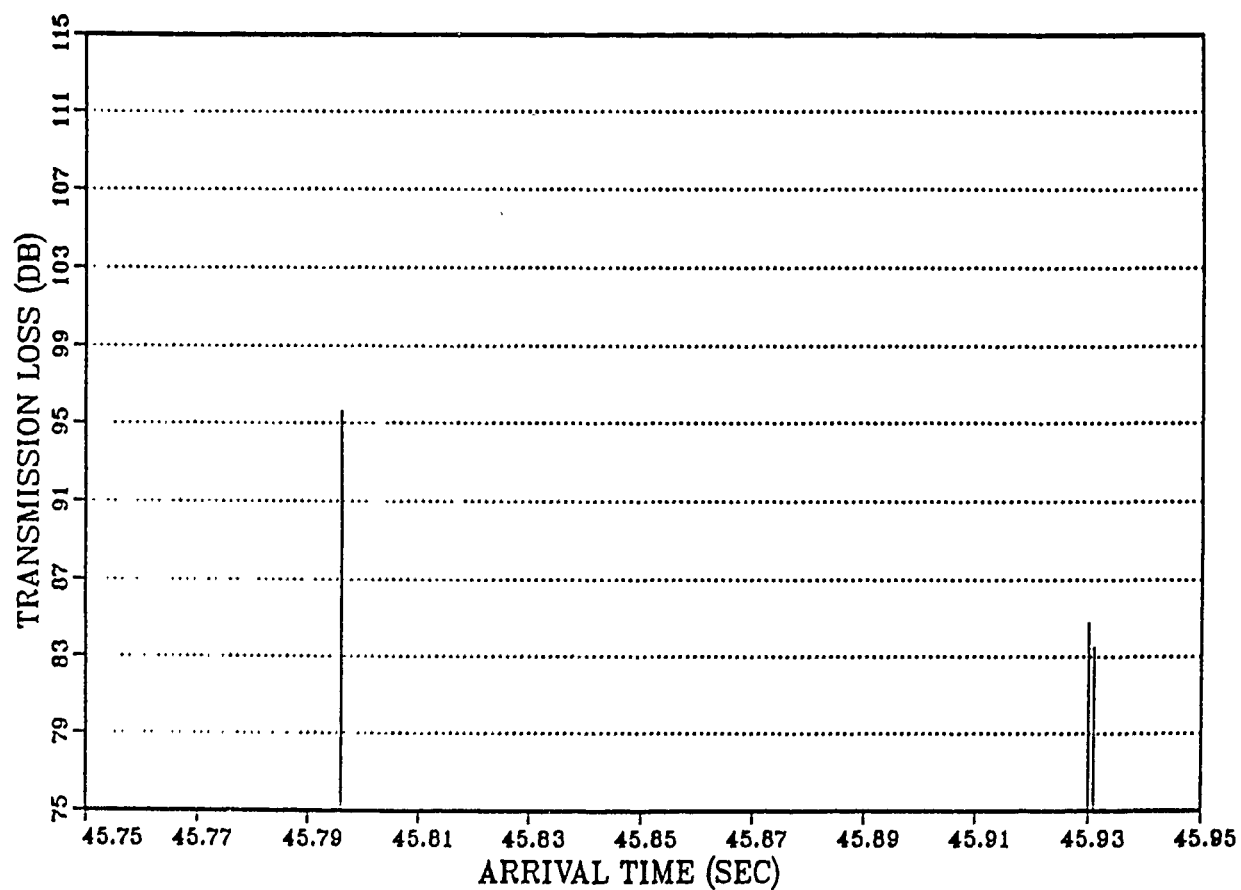


Figure A.6: Stick plot for receiver location 4.

## RECEIVER LOCATION 5: RAY TRACE

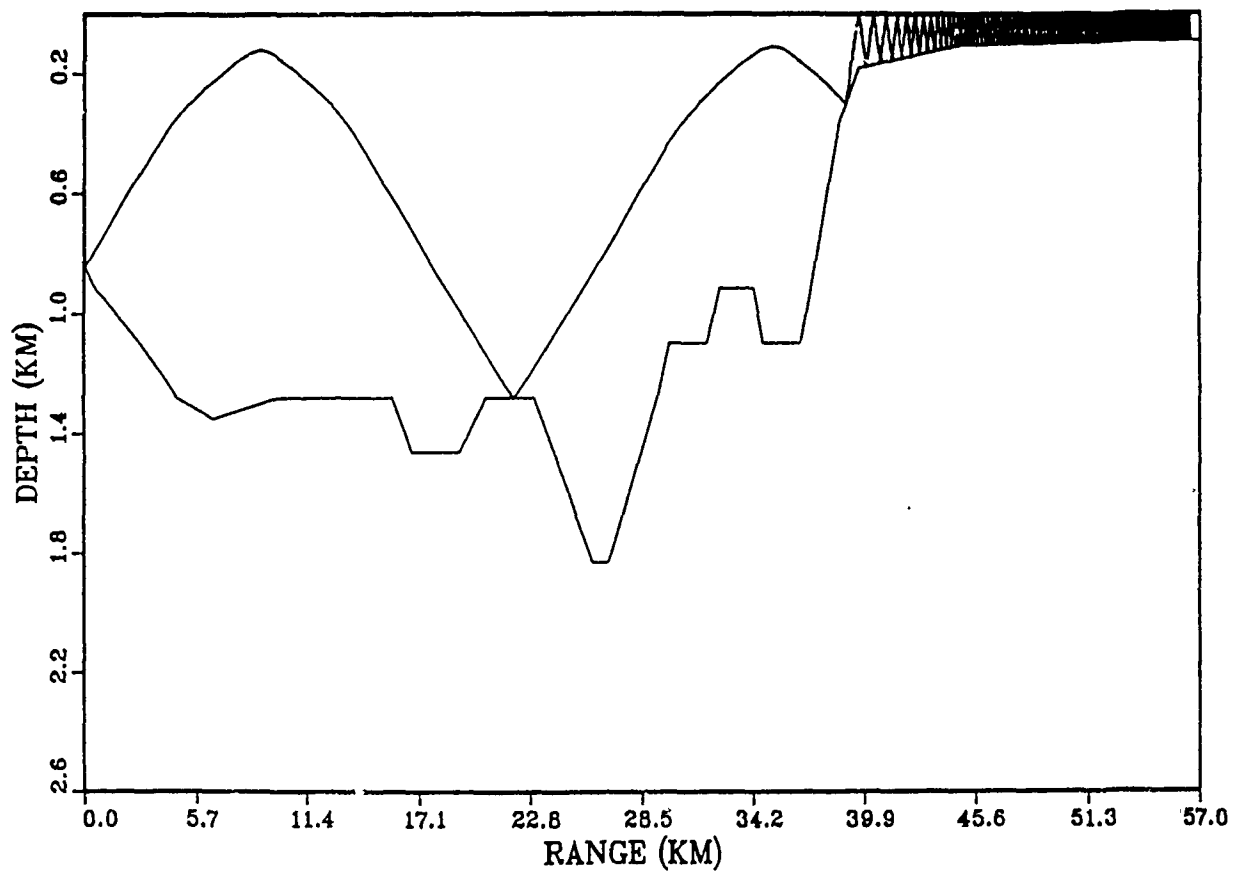


Figure A.7: Ray trace for receiver location 5.



## RECEIVER LOCATION 5: STICK PLOT

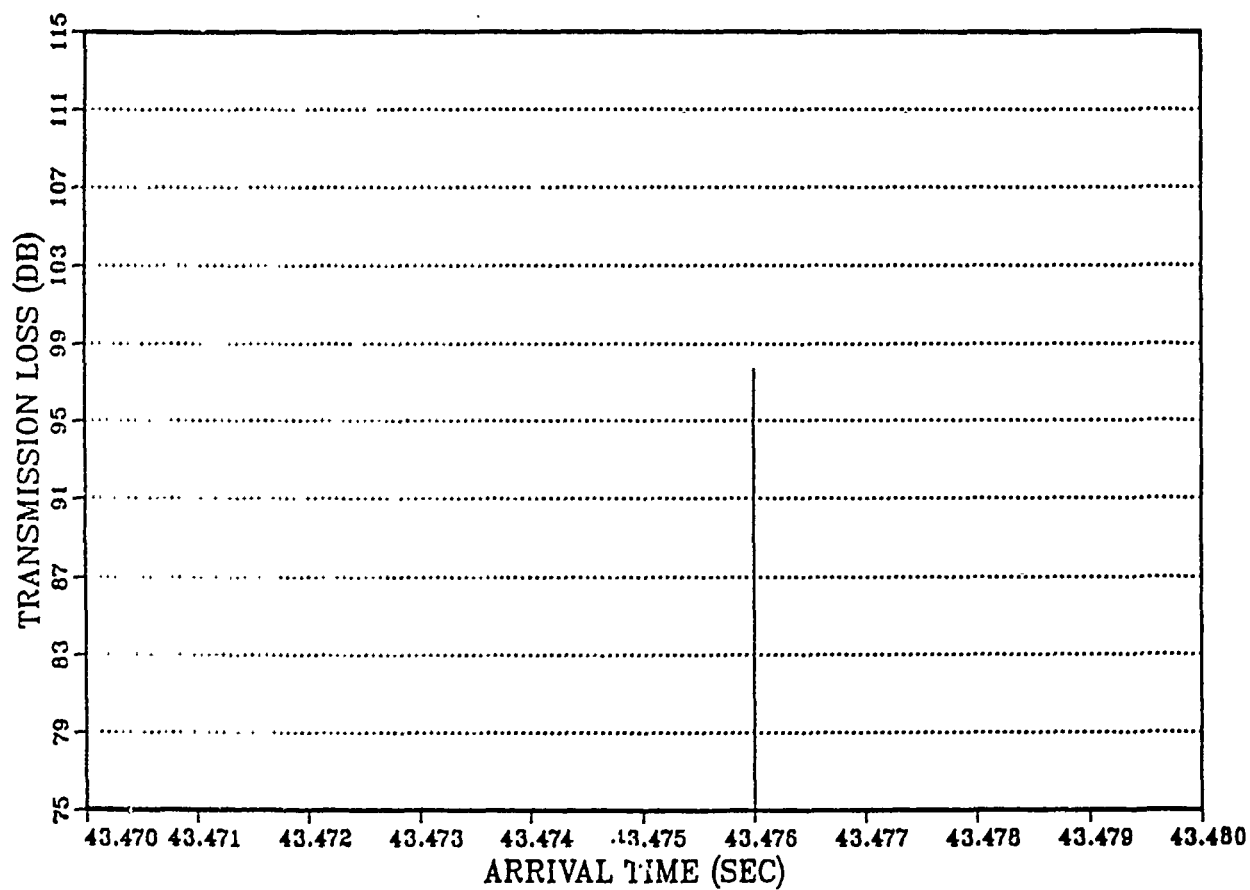


Figure A.8: Stick plot for receiver location 5.

## RECEIVER LOCATION 7: RAY TRACE

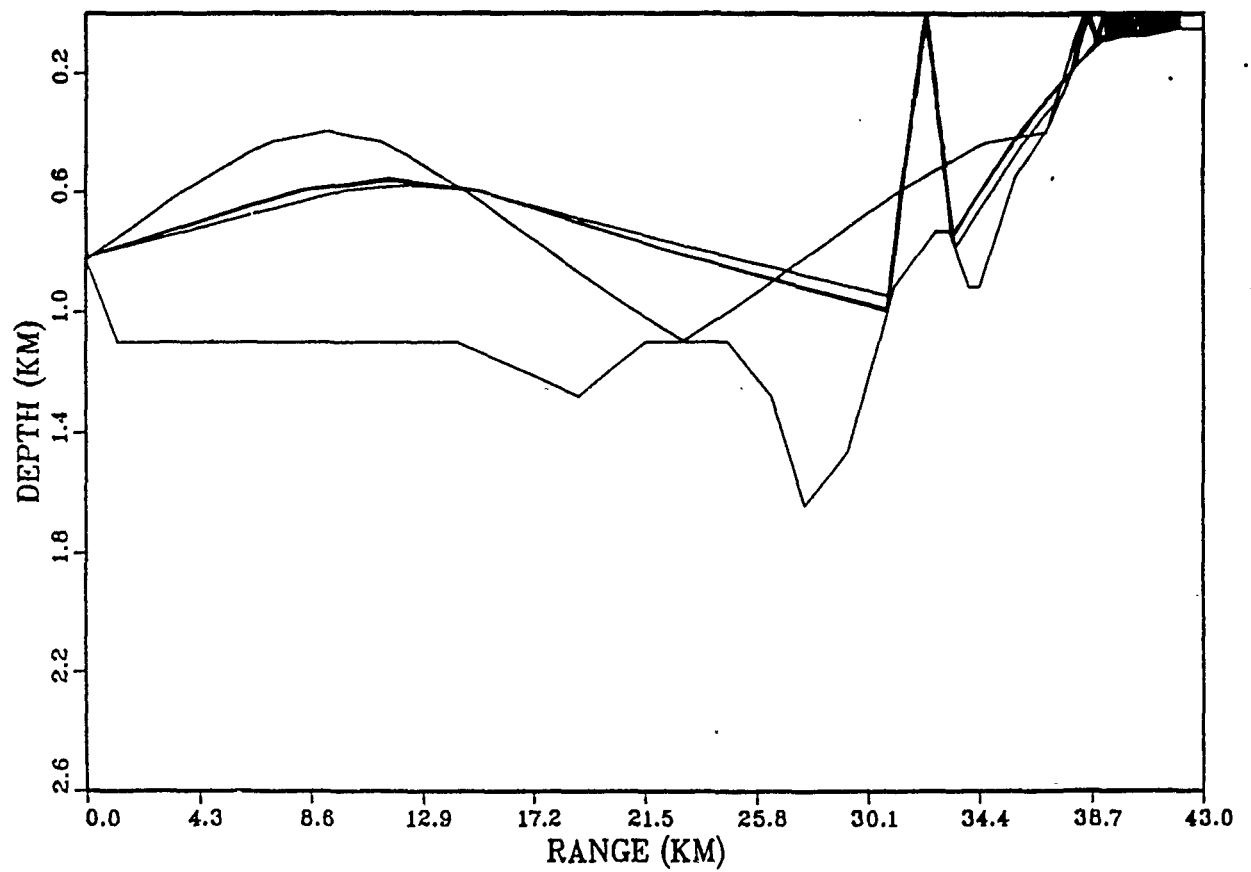


Figure A.9: Ray trace for receiver location 7.

## RECEIVER LOCATION 7: STICK PLOT

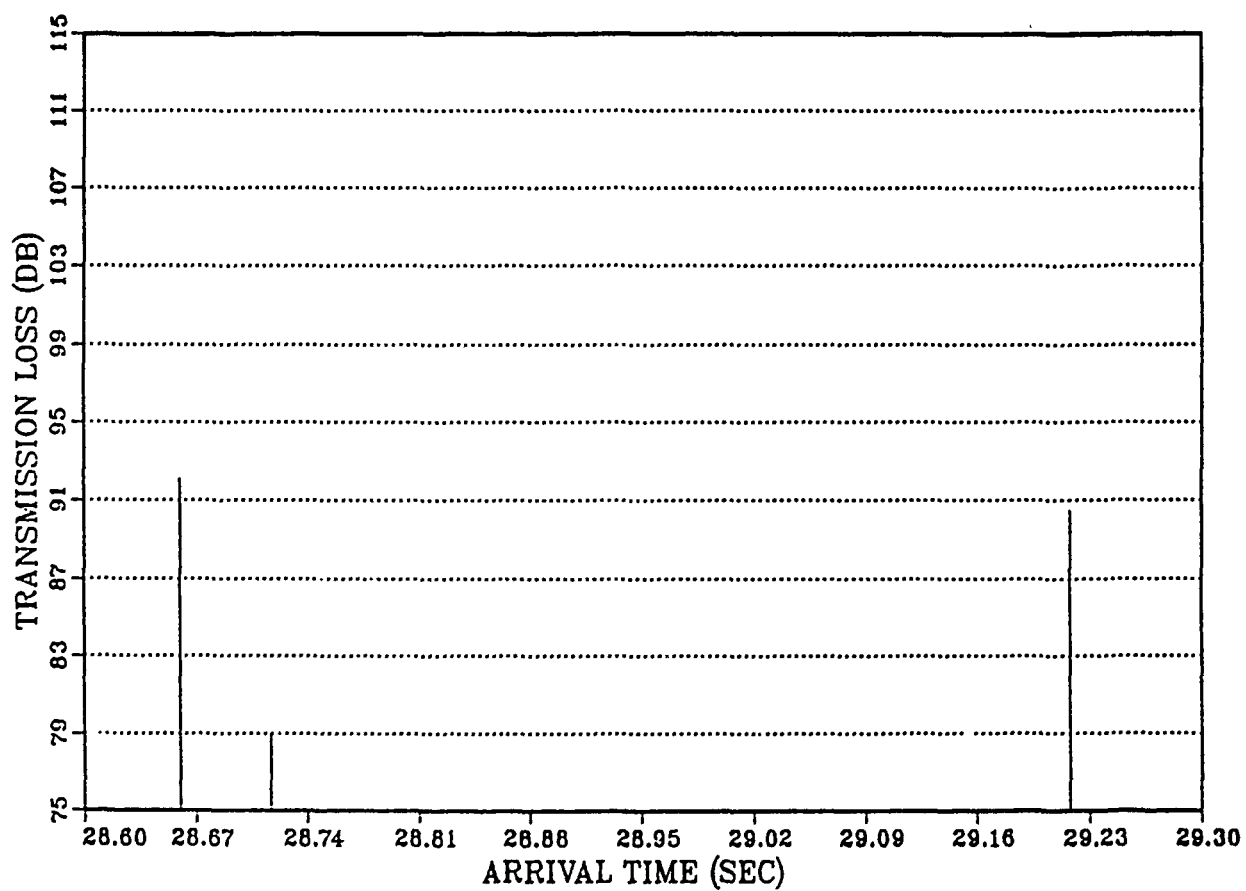


Figure A.10: Stick plot for receiver location 7.

## RECEIVER LOCATION 8: RAY TRACE

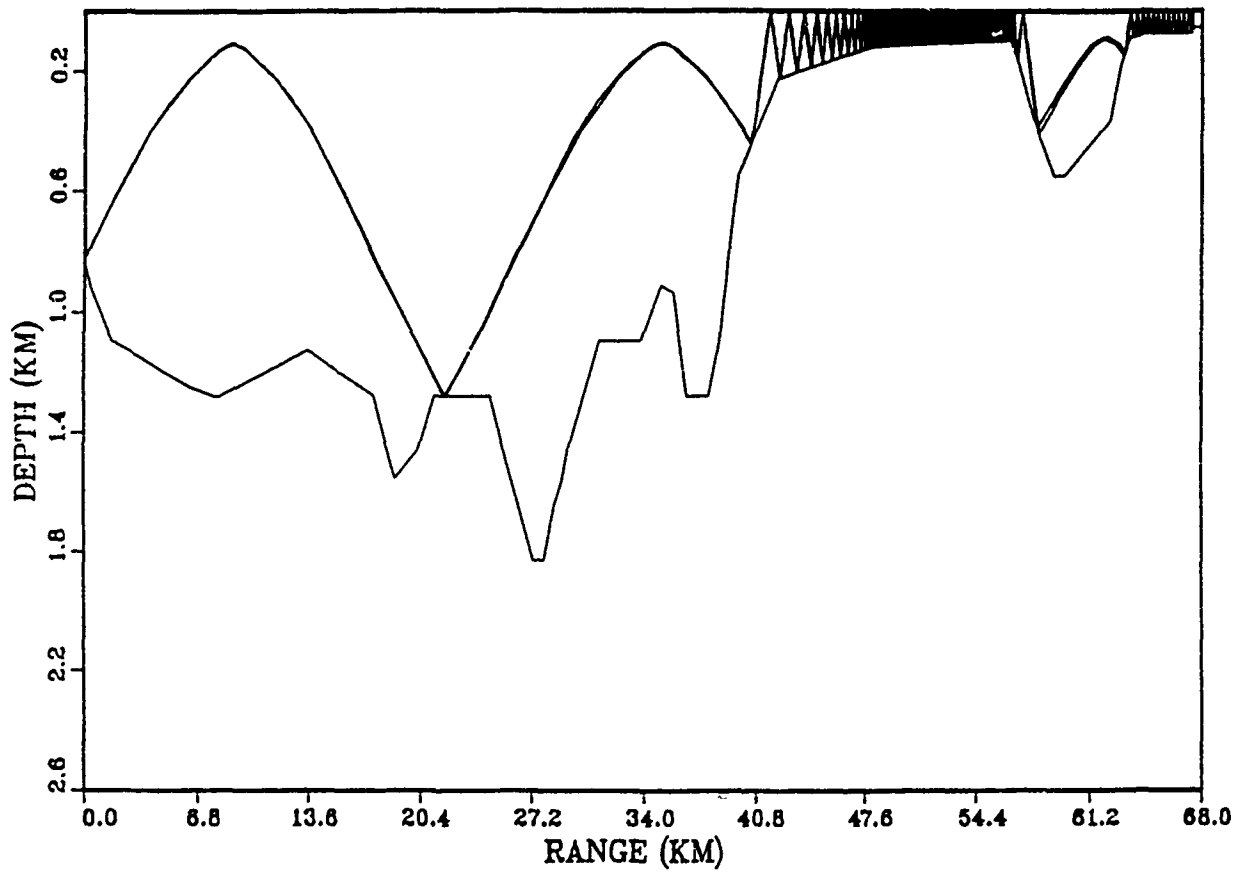


Figure A.11: Ray trace for receiver location 8.

## RECEIVER LOCATION 8: STICK PLOT

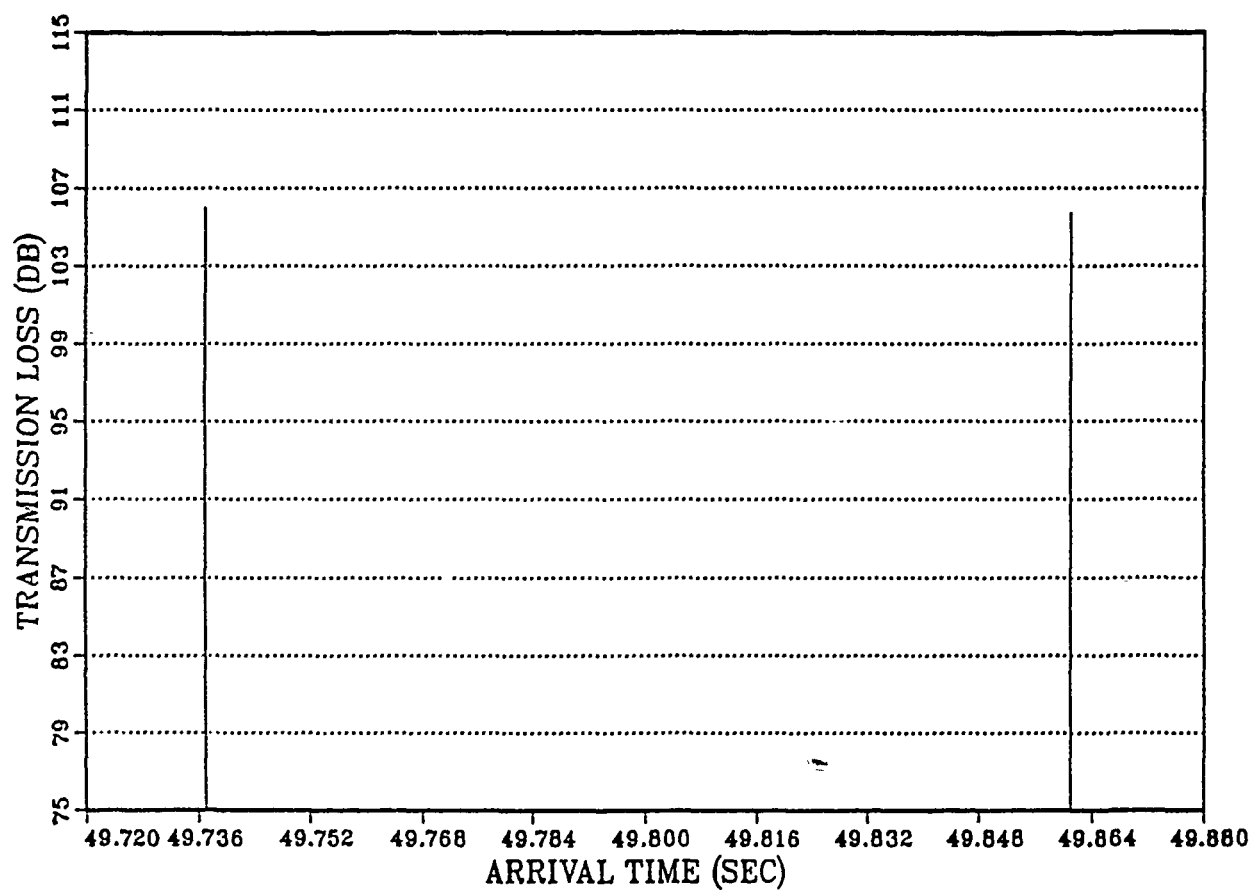


Figure A.12: Stick plot for receiver location 8.

## RECEIVER LOCATION 13: RAY TRACE

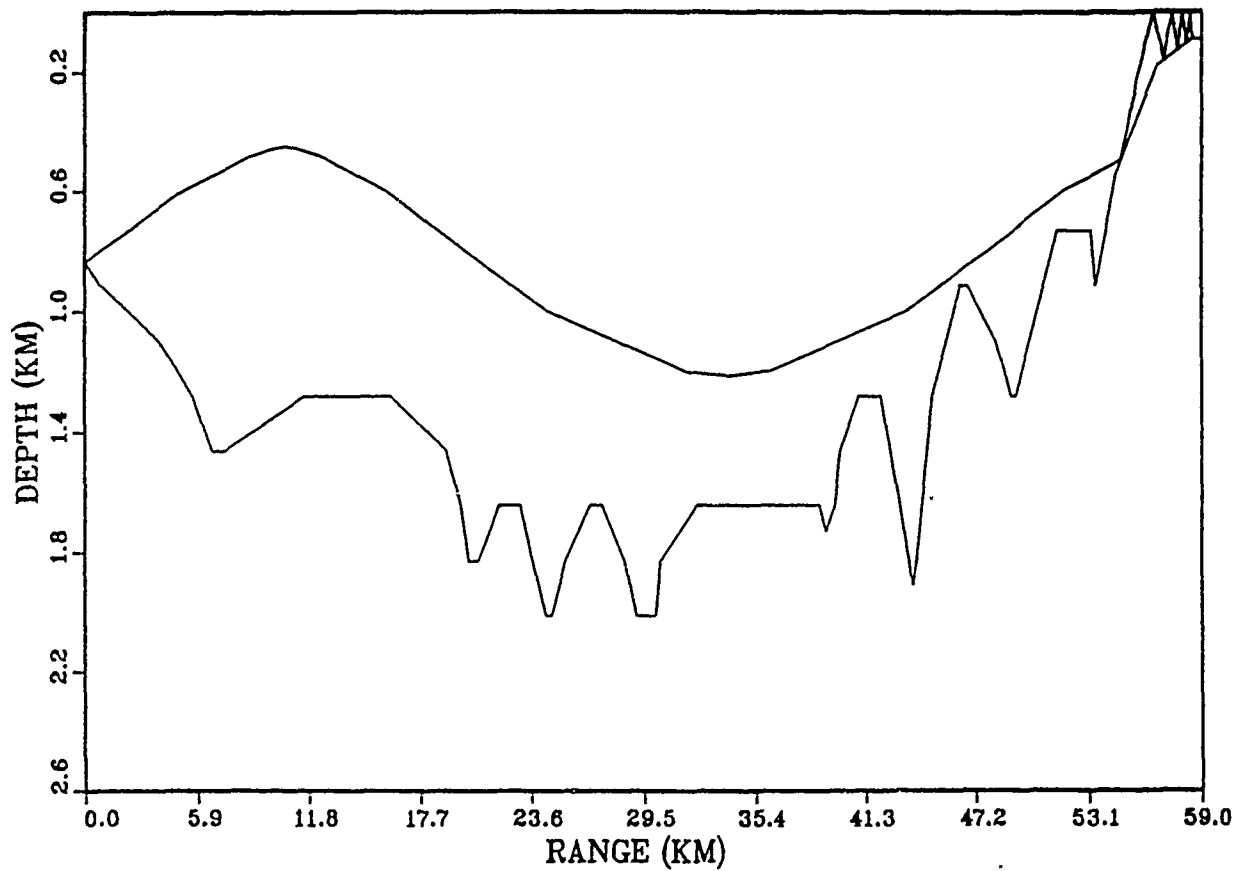


Figure A.13: Ray trace for receiver location 13.

## RECEIVER LOCATION 13: STICK PLOT

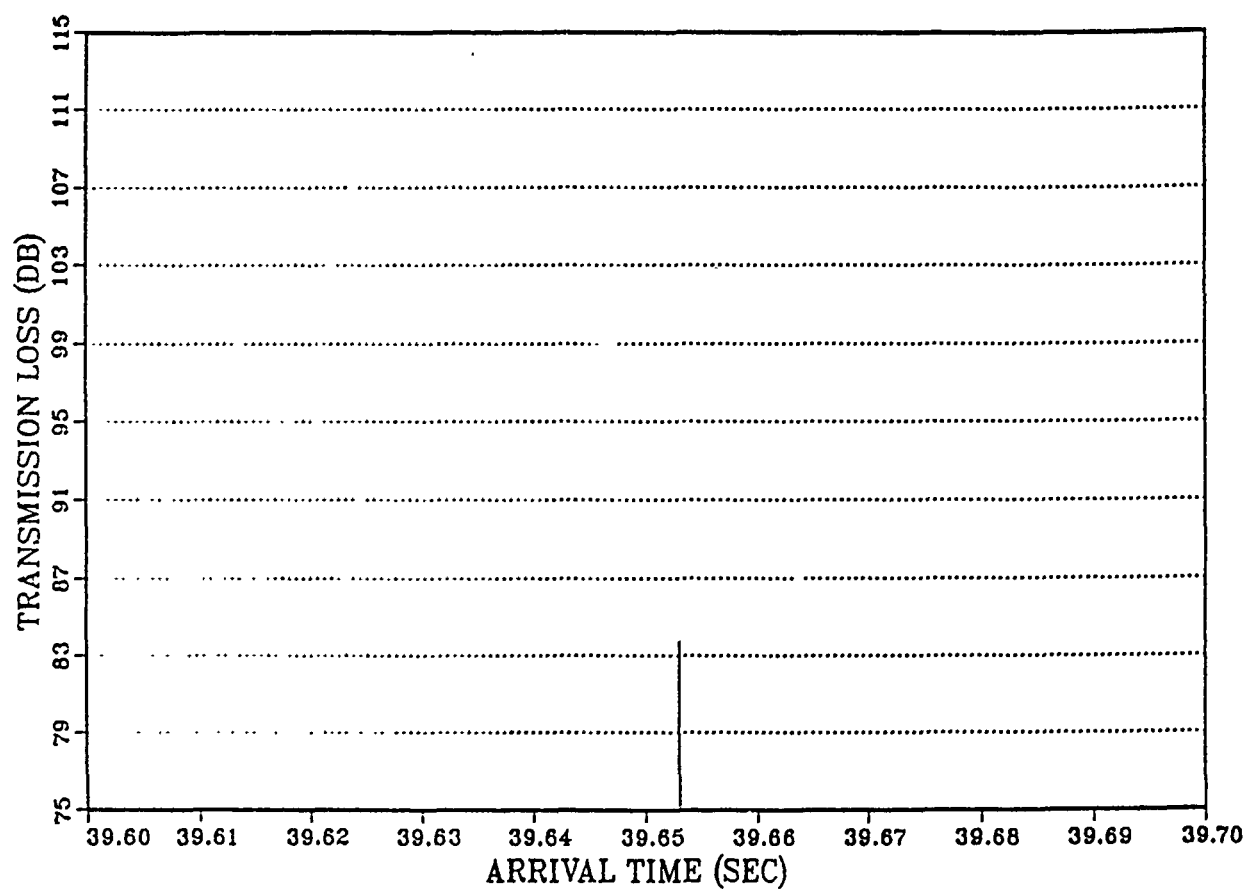


Figure A.14: Stick plot for receiver location 13.

## RECEIVER LOCATION 17: RAY TRACE

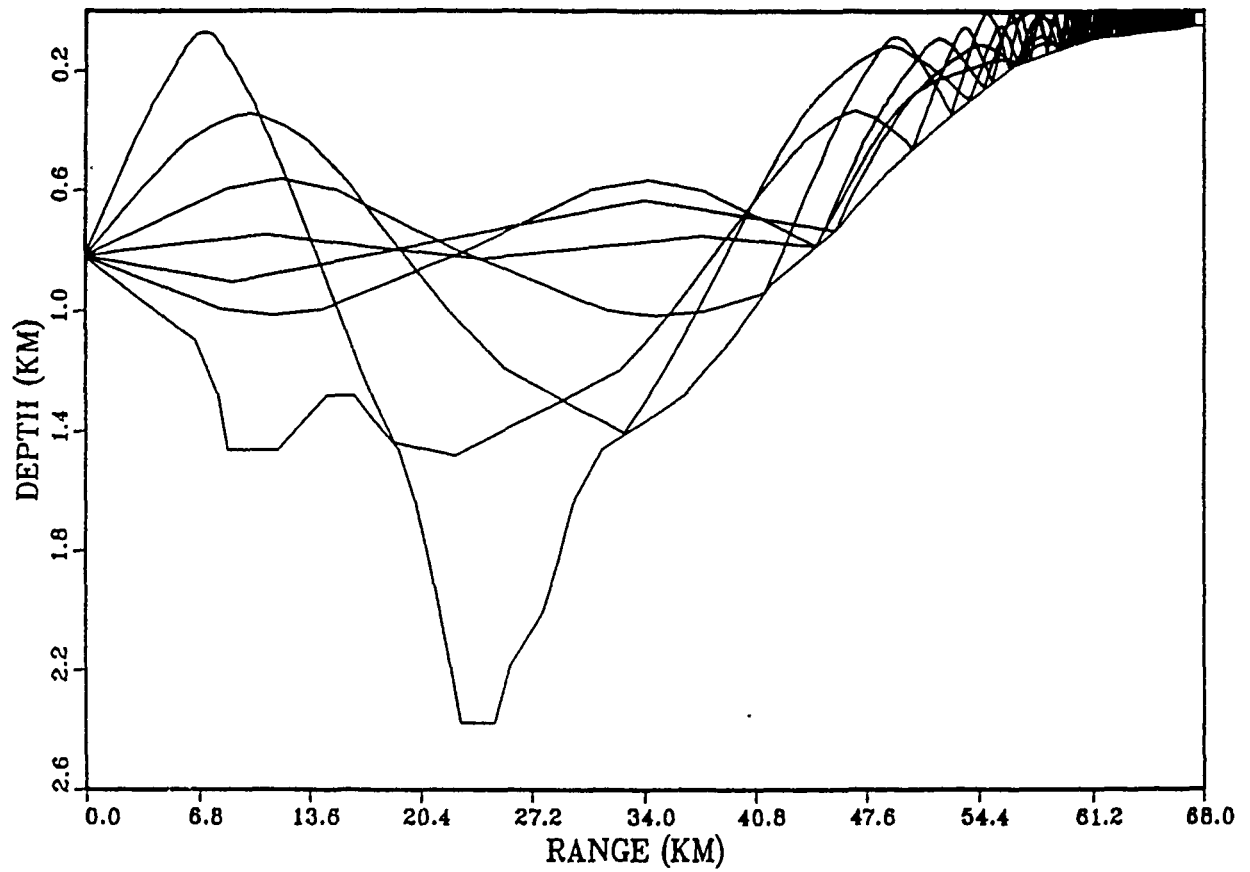


Figure A.15: Ray trace for receiver location 17.



## RECEIVER LOCATION 17: STICK PLOT

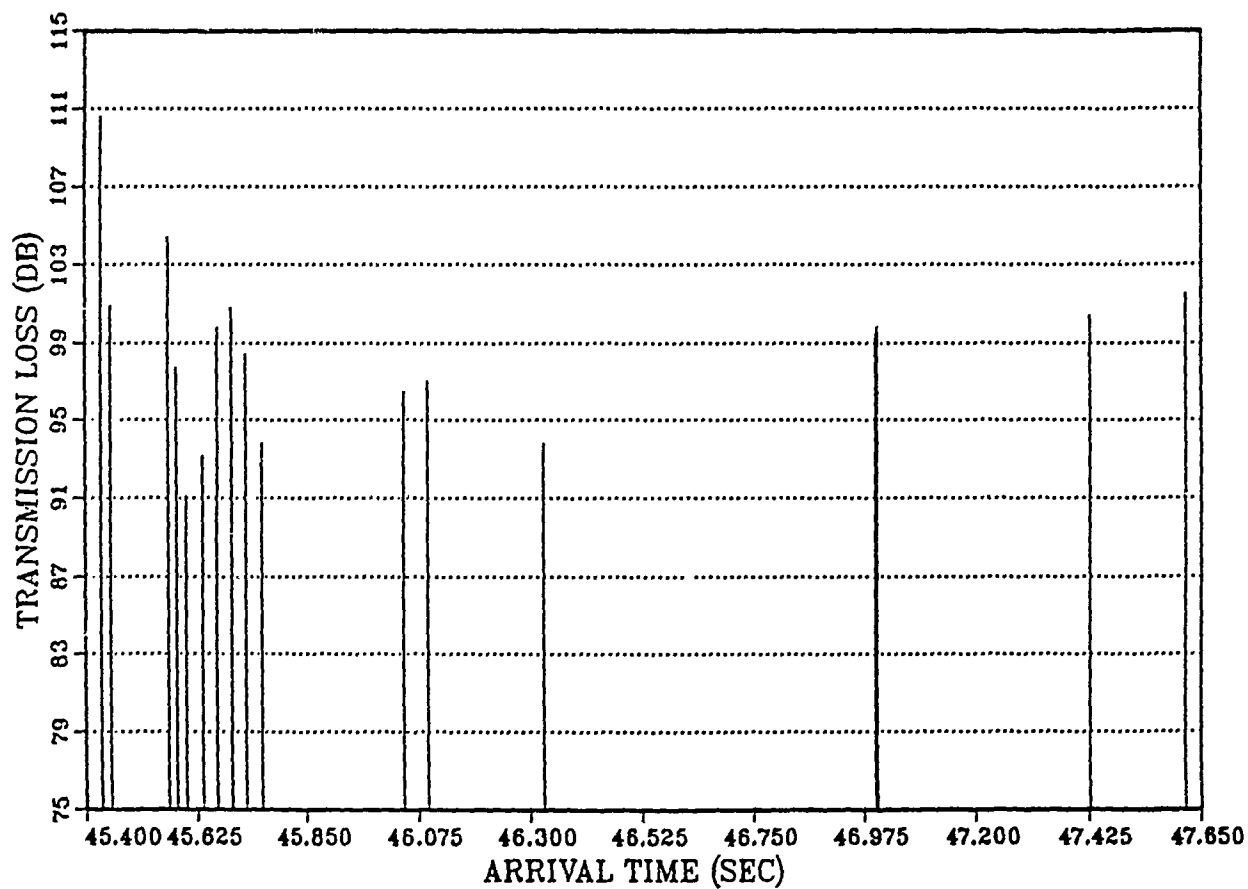


Figure A.16: Stick plot for receiver location 17.

## **Appendix B**

# **Chronologic Summary of Events in the 1988 Monterey Bay Experiment**

The following is a summary of the experiment as it happened from the deck log of R/V Point Sur. All dates and times are in Pacific Standard Time (PST).

### **B.1 12 December 1988**

0950 R/V Point Sur underway from Moss Landing. Receiver van is in place on Huckleberry Hill.

1150 Deployed modified AN/SSQ-57 buoy at station B, 36°56.3'N- 122°00.5'W

1241 Deployed MIUW buoy, station B1, 36°36.3'N-122°00.2'W

1705 Deployed transmitter in 870 meters of water 36°23.7'N- 122°17.84'W

2013 CTD measurement 36°23.2'N-122°17.8'W

2204 CTD measurement to 1800 meters 36°31.9'N-122°17.8'W

### **B.2 13 December 1988**

0013 CTD measurement to 155 meters 36°40.4'N-122°04.5'W

0105 CTD measurement to 1400 meters 36°40.4'N-122°04.4'W  
 0230 Lost contact with buoy at station B  
 0308 CTD measurement to 73 meters 36°48.6'N-122°57.9'W  
 0357 CTD measurement to 70 meters 36°46.5'N-122°05.6'W  
 0507 CTD measurement to 70 meters 36°44.7'N-122°13.3'W  
 0811 Deployed ARGOS wave buoy #6249 at 36°44.3'N-122°13.3'W but re-  
 covered buoy after no radio signal was received  
 1033 Deployed modified sonobuoy, station L, 36°52.9'N-122°10.8'W in 61  
 fathoms of water  
 1151 Deployed modified sonobuoy, station J, 36°51.1'N-122°04.8'W in 53  
 fathoms of water  
 1157 CTD measurement to 82 meters 36°51.0'N-122°01.5'W  
 1245 Deployed modified sonobuoy, station I, 36°49.1'N-122°01.5'W in 53  
 fathoms of water  
 1339 Deployed modified sonobuoy, station II, 36°51.8'N-122°57.2'W in 50  
 fathoms of water  
 1346 CTD measurement to 73 meters 36°48.5'N - 121°57.2'W  
 1452 Deployed modified sonobuoy, station G, 36°48.5'N - 121°57.9'W in 53  
 fathoms of water  
 1558 Deployed modified sonobuoy, station E, 36°48.5'N - 121°52.1'W in 45  
 fathoms of water  
 1605 CTD measurement to 52 meters 36°43.6'N-122°00.6'W  
 1713 Deployed ARGOS waves buoy 36°43.6'N-122°00.6'W  
 1805 Deployed ARGOS waves buoy 36°43.9'N-122°08.6'W. Because of the  
 weather forecast for high winds and seas, a decision was made not to  
 deploy the ARGOS thermistor string buoys.  
 1900 CTD "yo-yo" measurements to 600 meters 36°44.1'N-122°13.7'W  
 2200 Stop CTD to reposition - have drifted to 36°43.2'N-122°14.7'W  
 2245 CTD "yo-yo" measurements to 600 meters 36°44.5'N-122°13.3'W

### **B.3 14 December 1988**

- 0000 Continue CTD "yo-yo" measurements 36°44.7'N-122°14.7'W
- 0033 Halt CTD to move ship (traffic avoidance)
- 0052 Resume CTD "yo-yo" to 600 meters 36°14.5'N-122°13.3'W
- 0338 Stop CTD to reposition - have drifted to 36°45.9'N-122°16.7'W
- 0408 CTD "yo-yo" measurements to 600 meters 36°44.6'N-122°13.5'W
- 0557 Stop CTD measurements - have drifted to 36°45.2'N-122°14.8'W
- 0832 Returned to Moss landing to offload 3 ARGOS buoys and 2 personnel.  
Remain in port about two hours.
- 1246 Replace station J modified sonobuoy (replaced with malfunctioning  
buoy repaired by changing hydrophone, original J buoy recovered)
- 1435 Deployed MIUW buoy at station L-1 (repaired by splicing power con-  
nection in electronics package) 36°55.1'N-122°14.0'W
- 1528 Deployed modified sonobuoy at station L-2 (repair unsuccessful and  
buoy recovered at 1643)
- 1542 CTD measurement to 80 meters 36°57.6'N-122°17.7'W
- 1738 CTD measurement to 90 meters 36°52.8'N-122°10.7'W
- 1854 CTD measurement to 1000 meters 36°42.9'N-122°13.7'W
- 2046 CTD measurement to 1500 meters 36°32.9'N-122°16.7'W
- 2238 CTD measurement to 800 meters 36°23.6'N-122°17.9'W

### **B.4 15 December 1988**

- 0055 CTD "yo-yo" measurement to 600 meters 36°39.0'N-122°18.0'W
- 0411 Stop CTD to reposition - have drifted to 36°39.4'N-122°23.2'W. Winds  
exceed 40 knots for much of the night.
- 0445 CTD "yo-yo" measurements to 600 meters 36°38.8'N-122°18.2'W

0617 CTD to 1200 meters

0644 Stop CTD - have drifted to 36°39.2'N-122°22.4'W

1138 Recovered ARGOS wave buoy. Begin search for second buoy. Positions are inexact due to three hour time lag in position report to ship. Swell height limits buoy visibility to about 700 meters.

1623 Discontinue search for ARGOS buoy.

1853 Recovered MIUW buoy, station L-1

2007 Recovered buoy, station L

2114 Recovered buoy, station J

2148 Recovered buoy, station I

2226 Recovered buoy, station h

2257 Recovered buoy, station G

2330 Recovered buoy, station E

## B.5 16 December 1988

0134 Recovered MIUW buoy, station B1, Buoy for station B is not in place

0224 Stop search for station B buoy

0335 CTD measurement to 800 meters 36°30.6'N-122°09.7'W

0704 Transmitted release signal to acoustic releases on tomography transmitter, no transponder reply heard.

0805 Leave area of tomography transmitter to look for ARGOS buoy.

1030 Recover ARGOS buoy

1253 Transmitted release signal to acoustic releases, which released the anchor.

1331 Transmitter on surface

1421 Transmitter recovered

1830 Moored, Moss Landing

## **B.6 Data Disposition**

1. CTD and ADCP data to Woods Hole Oceanographic Institution for Processing.
2. Tomographic acoustic signal recordings to Naval Postgraduate School for processing.
3. NDBC and ARGOS buoy data to National Data Buoy Center for processing.

## Appendix C

# Maximal-length Sequences and the Fast Hadamard Transform

### C.1 Introduction

Impulsive excitation is an extremely easy and useful mathematical tool for measuring the impulse response of a system or determining travel time through a media. The problem is that an impulse is fairly difficult to achieve physically. As the transmitted pulse approaches an impulse, the required bandwidth and peak power of the transmitter increase. Impulsive sound signals can be generated by explosive or implosive sources but these have uneven frequency distribution energy, and repeatability. Another solution is to use pseudorandom noise. The period, frequency distribution, and energy are deterministic and can be tailored to meet system requirements. The signal can be repeated identically for additional signal processing gain. Importantly, when sampled and digitized the signal becomes an impulse of much shorter duration and higher peak power than the original signal. The method for generating the sequence as well as a fast method for processing the received signal will be described here.

The pseudorandom noise signal is a binary maximal-length shift register sequence. The sequence's most important characteristic its autocorrelation, which is constant except at a shift of zero, making the sequence the equivalent of white noise. The energy at zero is much higher than for each individual digit, making it easier to estimate the arrival time of the signal.

Other properties of maximal-length sequences (m-sequences) are detailed by Ziemer and Peterson [43], including a list of polynomials which produce m-sequences. Not all shift register sequences are of maximal-length, only those which do not repeat until after  $2n-1$  delays, where  $n$  is the number of delays in the shift register.

As an example the table entry for a maximal-length sequence of degree three will be developed into a code and a fast method for its autocorrelation will be examined. Various sources were used.[44,45,46]

## C.2 Generating the M-sequence

Table 8-5 of Ziemer and Peterson [43] lists only one polynomial for generating an m-sequence of degree three. The length of the sequence will be seven digits. The listing in the table is an octal representation of the binary coefficients of the generating polynomial. Translating to binary this becomes

$$[13]_8 \text{ --- } [1011]_2. \quad (C.1)$$

The corresponding polynomial is

$$g(D) = D^3 + D + 1, \quad (C.2)$$

where  $D$  is a delay of one unit ( $D^3$  is three delays). The shift register register realization follows directly as shown in Figure C.1.

Loading the initial state is arbitrary since the register will cycle through all possible combinations before repeating. For an initial state  $a_2 = 1$ ,  $a_1 = 0$ ,  $a_0 = 0$ , this is one period of the sequence as shown in Table C.1.

The m-sequence is a single column of the register states. The characteristics of the autocorrelation are unaffected by whether the m- sequence is read from top to bottom or the reverse, but the method for formulating the Hadamard demodulation does change. The top to bottom sequence will be designated the "forward" code,

$$S = \begin{cases} 1001110 & \text{forward code} \\ 0111001 & \text{reverse code.} \end{cases} \quad (C.3)$$

In use, the m-sequence digits are transformed by replacing 1 with -1 and 0 with 1. When dealing with the structure and mathematics it is easier to use 0 and 1 because many people are familiar with binary mathematics and can more easily adapt to modulo-two mathematics The received signal has



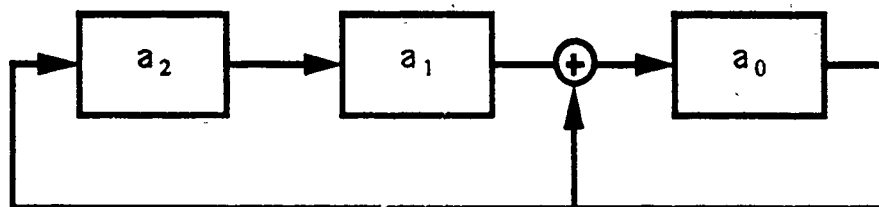


Figure C.1: Shift register realization of Eq. C.2

Cycle	$a_2$	$a_1$	$a_0$
1	1	0	0
2	0	1	0
3	0	0	1
4	1	0	1
5	1	1	1
6	1	1	0
7	0	1	1
8	1	0	0

Table C.1: Shift register contents when generating M-sequence.

an unknown time delay and so must be correlated with all possible shifts of the code. Let the seven shifted sequences form the matrix  $M$ :

$$M = \begin{bmatrix} 1 & 0 & 0 & 1 & 1 & 1 & 0 \\ 0 & 1 & 0 & 0 & 1 & 1 & 1 \\ 1 & 0 & 1 & 0 & 0 & 1 & 1 \\ 1 & 1 & 0 & 1 & 0 & 0 & 1 \\ 1 & 1 & 1 & 0 & 1 & 0 & 0 \\ 0 & 1 & 1 & 1 & 0 & 1 & 0 \\ 0 & 0 & 1 & 1 & 1 & 0 & 1 \end{bmatrix}. \quad (C.4)$$

When this matrix and the code are transformed to + and -1's, multiplying the signal by the matrix will result in the correlation,

$$R_{sm} = MS. \quad (C.5)$$

This is the entire goal of the initial signal processing, all that remains is to develop a fast, efficient algorithm to accomplish this multiplication.

### C.3 The Hadamard Matrix

To describe the fast algorithm, it is necessary to introduce the Hadamard matrix. The Sylvester-type Hadamard Matrix has a recursive form for higher orders given by

$$H_1 = [1], H_{2i} = \begin{bmatrix} H_i & H_i \\ H_i & -H_i \end{bmatrix}. \quad (C.6)$$

The third degree matrix  $H$  is

$$H = \begin{bmatrix} 1 & 1 & 1 & 1 & 1 & 1 & 1 & 1 \\ 1 & -1 & 1 & -1 & 1 & -1 & 1 & -1 \\ 1 & 1 & -1 & -1 & 1 & 1 & -1 & -1 \\ 1 & -1 & -1 & 1 & 1 & -1 & -1 & 1 \\ 1 & 1 & 1 & 1 & -1 & -1 & -1 & -1 \\ 1 & -1 & 1 & -1 & -1 & 1 & -1 & 1 \\ 1 & 1 & -1 & -1 & -1 & -1 & 1 & 1 \\ 1 & -1 & -1 & 1 & -1 & 1 & 1 & -1 \end{bmatrix}, \quad (C.7)$$

or, represented by ones and zeros,

$$H = \begin{bmatrix} 0 & 0 & 0 & 0 & 0 & 0 & 0 & 0 \\ 0 & 1 & 0 & 1 & 0 & 1 & 0 & 1 \\ 0 & 0 & 1 & 1 & 0 & 0 & 1 & 1 \\ 0 & 1 & 1 & 0 & 0 & 1 & 1 & 0 \\ 0 & 0 & 0 & 0 & 1 & 1 & 1 & 1 \\ 0 & 1 & 0 & 1 & 1 & 0 & 1 & 0 \\ 0 & 0 & 1 & 1 & 1 & 1 & 0 & 0 \\ 0 & 1 & 1 & 0 & 1 & 0 & 0 & 1 \end{bmatrix}, \quad (C.8)$$

One way to form the matrix is by multiplying matrices formed of the binary 'counting' matrix from 0 to 7,

$$H = AA^T = \begin{bmatrix} 0 & 0 & 0 \\ 0 & 0 & 1 \\ 0 & 1 & 0 \\ 0 & 1 & 1 \\ 1 & 0 & 0 \\ 1 & 0 & 1 \\ 1 & 1 & 0 \\ 1 & 1 & 1 \end{bmatrix} \begin{bmatrix} 0 & 0 & 0 & 0 & 1 & 1 & 1 & 1 \\ 0 & 0 & 1 & 1 & 0 & 0 & 1 & 1 \\ 0 & 1 & 0 & 1 & 0 & 1 & 0 & 1 \end{bmatrix}. \quad (C.9)$$

The matrix M can be factored in the same fashion, but not as simply. Form the first matrix B from the successive contents of the shift register, but bit reversed (from right to left) and in reverse order (from bottom to top). The original order is then preserved by shifting the rows of the matrix to bring the 3x3 identity matrix to the top,

$$B = \begin{bmatrix} 1 & 0 & 0 \\ 0 & 1 & 0 \\ 0 & 0 & 1 \\ 1 & 1 & 0 \\ 0 & 1 & 1 \\ 1 & 1 & 1 \\ 1 & 0 & 1 \end{bmatrix}. \quad (C.10)$$

Form the second matrix C from three shifted versions of the m-sequence

$$C = \begin{bmatrix} 1 & 0 & 0 & 1 & 1 & 1 & 0 \\ 0 & 1 & 0 & 0 & 1 & 1 & 1 \\ 1 & 0 & 1 & 0 & 0 & 1 & 1 \end{bmatrix}. \quad (C.11)$$

It is easy to verify that

$$BC = M. \quad (C.12)$$

Note that M, B, and C matrices must be expanded by a leading row and/or column of zeros to be of the proper size. The new matrices will be denoted with a prime. If mapping matrices can be found such that  $QA = B'$  and  $A^tP = C'$ , then the same matrices will map the Hadamard matrix to the m- sequence matrix

$$M' = B'C' = QAA^tP = QHP. \quad (C.13)$$

Recall that the correlation for the signal with the output code is given by multiplication, Eq. C.5, which now becomes

$$R'_{sm} = M'S'. \quad (C.14)$$

(S' because the leading zeros must be added. ) Combining Eqs. C.13 and C.14 results in

$$R'_{sm} = QHPS'. \quad (C.15)$$

This gives the signal correlation that is required. The initial entry is removed to change  $R'_{sm}$  to  $R_{sm}$ .

## C.4 Input and Output Vector Order Permutation

The matrices P and Q must be found such that  $QA = B'$  and  $A^tP = C'$ . A natural index for each row or column is its equivalent octal value since the values range from 0 to 7 and do not repeat as shown in Figure C.4.

The permutation matrices will have ones in the following positions:

$$\begin{array}{ll} \text{Q row} & 0 \ 1 \ 2 \ 3 \ 4 \ 5 \ 6 \ 7 \\ \text{Q column} & 0 \ 4 \ 2 \ 1 \ 6 \ 3 \ 7 \ 5 \\ \\ \text{P row} & 0 \ 5 \ 2 \ 1 \ 4 \ 6 \ 7 \ 3 \\ \text{P column} & 0 \ 1 \ 2 \ 3 \ 4 \ 5 \ 6 \ 7. \end{array} \quad (C.16)$$

These indices are important. With the indices, the matrices do not have to be constructed. The 'multiplication' by the permutation matrices is accomplished by shuffling the order of the signal vector, rather than direct multiplication, as shown in Figure C.2. Note that no multiplications are required, only the reordering. For a given code the permutations can be evaluated once and the result stored as an index array to be applied to each vector.

$$\begin{array}{lcl}
 A = \begin{bmatrix} 0 & 0 & 0 \\ 0 & 0 & 1 \\ 0 & 1 & 0 \\ 0 & 1 & 1 \\ 1 & 0 & 0 \\ 1 & 0 & 1 \\ 1 & 1 & 0 \\ 1 & 1 & 1 \end{bmatrix} & \begin{matrix} 0 \\ 1 \\ 2 \\ 3 \\ 4 \\ 5 \\ 6 \\ 7 \end{matrix} & B' = \begin{bmatrix} 0 & 0 & 0 \\ 1 & 0 & 0 \\ 0 & 1 & 0 \\ 0 & 0 & 1 \\ 1 & 1 & 0 \\ 0 & 1 & 1 \\ 1 & 1 & 1 \\ 1 & 0 & 1 \end{bmatrix} \begin{matrix} 0 \\ 4 \\ 2 \\ 1 \\ 6 \\ 3 \\ 7 \\ 5 \end{matrix} \\
 A^T = \begin{bmatrix} 0 & 0 & 0 & 0 & 1 & 1 & 1 & 1 \\ 0 & 0 & 1 & 1 & 0 & 0 & 1 & 1 \\ 0 & 1 & 0 & 1 & 0 & 1 & 0 & 1 \end{bmatrix} & C' = \begin{bmatrix} 0 & 1 & 0 & 0 & 1 & 1 & 1 & 0 \\ 0 & 0 & 1 & 0 & 0 & 1 & 1 & 1 \\ 0 & 1 & 0 & 1 & 0 & 0 & 1 & 1 \end{bmatrix} & \\
 0 & 1 & 2 & 3 & 4 & 5 & 6 & 7 & 0 & 5 & 2 & 1 & 4 & 6 & 7 & 3
 \end{array}$$

Figure C.2: Indices formed from matrix octal equivalents.

## C.5 The Fast Hadamard Transform

There exists an efficient method of performing the multiplication by the Hadamard matrix. If a vector is multiplied by the Hadamard matrix (the normal Hadamard matrix of  $\{+1, -1\}$ ). The result is a vector of sums of all the components of the vector with various + and - weighting. Define a vector  $V$  such that

$$V = \begin{bmatrix} a \\ b \\ c \\ d \\ e \\ f \\ g \\ h \end{bmatrix}. \quad (C.17)$$

After multiplying this by the Hadamard matrix the vector becomes

$$HV = \begin{bmatrix} 1 & 1 & 1 & 1 & 1 & 1 & 1 & 1 \\ 1 & -1 & 1 & -1 & 1 & -1 & 1 & -1 \\ 1 & 1 & -1 & -1 & 1 & 1 & -1 & -1 \\ 1 & -1 & -1 & 1 & 1 & -1 & -1 & 1 \\ 1 & 1 & 1 & 1 & -1 & -1 & -1 & -1 \\ 1 & -1 & 1 & -1 & -1 & 1 & -1 & 1 \\ 1 & 1 & -1 & -1 & -1 & -1 & 1 & 1 \\ 1 & -1 & -1 & 1 & -1 & 1 & 1 & -1 \end{bmatrix} \begin{bmatrix} a \\ b \\ c \\ d \\ e \\ f \\ g \\ h \end{bmatrix} \quad (C.18)$$

$$HV = \begin{bmatrix} a + b + c + d + e + f + g + h \\ a - b + c - d + e - f + g - h \\ a + b - c - d + e + f - g - h \\ a - b - c + d + e - f - g + h \\ a + b + c + d - e - f - g - h \\ a - b + c - d - e + f - g + h \\ a + b - c - d - e - f + g + h \\ a - b - c + d - e + f + g - h \end{bmatrix}. \quad (C.19)$$

When calculating correlations, let  $a = 0$  so that no new information is added. The zeroth position result is the sum of all the elements of the code and is therefore equal to the DC pedestal. This pedestal can be removed by subtracting this sum of all elements, or not, depending on the application. Compare this result to the result using a flow diagram identical to the pro-

<u>P column</u>	<u>P row</u>	<u>S' becomes</u>	<u>PS'</u>
0	0	$S_0$	$G_0$
1	5	$S_1$	$G_5$
2	2	$S_2$	$G_2$
3	1	$S_3$	$G_1$
4	4	$S_4$	$G_4$
5	6	$S_5$	$G_6$
6	7	$S_6$	$G_7$
7	3	$S_7$	$G_3$

<u>O row</u>	<u>O column</u>	<u>F=HPS' becomes</u>	<u>R=OHPS'</u>
0	0	$F_0$	$R_0$
1	4	$F_4$	$R_1$
2	2	$F_2$	$R_2$
3	1	$F_1$	$R_3$
4	6	$F_6$	$R_4$
5	3	$F_3$	$R_5$
6	7	$F_7$	$R_6$
7	5	$F_5$	$R_7$

Table C.2: Re-ordering of input and output vectors according to the permutation matrices P and Q. For the input vector, let  $G = PS'$  and for the output vector, let  $F = HPS'$ .

cedure used with the Fast Fourier Transform, except that all the 'twiddle' factors are equal to one, Figure C.3.

The result of the Fast Hadamard Transform is the same as for multiplication. The algorithm used for the Fast Fourier Transform is trivialized in this case - there is no bit reversal or multiplication by a phase factor. Because the method requires only additions, the exact computational speed increase is difficult to calculate. (The speed improvement for FFT over DFT is usually calculated by comparing the number of multiplications required) The 'multiplication' by P and Q has been replaced by reordering, so that there is no multiplication required. The speed of execution now depends on other statements in the program as well as the correlation because loop increments and tests for completion may take as long as the additions.

## C.6 Using the Reverse Code

The permutation matrices for the reverse code are found in a slightly different way. The matrix B is found from the contents of the shift register directly, not bit reversed and in reverse order as for the forward code. The matrix C is formed by shifting the code to the left (vice right). The permutation indices are determined and used in the same fashion as before.

## C.7 Correlation Procedure

The procedure for performing the correlation can now be summarized in five straightforward steps:

1. Augment the signal vector S by adding a zero in the zeroth position.
2. Permute the vector according to P.
3. Perform the Fast Hadamard Transform.
4. Permute the resulting vector according to Q.
5. Remove the zeroth entry.



### Basic Element

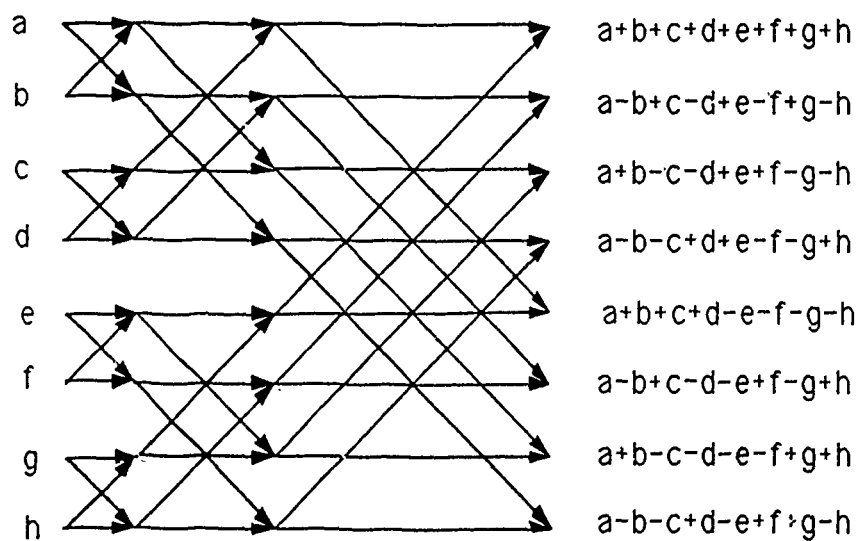
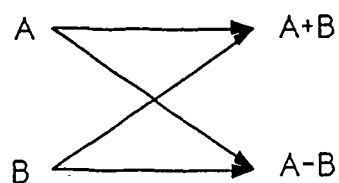


Figure C.3: Basic Fast Hadamard Transform element for cascading additions and the full diagram for an eight point FHT.

## C.8 Example

Consider the first and third rows of the m-sequence matrix as input signals:

first		third											
1	0	0	1	1	1	0	1	0	1	0	0	1	1

Transform to  $\{-1, +1\}$ . The result is the signal vector  $S$  as would be received.

-1	1	1	-1	-1	-1	1	-1	1	-1	1	1	-1	-1
----	---	---	----	----	----	---	----	---	----	---	---	----	----

Add beginning 0

0	-1	1	1	-1	-1	-1	1	0	-1	1	-1	1	1	-1	-1
---	----	---	---	----	----	----	---	---	----	---	----	---	---	----	----

Permute according to P

0	1	1	1	-1	-1	-1	-1	0	-1	1	-1	1	-1	1	-1
---	---	---	---	----	----	----	----	---	----	---	----	---	----	---	----

Perform Fast Hadamard Transform (can be done in this case by comparing to rows in the Hadamard matrix for a match)

-1	-1	-1	-1	7	-1	-1	-1	-1	7	-1	-1	-1	-1	-1	-1
----	----	----	----	---	----	----	----	----	---	----	----	----	----	----	----

Permute according to Q

-1	7	-1	-1	-1	-1	-1	-1	-1	-1	-1	7	-1	-1	-1	-1
----	---	----	----	----	----	----	----	----	----	----	---	----	----	----	----

Remove the zeroth element

7	-1	-1	-1	-1	-1	-1	-1	-1	7	-1	-1	-1	-1
---	----	----	----	----	----	----	----	----	---	----	----	----	----

As expected, the correlation produces a peak in the first and third positions, respectively.

## C.9 Summary

When performing the correlation of a signal and the m-sequence using the Fast Hadamard Transform and a quadrature demodulation system the real and imaginary components of the signal are correlated separately and later combined for magnitude and phase. Note that the FHT only works on one

sample per digit of the m-sequence in the signal. For improved accuracy in estimating the arrival time of the impulse, it is valuable to sample at a higher frequency. This may also allow digital filtering. The sampling frequency should be an integer multiple of the code clock rate (also known as the "chip" rate). The data samples should then be decimated into records at the code clock frequency so that they are again one sample per digit. After the FHT correlation the data interleaves are recombined to their original positions. For example, if a code clocked at 16 Hz is sampled at 64 Hz, then 4 separate correlations will have to be performed on each of the in-phase and quadrature channels. The FHT correlation is still much faster than using DFT or FFT methods, or matrix multiplies. The result of the FHT correlation in the case of data sampled at higher than the code clock rate is not the same as for conventional correlation. In an ideal case, each of the interleaves will produce an output peak of equal magnitude, resulting in a 'flat-topped' correlation peak, vice a 'pointy' correlation peak. The estimation of travel time must look for this shape, rather than the 'point'.

## Appendix D

# Additional Data for Station J

### D.1 Hadamard Transformed Acoustic Signal

Signal Magnitude Squared Station J 14DEC88

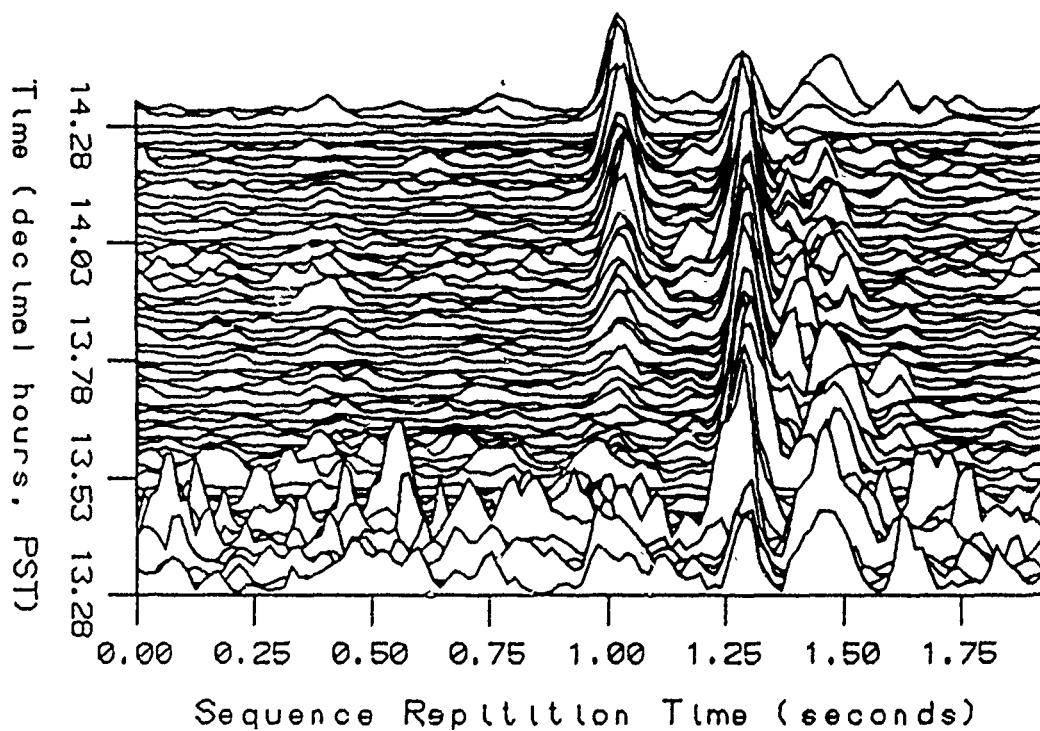


Figure D.1: Tomographic signal, coherently averaged 16 times then magnitude squared. Station J, 1317 to 1419 14DEC88. High ambient noise at the start is from the R/V Point Sur after deploying buoy.

Signal Magnitude Squared Station J 14DEC88

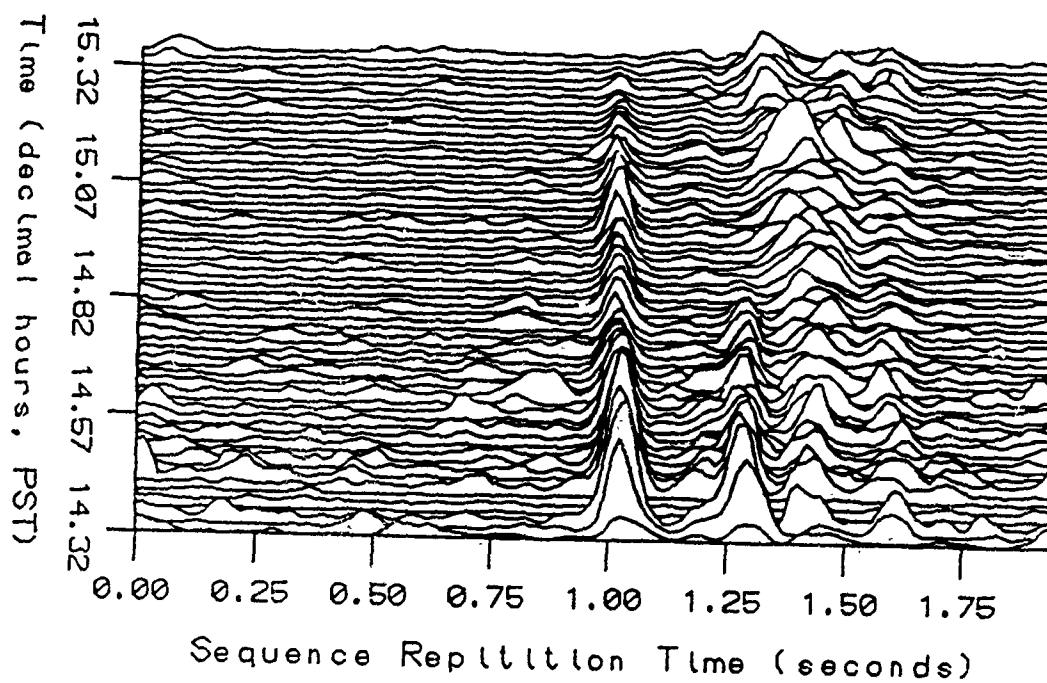


Figure D.2: Tomographic signal, coherently averaged 16 times then magnitude squared. Station J, 1419to 1521 14DEC88.

Signal Magnitude Squared Station J 14DEC88

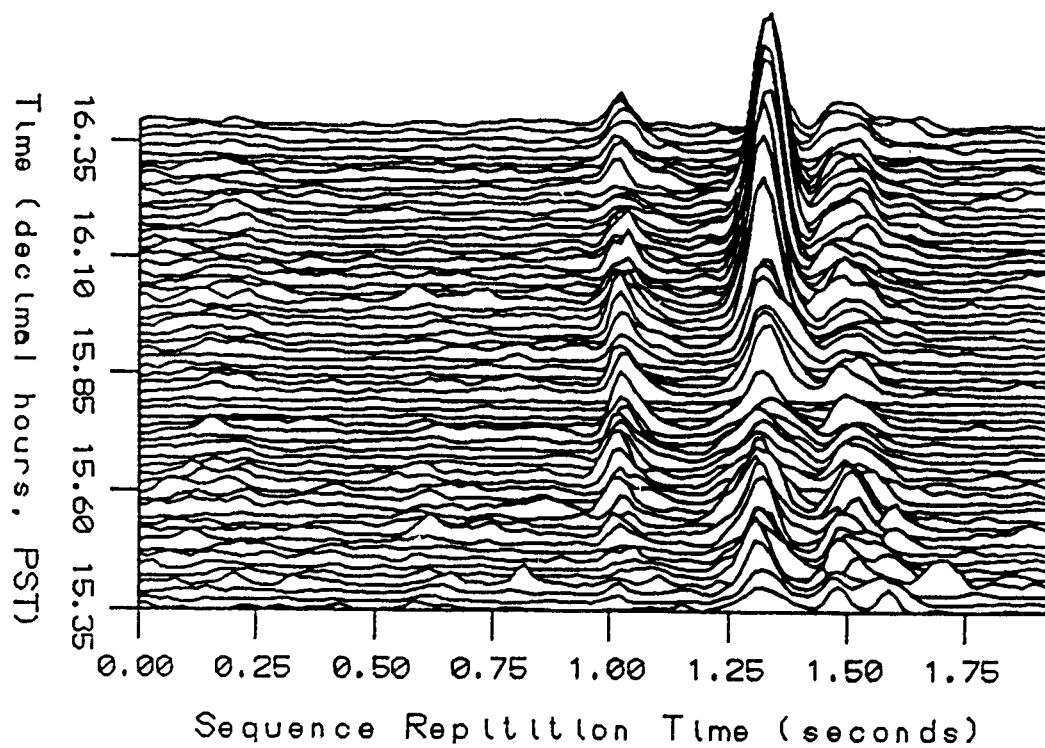


Figure D.3: Tomographic signal, coherently averaged 16 times then magnitude squared. Station J, 1521 to 1623 14DEC88.

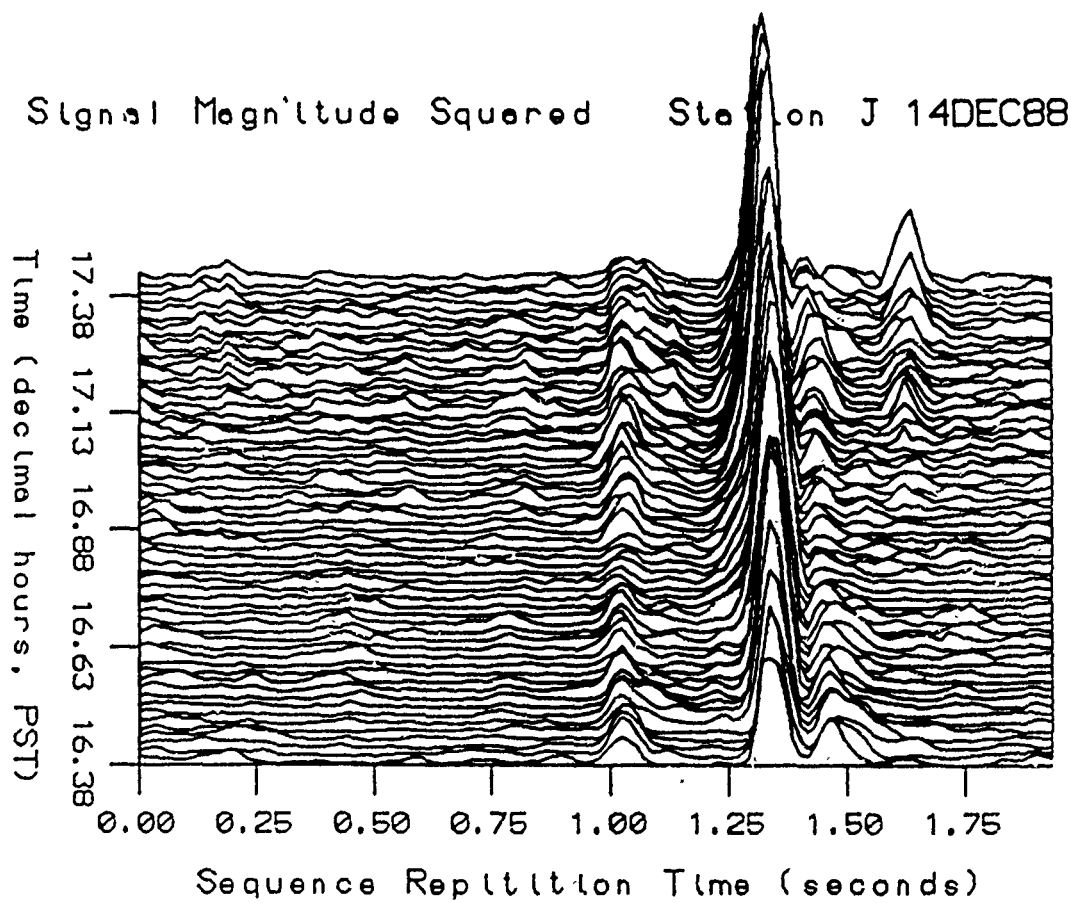


Figure D.4: Tomographic signal, coherently averaged 16 times then magnitude squared. Station J, 1623 to 1725 14DEC88.



Signal Magnitude Squared Station J 14DEC88

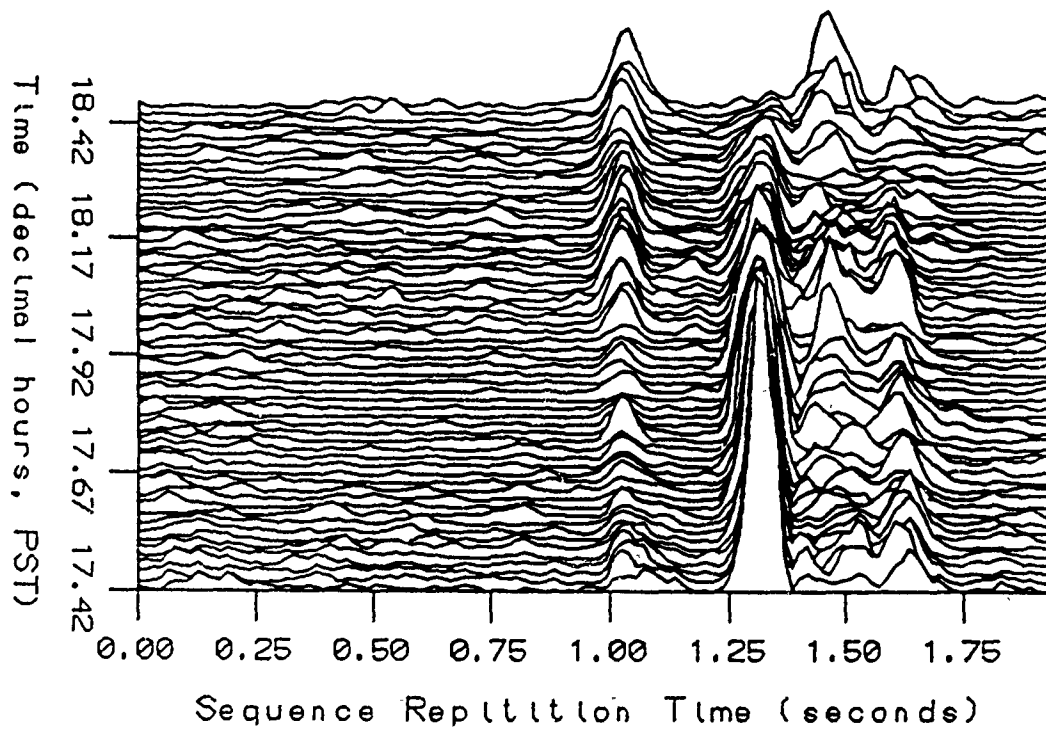


Figure D.5: Tomographic signal, coherently averaged 16 times then magnitude squared. Station J, 1725 to 1827 14DEC88.

Signal Magnitude Squared Station J 14DEC88

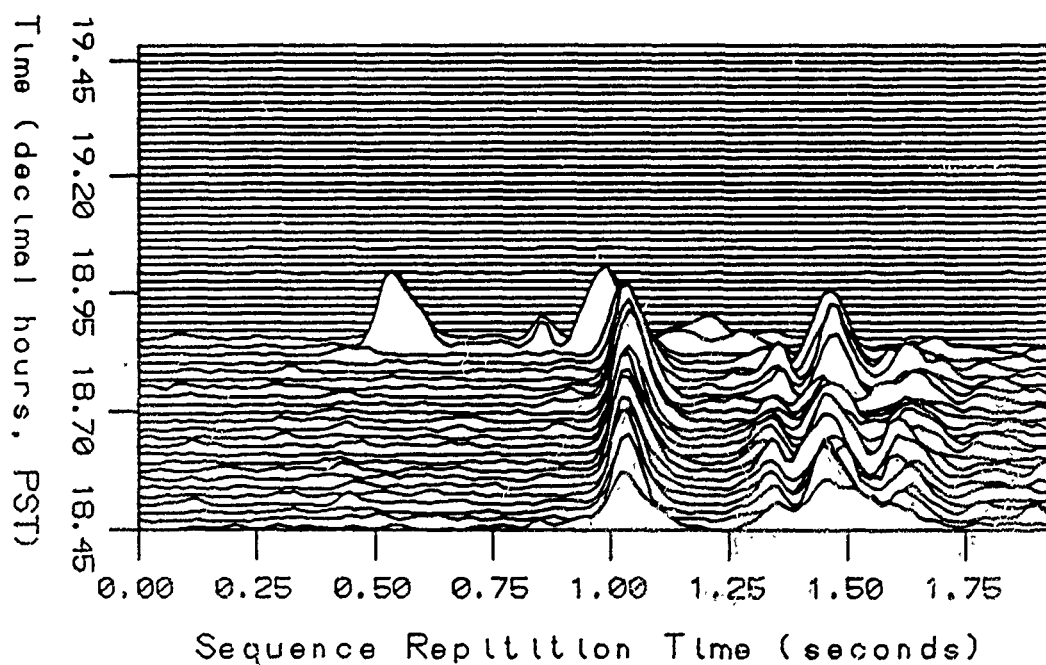


Figure D.6: Tomographic signal, coherently averaged 16 times then magnitude squared. Station J, 1827 to 1929 14DEC88. Signal cutoff is due to tape change.

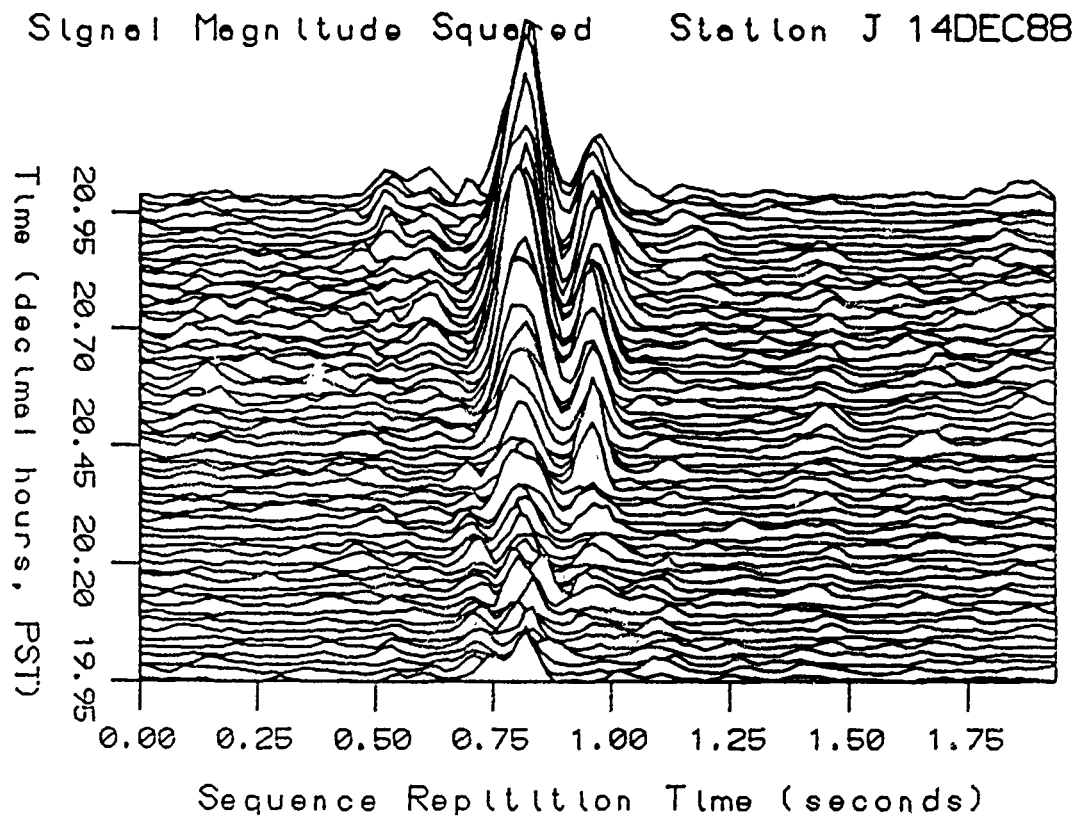


Figure D.7: Tomographic signal, coherently averaged 16 times then magnitude squared. Station J, 1957 to 2059 14DEC88. The previous hour is included as Figure 12 on page 58. Note that the arrival structure is shifted for data from a new tape.

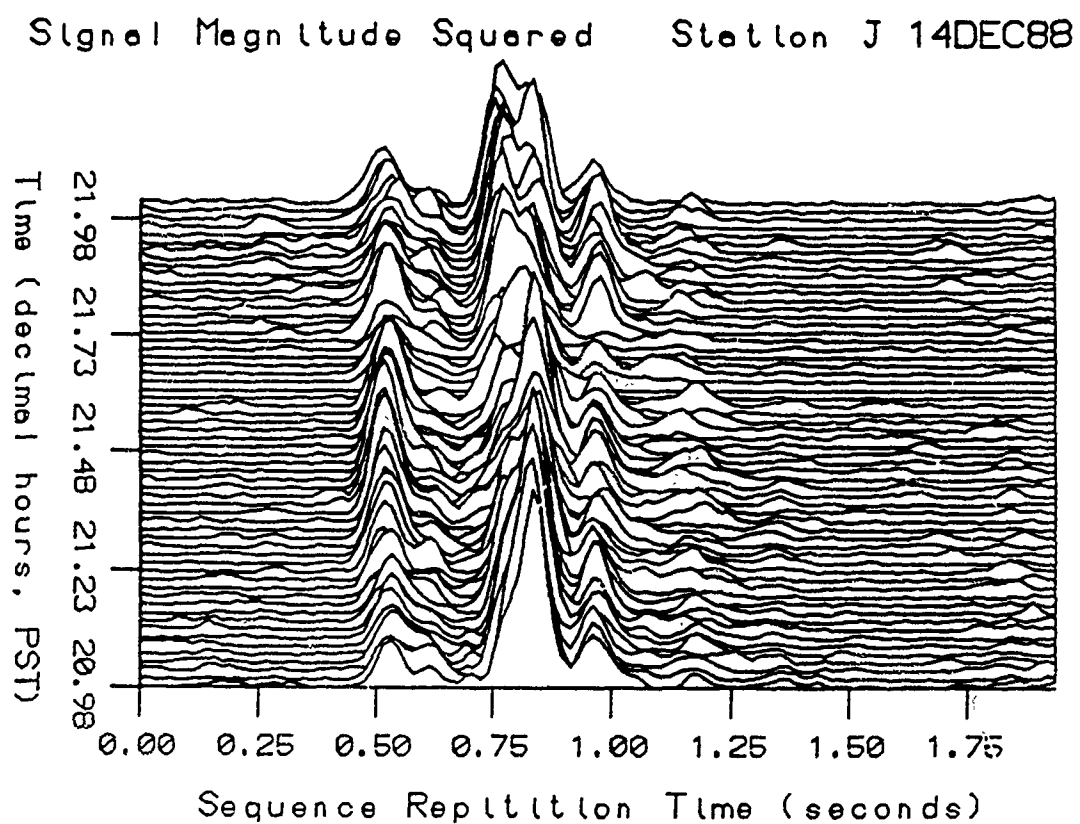


Figure D.8: Tomographic signal, coherently averaged 16 times then magnitude squared. Station J, 2059 to 2201 14DEC88.

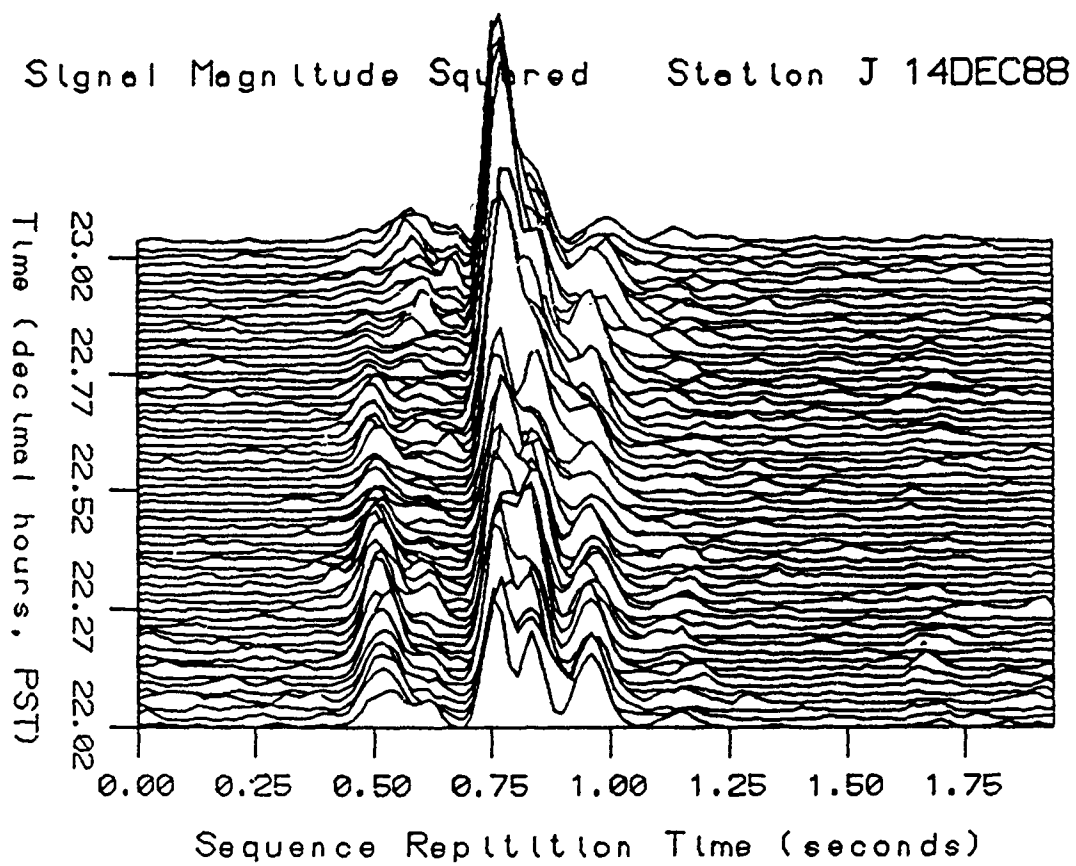


Figure D.9: Tomographic signal, coherently averaged 16 times then magnitude squared. Station J, 2201 to 2303 14DEC88.

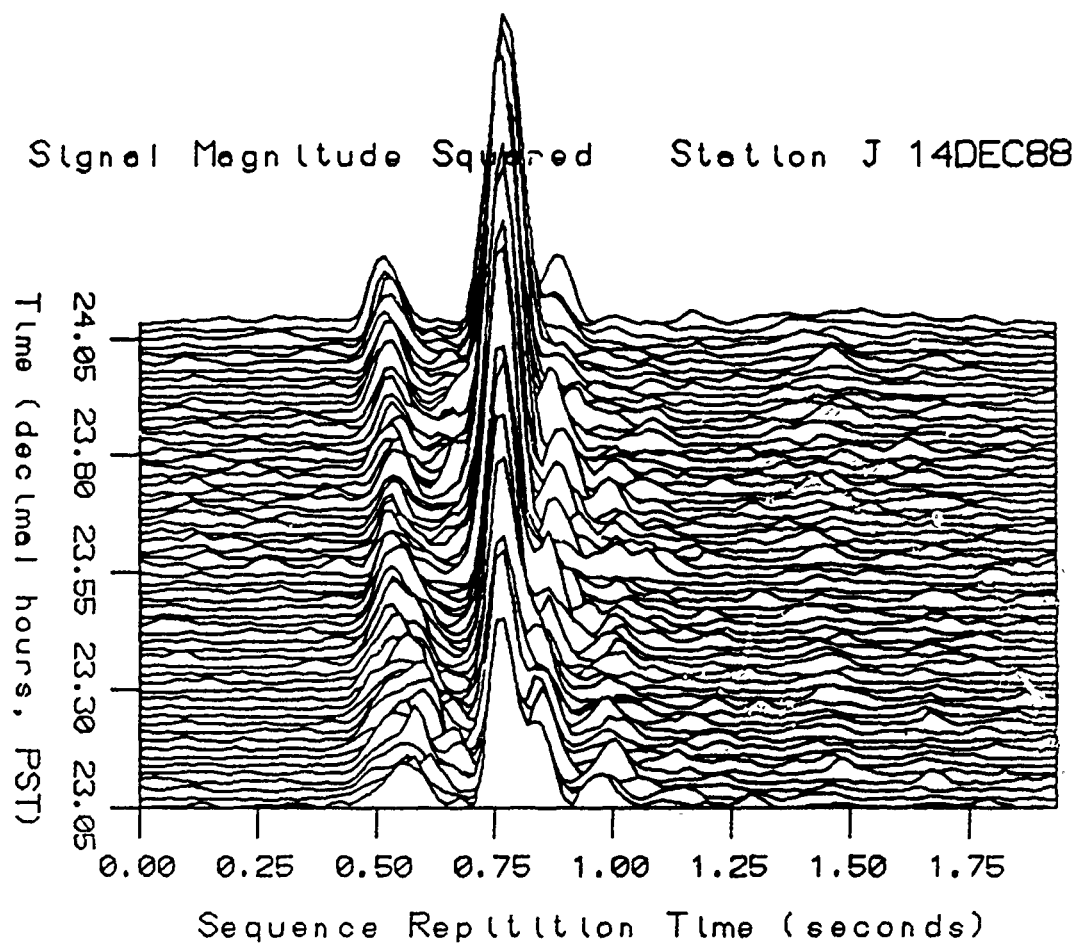


Figure D.10: Tomographic signal, coherently averaged 16 times then magnitude squared. Station J, 2303 14DEC88 to 0005 15DEC88.

Signal Magnitude Squared Station J 14DEC88

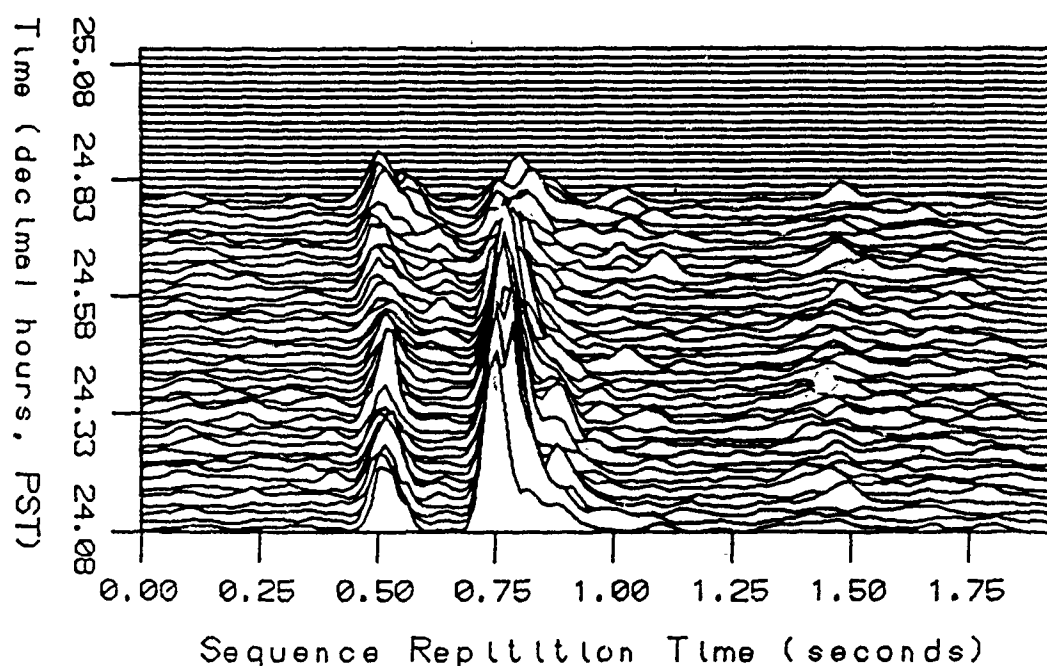


Figure D.11: Tomographic signal, coherently averaged 16 times then magnitude squared. Station J, 0005 to 0107 15DEC88. Note that computer generated time scale is extended past 0000 for convenience in processing. The reason for signal cutoff is that the end of the tape was reached.

Signal Magnitude Squared Station J 15DEC88

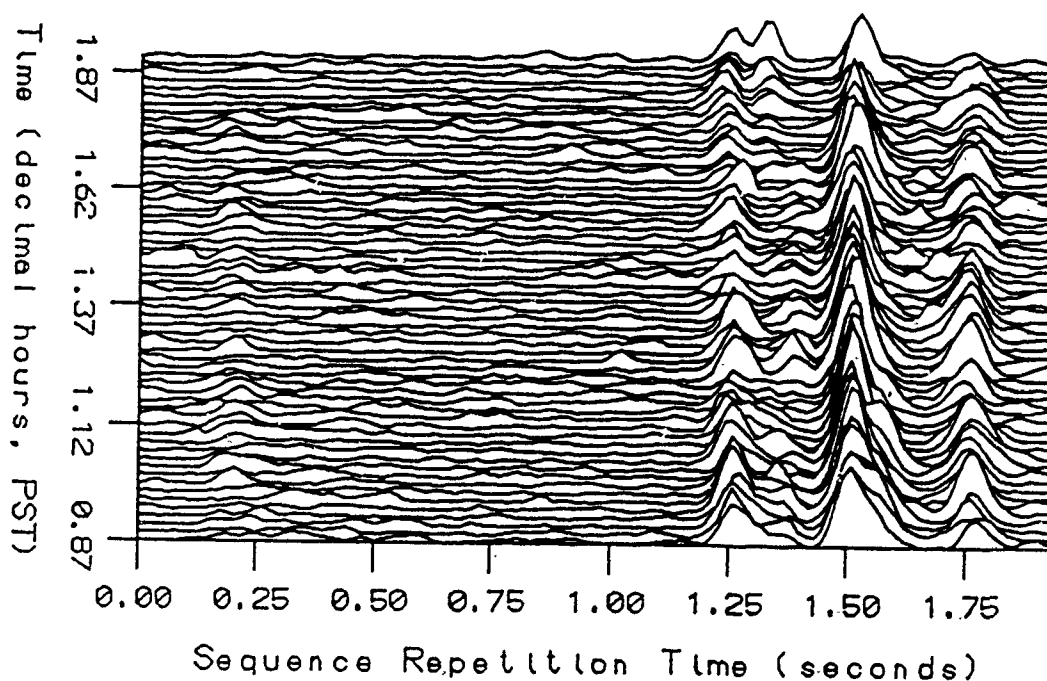


Figure D.12: Tomographic signal, coherently averaged 16 times then magnitude.squared. Station J, 0052 to 0154 15DEC88. Note that the arrival structure is shifted because of the start of a new tape.



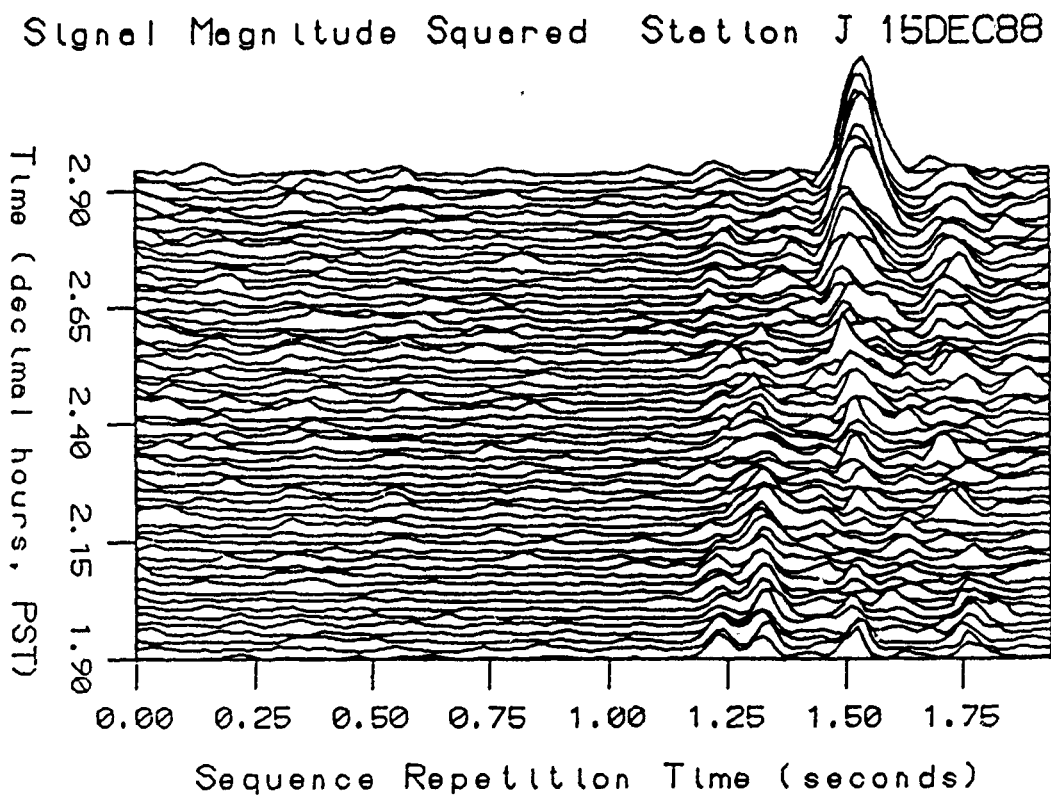


Figure D.13: Tomographic signal, coherently averaged 16 times then magnitude squared. Station J, 0154 to 0256 15DEC88.

Signal Magnitude Squared Station J 15DEC88

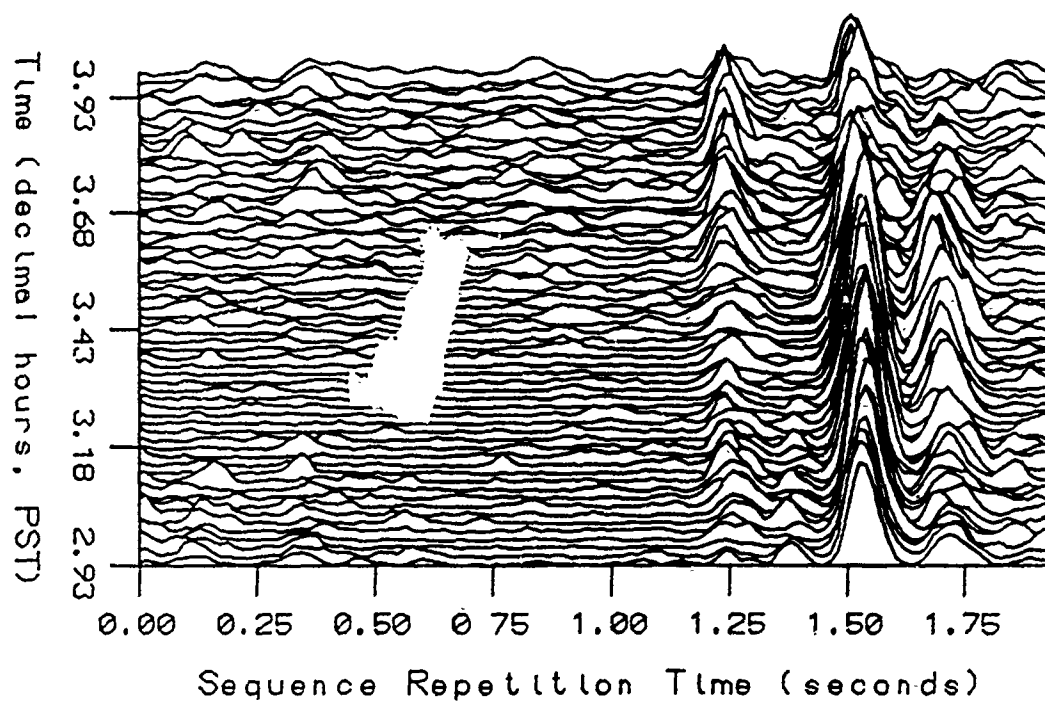


Figure D.14: Tomographic signal, coherently averaged 16 times then magnitude squared. Station J, 0256 to 0358 15DEC88.

Signal Magnitude Squared Station J 15DEC88

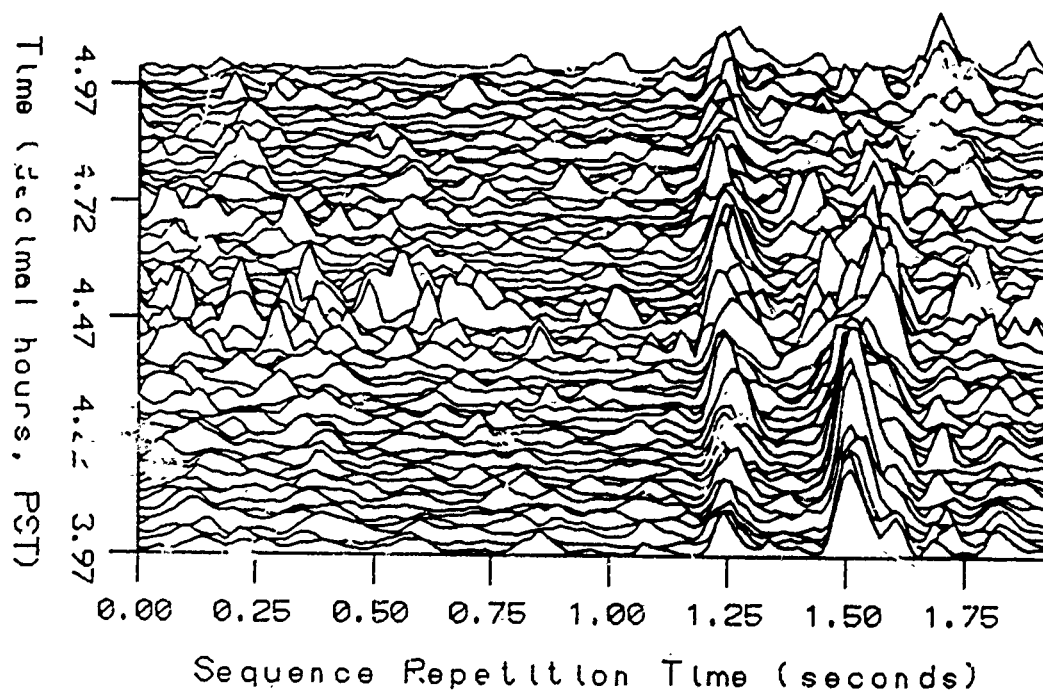


Figure D.15: Tomographic signal, coherently averaged 16 times then magnitude squared. Station J, 0358 to 0500 15DEC88. High scattering and ambient noise were present at this time because of high winds (the worst windstorm of the year to hit the central-California coast).

Signal Magnitude Squared Station J 15DEC88

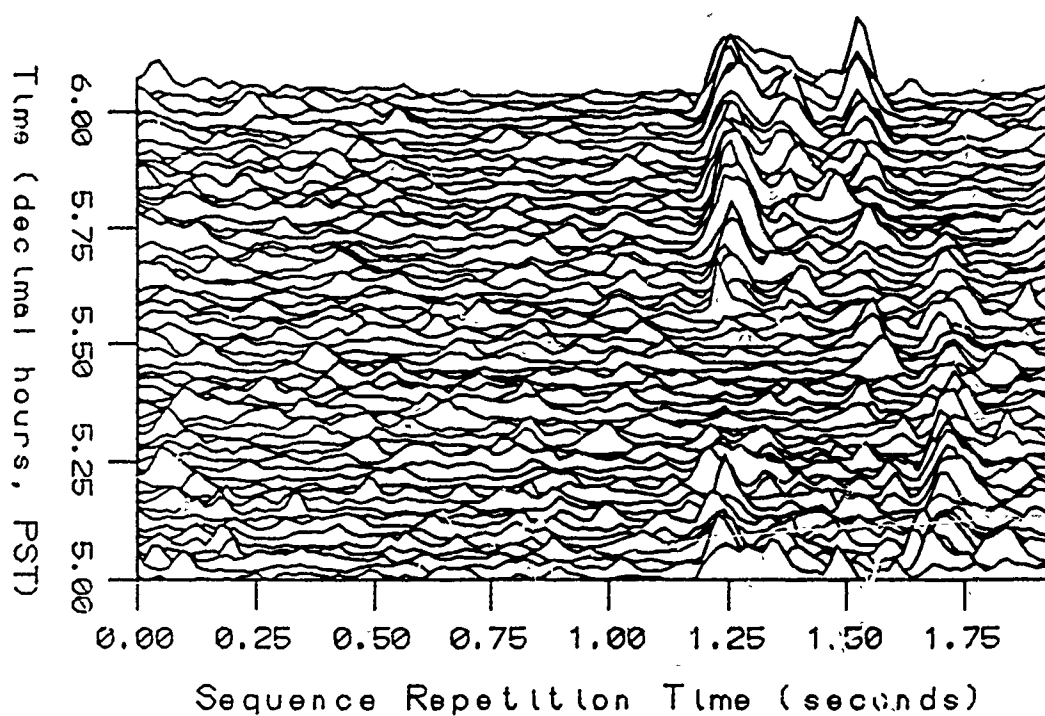


Figure D.16: Tomographic signal, coherently averaged 16 times then magnitude squared. Station J, 0500 to 0602 15DEC88. High ambient noise and high scattering continue from windstorm.

Signal Magnitude Squared Station J 15DEC88

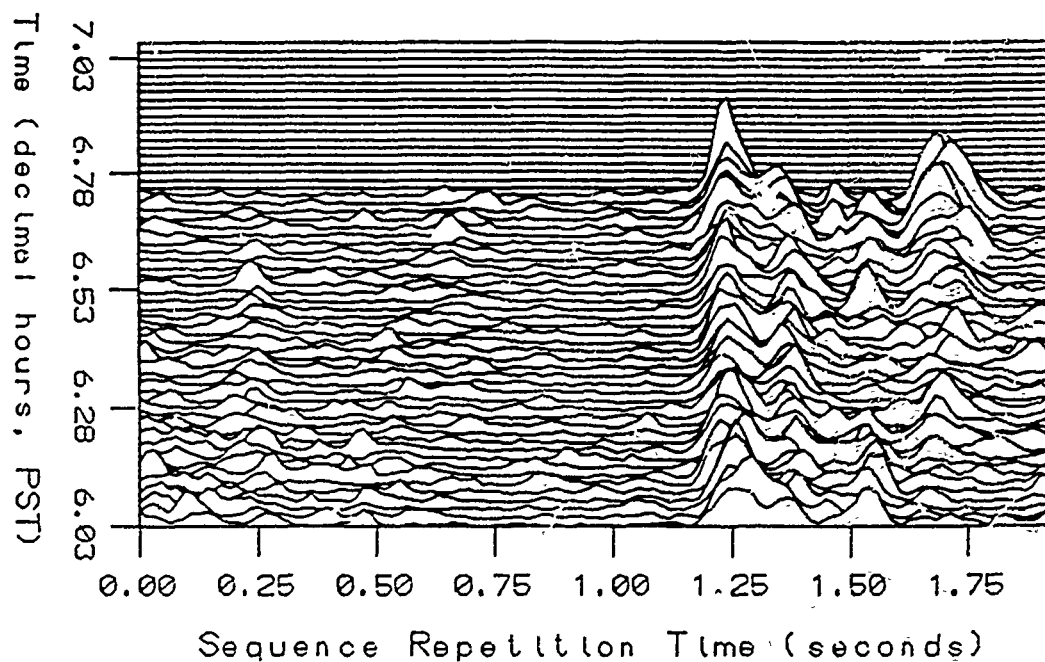


Figure D.17: Tomographic signal, coherently averaged 16 times then magnitude squared. Station J, 0602 to 0704 15DEC88. The reason for signal cutoff is that the end of the tape was reached.

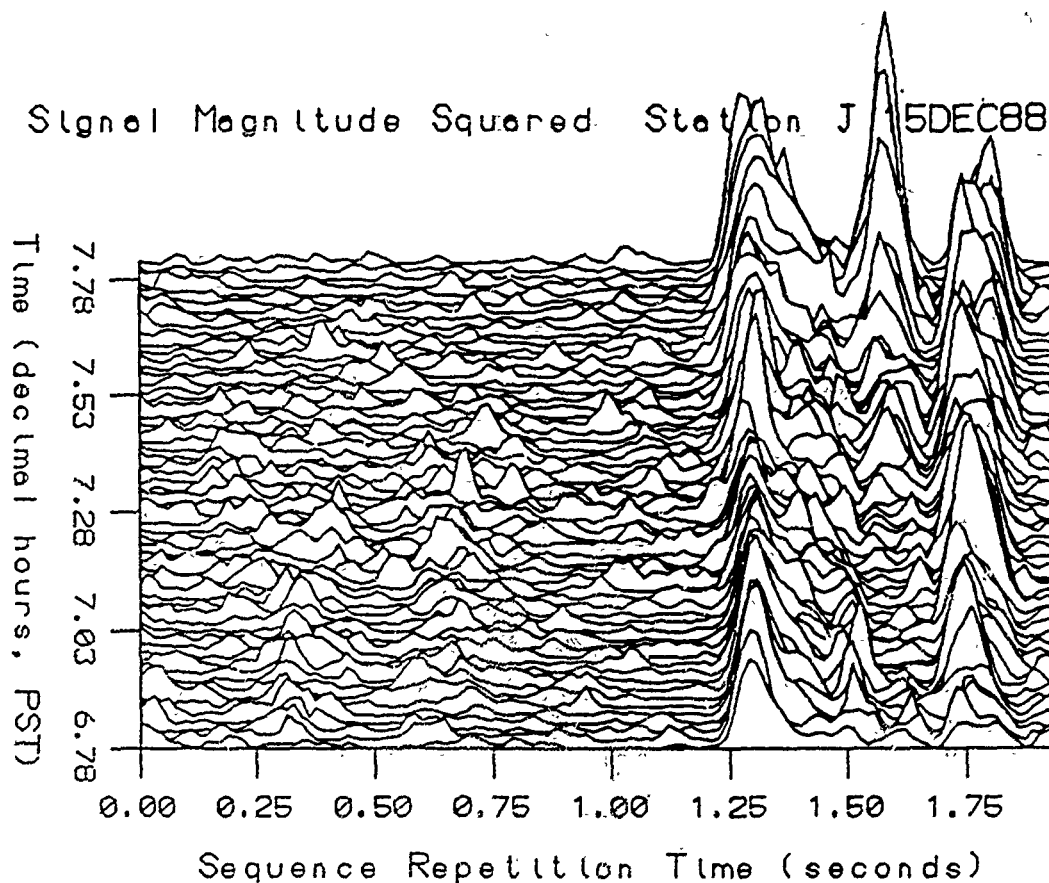


Figure D.18: Tomographic signal, coherently averaged 16 times then magnitude squared. Station J, 0647 to 0749 15DEC88. The reason for the increased amplitude is unknown. Note that the arrival structure is shifted at the start of the new tape.

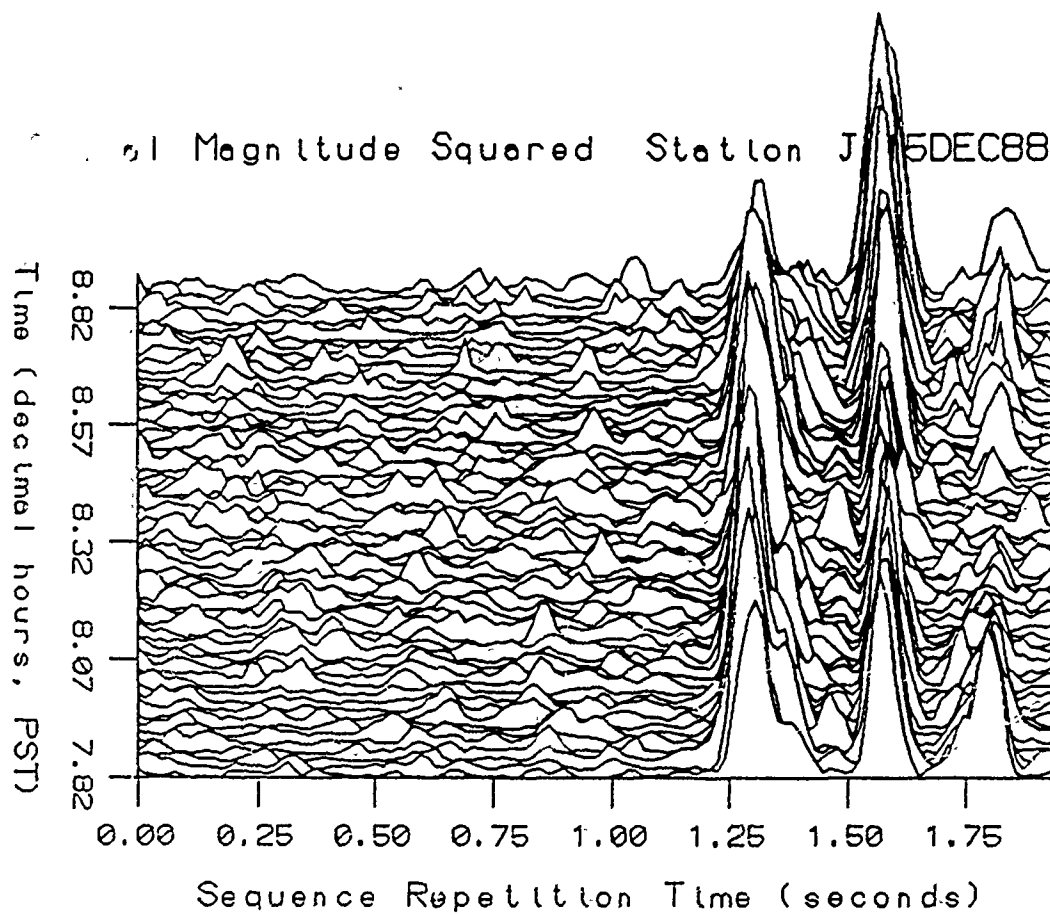


Figure D.19: Tomographic signal, coherently averaged 16 times then magnitude squared. Station J, 0749 to 0851 15DEC88.

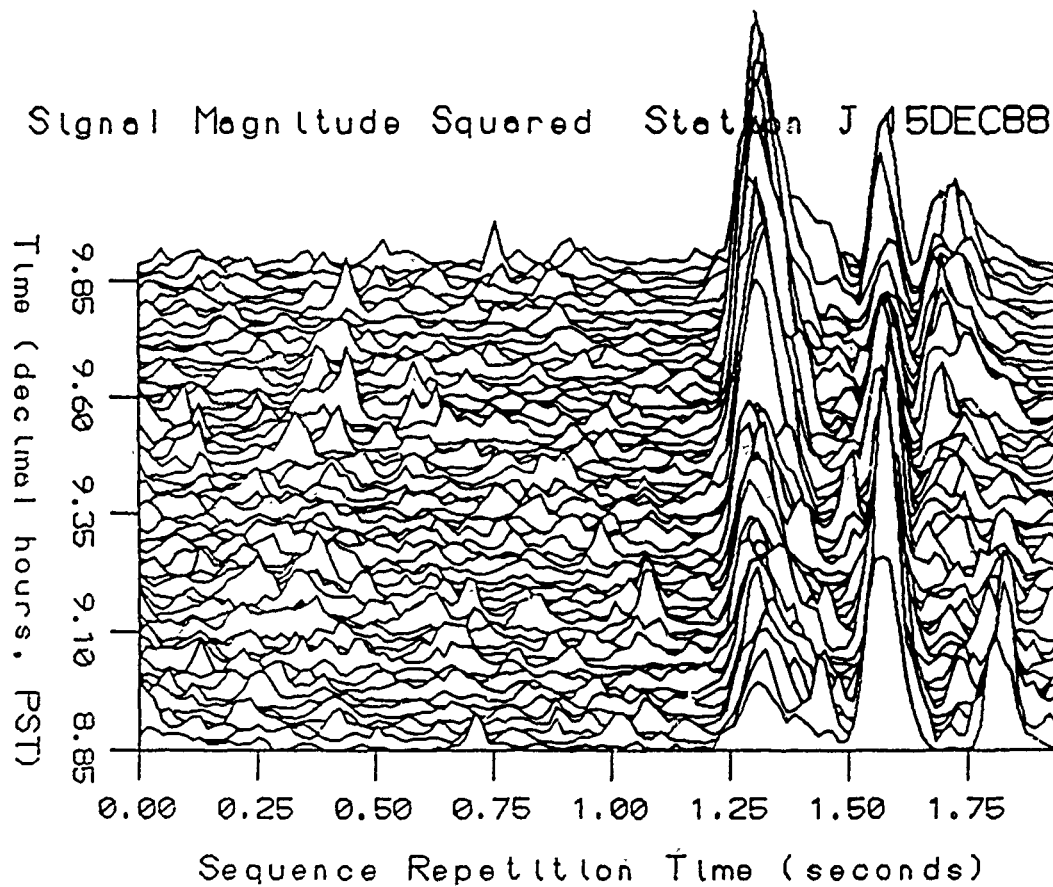


Figure D.20: Tomographic signal, coherently averaged 16 times then magnitude squared. Station J, 0851 to 0953 15DEC88.



Signal Magnitude Squared Station J 15DEC88

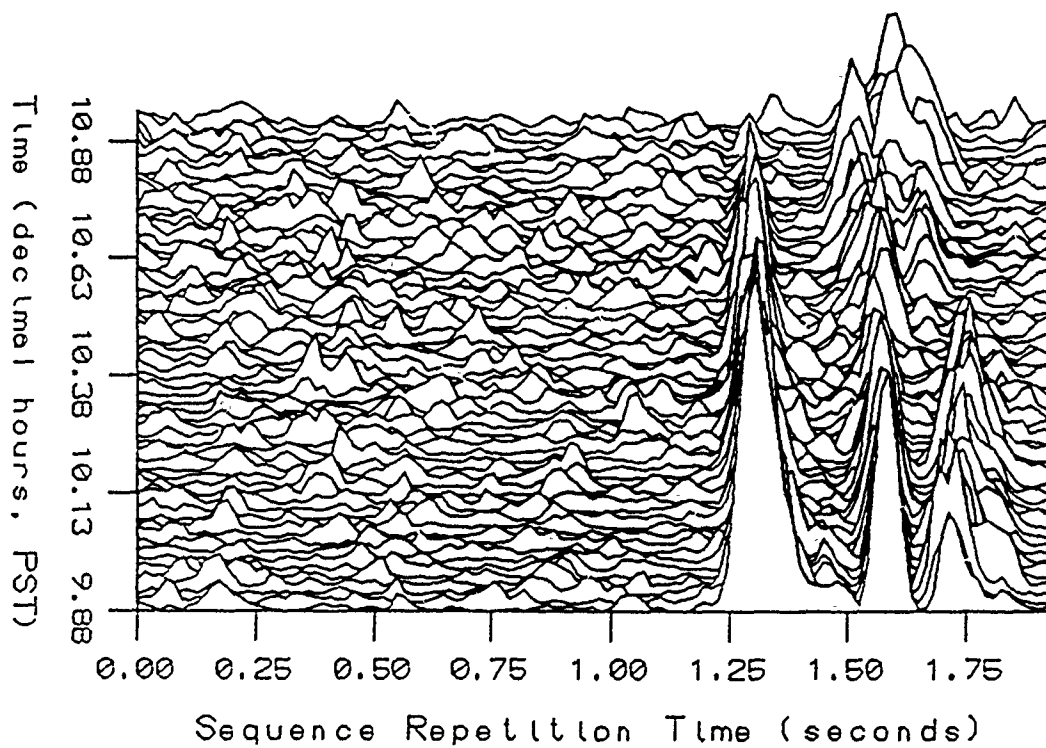


Figure D.21: Tomographic signal, coherently averaged 16 times then magnitude squared. Station J, 0953 to 1055 15DEC88.

Signal Magnitude Squared Station J 15DEC88

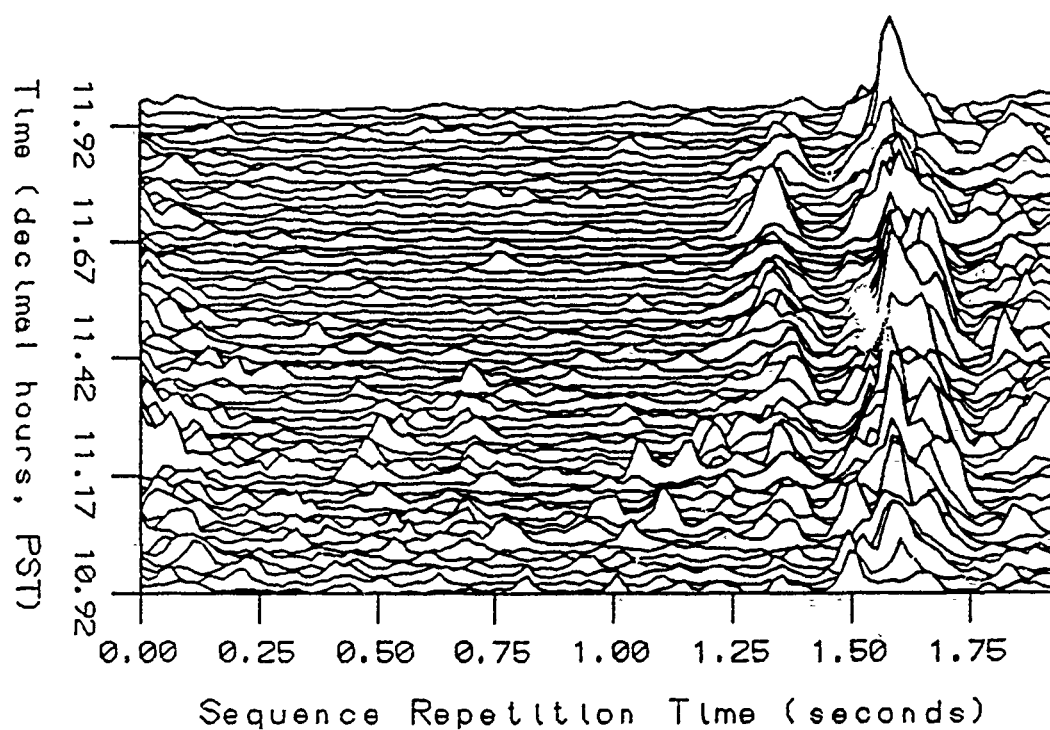


Figure D.22: Tomographic signal, coherently averaged 16 times then magnitude squared. Station J, 1055 to 1157 15DEC88.

Signal Magnitude Squared Station J 15DEC88

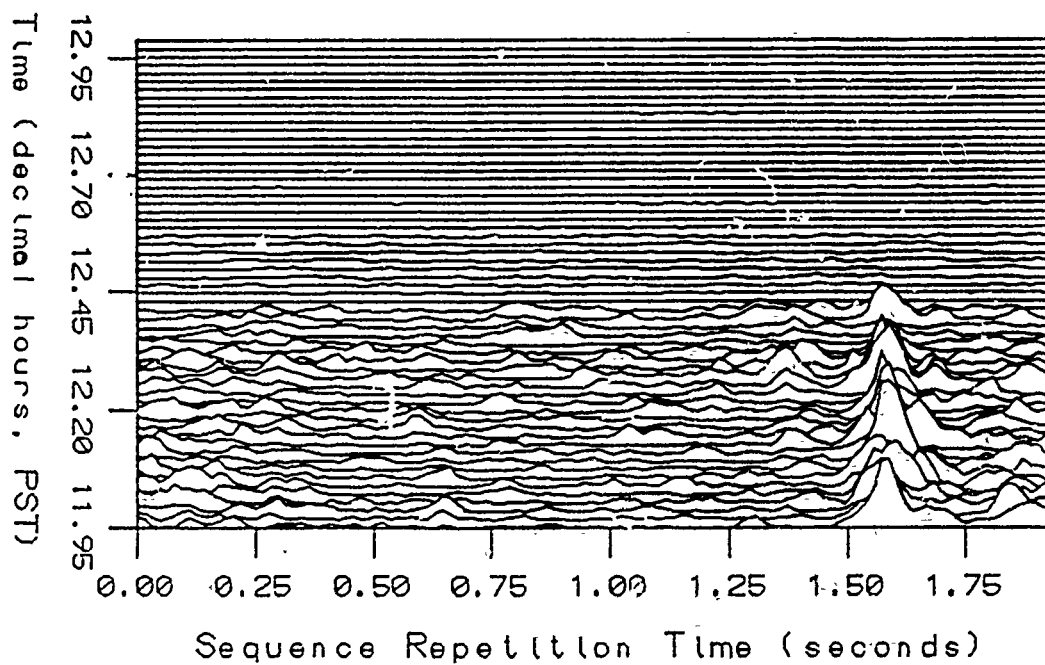


Figure D.23: Tomographic signal, coherently averaged 16 times then magnitude squared. Station J, 1157 to 1259 15DEC88. The reason for the signal cutoff is that the end of the tape was reached.

Signal Magnitude Squared Station J 15DEC88

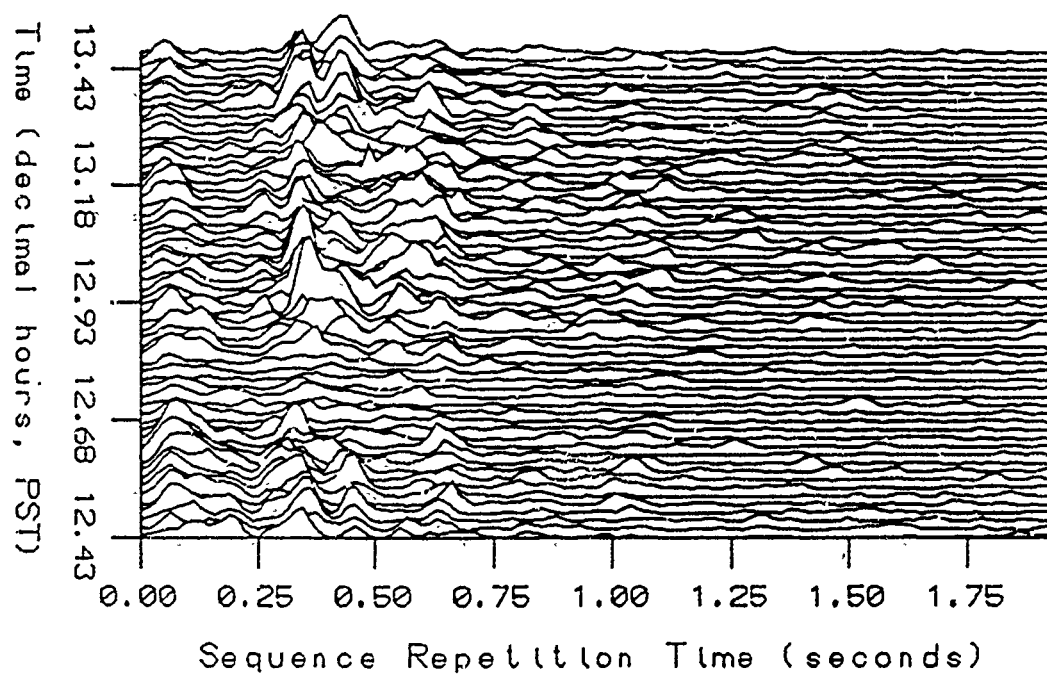


Figure D.24: Tomographic signal, coherently averaged 16 times then magnitude squared. Station J, 1226 to 1328 15DEC88. Note that the arrival structure is shifted at the start of the new tape.

Signal Magnitude Squared Station J 15DEC88

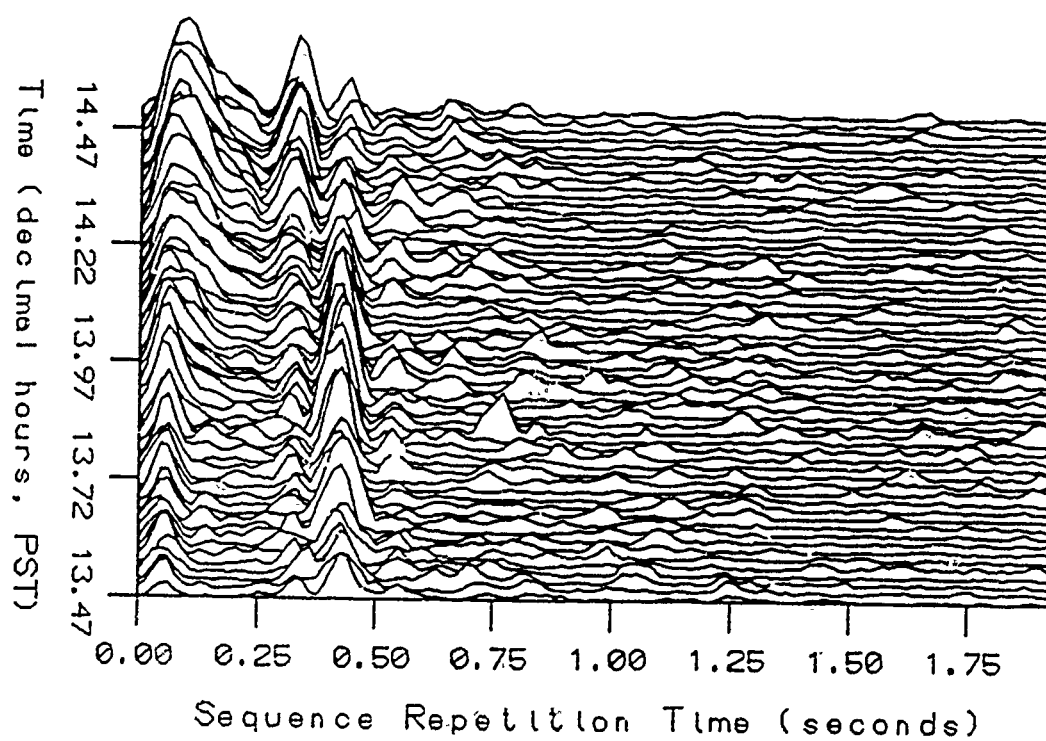


Figure D.25: Tomographic signal, coherently averaged 16 times then magnitude squared. Station J, 1328 to 1430 15DEC88.

Signal Magnitude Squared Station J 15DEC88

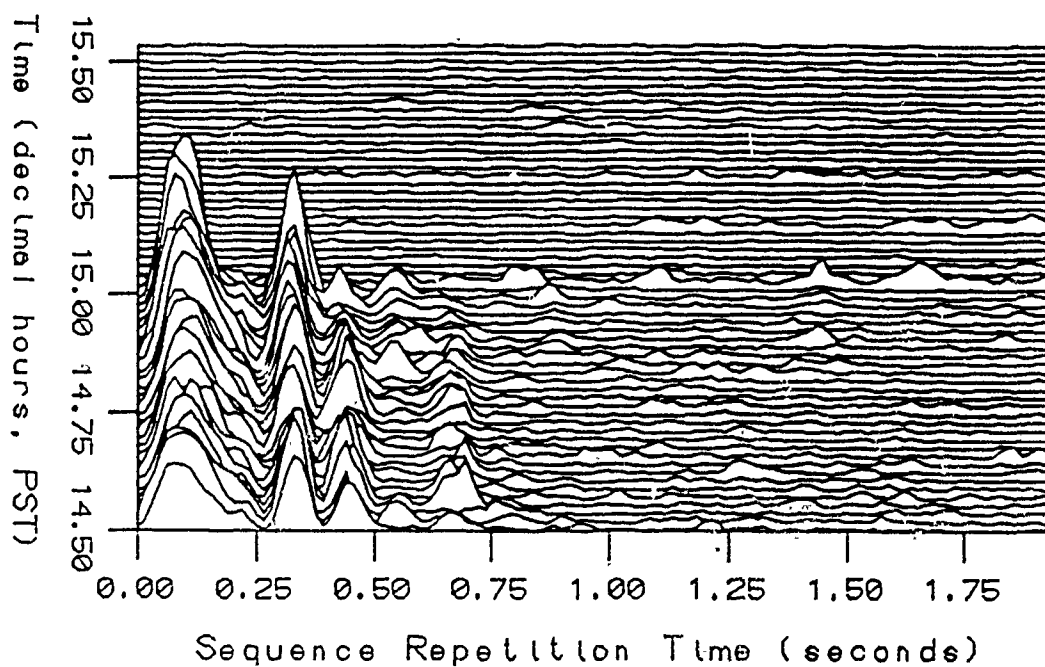


Figure D.26: Tomographic signal, coherently averaged 16 times then magnitude squared. Station J, 1430 to 1532 15DEC88. Signal cutoff is due to buoy failure.

## **D.2 Arrival Time and Surface Wave Spectra**

**Arrival Time Power Spectrum  
Station J 14DEC88 2107 PST**

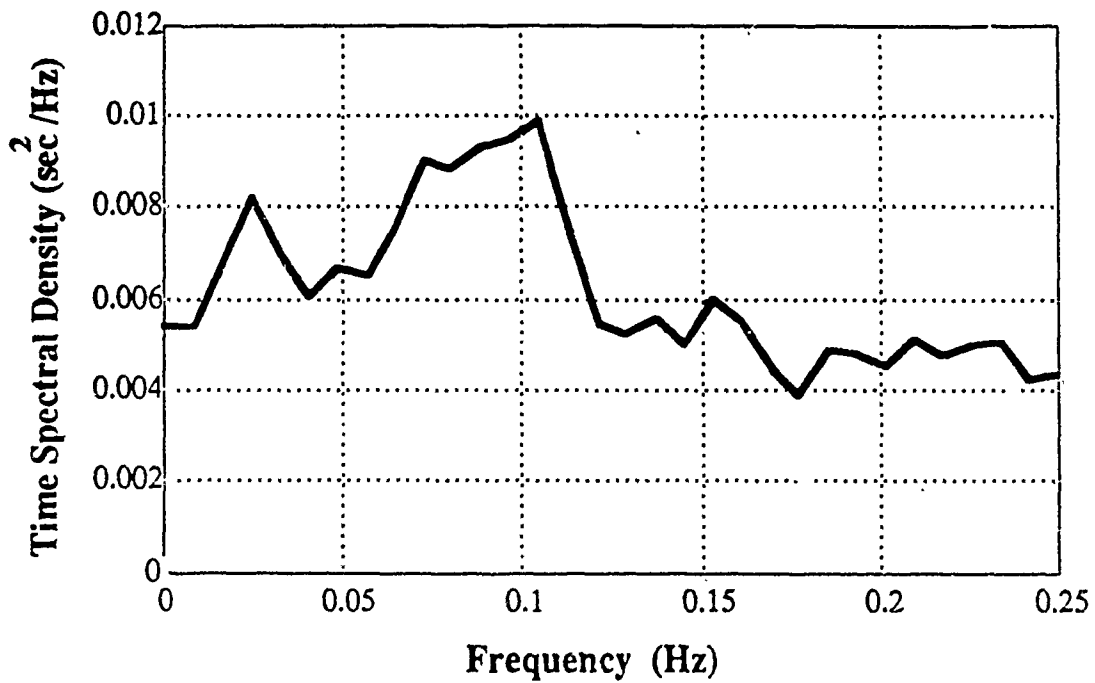
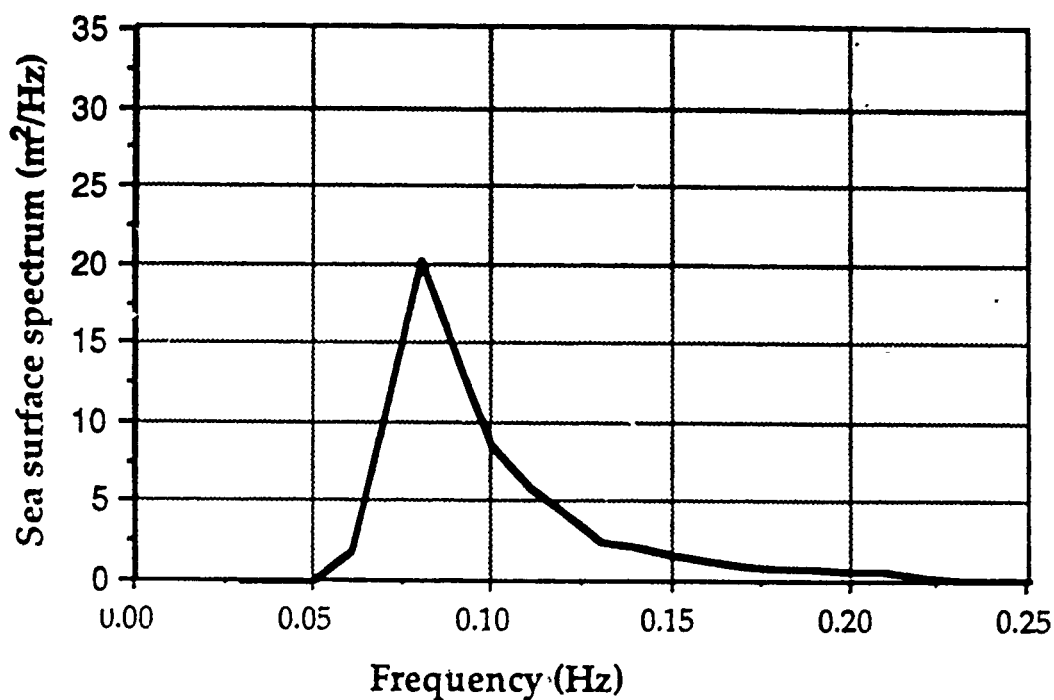


Figure D.27: Arrival time power spectrum for Station J. Spectrum from 2.2 hours of Arrival Time Series, 2001 to 2213 14DEC88 PST.



**Sea Surface Spectrum**  
**NDBC Buoy 14DEC88 2100 PST**



**Significant Wave Height 3.54 m**  
**Average Period 9.11 sec**  
**Dominant Period 12.50 sec**  
**Dominant Direction 314 N**

Figure D.28: Surface wave power spectrum in Monterey Bay. Data is from the NDBC buoy southwest of Santa Cruz, 2100 14DEC88 PST.

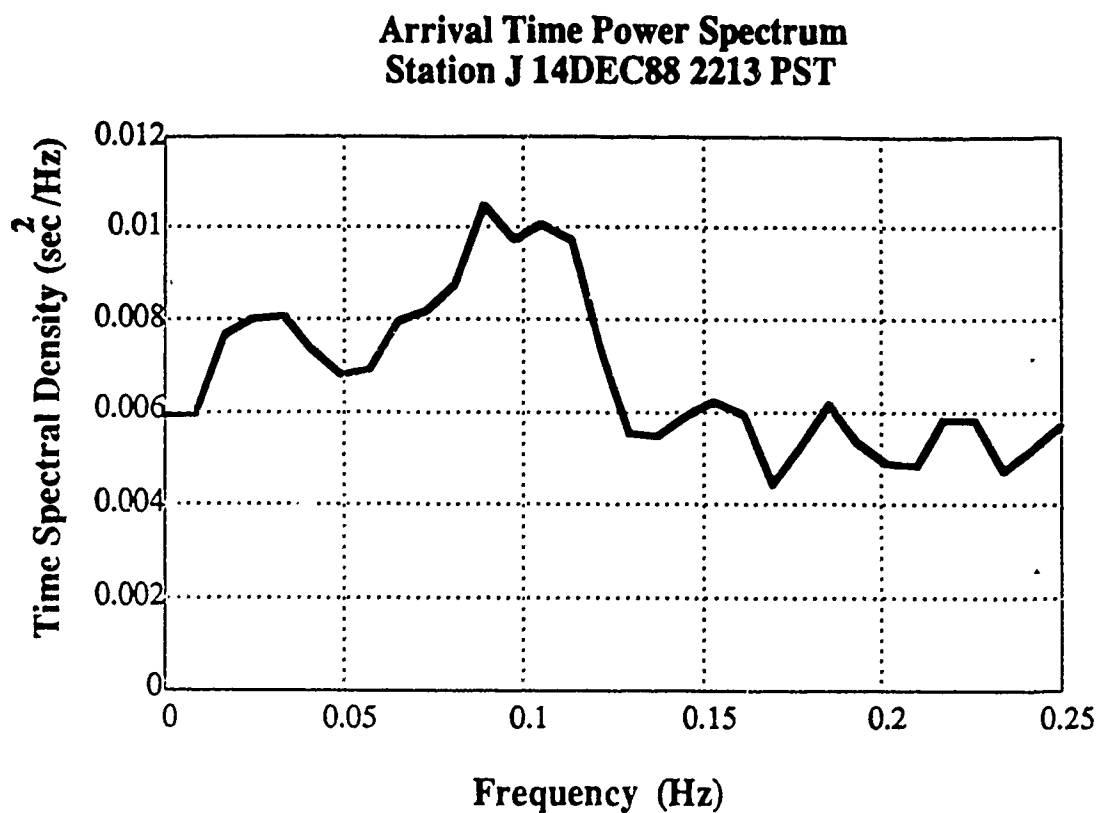
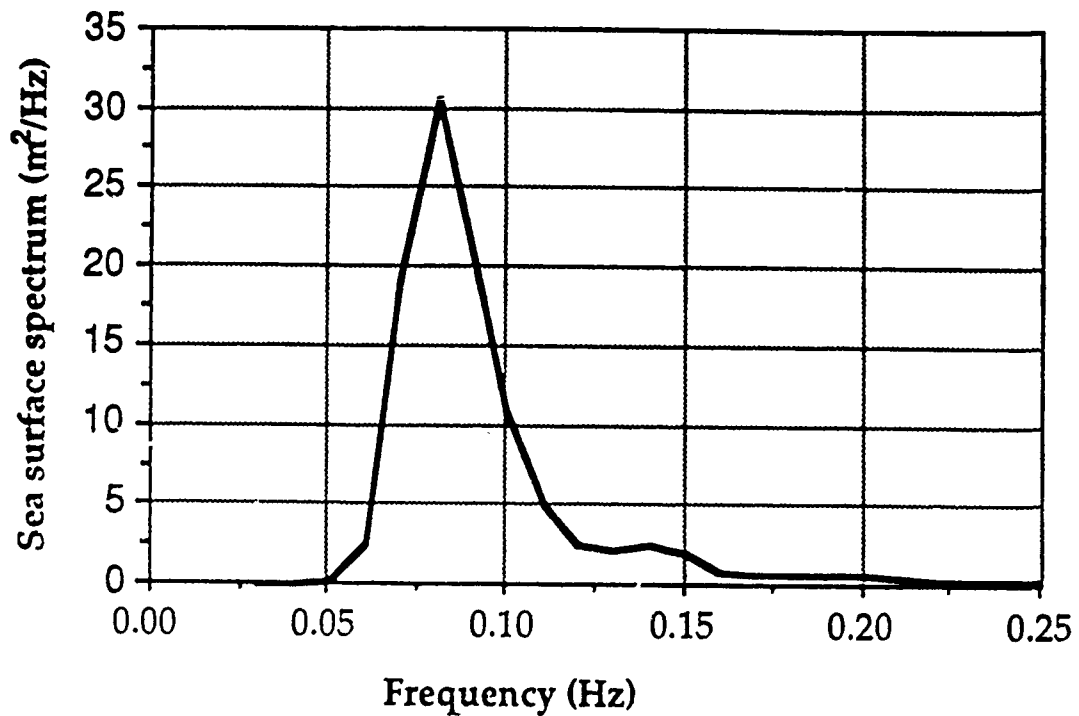


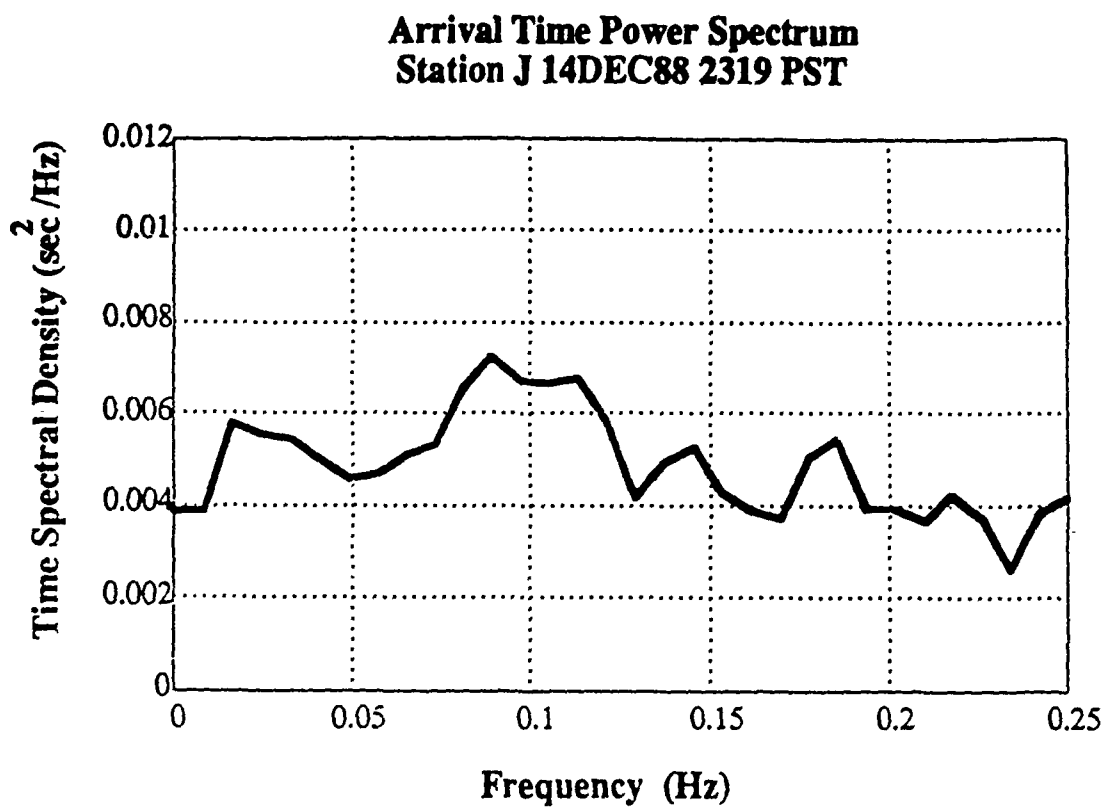
Figure D.29: Arrival time power spectrum for Station J. Spectrum from 2.2 hours of Arrival Time Series, 2107 to 2319 14DEC88 PST.

**Sea Surface Spectrum  
NDBC Buoy 14DEC88 2200 PST**



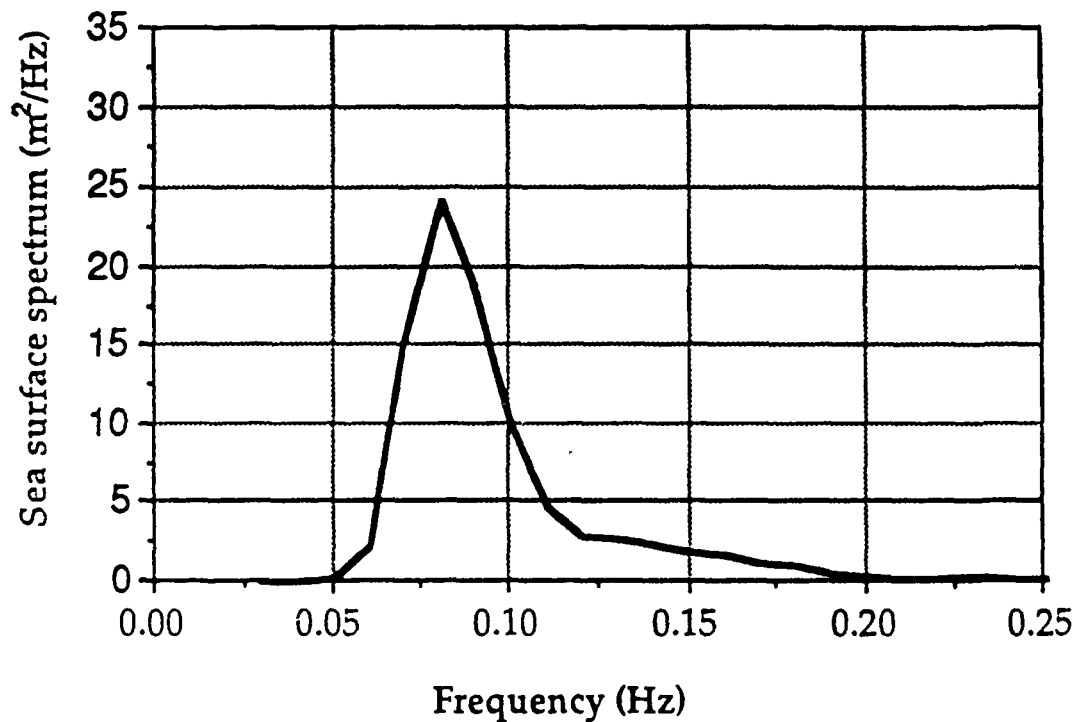
**Significant Wave Height 4.10 m  
Average Period 9.67 sec  
Dominant Period 12.50 sec  
Dominant Direction 308 N**

Figure D.30: Surface wave power spectrum in Monterey Bay. Data is from the NDBC buoy southwest of Santa Cruz, 2200 14DEC88 PST.



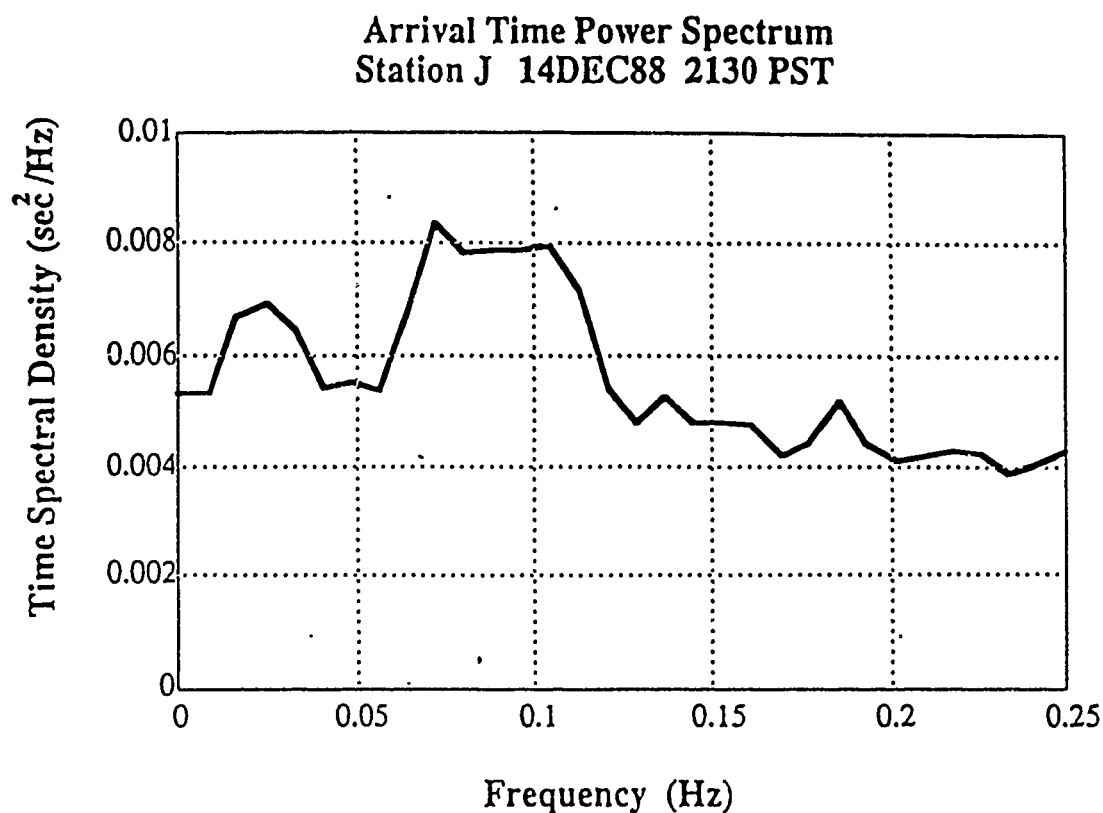
**Figure D.31: Arrival time power spectrum for Station J. Spectrum from 1.9 hours of Arrival Time Series, 2213 14DEC88 to 0005 15DEC88 PST.**

**Sea Surface Spectrum  
NDBC Buoy 14DEC88 2300 PST**



**Significant Wave Height 3.85 m  
Average Period 9.36 sec  
Dominant Period 12.50 sec  
Dominant Direction 321 N**

Figure D.32: Surface wave power spectrum in Monterey Bay. Data is from the NDBC buoy southwest of Santa Cruz, 2300 14DEC88 PST.



Spectrum from 5.2 hours of Arrival Time Series, 1855  
14DEC88 to 0005 15DEC88 PST

Figure D.33: Arrival time power spectrum for Station J. This spectrum was generated using the segmented FFT method on the data from an entire 6 hour tape (the maximum length time series without tape-to-tape synchronization).

# Bibliography

- [1] Spindel, R.C., "Ocean Acoustic Tomography: A Review," *Current Practices and New Technology in Ocean Engineering*, v. 11, pp. 7-13, 1986.
- [2] The Ocean Tomography Group, "A Demonstration of Ocean Acoustic Tomography," *Nature*, v. 299, pp. 121-125, 1982.
- [3] Munk, W. and Wunsch, C., "Ocean Acoustic Tomography: A Scheme for Large Scale Monitoring," *Deep-Sea Research*, v. 26A, pp. 123-161, 1979.
- [4] *Sound Transmission through a Fluctuating Ocean*, ed. Flatté, Stanley, pp. 3-61, Cambridge University Press, 1979
- [5] Spindel, Robert C., "Signal Processing in Ocean Tomography," *Adaptive Methods in Underwater Acoustics*, ed. H.G. Urban, pp. 687-710, D. Reidel Publishing Company, 1985.
- [6] Kinsler, L.E., Frey, A.R., Coppens, A., and Sanders, J. , *Fundamentals of Acoustics*, 3rd ed., pp. 117-120, John Wiley & Sons, 1982.
- [7] Liebelt, P.B., *An Introduction to Optimal Estimation*, Addison-Wesley, Reading, MA, 1967.
- [8] Franklin, J.N., "Well-posed stochastic extensions of ill-posed linear problems," *J. Math. Anal. Appl.*, v. 31, pp. 682-716, 1970.
- [9] Jackson, D.D., "Interpretation of inaccurate, insufficient, and inconsistent data," *Geophys. J. R. Astr. Soc.*, v. 28, pp. 97-109, 1972.
- [10] Jordan, T.H. and Franklin, J.N., "Optimal solutions to a linear inverse problem in geophysics," *Proc. Nat. Acad. Sci.*, vol. 68, pp. 291-293, 1971.

- [11] Provost, C., *A Variational Method for Estimating the General Circulation in the Ocean*, PhD Thesis, University of California, San Diego, 1983.
- [12] Menke, William, *Geophysical Data Analysis: Discrete Inverse Theory*, pp. 35 -160, Academic Press, 1984.
- [13] Smethie, Jr., W.M., *Some Aspects of the Temperature, Oxygen, and Nutrient Distributions in Monterey Bay, California*, Moss Landing Marine Laboratories Technical Publication 73-01, 1973.
- [14] Broenkow, W.W. and W. M. Smethie, Jr., "Surface Circulation and Replacement of Water in Monterey Bay," *Estuarine and Coastal Marine Science*, v. 6, pp. 583-603, 1978.
- [15] Lasley, S. R., "Hydrographic Changes in Monterey Bay Surface Waters in Relation to Nearshore Circulation," M.A. Thesis, San Jose State University, San Jose. CA, May, 1977.
- [16] Engineering-Science, Inc., *Montcrey Peninsula Water Pollution Control Agency Interim Report No. 4, Draft Oceanographic Predesign Report Volume 1*, pp.II21-II53, October, 1976.
- [17] Shepard, F.P. and Emery, K.O., *Submarine Topography off the California Coast: Canyons and Tectonic Interpretation*, Geological Society of America, pp. 72-79, 1941.
- [18] Scholl, D.W. and others, "The Structure and Origin of the Large Submarine Canyons of the Bering Sea," *Marine Geology*, v.8(3/4), pp.187-210, 1970.
- [19] Shepard, F.P. and Dill, R.F., *Submarine Canyons and Other Sea Valleys*, pp. 81-90, 223-231, 343-345, Rand McNally and Company, 1966.
- [20] Normack, W.R., "Growth Patterns of Deep-Sea Fans," *Am. Assoc. of Petrol. Geol. Bull.*, v. 54(11), pp. 2187-2192, 1970.
- [21] Combellick, R.A., and Osborne, R.H., "Sources and Petrology of Beach Sand from Southern Monterey Bay, California," *J. Sedim. Petrol.*, v. 47(2), pp. 891-907, 1977.
- [22] Welday, E.E., and Williams, J.W., *Offshore Surficial Geologic Map of California*, Map Sheet 26, 1975.



- [23] Shepard, F.P. and others, *Currents in Submarine Canyons and Other Sea Valleys*, pp. 14-51, 78-95, The American Association of Petroleum Geologists, 1979.
- [24] U.S. Army Corps of Engineers and the California Department of Boating and Waterways, *Coastal Data Information Program, Monthly Summary Report # 143 (December 1987)*, 6 January 1988.
- [25] U.S. Army Corps of Engineers and the California Department of Boating and Waterways, *Coastal Data Information Program, Twelfth Annual Report, January 1987 through December 1987*, by R.J. Seymour, D. Castel, and J.O. Thomas, 19 May 1988.
- [26] Clay, C.S. and Medwin, H., *Acoustical Oceanography: Principles and Applications*, pp. 11 - 16, 78-79 John Wiley & Sons, 1977.
- [27] Shea, R.E., and Broenkow, W.W., "The Role of Internal Tides in the Nutrient Enrichment of Monterey Bay, California," *Estuarine, Coastal and Shelf Science*, v. 15, pp.56-66, 1982.
- [28] Shepard, F.P., "Progress of Internal Waves Along Submarine Canyons," *Marine Geology*, v. 19, pp. 131-138, 1975.
- [29] Bascom, William, *Waves and Beaches*, pp. 5 - 73, Anchor Books, 1980.
- [30] Miller, J.H., Lynch, J.F., and Chiu, C.S., "Estimation of Sea Surface Spectra using Acoustic Tomography", *J. Acoust. Soc. Am.*, 86(1) pp. 326- 345, July 1989.
- [31] Sparton Defense Electronics ASW Technical Center, *Operation Manual for Mobile Inshore Underwater Warfare Moored Sensor Buoy AN/SSQ-58*, (7938-OPMAN-1), Sparton Corporation, Jackson, MI.
- [32] Naval Air Systems Command, *Sonobuoy Instructional Manual*, (NAVAIR 28-SSQ-500-1), Naval Weapons Support Center, Crane, IN.
- [33] Steele, Kenneth E., Lau, J.C., and Hsu, Y.L., "Theory and Application of Calibration Techniques for an NDBC Directional Wave Measurements Buoy," *IEEE Journal of Oceanic Engineering*, v. OE-10, no. 4, October 1985.
- [34] *Collecte Localisation Satellites*, ARGOS Location and Data Collection System, C.L.S., Toulouse, France, July 1987.

- [35] Ocean Data Systems, Inc., *Multiple Profile Restructuring and Supplemental Plot Programs*, by G. Jacobs, 30 June 1974.
- [36] Van Trees, Harry L., Detection, *Estimation and Modulation Theory, Part I*, pp. 273-287, John Wiley & Sons, 1968.
- [37] Press, William H. and others, *Numerical Recipes, The Art of Scientific Computing*, pp. 86-89, Cambridge University Press, 1986.
- [38] Bendat, Julius S. and Piersol, Allan G., *Random Data: Analysis and Measurement Procedures*, pp. 314 - 365, John Wiley & Sons, 1971.
- [39] U. S. Naval Oceanographic Office, *Integrated Command ASW Prediction Systems (ICAPS)*, NSTL, Bay St. Louis, MS.
- [40] National Oceanic and Atmospheric Administration, *Nautical Chart of Point Sur to San Francisco*, 24th ed., DMA Stock No. 18ACO18680, 21 February 1987.
- [41] Jones, R.M, Riley, J.P., and Georges, T.M., *HARPO: A Versatile Three-Dimensional Hamiltonian Ray-Tracing Program for Acoustic Waves in an Ocean with Irregular Bottom*, NOAA Wave Propagation Laboratory, Boulder, CO, October, 1986.
- [42] Newhall, A.E., Lynch, J.F., Chiu, C.S., and Daugherty, J.R., "Improvements in Three-Dimensional Raytracing Codes for Underwater Acoustics," ms. submitted to IMACS, April, 1989.
- [43] Ziemer, Rodger E. and Peterson, Rodger L., *Digital Communications and Spread Spectrum Systems*, pp. 385-404, Macmillan Publishing Company, 1985.
- [44] Birdsall, Ted, letter dated 27 May 1987, "My Introduction to Hadamard Processes for M-Sequences."
- [45] Cohn, Martin and Lempel, Abraham, "On Fast M-Sequence Transforms," *IEEE Transactions on Information Theory*, pp. 135 - 137, January 1976.
- [46] Borish, Jeffrey and Angell, James, "An Efficient Algorithm for Measuring the Impulse Response Using Pseudorandom Noise," *J. Audio Eng. Soc.*, v. 31, No. 7, pp. 478 - 488, July/August 1983.

## INITIAL DISTRIBUTION LIST

		No. Copies
1.	Dr. Richard Barber Monterey Bay Aquarium Research Institute 160 Central Avenue Pacific Grove, CA 93950	8
2.	Defense Technical Information Center Cameron Station Alexandria, Virginia 22314-6145	2
3.	Library, Code 0142 Naval Postgraduate School Monterey, California 93943-5002	2
4.	Prof. James H. Miller, Code 62Mr Department of Electrical and Computer Engineering Naval Postgraduate School Monterey, CA 93943	10
5.	LT Robert C. Dees, USN 207 Lauber Lane Derby, KS 67037	1
6.	Prof. Soenke Paulsen, Code 62Pa Department of Electrical and Computer Engineering Naval Postgraduate School Monterey, CA 93943	1
7.	Mrs. Theresa Rowan, Code 742 Naval Training Systems Center 12350 Research Parkway Orlando, FL 32826	1

- |     |   |   |
|-----|---|---|
| 8.  | Laura L. Ehret, Code 62Eh<br>Department of Electrical and Computer Engineering<br>Naval Postgraduate School<br>Monterey, CA 93943                 | 1 |
| 9.  | Prof. Timothy Stanton, Code 68St<br>Department of Oceanography<br>Naval Postgraduate School<br>Monterey, CA 93943                                 | 1 |
| 10. | Prof. Edward Thornton, Code 68Tm<br>Department of Oceanography<br>Naval Postgraduate School<br>Monterey, CA 93943                                 | 1 |
| 11. | Prof. Lawrence J. Ziomek, Code 62Zm<br>Department of Electrical and Computer Engineering<br>Naval Postgraduate School<br>Monterey, CA 93943       | 1 |
| 12. | Prof. John P. Powers, Code 62<br>Chairman<br>Department of Electrical and Computer Engineering<br>Naval Postgraduate School<br>Monterey, CA 93943 | 1 |
| 13. | Director of Research, Code 012<br>Naval Postgraduate School<br>Monterey, CA 93943   | 1 |